ERRATA

Technical Report No. 134

Cooley Electronics Laboratory

Page 15, Equation 2.7	n in numerator of first term should be m.
Page 15, line following Equation 2.7	(2.4b) should be (2.4).
Page 95, Section 4.3	Should be labeled Section 6.3.
Page 95, third line following Equation 6.49	Fig. 4.3 should be Fig. 6.3.
Page 125, Fig. 8.5	Ordinate should be labeled t.
Page 145, Fig. 9.5	Ordinate should be labeled GAIN (DB).
Page 155, Fig. 9.7	Abscissa should be labeled $\omega_p/\sqrt{1.56\,\beta\omega_d}$.
Page 198, Footnote 1	Should refer to footnote on page 56.
Page 199, Fig. 10.6	Ordinate should be labeled T/T_D.

Page 58, Equation 4.30

Should read

$$F_{ru} = 1 + \frac{T_d}{T_o}\left[\frac{g_{dr}}{g_s} + \frac{\bar{\omega}_r g_r g_{du}}{\bar{\omega}_u g_u g_s \rho_u} + \left(\frac{\bar{\omega}_r g_r}{\omega_u g_s \rho_u} - \frac{1}{G_{ru}}\right)\frac{T_L}{T_d}\right]$$

Page 134, third paragraph

All references to "noise figure" should be, more specifically, to "noise temperature."

The noise temperatures in the Table are relative to T_d.

Technical Report No. 134

4853-7-T

A STUDY OF DOUBLE-SIDEBAND REACTIVE MIXERS

by

D. K. Adams

Approved by: B. F. Barton

for

COOLEY ELECTRONICS LABORATORY

Department of Electrical Engineering
The University of Michigan
Ann Arbor

Contract No. DA-36-039 sc-89227
Signal Corps, Department of the Army
Department of the Army Project No. 3A99-06-001-01

Submitted in partial fulfillment of the requirements for
the degree of Doctor of Philosophy in
The University of Michigan

December 1962

ACKNOWLEDGEMENTS

The author wishes to thank the members of his doctoral committee for their comments and technical guidance. Special appreciation is due Professor C. B. Sharpe for his encouragement and council.

Further, the author wishes to thank Mr. Wilbur J. Nelson for his patient help with the experimental portions of this work, and to Mr. Herb Brett of the U. S. Army Signal Corps for his suggestion that the phase modulation amplifier problem be treated.

Special gratitude is owed to Mr. Robert E. Graham, Mrs. Lillian M. Thurston, and to Miss Ann M. Rentschler for preparing this manuscript for publication.

Finally, the author is appreciative of the support the U. S. Army Signal Corps has given this work.

TABLE OF CONTENTS

TABLE OF CONTENTS (Cont.)

LIST OF ILLUSTRATIONS

LIST OF ILLUSTRATIONS (Cont.)

LIST OF ILLUSTRATIONS (Cont.)

LIST OF SYMBOLS

SYMBOL	MEANING	DEFINED BY, OR FIRST USED IN
ω	angular frequency	Fig. 1.2.
$\overline{\omega}$	midband frequency	footnote 1, Ch. I
ω_p, ω_r	two reference frequencies	(1.1)
ω_{mn}	$m\omega_p + n\omega_r$	(1.1)
m, n	subscript integers	(1.1)
m'', m', n'	dummy subscript integers	(3.1)

Table of Special Subscripts

Subscript	Equivalent m and n	
	m	n
p	1	0
r	0	1
u	1	1
ℓ	1	-1
2p	2	0

Fig. 1.4

x (Ch. II)	$\omega_p t$	(2.1c)
y (Ch. II)	$\omega_r t$	(2.1c)
i(t)	instantaneous current	Fig. 1.3
v(t)	instantaneous voltage	Fig. 1.3
q(t)	instantaneous charge	(2.3)
$\mathbb{I}$(t)	instantaneous source current	Fig. 1.3
q(v)	charge-voltage law of nonlinear capacitor	(2.2)
I_{mn}	Fourier coefficient of i(t) at ω_{mn}	(2.1b)
V_{mn}	Fourier coefficient of v(t) at ω_{mn}	(2.1a)
Q_{mn}	Fourier coefficient of q(t) at ω_{mn}	(2.4)
$\mathbb{I}_{mn}$	Fourier coefficient of $\mathbb{I}$(t) at ω_{mn}	Fig. 1.3
W_{mn}	average power entering mixing element at ω_{mn}	(2.5a)

LIST OF SYMBOLS (Cont.)

SYMBOL	MEANING	DEFINED BY, OR FIRST USED IN
V	dc voltage	(2.11)
Q	dc charge	(2.11)
a_1, a_2	Taylor series coefficients in charge-voltage representation	(2.11)
$i_{sc}(t)$	instantaneous short circuit current	(2.13)
$v'(t)$, $v''(t)$	special voltage waveforms	(2.19)
$c'(t)$	special capacitance waveform	(2.20)
$Y(\omega)$	total admittance	(2.17a)
$\widetilde{Y}(\omega)$	external admittance (not parasitic)	Fig. 1.3
$Y'(\omega)$	parasitic admittance	(2.17a)
g, $\widetilde{g}$, g'	conductive parts of total, external, and parasitic admittances, respectively	Fig. 3.4
b, $\widetilde{b}$, b'	susceptive parts of total, external, and parasitic admittances, respectively	Fig. 3.4
Y_{mn}, $\widetilde{Y}_{mn}$, Y'_{mn}	Fourier components of total, external, and parasitic admittance respectively, at ω_{mn}	(2.17a), (1.2)
C	average capacity of pumped, nonlinear capacitor	(2.14)
Y_{in}, g_{in}	input admittance and conductance, respectively	Fig. 3.4
γ_p	Fourier component of time-varying capacity at ω_p	(2.24b)
γ_{2p}	Fourier component of time-varying capacity at $2\omega_p$	(2.24c)
γ_r	Fourier component of time-varying capacity at ω_r	(2.30b)
C_{mn}	total shunt capacity at ω_{mn}	(4.14)
$[Y_A]$, $[Y_B]$,	admittance matrices	(2.32b)
$[P]$, $[V]$, $[I]$	matrices	(2.32c)
$[\mathbb{I}]$, $[Y_{mn}]$	matrices	(2.33b)
g_S, g_L	source and load conductance, respectively	Fig. 3.4
σ, A	parameters	(2.10)

SYMBOL	MEANING	DEFINED BY, OR FIRST USED IN
$\hbar$	(Planck's constant)/2π	(3.8)
N	events/second	(3.8)
G_{ij}	transducer gain from ω_i to ω_j	(3.15b)
$\widetilde{G}_{ij}$	G_{ij}, neglecting parasitic loss	(3.16b)
$\overline{G}_{ij}$	midband gain	(3.17)
B	bandwidth in cycles/second	(3.17)
β	bandwidth in radians/second	(3.18)
k	Boltzmann's constant	Fig. 3.5
T	noise temperature	Fig. 3.5
T_o	290^o K	Fig. 3.5
F_{ij}	noise figure from conversion from ω_i to ω_j	(3.19)
T_{ij}	noise temperature for conversion from ω_i to ω_j	(3.20b)
T'	noise temperature of parasitic conductance	Fig. 3.6
T_L	noise temperature of load conductance	Fig. 3.6
$\widetilde{T}_\ell$	noise temperature of dummy load	(8.39)
T_d	noise temperature of varactor diode	(4.26)
t	T_L/T_d	(5.31b)
s	$\widetilde{T}_\ell/T_d$ } s = t, if ω_ℓ is the output frequency	(8.40)
r_d	parasitic series resistance of varactor	Fig. 3.7
g_d	effective parasitic shunt conductance of varactor	Fig. 3.7
Q_d	Q of varactor	(3.28)
g_{dr}, $g_{d\ell}$, g_{du}	g_d at ω_r, ω_ℓ, ω_u, respectively	(3.33)
ω_d	frequency where varactor Q equals one (neglecting parasitic inductance)	(3.29)
ω'_d	$\omega_d\gamma_p/C$	footnote 1, Ch. IV
L	self inductance	Fig. 4.1
M	mutual inductance	Fig. 4.1

LIST OF SYMBOLS (Cont.)

SYMBOL	MEANING	DEFINED BY, OR FIRST USED IN
k_p	pumping coefficient at ω_p	(4.15)
ρ_u	a parameter relating effect of ω_u on ω_r	(4.18c)
ρ_ℓ	a parameter relating the effect of ω_ℓ on ω_r	(5.8)
K	a parameter for measuring the effect of varactor loss	(4.22)
R_r, R_u	$(\omega_r/\omega'_d)^2$, $(\omega_u/\omega'_d)^2$	(4.32), (4.38)
x, y, z	efficiency factors	(4.33)
P_A	power available	(5.7)
S	sensitivity	(5.18)
a_n, b_m	coefficients	(6.1)
$\phi_{ij}(t)$, $\theta_i(t)$	periodic coefficients	(6.3)
x_i	dependent variable in a set of linear differential equations	(6.3)
μ	characteristic root	(6.4)
μ_k	kth characteristic root	(6.5)
μ_k^o, μ_k', μ_k''	zeroth, first, and second-order approximations to μ_k	(6.33)
y_i, y_{ik}	periodic functions	(6.4)
η_k, $\eta_{\nu k}$	parameters	(6.7), (6.39)
η	detector efficiency factor	(9.20)
Δ, Δ_s	determinants	(6.9)
D, D_s	determinants	(6.11b)
N_{nm}^s	a parameter	(6.12)
B_s	an initial condition	(6.13)
P_s	a periodic function	(6.13)
P_r, P_ℓ	poles of a network	(6.19)
σ, Ω	real and imaginary part of network poles	(6.19)
Z_1, Z_2	zeros of a network	(6.19)
k_1, k_2	real parts of network zeros	(6.19)

LIST OF SYMBOLS (Cont.)

SYMBOL	MEANING	DEFINED BY, OR FIRST USED IN
e, f	parameters	(6.24)
L, C, R	inductance, capacitance, and resistance of network	Fig. 6.3
α (Ch. VI)	a perturbation parameter	(6.27b)
α	a noise figure parameter	(A-5)
a_{ij}	a matrix element	(6.38)
a_{ij}^{o}, $a_{ij}^{'}$	zeroth and first approximations to a_{ij}	(6.34)
s (Ch. VI)	a parameter	(6.28)
s	T_L/T_d	(8.40)
s_c	a critical value of s (Ch. VI)	(6.36)
c_{ij}	a matrix element	(6.38)
Δ	system determinant	(8.6)
a (Ch. VIII)	a parameter	(8.49)
N(Ch. VIII)	a parameter	(8.73)
β_r, β_p	bandwidth at ω_r, ω_p respectively	(9.1), (9.21)
M (Ch. IX)	index of phase modulation	(9.4b)
G_{PM}	transducer gain by phase modulation	(9.19)
η	detector efficiency factor	(9.20)
G_r	$\eta^2 G_{PM}$	(9.20)
T_p	effective noise temperature of pump tank	(9.58)
$\widetilde{T}_p$	effective noise temperature of external circuit losses in pump tank	(9.58)
di_N	incremental noise current	(9.59)
$\widetilde{P}_p$	total noise power reaching external load	(9.64)
B, ϕ_B	amplitude and phase of inserted carrier	(9.67)
N, ψ	amplitude and phase of resultant carrier	(9.68a)
λ, ν, μ (Ch. IX)	parameters	(9.78b)
ξ	phase parameter	(10.1)

LIST OF SYMBOLS (Cont.)

SYMBOL	MEANING	DEFINED BY, OR FIRST USED IN
τ_r, τ_ℓ, τ_u	normalized admittances of ω_r, ω_ℓ, ω_u, respectively	(10.1)
τ'_r, τ'_ℓ, τ'_u	normalized conductance at ω_r, ω_ℓ, ω_u, respectively	(10.1b)
τ''_r, τ''_ℓ, τ''_u	normalized susceptance at ω_r, ω_ℓ, ω_u, respectively	(10.1)
$\tilde{\Delta}$	normalized system determinant	(10.2a)
$\tau_{r_{in}}$, $\tau_{u_{in}}$, $\tau_{\ell\,in}$	normalized input admittance at ω_r, ω_u, ω_ℓ, respectively	(10.4)
Y_{12}	image admittance at ω_1, due to conversion to ω_2	(10.5)
τ_{12}	normalized image admittance	(10.6)
θ_{12}	propagation constant between ω_1 and ω_2	(10.6)
τ_o	$\lvert\sin\xi\rvert + j\cos\xi$	(10.14a)
k_{2p}	coefficient of harmonic pumping	(10.23)
p (Ch. X)	$\lvert\gamma_{2p}/\gamma_p\rvert$	(10.43b)
ρ	reflection coefficient	(11.1)
p, q, u (App. B)	parameters	(B-1)

LIST OF APPENDICES

ABSTRACT

Reactive mixing can be accomplished by any nonlinear, or time-varying, energy storage element. In double-sideband reactive mixing, interactions take place between information carrying signals at only three frequencies. Such interactions require the presence of pumping or local oscillator signals at appropriate frequencies. The basic mixing spectrum treated in this study employs ω_r, ω_ℓ, and ω_u as information carrying signals, and ω_p and $2\omega_p$ as pumping frequencies; where $\omega_u = \omega_p + \omega_r$ and $\omega_\ell = \omega_p - \omega_r$. In the text, these pumping frequencies are shown to provide all possible first-order interactions between ω_r, ω_ℓ and ω_u. Also, the interactions in the latter set are shown to occur in an infinite number of other signal sets. Therefore, the double-sideband reactive mixers problem is generic to many reactive mixer configurations of practical interest. The purpose of this study is to extend the understanding of reactive mixers through an analysis of the double-sideband configuration.

Two basic cases are treated, one with a single pump at ω_p and the other with double pumping at ω_p and $2\omega_p$. The useful engineering properties of each system are evaluated, and compared with the better known properties of single-sideband reactive mixers. Consideration is given to such circuit properties as conversion gain, stability, bandwidth, and noise figure. In many cases, significant improvements are noted, which are explained by a new technique of reactive mixer modeling.

In the single-pump case, single-sideband conversion between ω_r and ω_u offers the greatest gain-bandwidth product, but conversion between ω_r and ω_ℓ offers the greatest gain. When combining these cases, it is shown that the presence of ω_ℓ can produce a finite increase in gain between ω_r and ω_u, without reducing the original gain-bandwidth product. Alternately, an arbitrary increase in gain is possible with a 30 percent reduction in gain-bandwidth product. By the same technique, improvements are also noted in the conversion noise figure between ω_r and ω_u, particularly in the down-conversion mode.

In the double-pumping case, an interesting class of unilateral conversions are obtained. One of these offers arbitrarily large conversion gains between ω_r and ω_u, with gain-independent input and output terminal impedances. This mode of operation is capable of yielding larger gain-bandwidth products, greater circuit stability, and significant improvements in down-conversion noise figure.

Perhaps the most significant practical outcome of this study is the development of a stable, ultra-wideband, video amplifier by double-sideband reactive mixing. Gains of 20 db and bandwidth from dc to 100 Mc are predicted for a single mixer element. Experimental realizations of this system are shown and discussed. It is also demonstrated that this is a form of parametric amplification by phase modulation.

Another theoretical problem that has been closely related to this study is the stability of periodically-varying networks. The interrelation of these problems has led to a new method of predicting the stability of linear systems with periodically varying parameters. This method requires a knowledge of sinusoidal steady-state response, but it does not entail a solution of the system differential equations. Therefore, this method of determining stability is less tedious than the normal method of calculating characteristic roots. It also provides a new approach for approximating the characteristic roots of a periodically-varying system.

CHAPTER I

INTRODUCTION

The general properties of reactive mixers have been illustrated in classical problems dating back 100 years or more to the work of Faraday, Melde, and Lord Rayleigh (Ref. 1). Although these early illustrations of reactive mixing were nonelectrical by nature, they demonstrate a principle that can be readily depicted by a simple electrical example. Consider the parallel plate capacitor in Fig. 1. 1. When charge exists on the plates, work will be done when the plate separation is increased, but if the charge is then removed, the plates can be returned to their original position without involving further work. This process can be made continuous by adding an inductor to form an oscillating circuit. The capacitor is then alternately charged and discharged twice each cycle, so by separating the capacitor plates suddenly when it is charged and returning them when it is discharged, energy will be continually added to the oscillating system.

If a resistor is now added that exactly dissipates the supplied mechanical energy, steady ac power will be delivered to the resistor at half the frequency of the moving capacitor plates. But if the resistor is further reduced until the oscillation stops, it can then be established that an applied signal will be amplified if its frequency is near the oscillation frequency. In this case, the signal mixes with the time-varying capacitor and produces a difference frequency or lower sideband near the oscillation frequency, as depicted in Fig. 1. 2. The added presence of a lower sideband allows the applied signal to be amplified regardless of the timing (or phase) of the mechanical work. A more comprehensive explanation of this effect will follow from a general study of reactive mixing.

Mixing is a general phenomena that arises whenever there is coupling between sinusoidal variations with different frequencies. In the most common instance, mixing is caused by nonlinear couplings; but it can also be associated with linear, time-varying

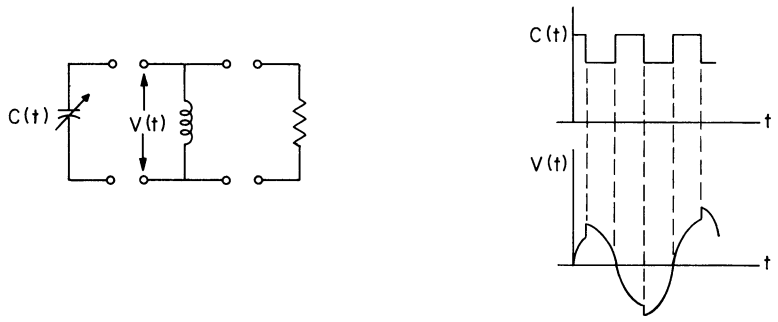

Fig. 1.1. Energy conversion by a time-varying capacitor.

couplings if the coupling element itself constitutes one of the two required variations. The previous example is illustrative of the latter case. Only in linear time-invariant couplings does mixing fail to occur, but such couplings exist only as an idealization, so it can be concluded that frequency mixing is prevalent in all physical systems.

The basic process of frequency mixing can be described as follows. If two signals with angular frequencies ω_r and ω_p are coupled by a mixing element, the resultant steady-state signal will tend to contain all positive frequencies in the set

$$\omega_{mn} = m\omega_p + n\omega_r ; \qquad m,n = 0, \pm 1, \pm 2, \ldots , \tag{1.1}$$

which set is fundamental to all steady-state mixing processes. An additional characteristic of mixing is the Fourier distribution of signal among (1.1), but this distribution is strongly dependent upon the type of mixing element.

There are two extreme element types that are useful for characterizing mixing distributions. One is the storage element, which is commonly called a reactance, and the other is the dissipative element, which can be characterized by a resistor. A marked difference in mixing properties is noted when resistive and reactive elements are compared. This difference arises even though it is always a nonlinear or time-varying coupling that produces mixing in any element type. Since the mixing properties of resistive elements are well-known, the contrasting properties of reactive mixers seem quite unusual. In fact, when compared with the resistive mixer, the reactive mixer is an intriguing physical system. Therefore, an investigation of the unusual properties of reactive mixers has been chosen as the general purpose of this analysis.

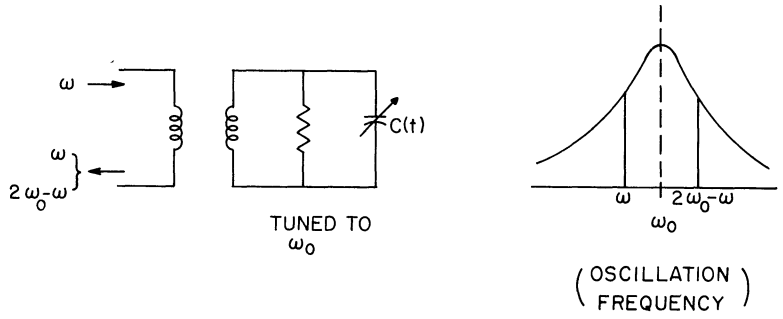

Fig. 1.2. Amplification by mixing with a time-varying capacitor at period π/ω_0.

Once the mixing element itself is restricted to a certain class, either resistive or reactive, the auxiliary circuitry surrounding this element gives rise to the next order of influence on its mixing properties. Such external circuitry will be assumed to be linear and time-invariant, so it can be represented at the terminals of the mixing element by a Norton equivalent admittance, $\tilde{Y}(\omega)$.

For the present, let it be considered that mixing is due to nonlinearity. The basic signals at ω_{01} and ω_{10} (i.e., at ω_r and ω_p) can then be applied by current generators with complex amplitudes $\mathbb{I}_{01}$ and $\mathbb{I}_{10}$, respectively. However, the tendency for currents to flow through the mixing element at all frequencies in (1.1) is unchanged when external generators are applied at any, or all, of the ω_{mn}. Therefore, a general model for the nonlinear reactive mixer is provided by the circuit in Fig. 1.3. Later, it will be shown that linear reactive mixers can also be treated by Fig. 1.3, as a special case.

The components I_{mn} in the general source waveform $\mathbb{I}(t)$ can exist at each frequency in the set ω_{mn}, so a great variety of source waveforms are possible. The procedure of this investigation will be to determine the steady-state v(t) and i(t) that result from specific $\mathbb{I}(t)$ waveforms. In particular, source waveforms will be considered that are made up of certain combinations of sinusoidal signals in the set $\mathbb{I}_{mn}$. In each case, the discrete set ω_{mn} will include all involved frequencies, so it will be convenient to define

$$\tilde{Y}_{mn} = \tilde{Y}(\omega_{mn}) \tag{1.2}$$

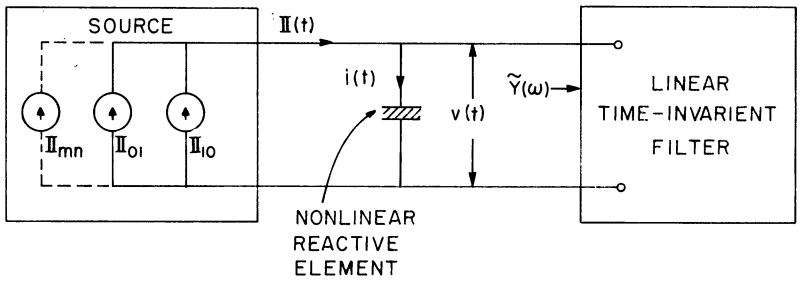

Fig. 1.3. The basic representation of a reactive mixer.

Although v(t) and i(t) tend to contain all positive ω_{mn}, the steady-state power flow will be restricted to a finite band in all cases of interest here. The filter characteristic $\tilde{Y}_{mn}$ will thus be chosen to short circuit, or otherwise suppress, all but a finite set of frequencies. This step calls for unrealizable $\tilde{Y}(\omega)$, but realizable $\tilde{Y}(\omega)$ will be shown to yield satisfactory approximations in many cases, partly because ω_r and ω_p will be assigned different roles in the mixing process.

The frequency ω_r will be treated as the reference frequency for a signal being processed by the mixer, while ω_p and its harmonics $m\omega_p$ will be considered local oscillators, or "pumps," for supplying RF power to the mixer. In some configurations, the signal will actually be applied at ω_r, in which case ω_r can be properly termed the signal frequency. In other cases, the applied signal will have one of the "sideband" frequencies $m\omega_p + n\omega_r$ ($n \neq 0$), which explains why ω_r is given the more general term, the signal reference frequency. When $n \neq 0$, the set $m\omega_p + n\omega_r$ will be termed the set of signal frequencies. The latter set is to be contrasted with the set of pump frequencies which are characterized by $n = 0$.

When reactive mixers of higher complexity are employed in a system, it should be noted that a higher over-all system complexity does not necessarily result. For example, the reactive mixer configurations in common usage today frequently require auxiliary equipment, such as circulators, to yield useful characteristics. Also, the broadbanding techniques that have been developed for simple reactive mixers call for a higher complexity of nonmixing (i.e., linear) circuitry. This analysis will show, however, that high spectral complexity can yield the same improvements. In addition, reactive mixers offer circuit effects that are not easily duplicated with ordinary circuit components. Therefore, multiple-sideband reactive mixers are of practical engineering interest.

1.1 Statement of the Problem

The main interest in reactive mixers to date has been in cases where the signal components are linearly related. This situation tends to prevail when the applied signal amplitude is small when compared to the pump amplitudes, and in this case several important circuit effects have been successfully realized. Foremost of these is conversion gain between two or more signal frequencies. In addition, such conversion gain is frequently accompanied by low noise figures and by gain-bandwidth products that tend to be proportional to pump frequency. These attributes are readily demonstrated in reactive mixers employing simple spectral configurations, which immediately prompts such questions as, "What benefits can be derived from reactive mixers employing more complicated sideband configurations?", and "What analytical procedures are required to explain and to evaluate these higher-order systems?" This analysis will attempt to answer these questions.

Particular attention will be given to the spectral configurations that occur when $\tilde{Y}(\omega)$ suppresses all but three frequencies in the signal frequency set, and all but two of the pump frequencies. These double-sideband cases will be termed symmetrical or unsymmetrical according to the symmetry of the signal frequencies, exclusive of ω_r, with respect to ω_p. For example, a case of symmetrical, double-sideband mixing occurs when the mixing products of ω_p and ω_r are restricted to the pair $\omega_p \pm \omega_r$. However, the term symmetrical, as used here, does not distinguish the frequency at which signal is applied. For instance, in the symmetrical example just cited, the applied signal may be at ω_r, $\omega_p - \omega_r$, or $\omega_p + \omega_r$.

Two reasons can be given for restricting the emphasis in this analysis to three-signal frequency (or double-sideband) cases. These are:

(1) In concentrating on single-sideband resistive mixers, previous treatments have shown that individual cases yield distinctive circuit properties. Therefore, circuit properties of greater scope can be anticipated when the effects of two individual sidebands are combined.

(2) The increased complexity of multiple-sideband mixers greatly incumbers detailed analysis. Therefore, when consideration is limited to double-sideband circuits, a reasonable compromise is made between preserving

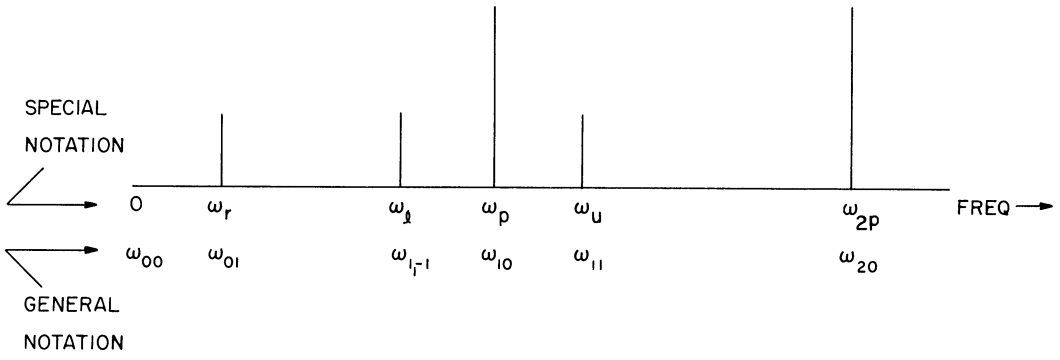

Fig. 1.4. A basic double-sideband spectrum. Since this analysis will be primarily concerned with such a spectrum, the special notation above will frequently be substituted for the general notation defined in (1.1).

analytical simplicity and obtaining an increased perception of the inherent properties of reactive mixers.

Whenever interest is restricted to a particular set of frequencies, it becomes convenient to introduce an alternate frequency notation. The special set of frequencies in Fig. 1.4 will receive considerable attention here, so much of the formulation to follow will be based on the special notation in this figure.

The assumption that all power flow is restricted to a few frequencies is an obvious idealization. It can always be employed heuristically, but for practical reasons an immediate appraisal of this assumption is required. Certainly real filtering techniques cannot prevent some power flow outside a desired set of frequencies. However, a peculiar aspect of reactive mixers influences this tendency. It will be shown that power flow between two frequencies chosen at random can occur in either direction. Therefore, with a large number of extraneous couplings, cancellation will tend to occur. On the other hand, a large number of extraneous couplings of approximately the same magnitude is unlikely, since multiple mixing is generally required for coupling to frequencies well removed from the desired signal set. Multiple mixing tends to produce weak coupling, particularly when small signal amplitudes are involved. Therefore, in any given circuit, it can be expected that only a few extraneous couplings will create problems. In this case, unrealizable $\tilde{Y}(\omega)$, that are assumed to suppress all but a certain set of sidebands, can be successfully approximated. One technique

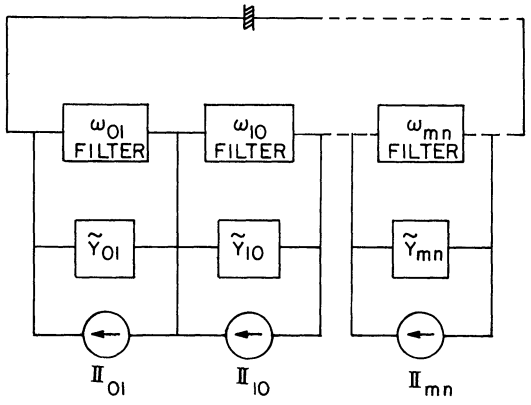

Fig. 1.5. An equivalent circuit for Fig. 1.3. It is equivalent to Fig. 1.3 when none of the ω_{mn} are suppressed, and is a convenient idealization when $Y(\omega)$ is assumed to suppress all but a finite number of the ω_{mn}.

is to design $\tilde{Y}(\omega)$ that support the desired sidebands and suppress any unwanted sidebands with large couplings. The asymptotic behavior of such $\tilde{Y}(\omega)$ would then be relied upon to suppress the more weakly coupled sidebands.

Filter networks of the type just described tend to yield relatively narrow bandwidths for the desired sidebands. It will be convenient to idealize this effect, by postulating a set of ideal filters with the following property: each filter is an open circuit in one narrow band of frequencies, centered at $\bar{\omega}_{mn}$,[1] and a short circuit elsewhere. The modification made by introducing these ideal filters is shown in Fig. 1.5, where each filter is represented by a box and is labeled with its open circuit center frequency. This equivalent of Fig. 1.3 is nonrealizable, but because of its computational value it will be the basis of much of the analysis to follow. Now, for example, the circuit admittance influencing each frequency band appears at a separate terminal pair, and hence can be independently varied.

In practical design problems, an optimum set of terminal admittances $\tilde{Y}_{mn}$ can be obtained more easily from the model in Fig. 1.5, than from Fig. 1.3. So to realize this design in an actual circuit (e.g., Fig. 1.3), the linear network $\tilde{Y}(\omega)$ would have to be chosen to approximate the desired $\tilde{Y}_{mn}$ when $\omega_{mn} \approx \bar{\omega}_{mn}$, and to become a short circuit elsewhere. This suggests that each $\tilde{Y}_{mn}$ must resemble a parallel resonant circuit with fairly high Q. When this is the case, a good first approximation to Fig. 1.3 will result if the ideal filters in

[1]The symbol $\bar{\omega}$ will be used to denote a midband value. For example, $\bar{\omega}_{mn}$ denotes the midband value of those frequencies generally identified as ω_{mn}.

Fig. 1.5 are simply removed.

In dealing with Fig. 1.5, it will be demonstrated that conversion gain is possible between a variety of terminal pairs. Reactive mixer conversion gain also occurs with far more extensive characteristics than are possible in linear, bilateral, multiport networks. To aid in cataloging these effects, the following basic circuit quantities will be of interest:

(1) Transducer conversion gain from ω_{mn} to $\omega_{m'n'}$

(2) Conversion bandwidth

(3) Noise figure

(4) Sensitivity to parameter variation

Each of these quantities will depend on

(1) the number and character of the unsuppressed signal sidebands,

(2) the terminal admittances $\tilde{Y}_{mn}$ at each unsuppressed signal frequency, and

(3) degrading influences, such as incidental loss in the mixing element.

The basic techniques for making these circuit evaluations will be reviewed in Chapter II.

1.2 Review of the Literature

One of the first practical applications of reactive mixers was by E. F. W. Alexanderson (Ref. 2), who, in 1916, used a saturable inductor to modulate a high-power alternator for a carrier telephone system. In this way, Alexanderson demonstrated how a nonlinear reactance can implement the control of high-level carrier power by low-level signal power. In turn, this suggested to Alexanderson, and to others, that immediate detection of the carrier could recover an amplified version of the applied signal. However, due to the rapid advance of other means of amplification, principally vacuum tubes, the latter step appears to have been postponed for many years.

Both the Alexanderson modulator and the simple circuit in Fig. 1.2 illustrate how the energy of an oscillating system (i.e., a signal) can be increased by supplying energy at another frequency (i.e., the carrier), which can be alternately viewed as frequency mixing. Hence the term reactive mixing could have been appropriately applied long before it was

actually introduced. In fact, the general topic of reactive mixers was obscure in technical literature for the next thirty years. Then, mainly by accident, certain diodes that were developed for mixers in radar receivers were found to yield gain. Being foreign to resistive mixers, this phenomenon was attributed to a voltage-dependent capacitance in the barrier junction. Shortly afterward, H. C. Torry (Ref. 3) developed a basic description of nonlinear capacitance converters, and showed theoretically how these effects were possible.

The next five or ten years saw parallel developments in theory (Refs. 4, 5, and 6) and in experimental verifications (Ref. 7), although certain experimental deficiencies were yet to be overcome. Theory was predicting low-noise conversion with gain, but the measured noise figures were not particularly impressive.

Then, in 1954, the work of Uhler (Ref. 8) and Bakanowski (Ref. 9) at Bell Telephone Laboratories led to the development of low-loss silicon diodes now known as varactors or vericaps. The quality of these components prompted more extensive theoretical studies (Refs. 10, 11, 12, 13, and 14) which by 1958 led to the realization of low-noise microwave mixers with gain (Ref. 15).

Only one mixing mode was seriously investigated at this time. It was a case of single-sideband mixing that manifested negative resistance, and it relied only on conversion to the lower sideband, but this technique made possible such improvement in microwave amplification that all efforts suddenly concentrated on this configuration. In time, however, some academic interest was shown in the less spectacular upper-sideband converter (Ref. 16).

The first specific suggestions regarding multiple-sideband reactive mixing appeared in qualitative papers by Hogan, Jepsen, and Vartanian (Ref. 17) and by Hsiung (Ref. 18). However, the first detailed discussion was by the present writer while speaking at the 1959 PGMTT National Symposium. This material was later published (Refs. 19 and 20).

The author's first efforts in multiple-sideband reactive mixing tacitly assumed that each sideband was independently loaded. Later, prompted by the interesting experimental work of Mr. H. Brett of the U. S. Army Signal Corps (Ref. 21), the author treated double-sideband mixing under the constraint of dependent sideband loading (Ref. 22). The result has been a uniting of the modern theory of multiple-sideband reactive mixers with earlier work, such as the Alexanderson modulator. The constraint of dependent sideband loading is dis-

cussed in Chapter IX, and it appears at the present time to be the most promising practical application of this study.

1.3 Topics of Investigation

As previously stated, the goal of this analysis is to extend our understanding of the circuit properties of reactive mixers through a study of the double-sideband configuration. In pursuing this goal, progress has been made in the following areas.

1. A detailed analysis has been made of two symmetrical double-sideband reactive mixers. One employs a single pumping frequency ω_p and involves the complete set ω_r, ω_p, ω_ℓ, and ω_u. The other employs double pumping, at ω_p and ω_{2p}, and so involves the set ω_r, ω_p, ω_{2p}, ω_ℓ and ω_u.
2. The cases in (1) have been treated under each of the following circumstances.
    a. When the sidebands are widely spaced in frequency so they can be easily separated and individually processed.
    b. When the sidebands are closely spaced in frequency so that individual processing is impractical.
3. The useful engineering properties of each system in (1) and (2) have been evaluated and compared with the better known properties of single-sideband reactive mixers. This comparison has demonstrated that double-sideband reactive mixers offer advantages with respect to gain, bandwidth, and noise figure.
4. Experimental observations have been made in support of the conclusions in (3). In particular, an ultra-wideband, low-noise video amplifier has been developed from the analysis in category (2b) above.

5. A fundamental relationship has been obtained between symmetrical double-sideband mixers and a class of unsymmetrical double-sideband mixers. Since this relationship enables the properties of the latter to be derived from the former, it adds to the generality of the results cited above.
6. A new representation has been discovered for single-sideband, reactive mixers which displays their properties through easily interpreted equivalent circuits. This representation can also be applied to double-sideband configurations, so it should aid even the mature investigator to more fully understand the surprising properties of double-sideband reactive mixers.
7. A new method for predicting the stability of a linear system with periodically-varying components has been derived. This method requires a knowledge of sinusoidal steady-state response, but it does not entail a solution of the system differential equations. Therefore, this method yields a determination of stability that is less tedious than the normal method of calculating characteristic roots. In addition, however, it provides a new approach for approximating the characteristic roots of a periodically varying system.

The results cited above will be described in detail in subsequent chapters. Chapter III discusses the general principles of reactive mixers and outlines methods for calculating their basic circuit properties. Chapters IV and V treat the two fundamental single-sideband cases, whose properties are well-known, but whose study serves as a useful basis for later comparisons. Chapter VI, which treats stability, stands somewhat alone in this discussion, but the results there support the main contributions of the remaining chapters. Chapters VII, VIII, and IX discuss the single-pump, double-sideband cases, and Chapter X discusses the double-pump case. The final chapter reviews the experimental program that has accompanied the preparation of this dissertation, and also summarizes the conclusions of this study.

CHAPTER II

MATHEMATICAL FORMULATION

The basic circuit model in Fig. 1.3 depicts a nonlinear system of arbitrary order, and hence its complete analysis is impossible with present mathematical methods. While encouraging progress continues to be made in obtaining such a general analysis (see Ref. 23, for example), the treatments of reactive mixers that have borne the greatest engineering fruits to date have been of the Fourier type. Hence they have dealt exclusively with steady-state behavior. But a shortcoming arises when steady-state methods are applied to the circuits represented by Fig. 1.3, because the latter are potentially unstable. Nevertheless, it will be shown (in Chapter VI) that steady-state analysis alone can be used to accurately predict regions of instability in many practical cases. Hence, these steady-state methods are capable of determining their own region of validity.

2.1 Selection of Variables

When v(t) and i(t) have steady-state waveforms, they can be expressed by

$$v(t) = \frac{1}{2} \sum_{m=-\infty}^{\infty} \sum_{n=-\infty}^{\infty} V_{mn} \epsilon^{j(mx + ny)} \tag{2.1a}$$

$$i(t) = \frac{1}{2} \sum_{m=-\infty}^{\infty} \sum_{n=-\infty}^{\infty} I_{mn} \epsilon^{j(mx + ny)} \tag{2.1b}$$

where

$$x = \omega_p t \qquad y = \omega_r t$$

$$V_{mn} = V^*_{-m,-n} \qquad I_{mn} = I^*_{-m,-n} \tag{2.1c}$$

The assumption will be made that the mixing element in Fig. 1.3 is capacitative, and that it is characterized by a charge-voltage curve of the form

$$q = q(v) \tag{2.2}$$

Of course, to be consistent with the assumption that the mixing element is lossless, q(v) must be single valued (e.g., free of hysteresis), but in any case the charge waveform will have the following form,

$$q(t) = \sum_{m=-\infty}^{\infty} \sum_{n=-\infty}^{\infty} Q_{mn} \epsilon^{j(mx + ny)} \tag{2.3}$$

and then

$$I_{mn} = j(m\omega_p + n\omega_r) Q_{mn} \tag{2.4}$$

In principle, I_{mn} can also be related to the set of V_{mn} by using (2.2) to eliminate Q_{mn}. However, this step can rarely be accomplished exactly. An alternate technique is to approximate (2.2) by the first few terms of a Taylor series, which is particularly useful when formulating a small signal analysis. In fact, this approach will be the basis of the analysis to follow, but first an important general consequence of (2.4) will be derived.

2.2 General Energy Relations

The average power entering the mixing element in Fig. 1.3 at frequency ω_{mn} is expressed by[1]

$$W_{mn} = (\tfrac{1}{4}) \operatorname{Re}(V_{mn} I^*_{mn}) \tag{2.5a}$$

where by (2.1c)

$$W_{mn} = W_{-m,-n} \tag{2.5b}$$

But the lossless character of this element dictates that

$$\sum_{m=-\infty}^{\infty} \sum_{n=-\infty}^{\infty} W_{mn} = 0 \tag{2.6}$$

---

[1] Read Re as "the real part of ..."

The previous sum can be written equivalently

$$\sum_{m=-\infty}^{\infty} \sum_{n=-\infty}^{\infty} (m\omega_p + n\omega_r) \left(\frac{W_{mn}}{m\omega_p + n\omega_r} \right) = 0$$

which, with the aid of (2.5b), can be separated into the following two terms

$$2\omega_p \left[\sum_{m=0}^{\infty} \sum_{n=-\infty}^{\infty} \frac{nW_{mn}}{m\omega_p + n\omega_r} \right] + 2\omega_r \left[\sum_{n=0}^{\infty} \sum_{m=-\infty}^{\infty} \frac{nW_{mn}}{m\omega_p + n\omega_r} \right] = 0 \qquad (2.7)$$

Now, by substituting (2.4b) into (2.5a), it can also be noted that

$$\frac{W_{mn}}{m\omega_p + n\omega_r} = \left(\frac{1}{4}\right) \mathrm{Re}(-j\, V_{mn}\, Q^*_{mn}) \qquad (2.8)$$

It was first observed by J. M. Manley and H. E. Rowe (Ref. 24) that (2.8) is independent of ω_p and ω_r if Q_{mn} and V_{mn} are associated with a pure (but nonlinear) capacitor. That is, if ω_p and ω_r are changed at will the tuning of $\tilde{Y}(\omega)$ can always be altered so that (2.8) remains constant. Consequently, each term in (2.7) must vanish independently, which yields

$$\sum_{m=0}^{\infty} \sum_{n=-\infty}^{\infty} \frac{mW_{mn}}{m\omega_p + n\omega_r} = 0 \qquad (2.9a)$$

$$\sum_{n=0}^{\infty} \sum_{m=-\infty}^{\infty} \frac{nW_{mn}}{m\omega_p + n\omega_r} = 0 \qquad (2.9b)$$

These equations are referred to as the Manley-Rowe general energy relations because they describe the equilibrium energy flow in an arbitrary reactive mixer. Although Manley and Rowe originally derived (2.9a) and (2.9b) by direct calculation (Ref. 25), their alternate proof which was quoted above shows the physical significance of these relations more clearly. It will be demonstrated that the generality of the Manley-Rowe relations occurs at the expense of information content, and for this reason a more detailed analysis of Fig. 1.3 remains to be made.

2.3 Formulation for First-Order Mixing

Only two facets of input information were used in the derivation of the general energy relations:

(a) the mixing element is lossless

(b) the mixing element is capacitative[2]

Because of the lack of detail in these assumptions, the Manley-Rowe relations provide only a limited description of reactive mixers. To make further progress, such as finding the actual voltage and current waveforms in Fig. 1.3, would require a further specification of q(v).

In practice, the q(v) characteristic can be obtained either empirically or by applying basic physical principles to a model of the particular reactive element. However, even with q(v) and v(t) specified, mathematical limitations often hinder ones attaining useful expressions for the Q_{mn} and hence for i(t). For example, Sensiper and Weglein (Ref. 26) derived the pump coefficients Q_{mo} for the typical q(v) characteristic of a reverse-biased semiconductor diode, namely

$$q(v) = Q\,(1 - v/A)^{1-\sigma} \qquad (2.10)$$

$$0 < \sigma < 1$$

They assumed a single pump generator for which $v(t) = V + V_p \cos \omega_p t$, where V is the dc bias, and then obtained the Fourier coefficients Q_{mo} in closed form. However, the resulting expressions involved gamma functions of V_p/V that were quite complex.

A more general (but less exact) approach has been to represent q(v) by a Taylor series

$$q(v) = Q + a_1(v - V) + \frac{1}{2} a_2(v - V)^2 + \ldots \qquad (2.11)$$

which has a twofold advantage.

---

[2] An inductive mixing element is also characterized by (2.9), but (2.8) would be replaced by its dual in this case.

a. The coefficients, a_j, can be derived from any differentiable q(v) characteristic.

b. The series can be truncated after a finite number of terms to permit a compromise between ease of analysis and accuracy.

Although a disadvantage arises when (2. 11) converges slowly, the flexibility of the Taylor series representation warrants its use in determining the first-order mixing properties of Fig. 1. 3. To this end, (2. 11) will now be applied to a significant special case.

As outlined in Section 1. 1, the situation that will receive primary attention in this analysis is the one where real power flow is limited to two pump frequencies, ω_p and ω_{2p}, and three signal frequencies ω_r, ω_ℓ, and ω_u. The spectrum of these frequencies was depicted in Fig. 1. 4 and its occurrence can be insured if $\tilde{Y}_{mn}$ is either a short or an open circuit to all other frequencies (i. e., $\tilde{Y}_{mn} = \infty$ or 0, respectively). Choosing the case where $\tilde{Y}_{mn}$ shorts all unwanted frequencies, the voltage waveform will be

$$v(t) - V = \mathrm{Re}\left[V_p \epsilon^{jx} + V_{2p}\epsilon^{2jx} + V_r\epsilon^{jy} + V_u\epsilon^{j(x+y)} + V_\ell\epsilon^{j(x-y)}\right] \qquad (2.12a)$$

$$= \frac{1}{2}\left[\left(V_p\epsilon^{jx} + V_p^*\epsilon^{-jx}\right) + \left(V_{2p}^*\epsilon^{2jx} + V_{2p}\epsilon^{-2jx}\right) + \cdots\cdots\right] \qquad (2.12b)$$

The current waveform contains the same frequencies, and short circuited components in addition, so if the latter are collectively termed the short circuit current $i_{sc}(t)$, the total current waveform can be written

$$i(t) = i_{sc}(t) + \mathrm{Re}\left[I_p\epsilon^{jx} + I_{2p}\epsilon^{2jx} + I_r\epsilon^{jy} + I_u\epsilon^{j(x+y)} + I_\ell\epsilon^{j(x-y)}\right]. \qquad (2.12c)$$

The advantage of Fourier representation now appears because the unshorted components of i(t) and v(t) are related by the equations below, which have been obtained from (2. 4), (2. 11), and (2. 12).

$$I_p = j\omega_p \left[a_1 V_p + \frac{a_2}{2} (V_{2p} V_p^* + V_u V_r^* + V_\ell V_r) \right] \tag{2.13a}$$

$$I_{2p} = 2j\omega_p \left[a_1 V_{2p} + \frac{a_2}{2} (\frac{1}{2} V_p^2 + V_\ell V_u) \right] \tag{2.13b}$$

$$I_r = j\omega_r \left[a_1 V_r + \frac{a_2}{2} (V_p^* V_u + V_p V_\ell^*) \right] \tag{2.13c}$$

$$I_u = j\omega_u \left[a_1 V_u + \frac{a_2}{2} (V_p V_s + V_{2p} V_\ell^*) \right] \tag{2.13d}$$

$$I_\ell = j\omega_\ell \left[a_1 V_\ell + \frac{a_2}{2} (V_p V_r^* + V_{2p} V_u^*) \right] . \tag{2.13e}$$

The special case described above is representative of first-order interaction in all reactive mixers. For example, the following observations can be made on the basis of the set (2.13), and can be applied to reactive mixers in general.

(1) If all voltages except one, say V_{mn}, were short circuited, then a single sinusoidal voltage will appear across the mixing element and (2.13) will reduce to $I_{mn} = j\omega_{mn} a_1 V_{mn}$. Thus, an isolated signal will experience an effective capacity

$$C = a_1 = \left. \frac{dq(v)}{dv} \right|_{v = V} \tag{2.14}$$

(2) All first-order interaction (or mixing) is assoicated with the coefficient a_2.

(3) Given any set of allowed voltage components, the expression for I_{mn} can be written by inspection, because I_{mn} depends only upon frequency pairs that add algebraically to $m\omega_p + n\omega_r$. For example, the contribution to I_{mn} due to first-order mixing will be given by

$$I_{mn} \epsilon^{j(mx + ny)}$$

$$= j(m\omega_p + n\omega_r)\, a_2 \left\{ \sum_{\substack{m', -n' \\ =-\infty}}^{\infty} V_{m'n'} \epsilon^{j(m'x + n'y)}\, V_{m-m', n-n'} \epsilon^{j[(m-m')x + (n-n')y]} \right\} \tag{2.15}$$

where $V_{-m,-n} = V^*_{mn}$. Typically only a few terms in (2. 15) will be nonvanishing.

2. 4 Methods of Solving the Set (2. 13)

The source waveform in Fig. 1. 3 is expressed by the Fourier series

$$\mathbb{I}(t) = \mathrm{Re} \sum_{m=-\infty}^{\infty} \sum_{n=-\infty}^{\infty} \mathbb{I}_{mn} \epsilon^{j(mx+ny)} \tag{2. 16a}$$

so $\mathbb{I}(t)$ can be related to i(t), component by component, through the Thevenin-Norton theorem

$$\mathbb{I}_{mn} = I_{mn} + \tilde{Y}_{mn} V_{mn} \tag{2. 16b}$$

which was previously illustrated in Fig. 1. 5. However, the mixer current I_{mn} contains a component due to the average capacity C, which can be conveniently lumped with $\tilde{Y}_{mn}$ to yield an effective terminal admittance $\tilde{Y}_{mn}$. In fact, this procedure can be generalized by introducing the notation

$$Y_{mn} = \tilde{Y}_{mn} + Y'_{mn}, \tag{2. 17a}$$

where $\tilde{Y}_{mn}$ denotes all useful external admittance at ω_{mn}, while Y'_{mn} denotes all parasitic or generally unwanted admittance. Up to this point, only one contribution to Y'_{mn} has been noted, and this is the static susceptance of the mixer element, so using the modified frequency notation in Fig. 1. 4, (2. 17a) becomes in this case

$$Y_r = \tilde{Y}_r + j\omega_r C$$

$$Y_\ell = \tilde{Y}_\ell + j\omega_\ell C. \tag{2. 17b}$$

The influence of the mixing element upon the components of source current may now be formulated by substituting (2. 16) and (2. 17) into (2. 13), which yields

$$\mathbb{I}_p = Y_p V_p + \frac{j\omega_p a_2}{2} (V_{2p} V^*_p + V_u V^*_r + V_\ell V_r) \tag{2. 18a}$$

$$\mathbb{I}_{2p} = Y_{2p} V_{2p} + \frac{j\omega_p a_2}{2} \left(\frac{1}{2} V_p^2 + V_\ell V_u\right) \tag{2.18b}$$

$$\mathbb{I}_r = Y_r V_r + \frac{j\omega_r a_2}{2} \left(V_p^* V_u + V_p V_\ell^*\right) \tag{2.18c}$$

$$\mathbb{I}_u = Y_u V_u + \frac{j\omega_u a_2}{2} \left(V_p V_r + V_{2p} V_\ell^*\right) \tag{2.18d}$$

$$\mathbb{I}_\ell = Y_\ell V_\ell + \frac{j\omega_\ell a_2}{2} \left(V_p V_r^* + V_{2p} V_u^*\right). \tag{2.18e}$$

Because the $\mathbb{I}_{mn}$ are known, the most general application of the set (2.18) [and hence of the set (2.13)] will be to require a solution for the V_{mn}. However, the inversion of (2.18) is complicated by its nonlinear nature.

There are several alternate representations of Fig. 1.3 that help to organize the mathematical steps involved in the inversion of (2.18). They also facilitate the physical interpretation of reactive mixer properties. If the nonlinear element is replaced by a time-varying element with a waveform that follows only a portion of the applied signals, the remaining signals can be related entirely by linear mixing action. To demonstrate, let a nonlinear capacitor have the charge-voltage characteristic in (2.11), and let its voltage waveform be separated into two components, namely

$$v(t) - V = v'(t) + v''(t) \tag{2.19}$$

If it is assumed that the instantaneous capacity follows only the portion v'(t), then

$$c'(t) = a_1 + a_2 v'(t) \tag{2.20}$$

and if the remaining voltage v''(t) is now applied across this time-varying capacitance, the resulting current will be

$$i(t) = \frac{d}{dt} \left[c'(t)\, v''(t)\right] \tag{2.21}$$

The relevance of this approach to the inversion or solution of the set (2.18) will now be demonstrated in two separate cases.

2.4.1 Mixing by Time-Varying Capacitance at ω_p and ω_{2p}. To formulate the first case, the voltage waveform in (2.2) will be partitioned in the following manner.[3]

$$v'_p(t) = \mathrm{Re}[V_p \epsilon^{jx} + V_{2p} \epsilon^{2jx}] \tag{2.22a}$$

$$v''_p(t) = \mathrm{Re}[V_r \epsilon^{jy} + V_u \epsilon^{j(x+y)} + V_\ell \epsilon^{j(x-y)}] \tag{2.22b}$$

Now, to follow the procedure outline in the previous section, $v'_p(t)$ will be assumed to control the nonlinear capacitance. The resulting capacitance waveform will then be

$$c'_p(t) = C + 2\,\mathrm{Re}[\gamma_p \epsilon^{jx} + \gamma_{2p} \epsilon^{2jx}] \tag{2.23}$$

where, by (2.20),

$$C = a_1 \tag{2.24a}$$

$$\gamma_p = a_2 V_p/2 \tag{2.24b}$$

$$\gamma_{2p} = a_2 V_{2p}/2 \tag{2.24c}$$

Next, the voltage $v''_p(t)$ in (2.22b) will be applied across this capacitance, so the resulting current waveform will be

$$i''_p(t) = i''_{sc_p}(t) + \mathrm{Re}[I_r \epsilon^{jy} + I_u \epsilon^{j(x+y)} + I_\ell \epsilon^{j(x-y)}] \tag{2.25}$$

When (2.21) is applied, the voltage coefficients in (2.25) are found to be related to the current coefficients in (2.22) by the following linear[4] matrix equation.

---

[3] The subscript (p) is introduced here to distinguish this voltage partitioning from a similar one in the next section.

[4] Equation 2.26 is linear unless $\omega_r = \omega_p/2$.

$$\begin{bmatrix} I_r \\ I_u \\ I_\ell^* \end{bmatrix} = \begin{bmatrix} j\omega_r C & j\omega_r \gamma_p^* & j\omega_r \gamma_p \\ j\omega_u \gamma_p & j\omega_u C & j\omega_u \gamma_{2p} \\ -j\omega_\ell \gamma_p^* & -j\omega_\ell \gamma_{2p}^* & -j\omega_\ell C \end{bmatrix} \begin{bmatrix} V_r \\ V_u \\ V_\ell^* \end{bmatrix} \qquad (2.26)$$

It can now be observed that (2.26) is equivalent to (2.13c) through (2.13e), if the identification in (2.24) is made.

By employing the ideal filters introduced in Section 1.1, the set (2.26) can be associated with the linear equivalent circuit in Fig. 2.1. Incidentally, this figure also illustrates how the average capacity of a mixing element can be lumped with each terminal admittance, as expressed by the modified terminal admittances relation in (2.17)

$$Y_{mn} = \tilde{Y}_{mn} + j\omega_{mn} C$$

When the sources in Fig. 2.1 are included with (2.26), the equivalent of (2.18c) through (2.18e) results, namely:

$$\begin{bmatrix} \mathrm{I}_r \\ \mathrm{I}_u \\ \mathrm{I}_\ell^* \end{bmatrix} = \begin{bmatrix} Y_r & j\omega_r \gamma_p^* & j\omega_r \gamma_p \\ j\omega_u \gamma_p & Y_u & j\omega_u \gamma_{2p} \\ -j\omega_\ell \gamma_p^* & -j\omega_\ell \gamma_{2p}^* & Y_\ell^* \end{bmatrix} \begin{bmatrix} V_r \\ V_u \\ V_\ell^* \end{bmatrix} \qquad (2.27)$$

Therefore, one method of solution for (2.18) is to invert (2.27) and to substitute the results into (2.18a) and (2.18b). In this way, the relations between V_p and I_p, and between V_{2p} and I_{2p} are established, so γ_p and γ_{2p} in (2.24) can be eliminated. This establishes that the analysis in Fig. 1.3, subject to the frequency constraint in Fig. 1.4, can be accomplished directly from an analysis of the linear model in Fig. 2.1.

It should be noted that Fig. 2.1 has been the basis of previous reactive mixer analyses, but that this model is normally arrived at by direct small signal argument. In

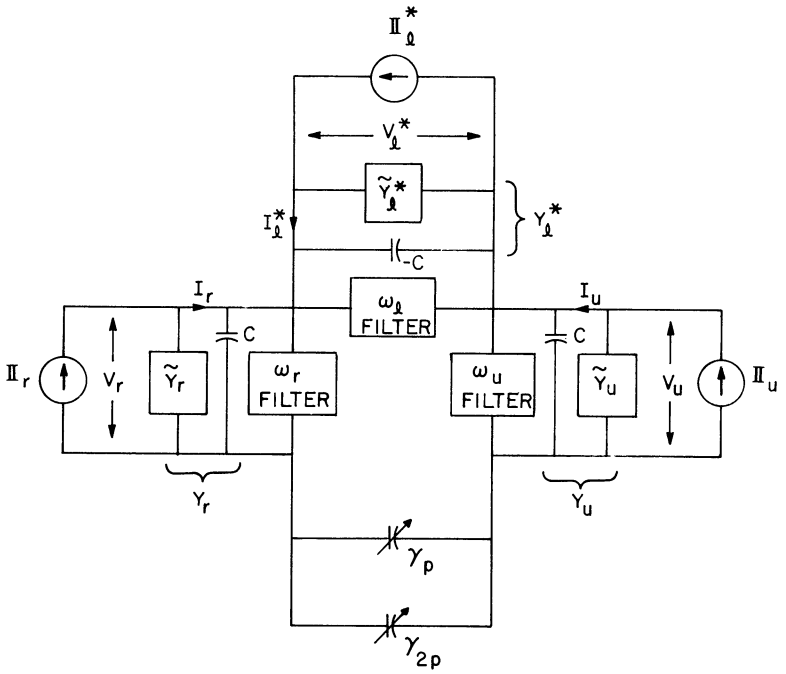

Fig. 2. 1. An equivalent circuit for equations (2. 18c)--(2. 18e). Each filter is an open circuit near the labeled frequency and a short circuit elsewhere.

such an argument, all signal voltages V_{mn} $(n \neq 0)$ are assumed small in comparison with the pump voltages V_{m0}; and then, simply by virtue of size, it is assumed that the reactive element follows the pump waveform entirely, and that small signals will experience a linear reactance element varying harmonically at the pumping frequencies.

These small-signal assertions are shown to be valid (for first-order interactions) by observing the relationship between (2. 27) and the last three equations in (2. 18). Thus, small signal arguments view all interactions as pump acting on signal. In fact, (2. 18a) and (2. 18b), which describe the first-order influence of the signal frequencies on the pump, were omitted in deriving (2. 27). In the next section, an alternate model for small signal analysis will be formulated that emphasizes the converse case. In fact, the effect of signal on pump will be shown to be equally as basic as that described by (2. 27).

2. 4. 2 Mixing by Time-Varying Capacitance at ω_r and ω_{2p}. In the previous section a symmetrical, double-sideband reactive mixer was represented in terms of time-varying capacitance at ω_p and ω_{2p}. This model provided a linear representation for Fig.

1.3. In addition, it was demonstrated that the signal frequencies voltages, V_r, V_u, and V_ℓ are related entirely by the mixing action of the linear capacitance waveform in (2.23). A second model will now be derived that describes the mixing in (2.27) through a different set of voltage components. It is equivalent to the first model in the sense that it leads to an equivalent mathematical solution of (2.13) by a similar method. However, this alternate representation has distinguishing characteristics that offer new physical interpretation of the same mixing process.

To formulate this case, the voltage waveform in (2.2) will be reapportioned as follows:

$$v'_r(t) = \mathrm{Re}\left[V_r \epsilon^{jy} + V_{2p} \epsilon^{2jx}\right] \tag{2.28a}$$

$$v''_t(t) = \mathrm{Re}\left[V_p \epsilon^{jx} + V_u \epsilon^{j(x+y)} + V_\ell \epsilon^{j(x-y)}\right] \tag{2.28b}$$

Again, following the method in Section 2.3, the nonlinear capacitor is assumed to follow $v'_r(t)$. The resulting capacitance waveform is

$$c'_r(t) = C + 2\,\mathrm{Re}\left[\gamma_r \epsilon^{jy} + \gamma_{2p} \epsilon^{2jx}\right] \tag{2.29}$$

where

$$C = a_1 \tag{2.30a}$$

$$\gamma_r = a_2 V_{r/2} \tag{2.30b}$$

$$\gamma_{2p} = a_2 V_{2p/2} \tag{2.30c}$$

If the remaining voltage $v''_r(t)$ is applied across $c'_r(t)$, the resulting current will be

$$i''_r(t) = i''_{sc_r}(t) + \mathrm{Re}\left[I_p \epsilon^{jx} + I_u \epsilon^{j(x+y)} + I_\ell \epsilon^{j(x-y)}\right] \tag{2.31}$$

Applying (2.20) again, the unshorted current and voltage components are found to be related as follows:

$$\begin{vmatrix} I_\ell \\ I_p \\ I_u \end{vmatrix} = \begin{vmatrix} j\omega_\ell C & j\omega_\ell \gamma_r^* & 0 \\ j\omega_p \gamma_r & j\omega_p C & j\omega_p \gamma_r^* \\ 0 & j\omega_u \gamma_r & j\omega_u C \end{vmatrix} + \begin{vmatrix} 0 & 0 & j\omega_\ell \gamma_{2p} \\ 0 & j\omega_p \gamma_{2p} & 0 \\ j\omega_u \gamma_{2p} & 0 & 0 \end{vmatrix} \begin{vmatrix} V_\ell^* \\ V_p^* \\ V_u^* \end{vmatrix} \qquad (2.32a)$$

This rather unusual matrix equation has the form

$$[I] = [Y_A][V] + [Y_B][V^*] \qquad (2.32b)$$

which will be termed semi-linear, because it fails to pass one of the two basic tests for linearity: superposition and scaling. The relation above is linear with respect to superposition, but nonlinear with respect to scaling, which can be demonstrated if $[V]$ is multiplied by a nonreal, diagonal matrix $[P]$. The result is not equivalent to multiplying $[I]$ by $[P]$, since

$$[P][I] = [Y_A][P][V] + [Y_B][P][V^*]$$

$$\neq [Y_A][P][V] + [Y_B][P^*][V^*]$$

Of course it is only the second term (2.32) that violates this test for linearity, so when γ_{2p} is zero (2.32) will be linear. Later it will be demonstrated that semi-linearity arises in this case because the frequency of γ_{2p} is precisely twice that of V_p.

In (2.32), the surviving linear quality of superposition simplifies the direct solution of this equation. The equivalent circuit in Fig. 2.2 can be formed from (2.32), if the semi-linear term is lumped into controlled sources at each terminal and if γ_r is taken to be real.[5] When the external sources in Fig. 2.2 are included with (2.32), the latter equation becomes

---

[5] Choosing the phase of one component, say γ_r, is not an added restriction because it is equivalent to choosing the time origin.

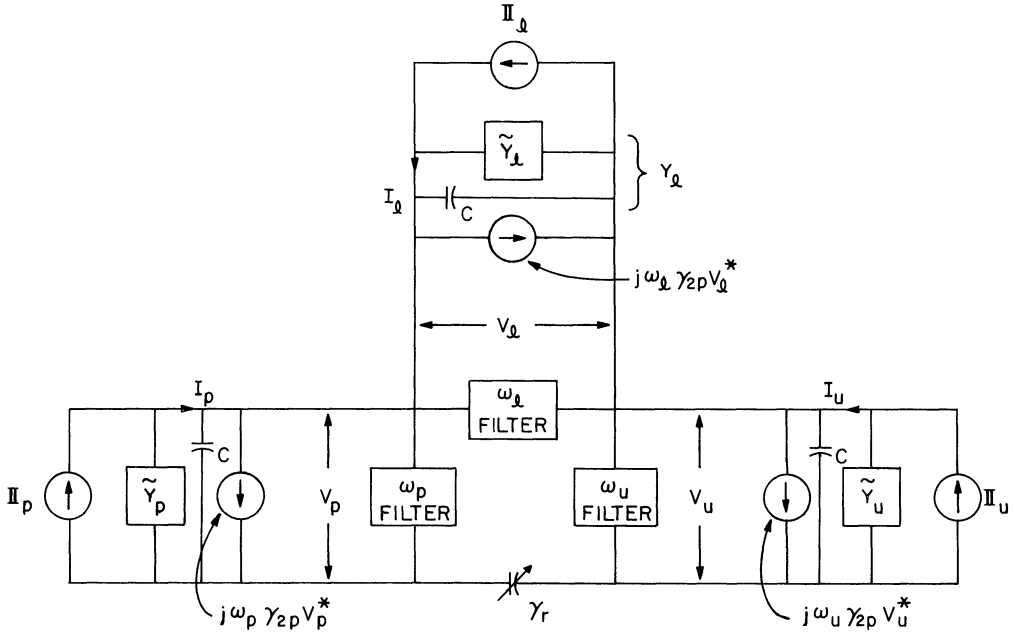

Fig. 2.2. An equivalent circuit for equations (2.18a), (2.18c), and (2.18d). The ideal filters have the same significance as in Fig. 2.1.

$$\begin{bmatrix} \mathbb{I}_\ell \\ \mathbb{I}_p \\ \mathbb{I}_u \end{bmatrix} = \begin{bmatrix} Y_\ell & j\omega_\ell \gamma_r & 0 \\ j\omega_p \gamma_r & Y_p & j\omega_p \gamma_r \\ 0 & j\omega_u \gamma_r & Y_u \end{bmatrix} \begin{bmatrix} V_\ell \\ V_p \\ V_u \end{bmatrix} + \begin{bmatrix} 0 & 0 & j\omega_\ell \gamma_{2p} \\ 0 & j\omega_p \gamma_{2p} & 0 \\ j\omega_u \gamma_{2p} & 0 & 0 \end{bmatrix} \begin{bmatrix} V_\ell^* \\ V_p^* \\ V_u^* \end{bmatrix} \tag{2.33a}$$

which has the form

$$[\mathbb{I}] = ([Y_A] + [Y_{mn}])[V] + [Y_b][V^*] \tag{2.33b}$$

When the identification in (2.30) is made, it will be recognized that (2.33) is identical to (2.18a), (2.18d), and (2.18e). Thus, the set (2.18) can be solved by substituting the solution of (2.33) into the remaining two equations (2.18b) and (2.18c).

The most significant feature of this second formulation is that the linear time-varying element follows the waveform that is normally of smallest amplitude, but this model leads to the same solution as that in Section 2.4. Thus, the intuitive notion of basing an analysis on the apparently dominant influence of large pump waveforms is valid, but not

fundamental. The significance of this fact is best emphasized by suppressing the pump harmonic V_{2p}, which causes γ_{2p} to vanish. In this case, (2. 18b) can be dropped and the production of sideband frequencies by mixing becomes limited to the terms $a_2 V_p V_r/2$ or $a_2 V_p V_r^*/2$, which appear in (2. 18d) and (2. 18e) respectively. Because of the symmetry of these terms, it is equally valid to view mixing as a capacitance $a_2 V_p/2$ interacting with a voltage V_r (or V_r^*); or as a capacitance $a_2 V_r$ (or $a_2 V_r^*$) interacting with the voltage V_p. So although small signal considerations suggest mixing by pump acting on signal, the reverse mixing effect of signal affecting pump has identical characteristics. Also, either of these viewpoints is sufficient to solve the set in (2. 18). In later chapters, these formulations will be used to provide separate explanations of certain basic reactive mixer properties.

CHAPTER III

INTRODUCTION TO SINGLE-SIDEBAND REACTIVE MIXERS

Reactive mixing generally involves a multitude of sidebands, but in the past single-sideband cases have received the greatest attention. The term single-sideband will be applied when the signal set is restricted to two frequencies coupled by first-order interactions. It is soon apparent that an infinite number of such single-sideband pairs exist. However, they are all typified by two representative cases which involve ω_r as one frequency, and either $\omega_\ell = \omega_p - \omega_r$, or $\omega_u = \omega_p + \omega_r$, for the other.

To prove the latter statement let the general signal frequency pair ω_{mn} and $\omega_{m'n'}$ be coupled by a pump frequency $\omega_{m''0}$. When this coupling occurs by first-order interaction, the frequency indices must be related on the basis of (2. 15), which yields

$$\begin{aligned} m'' &= m - m' \\ n' &= n \end{aligned} \tag{3. 1}$$

The single-sideband cases involving ω_r, ω_p, and $\omega_p \pm \omega_r$ have the following values: $m' = 0$, $m'' = m = 1$, and $n' = n = \pm 1$; but all other cases can now be reduced to these by defining new pump and signal reference frequencies as follows:

$$\begin{aligned} \omega_{m''0} &= \omega'_{10} = \omega'_p \\ \omega_{m'n'} &= \pm \omega'_{01} = \pm \omega'_r \end{aligned} \tag{3. 2}$$

Then, by (3. 1)

$$\omega_{mn} = \omega'_{10} \pm \omega'_{01} = \omega'_p \pm \omega'_r = \begin{cases} \omega_u \\ \omega_\ell \end{cases}$$

which shows that mixing within the pairs (ω_r, ω_ℓ) and (ω_r, ω_u) is representative of all single-sideband mixing.

For most of this chapter, and for the next two chapters, $Y(\omega)$ will be chosen to short circuit all frequencies except ω_r, ω_p, and either ω_ℓ, or ω_u. The basic mixing properties of these sets are well known, but they will be reviewed in preparation for later chapters. Also in the course of this review, several novel approaches to reactive mixer analysis will be introduced, as well as some previously unpublished aspects of single-sideband conversion.

3.1 Application of the General Energy Relations

For the restricted set of frequencies just specified, the general energy relations in (2.9) reduce to

$$\frac{W_p}{\omega_p} + \frac{W_u}{\omega_u} + \frac{W_\ell}{\omega_\ell} = 0 \tag{3.2a}$$

$$\frac{W_r}{\omega_r} + \frac{W_u}{\omega_u} - \frac{W_\ell}{\omega_\ell} = 0 \tag{3.2b}$$

These equations will be applied to the two typical single-sideband configurations, which will be distinguished as Case 3.1.1, when $W_\ell = 0$, and Case 3.1.2 when $W_u = 0$. In applying the general energy relations to these cases, it should be noted that W_{mn} has been defined as the average power entering the reactive mixing element at frequency ω_{mn}. Therefore, when signal power is converted from one frequency to another, the associated conversion gain will be the negative ratio of the corresponding W_{mn}.

3.1.1 $W_\ell = 0$. In this case, (3.2b) predicts the following power gain for conversion form ω_r to ω_u.

$$\frac{-W_u}{W_r} = \frac{\omega_u}{\omega_r} \tag{3.3}$$

It is certainly noteworthy that this gain is greater than one. As a partial explanation of this result, the quotient of the two relations in (3.2) yields

$$\frac{W_p}{W_r} = \frac{\omega_p}{\omega_r} \tag{3.4}$$

which shows, in this special case, that the pump and signal sources contribute power to the mixing process in proportion to their frequency. Therefore, if $\omega_p > \omega_r$, the pump will contribute more power to the converted output at ω_u than the signal. On the other hand, if the signal is applied at ω_u and down-converted (demodulated) to ω_r, the corresponding gain will be the reciprocal of (3. 3), which is less than unity. Nevertheless, signal power that appears to be lost during down-conversion is not dissipated by the mixing element, which is lossless. Instead, it is reflected at the pump frequency. This point will become clearer after considering the lower-sideband converter.

3. 1. 3 $W_u = 0$. Conversion from ω_r to ω_ℓ has several intriguing aspects. First, because the frequencies ω_r and ω_ℓ both cover the range from zero to ω_p, they are indistinguishable in the following sense: when two frequencies sum to ω_p it is immaterial which is termed ω_r and which ω_ℓ. In either case, the conversion gain from one to the other is numerically equal to the ratio of output to input frequency, just as in the previous case. But by contrast, the conversion gain for lower-sideband reactive mixing is shown in (3. 2b) to be the negative of the frequency ratio, namely

$$-\frac{W_\ell}{W_r} = -\frac{\omega_\ell}{\omega_r} \tag{3.5}$$

This aspect of reactive mixers is unheard of in resistive mixers, and so it requires further interpretation. Note that W_ℓ cannot be positive in the absence of a source at ω_ℓ, and also that W_r must be nonpositive by (3. 5). Therefore, an applied signal at ω_r must experience power reflections exceeding 100 percent, which further implies that the lower-sideband converter is potentially unstable. In support of the latter statement, steady-state analysis (in Chapter V) will show how this form of single-sideband converter is characterized by input and output admittances with negative real parts. Further support can be found by applying (3. 2a) to the present case, which yields

$$-\frac{W_\ell}{W_p} = \frac{\omega_\ell}{\omega_p} \tag{3.6}$$

Therefore W_p is positive and exceeds the converted output power at ω_ℓ. In accord with the statements made about (3. 5), pump power, in excess of that converted to ω_ℓ, must be con-

verted to ω_r and become radiated as a reflected signal.

Returning now to the case in 3. 1. 1 that involved an applied signal at ω_u, the following variable changes show why signal power was absorbed by the pump:

$$\begin{aligned} \omega_u &= \omega'_p \\ \omega_p &= \omega'_\ell \\ \omega_r &= \omega'_p - \omega'_\ell \end{aligned} \tag{3.7}$$

Hence, as far as ω_u is concerned, the pump ω_p is a lower-sideband frequency. Large signals at ω_u could conceivably cause the circuit to oscillate at ω_p.

3.2 An Alternate Viewpoint (Ref. 27)

Let us recall that the general energy relations are based on two properties of lossless mixing elements: (a) that energy is conserved, and (b) that the average power flow at ω_{mn} is proportional to this frequency. These relations were derived by circuit analysis. Speaking in more general terms, however, the general energy relations deal with sinusoidal electromagnetic waves at each of the ω_{mn}, and wave motion is subject to a far greater variety of descriptions than is provided by circuit theory. For example, the quantum theory predicts that wave motion can be regarded as a flow of photons of energy $\hbar\omega_{mn}$.[1] Therefore, conversion from ω_r to the upper sideband ω_u can be regarded as signal photons mixing with pump photons to produce upper-sideband photons. This situation is depicted in Fig. 3. 1a. If there are N such events per second, the average output power will be

$$-W_u = N\hbar\omega_u \tag{3.8}$$

but the average signal input power will be

$$W_r = N\hbar\omega_r \tag{3.9}$$

The conversion gain will now be

$$-\frac{W_u}{W_r} = \frac{\omega_u}{\omega_r} \tag{3.10}$$

---

[1]The symbol $\hbar$ denotes $h/2\pi$, where h is the Planck constant.

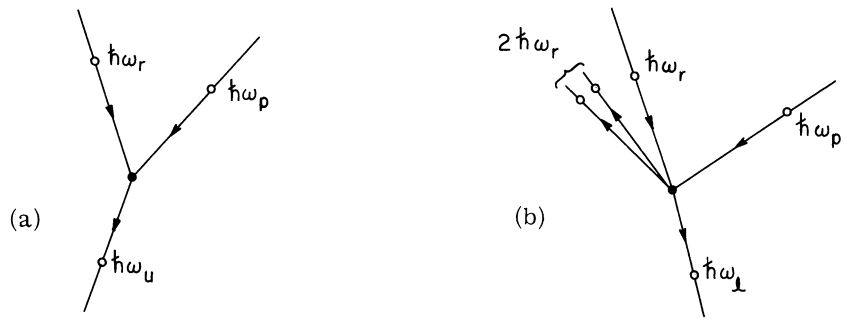

Fig. 3. 1. Single sideband conversion on a quantum basis:
(a) upper-sideband case;
(b) lower sideband case.

which is precisely the ratio predicted by the Manley-Rowe relations in (3. 3).

It is instructive to also consider lower-sideband conversion on a quantum basis. As depicted in Fig. 3. 1b, the mixing of one signal photon with one pump photon must produce one difference frequency photon and two reflected signal photons. Therefore, the net input signal power will be

$$W_r = N\hbar\omega_r - 2N\hbar\omega_r = -N\hbar\omega_r \tag{3.11}$$

The output power is

$$-W_\ell = N\hbar\omega_\ell \tag{3.12}$$

so the power gain will be

$$-\frac{W_\ell}{W_r} = -\frac{\omega_\ell}{\omega_r} \tag{3.13}$$

which is in agreement with (3. 5).

Evidently, the reactive mixer can serve as a model for certain quantum processes. Hence, Fig. 1. 3 could be regarded as an equivalent circuit for quantum devices that employ conversion between discrete energy levels. A good example of such a device would be the solid-state maser. It is suggested, therefore, that the basic conclusions of this analysis are pertinent to masers and other devices that are normally considered to be beyond the scope of circuit analysis.

3.3 Circuit Effects Due to First-Order Interactions

Several interesting properties of single-sideband reactive mixers have been described by the general energy relations. These properties have shown a sharp contrast between the two typical cases, where only the upper or the lower sideband is present. However, numerous questions remain to be answered, such as: "What must be done to inject signal power into a reactive mixer, in order to realize the potential gain?" and "When will reactive mixer conversion gain be stable?" etc. It will be shown that these further details depend upon the actual law of the nonlinear element. For this reason, the mathematical formulation in Section 2.2 will be the medium employed for further analysis, so let us now consider some typical single-sideband circuits.

The circuit in Fig. 3.2a is a simple realization of the basic single-sideband mixer, and it has the general form of Fig. 1.3. The nonlinear capacitor is assumed to be biased with average capacity C, according to (2.14), while the linear portion is made up of three parallel tanks in series. These tanks are assumed to be tuned so that when a fixed capacitor of value C is placed between terminals a-b, it will resonate the resulting linear network at $\overline{\omega}_r$, $\overline{\omega}_p$, and $\overline{\omega}_x$; where $\overline{\omega}_x$ denotes either $\overline{\omega}_\ell$ or $\overline{\omega}_u$.

Normally, a different tank will dominate in each of these resonances, so the voltage v(t) will appear primarily across one tank at each resonance frequency, which explains why the applied sources in Fig. 3.2a have been associated with individual tank circuits. This type of filtering is common in mixers, and motivates the use of idealized models like Fig. 1.5. For example, an ideal form of this type is shown in Fig. 3.2b. The latter will be equivalent to Fig. 3.2a, in the bands of interest, if the network associated with each filter in Fig. 3.2b is chosen to be the appropriate Norton equivalent of Fig. 3.2a. For example, $\widetilde{Y}_r$ must be the Norton equivalent admittance at terminals a-b, exclusive of C, for frequencies near $\overline{\omega}_r$, etc. Once again, the advantage provided by ideal filters is to separate the circuit admittances influencing each frequency band so they can be independently varied. The one main approximation incurred by these ideal filters, is that circuit effects originating beyond the desired bands are ignored.

Figure 3.2b will now be analyzed to determine the first order interactions between ω_r, and ω_ℓ or ω_u. Following the method of Section 2.4, the pump and nonlinear capaci-

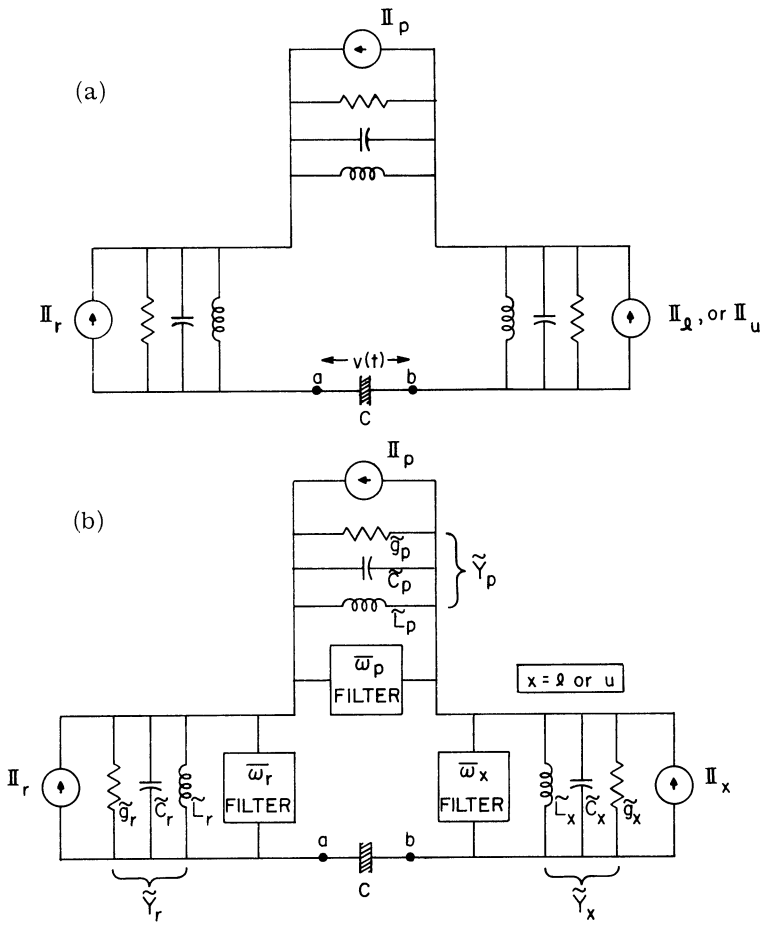

Fig. 3.2. Circuits for single sideband conversion: (a) is a practical realization and (b) is an idealized form of (a) having the form of Fig. 1.5. In (a), each frequency appears in varying degrees at all terminals. In (b), the ideal filters cause each frequency to appear at only one terminal.

tor will be replaced by the time-varying capacitor at ω_p, which produces a second equivalent circuit, namely the linear model in Fig. 3.3. This final linear model will be recognized as a special case of Fig. 2.2. It is obtained when γ_{2p} is set equal to zero, and when one of the two sidebands is shorted. When similarly modified, the matrix equation in (2.27) describes Fig. 3.3, and the two basic single-sideband cases can be treated separately by alternately setting V_ℓ and V_u to zero.

The two basic steps that have been taken in obtaining the single-sideband linear model in Fig. 3.3 can be summarized as follows. First, all extraneous mixing products have been suppressed by assuming ideal filters. Secondly, the mixing element has been linearized

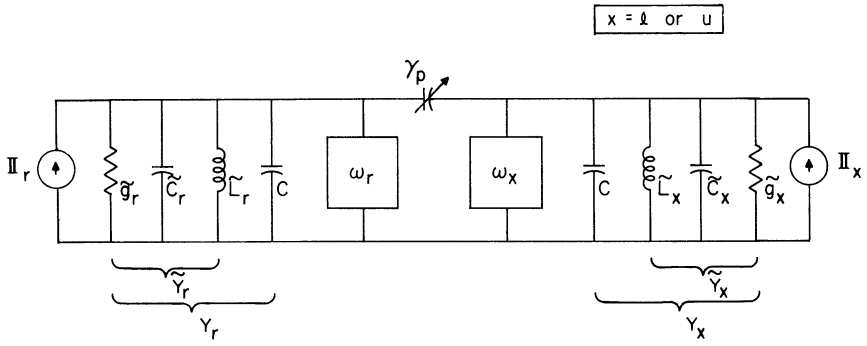

Fig. 3.3. A further reduction of Fig. 3.2b into a linear, time-varying model. The ideal filters allow C to be shown at both terminals.

by substituting a time-varying capacitor. To be valid, these steps require small applied signals, and that the individual resonances in Fig. 3.2a have fairly high Q's. Further evidence on the accuracy of these assumptions is given in Chapter VI.

3.4 Derivation of Circuit Quantities

The relationships established in the preceding sections are a convenient basis for systematic calculation of the fundamental circuit quantities listed in Section 1.1. Consider first the conversion gain between two members of the signal set, say ω_1 and ω_2. As far as these two frequencies are concerned, the entire mixer reduces to the two terminal network in Fig. 3.4, which will be convenient for introducing those external or parasitic parameters with important influence on the circuit properties of reactive mixers. The noteworthy parts of Fig. 3.4 are:

1. A source at ω_1 with short circuit current I_S and internal conductance g_S, which is normally the only contributor to $\tilde{g}_1$.
2. A load conductance g_L at ω_2, which is normally the only contributor to $\tilde{g}_2$.
3. Tuning susceptances $\tilde{b}_1$ and $\tilde{b}_2$ at ω_1 and ω_2.
4. Parasitic admittances $Y'_1 = g'_1 + jb'_1$ and $Y'_2 = g'_2 + jb'_2$ which may arise from cables, filters, or from parasitic losses in the mixer itself.

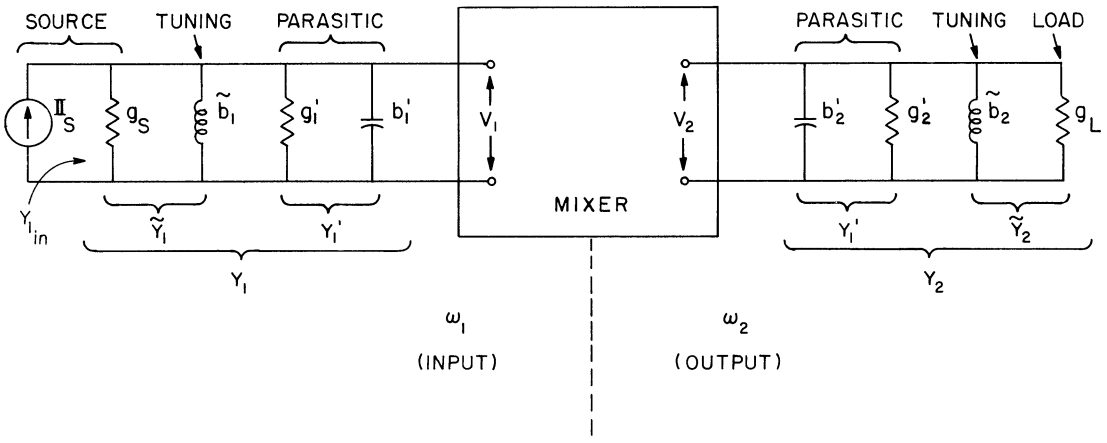

Fig. 3.4. A two terminal pair representation for conversion from ω_1 to ω_2 showing certain critical external parameters.

The practical evaluation of mixer properties is simplified by lumping all admittances into general terminal admittances as

$$Y_1 = \tilde{Y}_1 + Y'_1 = g_1 + jb_1$$

$$Y_2 = \tilde{Y}_2 + Y'_2 = g_2 + jb_2 \qquad (3.14)$$

Once done, a particular mixer can be evaluated first as a function of Y_1 and Y_2. Then the external parameters can be separated out, so their influence on a particular circuit property can be determined. This procedure will be outlined next.

3.4.1 Conversion Gain. The most convenient measure of conversion gain is transducer gain, which is defined as follows:

$$G_{12} = \frac{\text{average power delivered to } Y_L \text{ (at } \omega_2)}{\text{average power available from the source (at } \omega_1)} \qquad (3.15a)$$

In the notation in Fig. 3.4,

$$G_{12} = \frac{4g_S g_L}{|Y_{1_{in}}|^2} \left|\frac{V_2}{V_1}\right|^2 \qquad (3.15b)$$

where $Y_{1_{in}}$ denotes the total input admittance experienced by the ideal source I_S at the ω_1 terminals. Both $Y_{1_{in}}$ and V_2/V_1 can be calculated directly from appropriate mixer relations.

Comparing reactive mixers on the basis of transducer gain, rather than on pure power gain, has merit because different reactive mixers operate at radically different impedance levels. Hence the full realization of a potential power gain may call for unrealistic source impedances, but the optimum gain for a given source impedance is the maximum transducer gain.

The effect of parasitic loss on transducer gain can be easily introduced. Calling $\tilde{G}_{12}$ the modified transducer gain obtained by considering Y_1 and Y_2 the source and load admittances, respectively, then G_{12} can be expressed in terms of $\tilde{G}_{12}$, by the following rewording of (3.15a):

$$G_{12} = \left[\frac{\text{available source power from } \mathbb{I}_S \text{ and } (g_S + g_1')}{\text{available source power from } \mathbb{I}_S \text{ and } g_S}\right] \times \left[\frac{\text{power to } g_L}{\text{power to } (g_L + g_2')}\right] \times \left[\frac{\text{power to } (g_L + g_2')}{\text{available source power from } \mathbb{I}_S \text{ and } (g_S + g_1')}\right] \tag{3.16a}$$

Therefore

$$G_{12} = \left(\frac{g_S}{g_S + g_1'}\right)\left(\frac{g_L}{g_L + g_2'}\right)\tilde{G}_{12} = \left(\frac{g_S}{g_1}\right)\left(\frac{g_L}{g_2}\right)\tilde{G}_{12} \tag{3.16b}$$

The latter equation is useful because $\tilde{G}_{12}$ is independent of how the terminal admittances are partitioned between desired and parasitic components. Hence, (3.16b) is a fundamental form that tends to remain fixed during various optimization procedures.

3.4.2 Noise Figure. In reactive mixers, as with most systems, both internal and external noise sources must be considered. For the mixers treated here, the external noise will be assumed to be of thermal origin, being due to resistance at the mixer terminals.[2] The internal sources of noise will tend to be more varied, but the predominant internal noise in most reactive mixers is the thermal noise associated with parasitic losses. Therefore, two basic assumptions will be made for this noise analysis: (1) that all noise is thermal, and (2) that all noise sources are uncorrelated.

[2]Other nonthermal noise sources can often be included by appropriately raising the thermal noise temperature T. This step is useful when conversion bandwidths are narrow.

The conversion noise figure of the network in Fig. 3.4 can be expressed in terms of the thermal noise of a conductance at standard temperature $T_o = 290^oK$. The available noise power from such a conductance is kT_oB_{12}, where k is the Boltzman constant and B_{12} is the noise bandwidth in cps for conversion from ω_1 to ω_2. The latter is normally defined by the expression

$$B = \frac{1}{2\pi\bar{G}} \int_0^\infty G(\omega)\, d\omega \tag{3.17}$$

where $G(\omega)$ is the system gain and $\bar{G}$ its midband value. For a mixer, however, this definition must be modified because the range of each sideband is limited by the pump frequency. Therefore, if the conversion gain G_{12} is assumed to diminish rapidly outside its conversion pass band (of width β_{12} rad/sec), the following definition can be adopted:

$$B_{12} = \frac{1}{2\pi\bar{G}} \left[\int_{\bar{\omega}_1 - n\beta_{12}}^{\bar{\omega}_1 + n\beta_{12}} G_{12}(\omega_1)\, d\omega \right] ; \quad n > 1 \tag{3.18}$$

A tacit assumption in (3.18) is that β_{12} will be essentially independent of n, if n is somewhat larger than one.

As a practical example, let $G(\omega)/\bar{G}$ correspond to a simple resonant circuit with 3 db bandwidth β. Then (3.17) yields a noise bandwidth $\pi\beta/2$ rad/sec or $\beta/4$ cps. In the corresponding case for a mixer, the pass band of $G_{12}(\omega)$ would resemble a tuned circuit with bandwidth β_{12}, and (3.18) will yield B_{12} very nearly equal to $\beta_{12}/4$ cps.

It will be convenient to assign the noise temperature T_o to the source conductance g_S in Fig. 3.4. Then the definition of noise figure can be stated as follows

$$F_{12} = \frac{\text{total noise power at } \omega_2}{\text{noise power at } \omega_2 \text{ due to } g_S \text{ alone}} \tag{3.19}$$

Since the output noise power at ω_2 is composed of excess noise contributions as well as uncorrelated noise from g_S alone, (3.21) can also be written in the form

$$F_{12} = 1 + \frac{\text{excess noise power at } \omega_2}{\text{noise power at } \omega_2 \text{ due to } g_S \text{ alone}} \tag{3.20a}$$

The quantity $F_{12}-1$ is often termed the excess noise figure.

A second alternate measure of excess noise can be introduced by writing (3.20a) as

$$F_{12} = 1 + \frac{T_{12}}{T_o} \tag{3.20b}$$

The quantity T_{12} is called the effective input noise temperature. If g_S had the noise temperature T_{12} it alone would yield the same excess output noise as all the actual noise sources put together. One advantage of measuring excess noise in terms of noise temperature is the elimination of the arbitrary reference temperature T_o.

As a simple illustration of (3.20), excess noise due to a parasitic input conductance g'_1 will be considered, so g'_1 will be assigned the noise temperature T'_1 as noted in Fig. 3.5. The presence of g'_1 reduces the reference noise power available to the converter to the value

$$\frac{kT_o B_{12} g_S}{g_S + g'_1} \tag{3.21}$$

Similarly, the excess noise power available to the converter due to g'_1 is

$$\frac{kT_1 B_{12} g'_1}{g_S + g'_1} \tag{3.22}$$

So if these are the only noise sources available to the output load, the noise figure becomes

$$1 + \frac{g'_1 T_1}{g_S T_o} \tag{3.23}$$

There are several other forms of excess noise that will arise in this analysis, and these are depicted in Fig. 3.6. It is again assumed that conversion from ω_1 to ω_2 is desired, but now an auxiliary sideband is introduced at ω_3. This might be done for example to enhance the desired conversion in some way. The auxiliary sideband is terminated by a conductance g_3 with a noise temperature T_3: and the midband transducer gain and noise band-

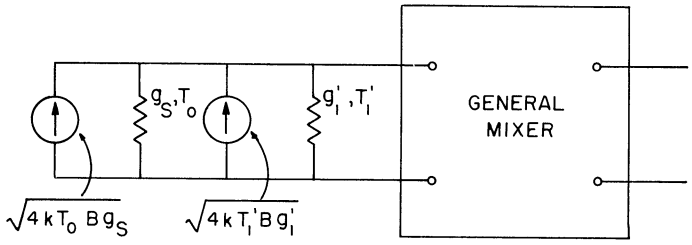

Fig. 3.5. The input noise sources associated with g_S and g_1'.

width for conversion between ω_3 and ω_2 are denoted by $\bar{G}_{32}$ and B_{32}, respectively. The contribution by g_3 to the excess noise figure F_{12}-1 is then

$$\frac{\bar{G}_{32} B_{32} T_3}{\bar{G}_{12} B_{12} T_o} \tag{3.24}$$

A third source of excess noise illustrated by Fig. 3.6 is load noise. Normally load noise is not counted as excess noise, but in systems with negative output conductance it must be included. Let the load conductance g_L and the parasitic conductance g_2' in Fig. 3.6 have noise temperatures T_L and T_2', respectively, and then their available noise powers will then be $kT_L B_{22}$ and $kT_2' B_{22}$ respectively, where B_{22} is the noise bandwidth of the transducer gain by reflection at ω_2. The latter quantity is defined as follows:

$$G_{22} = \frac{\text{power delivered to } g_L \text{ at } \omega_2}{\text{power available from a source at } \omega_2 \text{ with internal conductance } g_L} \tag{3.25}$$

Therefore the contribution to excess noise figure by the external noise sources at ω_2 is

$$\frac{B_{22}}{B_{12}} \left[\left(\frac{G_{22}-1}{\bar{G}_{12}} \right) \frac{T_L}{T_o} + \frac{G_{22} T_2' g_2'}{\bar{G}_{12} T_o g_L} \right] \tag{3.26}$$

The factor $\bar{G}_{22}$-1 is incorporated in the first term in (3.26), instead of $\bar{G}_{22}$, so T_L will not be held against a converter with a matched output.

If $\bar{G}_{12}$ is large, (3.26) will often be negligible in comparison with other noise figure contributions, unless $\bar{G}_{22}$, T_L, or T_2' are also particularly large. The latter circum-

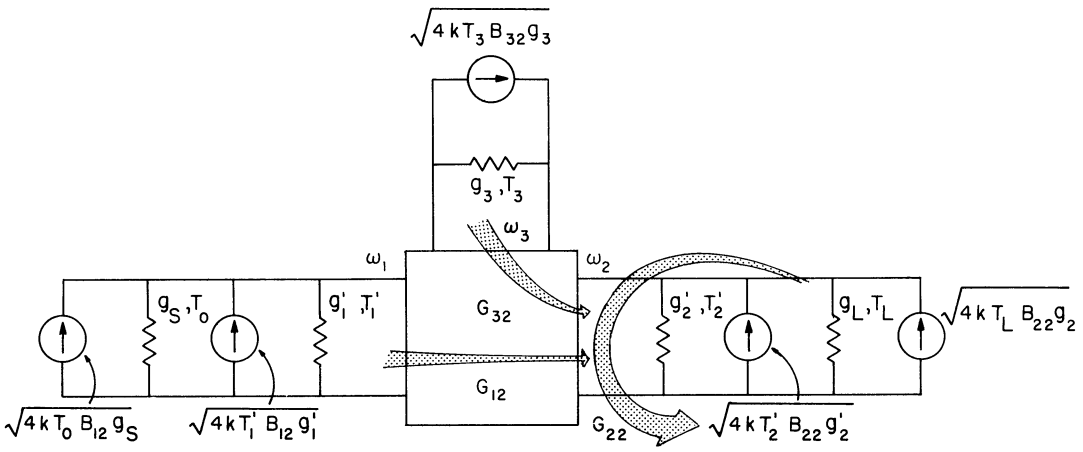

Fig. 3.6. A general set of noise sources that may contribute to the noise figure for conversion from ω_1 to ω_2.

stance occurs in certain reactive mixers, however, as later chapters will indicate. A final expression for the noise figure of Fig. 3.6 can now be formed by combining (3.23), (3.24), and (3.26) which yields

$$F_{12} = 1 + \frac{g_1'T_1'}{g_ST_o} + \frac{G_{32}B_{32}T_3}{\bar{G}_{12}B_{12}T_o} + \frac{B_{22}}{B_{12}}\left[\left(\frac{G_{22}-1}{\bar{G}_{12}}\right)\frac{T_L}{T_o} + \frac{\bar{G}_{22}T_2'g_2'}{\bar{G}_{12}T_og_L}\right] \qquad (3.27)$$

3.4.3 The Varactor as a Mixer Element. An often used reactive mixer component is the reverse biased semiconductor diode, which is customarily termed a varactor. Varactors have had their greatest success at microwave frequencies, where the only serious degrading influence is their series resistance. For this reason, Fig. 3.7(a) is a useful varactor equivalent circuit. Only the varactor capacity C varies with bias. The alternate representation in Fig. 3.7b is more convenient for the present analysis, even though it varies with frequency. The parasitic loss $g_d(\omega)$ can be included directly with the parasitic admittance Y'. It is convenient to express $g_d(\omega)$ in terms of the Q of the varactor. In Fig. 3.7a

$$Q_d = 1/\omega C r_d \qquad (3.28)$$

and if $Q_d^2 >> 1$, the effective shunt capacity in Fig. 3.7b is constant and equal to C, the series capacity, while the effective shunt conductance becomes

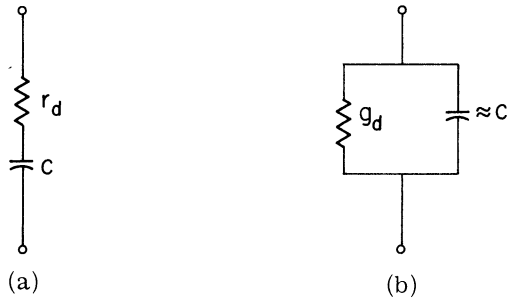

Fig. 3.7. The equivalent circuit of a varactor in (a) series form, and (b) in shunt form.

$$g_d \approx \omega^2 C^2 r_d = \frac{Q_d^2}{r_d} = \frac{\omega^2 C}{\omega_d} \tag{3.29}$$

where ω_d is the frequency at which $Q_d = 1$.

When varactors are used, g_d and C are the most fundamental contributors to the parasitic admittances Y'_1 and Y'_2. In this analysis, varactors will be used to model the relations derived, and no other forms of parasitic loss will be considered. However, it is important to note that g_d varies with frequency, so a different parasitic loss will appear at each mixer terminal.

At ω_1: $$g_d = \frac{\omega_1^2 C}{\omega_d} = g_{d1} \tag{3.30a}$$

At ω_2: $$g_d = \frac{\omega_2^2 C}{\omega_d} = g_{d2} \tag{3.30b}$$

Therefore, when varactor loss is the only parasitic loss considered

$$g'_1 = g_{d1}$$

$$g'_2 = g_{d2} \tag{3.31}$$

3.4.4 Comments on Notation. The general properties of Fig. 3.4 will be applied to a number of reactive mixer configurations by identifying the frequencies ω_1 and ω_2 with various signal frequencies such as ω_r, ω_u, ω_ℓ, etc. The total admittance at these

frequencies has been expressed by

$$Y_r = \tilde{Y}_r + Y'_r \tag{3.32a}$$

$$Y_\ell = \tilde{Y}_\ell + Y'_\ell \tag{3.32b}$$

--etc--

where Y'_r is the parasitic admittance at ω_r and $\tilde{Y}_r$ is the chosen terminal admittance.[3] Considering all parasitic loss to be due to a varactor, then

$$Y'_r = g'_{dr} + jb'_{dr} = \frac{\omega_r{}^2 C}{\omega_d} + j\omega_r C \tag{3.33a}$$

$$Y'_\ell = g'_{d\ell} + jb'_{d\ell} = \frac{\omega_\ell{}^2 C}{\omega_d} + j\omega_\ell C \tag{3.33b}$$

The basic contributions to useful terminal admittance will be source, load, and tuning admittances. When a source of internal conductance g_S and a tuning inductance $L = 1/\bar{\omega}_r{}^2 C$ are applied at ω_r, then

$$Y_r = g_S - \frac{j\bar{\omega}_r{}^2 C}{\omega_d} \tag{3.34a}$$

and

$$Y_r = g_S + g_{dr} + j\bar{\omega}_r C \left(\frac{\omega_r}{\bar{\omega}_r} - \frac{\bar{\omega}_r}{\omega_r} \right) \tag{3.34b}$$

which is the admittance function of a simple resonant circuit. It is typical of the admittance functions that will be employed throughout this analysis.

---

[3] The preferable term for $\tilde{Y}_r$ is chosen terminal admittance rather than the desired terminal admittance, because $\tilde{Y}$ will often contain components that compensate for Y'. In the absence of Y', these added components would also be undesirable.

CHAPTER IV

THE UPPER-SIDEBAND CONVERTER

Conversion between ω_r and ω_u, for the case where other signal frequencies are not present, will now be treated. An appropriate linear model for this problem is Fig. 3.3, with $\omega_x = \omega_u$. In turn it is described by (2.27), with $V_\ell = 0$, which leads to the following basic relation.

$$\begin{bmatrix} \mathrm{I\!I}_r \\ \\ \mathrm{I\!I}_u \end{bmatrix} = \begin{bmatrix} Y_r & j\omega_r \gamma_p^* \\ \\ j\omega_u \gamma_p & Y_u \end{bmatrix} \begin{bmatrix} V_r \\ \\ V_u \end{bmatrix} \tag{4.1}$$

While a resemblance will be noted between (4.1) and the admittance characterization of a passive, two-node, linear, bilateral circuit, there are two important differences that should be observed: (1) the node voltages in (4.1) are at different frequencies, and (2) its matrix is nonreciprocal. It can now be anticipated that the upper sideband converter will have some of the same properties as a passive, two-node, linear, bilateral network; but contrasting properties as well. Fortunately, these two property categories can be isolated in a manner having definite pedagogical value by converting (4.1) into the so-called ABCD representation given below:

$$\begin{bmatrix} V_r \\ \\ \mathrm{I\!I}_r \end{bmatrix} = \begin{bmatrix} A & B \\ \\ C & D \end{bmatrix} \begin{bmatrix} V_u \\ \\ \mathrm{I\!I}_u \end{bmatrix} \tag{4.2}$$

Before converting (4. 1) to (4. 2), it is convenient to separate the internal and external current components as follows

$$\begin{bmatrix} \text{I\!I}_r \\ \text{I\!I}_u \end{bmatrix} = \begin{bmatrix} \tilde{Y}_r & 0 \\ 0 & \tilde{Y}_u \end{bmatrix} \begin{bmatrix} V_r \\ V_u \end{bmatrix} + \begin{bmatrix} I_r \\ I_u \end{bmatrix} ; \begin{bmatrix} I_r \\ I_u \end{bmatrix} = \begin{bmatrix} j\omega_r C & j\omega_r \gamma_p \\ j\omega_u \gamma_p & j\omega_u C \end{bmatrix} \begin{bmatrix} V_r \\ V_u \end{bmatrix} \quad (4.3)$$

One additional modification in (4. 3) is that γ_p has been made real, which in no way restricts the validity of this relation, since the phase of one Fourier coefficient is always arbitrary. In fact, choosing γ_p real is equivalent to choosing a particular time origin.

When the individual relations in (4. 3) are transformed into ABCD notation, they yield

$$\begin{bmatrix} V_r \\ \text{I\!I}_r \end{bmatrix} = \begin{bmatrix} 1 & 0 \\ \tilde{Y}_r & 1 \end{bmatrix} \begin{bmatrix} V_r \\ I_r \end{bmatrix} \quad (4.4a)$$

$$\begin{bmatrix} V_r \\ I_r \end{bmatrix} = \begin{bmatrix} -C/\gamma_p & -j/\omega_u \gamma_p \\ -j\omega_r(\gamma_p^2 - C^2)/\gamma_p & \omega_r C/\omega_u \gamma_p \end{bmatrix} \begin{bmatrix} V_u \\ I_u \end{bmatrix} \quad (4.4b)$$

$$\begin{bmatrix} V_u \\ I_u \end{bmatrix} = \begin{bmatrix} 1 & 0 \\ -\tilde{Y}_u & 1 \end{bmatrix} \begin{bmatrix} V_u \\ \text{I\!I}_u \end{bmatrix} \quad (4.4c)$$

The (b) relation above contains all mixing effects. It can be further factored as follows.

$$\begin{bmatrix} V_r \\ I_r \end{bmatrix} = \begin{bmatrix} -C/\gamma_p & -j/\omega_r \gamma_p \\ \dfrac{-j\omega_r(\gamma_p^2 - C^2)}{\gamma_p} & C/\gamma_p \end{bmatrix} \begin{bmatrix} 1 & 0 \\ 0 & \omega_r/\omega_u \end{bmatrix} \begin{bmatrix} V_u \\ I_u \end{bmatrix} \quad (4.5)$$

The significance of the first term in (4. 5) is easily recognized by comparing with the ABCD representation of the symmetrical transformer. For the transformer in

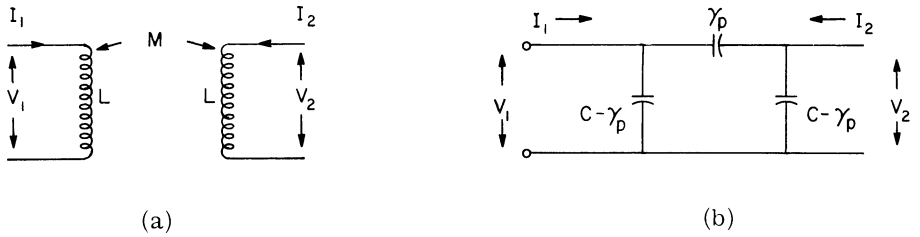

(a) (b)

Fig. 4. 1. A symmetrical transformer (a) and its dual (b) in π equivalent form.

Fig. 4. 1a, one can write

$$\begin{bmatrix} I_1 \\ V_1 \end{bmatrix} = \begin{bmatrix} -L/M & -j/\omega M \\ \dfrac{-j\omega(M^2 - L^2)}{M} & L/M \end{bmatrix} \begin{bmatrix} I_2 \\ V_2 \end{bmatrix} \tag{4.6}$$

which is the dual of the first factor in (4. 5). Therefore, the latter must represent two coupled capacitors with self-capacity C and mutual capacity γ_p. Admittedly, mutually coupled capacitors are seldom encountered in practice, but their properties are easily visualized from the well-known properties of their dual, the inductive transformer; or from their π equivalent, which is shown in Fig. 4. 1b.

The second factor in (4. 5) represents a broadband frequency converter operating between ω_r and ω_u. It has unity voltage gain, nonreciprocal current gain, and nonreciprocal power gain. The latter two gains equal the output to input frequency ratio, so this converter has exactly the power gain predicted by the general energy relations of Manley and Rowe (see Eq. 3. 3). Therefore, it is appropriately termed an ideal, upper-sideband, Manley-Rowe converter.

A further property of this ideal converter is admittance transformation, in which it obeys the relation

$$Y(\omega_r) = \frac{\omega_r}{\omega_u} \tilde{Y}_u(\omega_u) \tag{4.7}$$

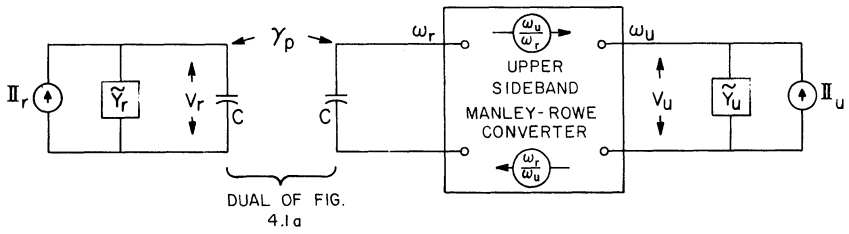

Fig. 4.2. A functional equivalent circuit for upper sideband conversion.

where $Y(\omega_u)$ is the reflected admittance at ω_r, and $\tilde{Y}_u(\omega_u)$ is the external admittance at the ω_u terminals.

From the interpretation of (4.4b) just given, the set of relations in (4.4) can be collectively represented by the circuit in Fig. 4.2, which is equivalent to Fig. 3.3. The advantage of Fig. 4.2 is its clear comparison of a first-order mixer operating between ω_r and ω_u, and a passive, two-node linear, bilateral network. Effects in the latter category will arise only from the external admittances and the mutually-coupled capacitor. The remaining effects, of mixing and nonreciprocal power gain, all take place in the Manley-Rowe converter. Therefore, the presence of the latter in Fig. 4.2 can be attributed entirely to asymmetry in (4.1).

Since the maximum power gain of a transformer is unity, the maximum power gain in Fig. 4.2 must be ω_u/ω_r, the gain of the Manley-Rowe converter. To actually achieve this gain, the capacitive transformer must match the load and source admittances. This matching process can be traced out by first noting that the load admittance at ω_u is transformed to ω_r by the converter, which reflects the load (4.7) into the secondary of the capacitive transformer. In turn, the transformer reflects loads between primary and secondary according to the rule:

$$\left[\begin{array}{c}\text{admittance reflected} \\ \text{into primary}\end{array}\right] = \frac{\omega_r^{\,2}\,\gamma_p^{\,2}}{\left[\begin{array}{c}\text{total admittance} \\ \text{in secondary}\end{array}\right]} \qquad (4.8)$$

Therefore, maximum power gain between ω_r and ω_u occurs for

$$\tilde{Y}_r^* - j\omega_r C = \frac{\omega_r^2 \gamma_p^2}{\frac{\omega_r}{\omega_u}\tilde{Y}_u + j\omega_r C} \tag{4.9a}$$

$$= \frac{\omega_r \omega_u \gamma_p^2}{\tilde{Y}_u + j\omega_u C} \tag{4.9b}$$

The technique of analyzing the upper-sideband converter by dissection has successfully illustrated the origin of its basic mixing properties. However, this procedure could hardly be called an expedient analytical tool. A more direct analysis would treat the circuit properties of (4. 1) as it stands. If the real parts of $\tilde{Y}_r$ and $\tilde{Y}_u$ are regarded as the source and load conductance respectively, then the transducer gain defined in (3. 15) can be found directly from (4. 1). Setting $\mathbb{I}_u = 0$, the voltage gain is

$$\frac{V_u}{V_r} = \frac{j\omega_u \gamma_p}{Y_u} \tag{4.10a}$$

while the input admittance seen by $\mathbb{I}_r$ is

$$Y_{r_{in}} = Y_r + \frac{\omega_r \omega_u \gamma_p^2}{Y_u} \tag{4.10b}$$

Therefore, by (3. 15b),

$$G_{ru} = \frac{4 \tilde{g}_r \tilde{g}_u \omega_u^2 \gamma_p^2}{\left| Y_r Y_u + \omega_r \omega_u \gamma_p^2 \right|^2} \tag{4.11}$$

which can be shown to be maximum under the condition (4. 9b). The maximum transducer gain then equals the maximum power gain, as it obviously should since (4. 9b) is the condition for admittance matching. Without the representation in Fig. 4. 2 to serve as a guide, the significance of (4. 11) would be more obscure. Therefore, Fig. 4. 2, and other dissected circuits that will be introduced in later chapters, will continue to be convenient for interpretation, but direct matrix analysis will be the primary method followed henceforth.

4.1 Bandwidth of the Upper-Sideband Converter

The bandwidth of the converter under discussion can be attribtued to the capacitive transformer in Fig. 4.2. Being a transformer, its properties depend upon the "coefficient of coupling" γ_p/C, which can be more appropriately termed the coefficient of pumping. Remember that γ_p is proportional to pump voltage, according to (2.23b). By transformer analogy, conversion pass bands that are either under, critical, or over-coupled can be anticipated for appropriate choices of pump level. Several other well known results from transformer theory will also be drawn upon (Ref. 28).

A given transformer bandwidth will require the least coefficient of coupling if its primary and secondary are synchronously tuned. In applying this result to the present discussion, maximum conversion bandwidth can be anticipated, for a given γ_p/C ratio, if $\tilde{Y}_u$ and $\tilde{Y}_r$ resonate C at $\bar{\omega}_u$ and $\bar{\omega}_r$ respectively. If $\tilde{Y}_u = \tilde{g}_u + j\tilde{b}_u$ and $\tilde{Y}_r = \tilde{g}_r + j\tilde{b}_r$, resonance corresponds to

$$\begin{aligned} \tilde{b}_r + \bar{\omega}_r C &= 0 \\ \tilde{b}_u + \bar{\omega}_u C &= 0 \end{aligned} \tag{4.12}$$

The condition for maximum power gain (4.9b) then becomes

$$\tilde{g}_r = \frac{\bar{\omega}_r \bar{\omega}_u \gamma_p^2}{g_u} \tag{4.13}$$

It can also be written

$$\frac{\beta_r \beta_u}{\bar{\omega}_r \bar{\omega}_u} = \frac{\gamma_p^2}{C_r C_u} = k_p^2 \tag{4.14}$$

where β_r and β_u are the individual bandwidths (in rad./sec) at ω_r and ω_u (in the absence of pumping), and where C_r and C_u are the total shunt capacities affecting the ω_r and ω_u resonances. Generally, C_r and C_u exceed C due to stray or filter capacity in Y_r and Y_u, and since bandwidth and conductance level are more easily measured that total shunt capacity, C_r and C_u will be defined by the relations $C_r = g_r/\beta_r$, and $C_u = g_u/\beta_u$, where g_r and g_u are

the individual conductance levels in the absence of pumping. It is now evident that

$$\frac{\gamma_p}{\sqrt{C_r C_u}} = k_p \tag{4.15}$$

should be considered the pumping coefficient rather than γ_p/C. This substitution will be introduced henceforth by assuming

$$C = \sqrt{C_r C_u}$$

Returning now to (4.14), the latter can be seen to predict the smallest pumping coefficient for obtaining a given terminal bandwidth with maximum conversion gain.

A second result from transformer theory can now be applied directly to the upper-sideband mixer. For a given coefficient of coupling, maximum transformer bandwidth results if the primary and secondary bandwidths are equal (Ref. 28). In the present analysis the bandwidth of the secondary depends upon the secondary admittance, which is given by

$$\frac{\omega_r}{\omega_u}(\tilde{Y}_u + j\omega_u C) = \frac{\omega_r}{\omega_u} Y_u \tag{4.16}$$

Over reasonably small bandwidths, ω_r/ω_u can be considered constant, and then the secondary bandwidth equals β_u, the bandwidth of Y_u. The condition for optimum conversion bandwidth is now $\beta_r = \beta_u$, but this condition can be satisfied with a variety of pass bands. As an example, Table 4.1 gives specifications for both the equal ripple and the maximally flat cases, which can be obtained directly from the corresponding transformer relations. A conclusion to be noted in Table 4.1 is that a given pumping coefficient will yield the greatest bandwidth in a maximally flat characteristic. For example, the ratio of bandwidth to pumping coefficient is 1/12 smaller for the equal ripple pass band, than for the maximally flat conversion pass band, with the same pumping coefficient. A comparison of the latter two cases is also shown in Fig. 4.3.

Pass Band	Bandwidth β	Pumping Coefficient k_p	$\sqrt{\bar{G}_{ru}}\,\beta$
Maximally Flat (critically coupled)	2(B.W)	(B.W) $\left[\frac{1}{\bar{\omega}_r\bar{\omega}_u}\right]$	$2\,k_p\bar{\omega}u$
Equal Ripple	2.2[2(B.W)]	2.4 (B.W) $\left[\frac{1}{\bar{\omega}_r\bar{\omega}_u}\right]$	$\frac{11}{12}[2\,k_p\bar{\omega}_u]$

Table 4.1. Realizable pass band characteristics for upper-sideband conversion. (B.W) denotes the bandwidth of the individual terminal admittance, which are assumed to be equal.

Although these conclusions were obtained from simple transformer theory, by identifying $\gamma_p/\sqrt{C_rC_u}$ with the coefficient of coupling, a practical difference must be noted. Pumping is a dynamic quantity, and any increase in the coefficient of pumping will generally call for more pump oscillator power. However, coupling is a static quantity, which can usually be incrased by a geometrical adjustment. Therefore, one should remember that conversion pass bands other than maximally flat demand premium pump power, and this must be paid for continually.

An alternate way of summarizing the performance of mixers is through gain-bandwidth product, which will be defined as (transducer gain)$^{\frac{1}{2}}$ x (bandwidth). This quantity appears in Table 4.1 for the case of upper-sideband conversion. Sometimes gain-bandwidth evaluation is made on the basis of voltage gain, but since (voltage gain) $\geq$ (transducer gain)$^{\frac{1}{2}}$ the latter yields a more conservative estimate of gain-bandwidth product. In reactive mixers it is important to observe that gain-bandwidth product is proportional to pump frequency (at least for ideal cases), while in conventional mixers it is independent of frequency.

4.2 Degrading Influences on Upper-Sideband Conversion

The most fundamental limitation on reactive mixer performance is loss in the mixer element. It has been previously mentioned that the varactors are the most commonly used reactive mixer components, and their losses have been represented by series resistance in Fig. 3.7a, or by equivalent shunt conductance in Fig. 3.7b. The latter representation can be used with the circuit in Fig. 3.4 to appropriately describe an upper-sideband converter with a nonideal varactor. In this case, ω_1 and ω_2 will be identified with ω_r and ω_u

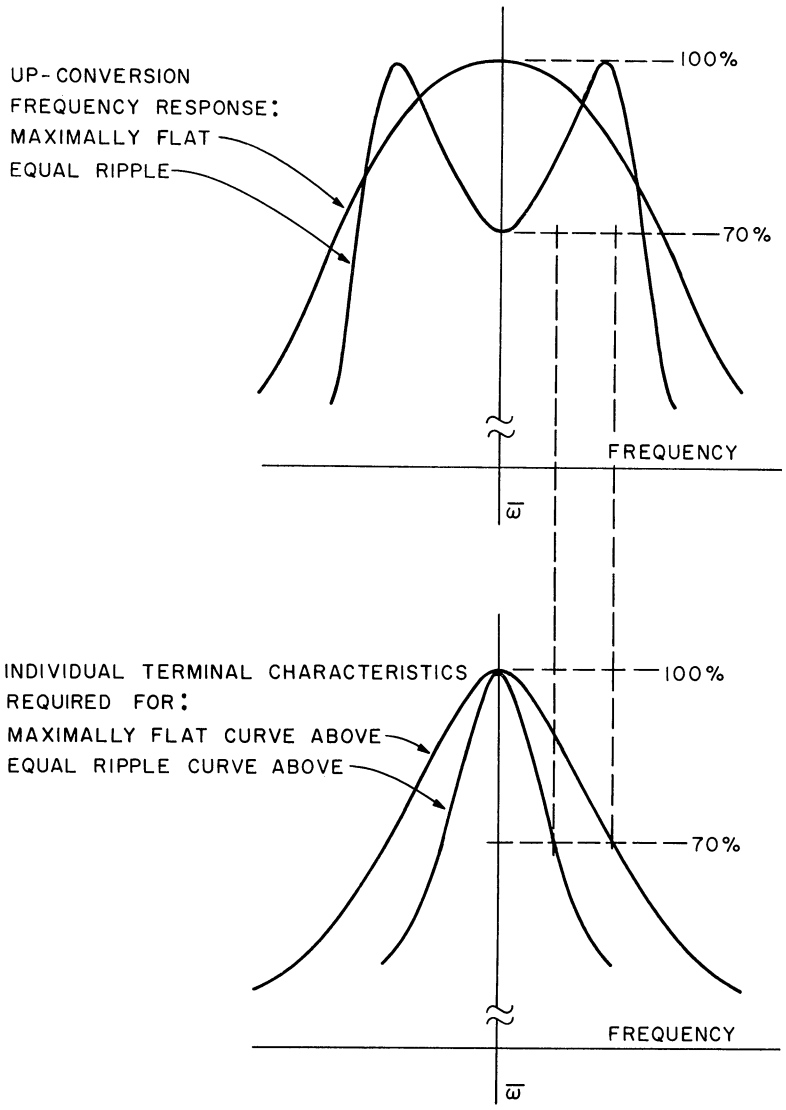

Fig. 4.3. A comparison of maximally flat and equal ripple pass bands for equal pumping coefficients.

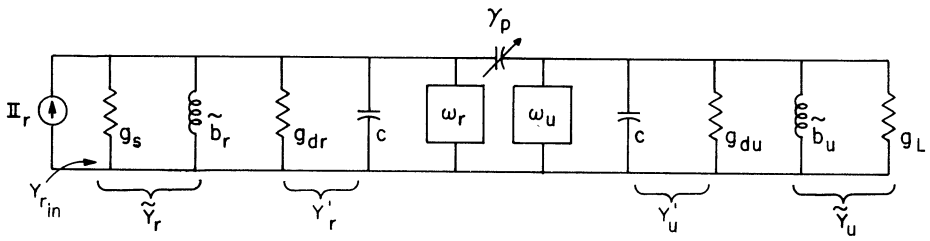

Fig. 4.4. A special case of Fig. 3.4 appropriate for upper-sideband conversion.

respectively, which yields the circuit in Fig. 4.4. Using the approximation in (3.29), the parasitic conductances in Fig. 4.4 have values

$$g_{dr} = -\frac{\omega_r^2 C}{\omega_d} \tag{4.17a}$$

$$g_{du} = -\frac{\omega_u^2 C}{\omega_d} \tag{4.17b}$$

4.2.1 Effects of Varactor Loss in Gain. With the source at ω_r and the load at ω_u, as shown, the effect of parasitic loss on gain can be evaluated by (3.16). In making this calculation, the condition that each terminal is independently tuned will be assumed, since it has been previously shown to yield optimum conversion bandwidths. The modified midband gain $\tilde{\bar{G}}_{ru}$ in (3.16) is equivalent to (4.11), which with all susceptance tuned out can be written

$$\tilde{\bar{G}}_{ru} = 4\frac{\bar{\omega}_u}{\bar{\omega}_r}\left[\frac{g_r g_u \bar{\omega}_r \bar{\omega}_u \gamma_p^2}{(g_r g_u + \bar{\omega}_r \bar{\omega}_u \gamma_p^2)^2}\right] \tag{4.18a}$$

$$= \frac{\bar{\omega}_u}{\bar{\omega}_r}\left[\frac{4\rho_u}{(1+\rho_u)^2}\right] \tag{4.18b}$$

where

$$\rho_u = -\frac{\omega_r \omega_u \gamma_p^2}{g_r g_u} \tag{4.18c}$$

Now, using (4.18b) in (3.16), yields the true midband gain

$$\bar{G}_{ru} = \frac{\bar{\omega}_u}{\bar{\omega}_r}\left(\frac{g_S g_L}{g_r g_u}\right)\frac{4\rho_u}{(1+\rho_u)^2} \tag{4.19}$$

Of course, in the limit of zero varactor loss, (4.19) reduces to (4.18b) which is a maximum when $\rho_u = 1$, corresponding to (4.13).

An interesting aspect of reactive mixer analysis now arises. When the varactor is ideal, conversion gain for a fixed ω_r increases indefinitely with ω_p, as shown by

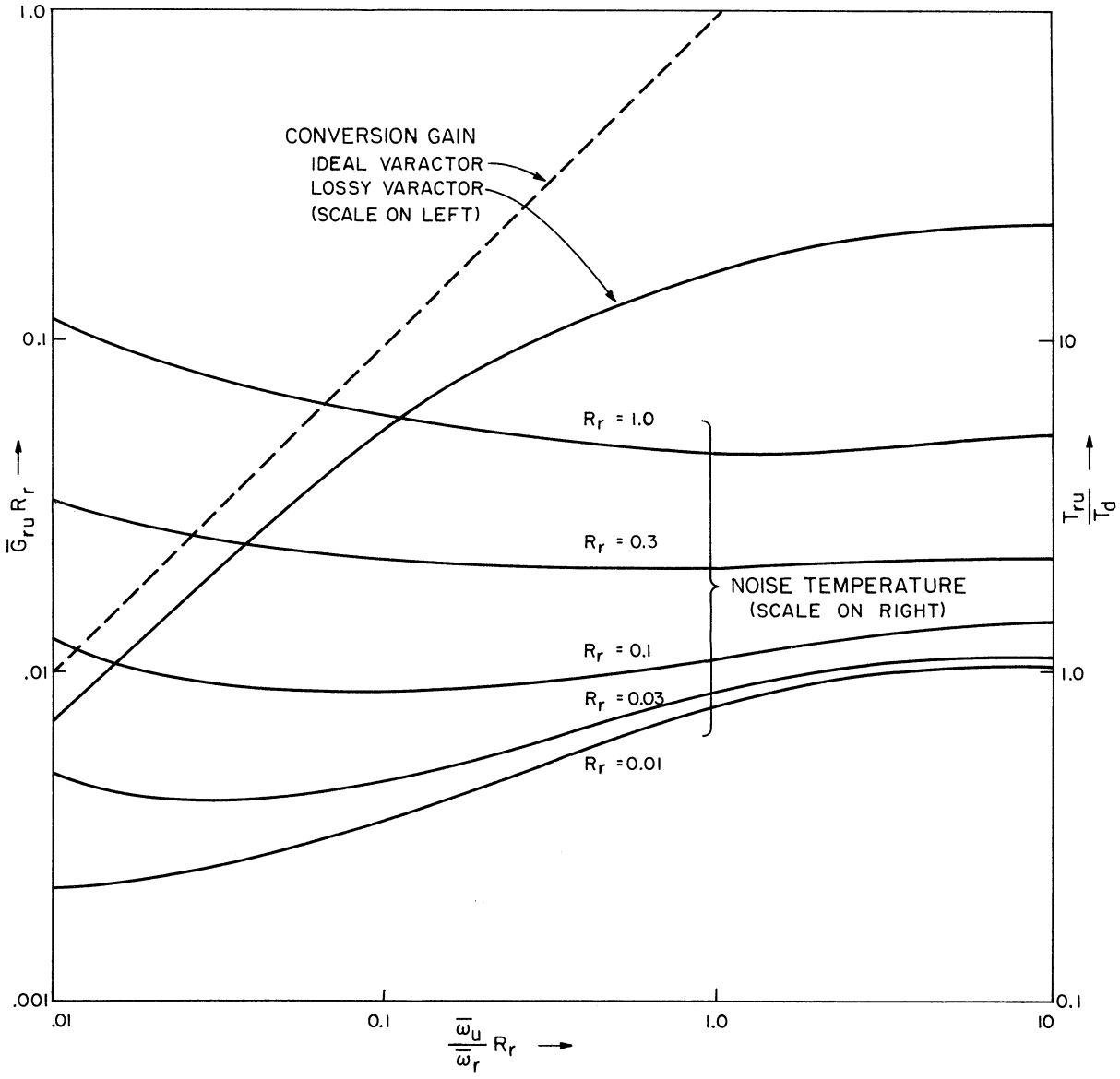

Fig. 4. 5. Plots of conversion gain and noise temperature vs. frequency ratio showing the influence of varactor loss.

the dotted curve in Fig. 4. 5. In the presence of degrading series resistance, the effective shunt loss at ω_u increases as the square of the pump frequency. Therefore, for a given ω_r (signal frequency), ω_d (varactor cut-off frequency), and pumping coefficient, ever diminishing returns will accompany increases in pump frequency.

For a fixed ω_r and ω_u, it has been shown by Jones and Honda (Ref. 29) and also by Kurokawa and Uenohara (Ref. 30) that (4. 19) has a maximum value given by

$$\left(\bar{G}_{ru}\right)_{max} = \left(\frac{K-1}{K+1}\right)\left(\frac{\omega_u}{\omega_r}\right) \tag{4.20}$$

subject to the condition

$$\frac{g_S}{g_{dr}} = \frac{g_L}{g_{du}} = K, \text{ or } \rho_u = \frac{K-1}{K+1} \tag{4.21}$$

where

$$K^2 = 1 + \frac{\bar{\omega}_r \bar{\omega}_u \gamma_p^2}{g_{dr} g_{du}} \tag{4.22}$$

The influence of frequencies variations can now be determined by substituting (4.17) into (4.21), which yields

$$K^2 = 1 + \frac{\omega_d^2 \gamma_p^2}{\bar{\omega}_r \bar{\omega}_u C^2} \tag{4.23a}$$

$$= 1 + \frac{\omega_d'^2}{\bar{\omega}_r \bar{\omega}_u} \tag{4.23b}$$

where[1] $\omega_d' = \omega_d \gamma_p / C$. Therefore, parasitic varactor loss causes K and ρ_u to fall off monotonically with ω_p (or with ω_u), such that the maximum realizable gain of the up converter is

$$\lim_{\omega_p \to \infty} \bar{G}_{ru} = \left(\frac{\omega_d'}{2\omega_r}\right)^2 \tag{4.24}$$

The plot of optimum gain vs. pump frequency, shown in Fig. 4.5, suggests that pump frequencies higher than $(\omega_d')^2/\omega_r$ offer little added advantage.

It is interesting to now interpret the conditions for maximum gain, as stated in (4.22). The reflected input conductance at ω_r is

$$\rho_u g_r = \rho_u (g_S + g_{dr}) = \left(\frac{K-1}{K+1}\right) g_S$$

$$= g_S - g_{dr} \tag{4.25a}$$

---

[1] The quantity $\gamma_p Q/\omega_c = \gamma_p \omega_d / C\omega$ is often called the dynamic figure of merit for a varactor, so ω_d' is the frequency where this figure of merit becomes unity.

Similarly, the reflected input conductance at ω_u is

$$\rho_u g_u = g_L - g_{du} \tag{4.25b}$$

Therefore, when the parasitic losses g_{dr} and g_{du} are included, the total input and output conductance seen by the source and load are g_S and g_L respectively. Hence optimum gain again corresponds to a matched condition, but now the source and load are matched to the degraded mixer terminals.

4.2.2 Noise Figure. A second measure of the degradation induced by varactors loss is noise figure. Varactor loss makes a contribution to the up converter noise figure in both the ω_r and the ω_u bands, but these contributions can be conveniently associated with the parasitic conductances g_{dr} and g_{du} in Fig. 4.4. Since these conductances are assumed to originate solely in varactor loss, as expressed by (4.17), they can be assigned a common noise temperature T_d. Therefore, applying the noise figure formula in (3.27) (without the T_3 term), yields

$$F_{ru} = 1 + \frac{T_d}{T_o}\left[\frac{g_{dr}}{g_S} + \frac{(\bar{G}_{uu}-1)\,T_L}{\bar{G}_{ru}\,T_d} + \frac{\bar{G}_{uu}\,g_{du}}{\bar{G}_{ru}\,g_L}\right] \tag{4.26}$$

where $\bar{G}_{uu}$ is the transducer gain by reflection at ω_u. By way of review, $\bar{G}_{uu}$ is the midband power delivered to g_L relative to the power available from a source at ω_u with internal conductance g_L [see (3.25)]. G_{uu} depends on the input admittance at ω_u, and by a calculation similar to that yielding (3.15b), the total input admittance at ω_u is

$$Y_{u_{in}} = Y_u + \frac{\omega_r \omega_u \gamma_p^{\,2}}{Y_r} \tag{4.27a}$$

At midband

$$\bar{Y}_{u_{in}} = \bar{g}_{u_{in}} = g_u(1+\rho_u) \tag{4.27b}$$

and using the source I_u shown in Fig. 4.4, the gain G_{uu} is easily shown to be

$$\bar{G}_{uu} = \frac{4g_L^{\,2}}{g_u^{\,2}}\left(\frac{1}{1+\rho_u}\right)^2 \tag{4.28}$$

Therefore

$$\frac{\overline{G}_{uu}}{\overline{G}_{ru}} = \frac{\overline{\omega}_r}{\overline{\omega}_u}\left(\frac{g_L g_r}{g_u g_s}\right)\frac{1}{\rho_u} \tag{4.29}$$

and

$$F_{ru} = 1 + \frac{T_d}{T_o}\left[\frac{g_{dr}}{g_S} + \left(\frac{\overline{\omega}_r g_r}{\overline{\omega}_u g_S \rho_u} - \frac{1}{G_{ru}}\right)\frac{T_L}{T_d}\right] \tag{4.30}$$

When (3.27) is satisfied, so $\overline{G}_{ru}$ is a maximum, (3.32a) yields

$$(F_{ru})_{\text{Max Gain}} = 1 + \frac{T_d}{T_o}\left(1 + \frac{1}{\overline{G}_{ru}}\right)\frac{1}{K} \tag{4.31}$$

which agrees with the results previously obtained in Ref. 29 and Ref. 30. An interesting property of (4.31) is its lack of dependence on T_2 which arises because the load g_L is matched. A generalization of this result is treated in Section 9.1.

Since K is a monotonically decreasing function of pump frequency, according to (4.23b), F_{ru} increases monotonically with pump frequency and approaches the value

$$1 + \frac{T_d}{T_o}(4R_r + 1) \tag{4.32a}$$

where

$$R_r = (\omega_r/\omega'_d)^2 \tag{4.32b}$$

More convenient for plotting, however, is the equivalent noise temperature $T_{ru} = (F_{ru} - 1)T_d$, which is shown in the lower portion of Fig. 4.5. The curves of T_{ru} show that it can be less than T_d, if $R_r < 0.1$ approximately. The minimum noise temperature occurs when $\omega_u/\omega_r = 1$, but this is an unlikely operating point because then $G_{ru} < 1$. Therefore to obtain high gains with low noise figures, R_r must be much less than 1, and $0.1 < R_r\,\overline{\omega}_u/\overline{\omega}_r < 1$.

The parameter R_r is a convenient basis for normalization because it only depends on input frequency, varactor quality, and the degree of pumping. Each of these quantities is usually specified in the early phases of a design problem. Also, the dynamic

figure of merit[2] is equal to $1/R_r$.

4.2.3 Efficiency Factors. The degradation due to varactor loss can be alternately expressed in terms of input and output efficiency factors. These will be introduced at this time because they will be more convenient than the parameter K in later analysis. Let

$$x = \frac{\tilde{g}_r}{g_r} \tag{4.33a}$$

by the efficiency factor at ω_r, and

$$y = \frac{\tilde{g}_u}{g_u} \tag{4.33b}$$

by the similar quantity at ω_u. Then, for the case of conversion from ω_r to ω_u

$$x = \frac{g_s}{g_r}, \quad y = \frac{g_L}{g_u} \tag{4.34}$$

which yields the following restatements of the conditions for optimum G_{ru}:

$$x = y = \frac{K}{1+K} \tag{4.35a}$$

$$G_{ru} = \frac{\bar{\omega}_u}{\bar{\omega}_r}\,\rho_u \tag{4.35b}$$

$$\rho_u = 2x - 1 = 1 + 2\,\frac{\bar{\omega}_u}{\bar{\omega}_r}\,R_r\left[1 - \sqrt{1 + \frac{\bar{\omega}_r}{\bar{\omega}_u R_r}}\right] \tag{4.35c}$$

$$\frac{\bar{\omega}_u}{\bar{\omega}_r} = \frac{(1-x)^2}{(2x-1)\,R_r} \tag{4.35d}$$

$$(F_{ru})_{\text{max gain}} = 1 + \frac{T_d}{T_o}\left[\frac{1-x}{x} + \frac{R_r}{x(1-x)}\right] \tag{4.35f}$$

The minimum of the latter expression occurs for

$$R_r = \frac{(1-x)^2}{2x-1}, \tag{4.36}$$

---

[2]See footnote, Page 56.

which calls for $\bar{\omega}_u/\bar{\omega}_r = 1$, as previously discussed.

4.3 Down-Conversion From ω_u to ω_r

The Manley-Rowe converter in Fig. 4.2 is nearly unilateral, because its gain is less than unity for down-conversion from ω_u to ω_r. While this case is of less practical interest than the up-converter, an analysis of the down-converter follows directly from the preceding analysis, simply by interchanging the subscripts r and u everywhere. This observation follows directly from the symmetry of (4.1), when γ_p is real. In other words, the response to $\mathbb{I}_u$ is the same mathematical form as that to $\mathbb{I}_r$, if r and u are interchanged. Therefore, by (4.20)

$$(\bar{G}_{ur})_{max} = \left(\frac{K-1}{K+1}\right)\frac{\bar{\omega}_r}{\bar{\omega}_u} = \rho_u \frac{\bar{\omega}_r}{\bar{\omega}_u} \tag{4.37}$$

since K and ρ_u are symmetric in r and u. As expected, $(\bar{G}_{ur})_{max}$ is less than unity.

The curves in Fig. 4.5 can also be applied to this case by interchanging r and u. This includes replacing $R_r = (\omega_r/\omega'_d)^2$ by

$$R_u = \left(\frac{\bar{\omega}_u}{\omega'_d}\right)^2 = \left(\frac{\bar{\omega}_u}{\bar{\omega}_r}\right)^2 R_r \tag{4.38}$$

so the abcissa in Fig. 4.5 becomes $(\bar{\omega}_r/\bar{\omega}_u)\, R_u$. A numerical comparison of up- and down-conversion is shown in Table 4.2.

	R	Abcissa in Fig. 4.5	Gain	Noise Temperature
Up-Conversion	$R_r = 0.01$	$R_r \frac{\omega_u}{\omega_r} = 0.1$	5.5	$0.35\ T_d$
Down-Conversion	$R_u = 1$	$R_u \frac{\omega_r}{\omega_u} = 0.1$	0.055	$5.8\ T_d$

Table 4.2. A comparison of up- and down-conversion for $\bar{\omega}_u/\bar{\omega}_r = 10$.

In summary, the ratio of down-conversion gain to up-conversion gain is approximately $(\omega_r/\omega_u)^2$, which rarely exceeds 0.1. The corresponding ratio of noise temperatures is approximately $\omega_u\ \omega_r$ which generally exceeds three. Therefore, the down-conversion mode offers low gains and high noise figures, making it rather unattractive.

4.4 Conclusion

In describing the basic properties of upper sideband conversion, the purpose of the present chapter has been fourfold: (1) to illustrate the variety of effects that relatively simple relations, such as (4.1), can yield; (2) to note how the basic circuit quantities outlined in Section 3.4 can be derived in a particular case; (3) to show a physical significance for the major results derived; and (4) to prepare for comparison with other systems that will be analyzed later.

CHAPTER V

THE LOWER-SIDEBAND CONVERTER

Perhaps the most fascinating aspect of reactive mixing is the radical difference that occurs between upper and lower sidebands. Having just studied the properties of the upper sideband, the contrasting properties of the lower sideband will now be developed.

Following the procedure of Chapter IV, a basic relation for lower-sideband mixing can be derived from (2. 27) by setting $V_u = 0$, which yields

$$\begin{vmatrix} \mathrm{I\!I}_r \\ \mathrm{I\!I}^*_\ell \end{vmatrix} = \begin{vmatrix} Y_r & j\omega_r\gamma_p \\ -j\omega_\ell\gamma_p^* & Y^*_\ell \end{vmatrix} \begin{vmatrix} V_r \\ V^*_\ell \end{vmatrix} \tag{5.1}$$

The similarity between (4. 1) and (5. 1) is quite apparent, if γ_p is again made real. In fact, by taking the conjugate of the second line of (4. 1), and by replacing the subscript u by ℓ, one obtains (5. 1) directly. The value of this resemblance is that many results from the study of (4. 1) can be carried over directly to the solution of (5. 1). For example, by making the substitution noted above, (5. 1) can immediately be written in the informative ABCD notation of (4. 4) and (4. 5). This step yields the following interpretive relation.

$$\begin{vmatrix} V_r \\ \mathrm{I\!I}_r \end{vmatrix} \underbrace{\begin{vmatrix} 1 & 0 \\ Y_r & 1 \end{vmatrix}}_{\substack{\text{terminal} \\ \text{admittance}}} \underbrace{\begin{vmatrix} C/\gamma_p & j/\omega_r\gamma_p \\ \dfrac{-j\omega_r(\gamma_p^2 - C^2)}{\gamma_p} & C/\gamma_p \end{vmatrix}}_{\substack{\text{capacitive} \\ \text{transformer}}} \underbrace{\begin{vmatrix} 1 & 0 \\ 0 & \dfrac{-\omega_r}{\omega_\ell} \end{vmatrix}}_{\substack{\text{ideal} \\ \text{converter}}} \underbrace{\begin{vmatrix} 1 & 0 \\ -Y^*_\ell & 1 \end{vmatrix}}_{\substack{\text{terminal} \\ \text{admittance}}} \begin{vmatrix} V^*_\ell \\ \mathrm{I\!I}^* \end{vmatrix} \tag{5.2}$$

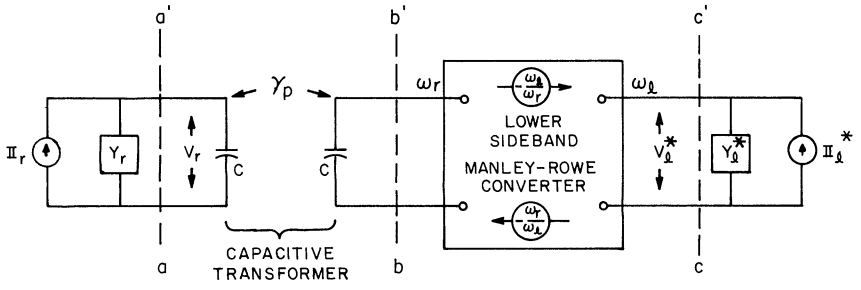

Fig. 5.1. A functional equivalent circuit for lower sideband conversion.

Since each factor above can be ascribed to one stage in a cascade, they together produce the equivalent circuit in Fig. 5.1. In resemblance to Fig. 4.2, Fig. 5.1 contains a capacitive transformer and an ideal frequency converter with unity voltage gain and nonreciprocal current and power gain. In contrast, however, the current and power gains of the latter are the negative of the output to input frequency ratio. Therefore, on the basis of (3.5), this converter should be termed an ideal, lower-sideband, Manley-Rowe converter.

A peculiar aspect of Fig. 5.1 is that all currents and voltages to the right of the line cc' are complex conjugates of the corresponding currents and voltages in an actual lower-sideband mixer. The effect of this alteration can be discovered by applying a load

$$Y_\ell = g_\ell + jb_\ell \tag{5.3}$$

at the ω_ℓ terminals. If Y_ℓ is assumed to be passively realizable, it will satisfy the conditions

$$g_\ell \geq 0; \qquad \frac{\partial b_\ell}{\partial \omega_\ell} > 0 \tag{5.4a}$$

which the conjugate of Y_ℓ would fail to pass. For it,

$$\frac{\partial b_\ell}{\partial \omega_\ell} < 0 \tag{5.4b}$$

and hence Y_ℓ^* is unrealizable. However, being in an equivalent circuit, the effect of Y_ℓ^* at

the ω_ℓ terminals of Fig. 5.1 will be the same as the effect of Y_ℓ in the actual mixer.

When the load Y_ℓ^* is transformed through the Manley-Rowe converter in Fig. 5.1, it appears in the secondary of the capacitive transformer in the form

$$Y = -\frac{\omega_r}{\omega_\ell} Y_\ell^* = \frac{\omega_r}{\omega_\ell}(-g_\ell + jb_\ell) \tag{5.5}$$

which is illustrated in Fig. 5.2. A significant feature of the admittance (5.5) is its negative real part and its nonmonotonic susceptance. Hence, some rather unusual circuit effects can be expected from lower-sideband mixing, but with the aid of the equivalent circuit just generated these effects can by systematically determined. The approach will be no more complicated than extending the known properties of the simple capacitive transformer to include unrealizable loads, like (5.5). For example, combining (5.5) and (4.8) shows the total input admittance at ω_r to be

$$Y_{r_{in}} = Y_r - \frac{\omega_r \omega_\ell \gamma_p^2}{Y_\ell^*} \tag{5.6}$$

Other results of this type will now be developed.

One unusual feature of the circuit in Fig. 5.2 is power gain (by reflection) in the primary, which occurs in addition to the transmission power gain from primary to secondary. To demonstrate these effects, let L and C in Fig. 5.2 be resonant at $\overline{\omega}_r$, and let the primary conductance g_r be partitioned into a load and a source conductance, g_L and g_S, respectively. The available source power is then

$$P_A = \frac{|I_r|^2}{4g_S} \tag{5.7}$$

The load power depends on the reflected primary admittance, which at midband is

$$-\frac{\overline{\omega}_r^2 \gamma_p^2}{g} = -\frac{\overline{\omega}_r \overline{\omega}_\ell \gamma_p^2}{g_\ell} = -\rho_\ell g_r \tag{5.8}$$

Here, ρ_ℓ is analogous to ρ_u in (4.18c). The power delivered to g_L is

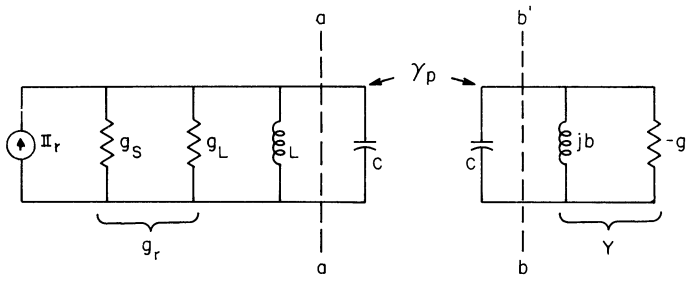

Fig. 5.2. The equivalent circuit of a lower-sideband converter after Y_ℓ is transformed to ω_r.

$$P_L = \left[\frac{\mathrm{I\!I}_r}{g_r(1-\rho_\ell)}\right]^2 g_L = \frac{4\, g_S g_L P_A}{g_r^2 (1-\rho_\ell)^2} \tag{5.9}$$

so it is evident that P_L can greatly exceed the available source power. In fact, P_L becomes infinitely large as

$$\rho_\ell \to 1 \tag{5.10}$$

The power amplification in this case can be attributed to an enhancement of the input voltage by negative conductance reflected into the primary.

The power converted from ω_r to ω_ℓ can also greatly exceed the available source power, but then the load g_L will be coupled to ω_ℓ, instead of to ω_r (i.e., $g_\ell = g_L$). In Fig. 5.2, the power reaching the secondary of the capacitive transformer is

$$P_\ell = \left(\frac{\omega_\ell}{\omega_r}\right) \frac{|\mathrm{I\!I}_r|^2 \rho_\ell}{g_r(1-\rho_\ell)} = 4\left(\frac{\omega_\ell}{\omega_r}\right)\left(\frac{g_S}{g_r}\right) \frac{\rho_\ell}{(1-\rho_\ell)^2} \; P_A \tag{5.11}$$

so the midband transducer gain from ω_r to ω_ℓ becomes

$$\overline{G}_{r\ell} = \frac{4\rho_\ell}{(1-\rho_\ell)^2}\left(\frac{\omega_\ell}{\omega_r}\right)\frac{g_S}{g_r} \tag{5.12}$$

Similarly, from (5.9), the midband transducer gain by reflection is

$$\overline{G}_{rr} = \frac{4\, g_S g_L}{g_r^2}\left(\frac{1}{1-\rho_\ell}\right)^2 \tag{5.13}$$

which reduces to

$$\overline{G}_{rr} = \left(\frac{1}{1-\rho_\ell}\right)^2 \tag{5.14}$$

if the first factor is optimized by letting $g_S = g_L = 1/2\, g_r$. Both $\overline{G}_{rr}$ and $\overline{G}_{r\ell}$ can be arbitrarily large, by allowing ρ_ℓ to approach one.

Considering (5.8) further, it is seen that the condition $\rho_\ell \to 1$ produces a cancellation of the external terminal conductance at $\overline{\omega}_r$ (or at $\overline{\omega}_\ell$) by the reflected conductance at $\overline{\omega}_r$ (and at $\overline{\omega}_\ell$). So as ρ_ℓ passes through one, the total input conductance passes from positive to negative, which raises the question of stability. A rigorous treatment of stability is made in Chapter VI, where it is demonstrated that the circuit under discussion is stable, to first approximation, if

$$\rho_\ell < 1 \tag{5.15}$$

This agrees with the intuitive prediction based on (5.10).

Both $\overline{G}_{r\ell}$ and $\overline{G}_{rr}$ depend upon ρ_ℓ in the same way, but g_r and g_ℓ will differ in these two cases because only one contains the load g_L. Also, a slight distinction is to be noted between the various reflection gains that have been introduced so far. For $\overline{G}_{uu}$ in (4.28) the source and load conductance are identical, but for $\overline{G}_{rr}$ in (5.13) the source and load conductance are separate components at the same terminal pair. Since a simple modification [based on (3.16)] can reverse the sense of either of these quantities, context will henceforth be relied upon for making these cases distinct.

5.1 Bandwidth and Sensitivity of the Lower-Sideband Converter

There are several auxiliary parameters that shed further light on the circuit properties of the lower-sideband converter. One is bandwidth, and here again the transformer rule applies: the greatest conversion bandwidth occurs when the individual circuit bandwidths are equal. For large gains, where $\rho_\ell - 1 \approx 0$, the conversion bandwidth is (Ref. 31)

$$\beta_{r\ell} = \frac{\gamma_p}{2C}\sqrt{\omega_r \omega_\ell}\,(1-\rho_\ell) \text{ rad./sec.} \tag{5.16}$$

Thus for high gains the gain-bandwidth product is

$$\sqrt{\overline{G}_{r\ell}}\ \beta_{r\ell} \approx \frac{\omega_\ell \gamma_p}{C} = \omega_\ell k_p \tag{5.17}$$

where k_p is the pumping coefficient.

In comparing with Table 4.1, which gives the gain-bandwidth product for upper-sideband conversion with the same ω_p and k_p, Table 4.1 is seen to exceed (5.17) by a factor of more than $\sqrt{2}$. So in spite of the fact that lower-sideband conversion offers much larger gains, its gain-bandwidth product is less, which speaks for the superior bandwidth of the upper-sideband converter. For the latter, ω_u increases when ω_r increases and both circuits become detuned in the same direction. However, transformer action tends to cancel these two detuning effects. The result can be critical or over-coupled characteristics that are extremely broadband. For the lower-sideband converter, ω_ℓ decreases as ω_r increases and the detuning effects are additive. Hence, narrow, under-coupled pass bands result, whose width decreases with increasing gain.

A detailed study of the bandwidth of lower-sideband converters has been made by Lombardo and Sard (Ref. 32). By direct analysis, they confirm the rule of equal terminal bandwidths which was introduced here by equivalent circuit arguments. They also confirm the optimum gain-bandwidth product in (5.17) for the case where parasitic loss is negligible. However, they predict an important correction when the effective shunt capacity at ω_r and ω_ℓ exceeds the varactor capacity C. In this case, C in (5.17) should be replaced by $\sqrt{C_r C_\ell}$, where C_r and C_ℓ equal C plus the stray or filter capacity at ω_r or ω_ℓ respectively. A similar observation was made regarding the pumping coefficient in Section 4.1.

A second parameter of interest in lower-sideband conversion is sensitivity, which can be explained as follows. If a circuit characteristic Z depends on a variable X, the sensitivity of Z to X is defined as

$$S_X = \frac{\partial \log Z}{\partial \log X} = \frac{X \partial Z}{Z \partial X} \tag{5.18}$$

In the case of lower-sideband conversion, the transucer gain is sensitive to variations in

the load or source conductance. According to (Ref. 31)

$$S_g = -\left(\frac{1+\rho_\ell}{1-\rho_\ell}\right) \tag{5.19}$$

while the sensitivity to pumping (γ_p) is

$$S_{\gamma_p} = -2\,S_g \tag{5.20}$$

Therefore, one serious drawback to lower-sideband conversion is the high sensitivity that accompanies large gains. Particularly disturbing is the large sensitivity to external source and load admittance variations since these admittances are not well stabilized in many applications. In the ensuing analysis, however, multiple-sideband schemes will be considered which offer considerably reduced sensitivities to the external admittance, as well as other benefits.

5.2 Degrading Influences on Lower-Sideband Conversion

The basic form of degradation to be considered is varactor loss, which influences both gain and noise figure. For upper-sideband converters, varactor loss not only reduces the gain from its frequency dependent value, but it also limits the usefulness of raising pump frequency. For lower-sideband converters, which offer infinite gain, varactor loss will be seen to increase gain sensitivity and to have a more pronounced effect on noise figure. The evaluation of these quantities will now be reviewed.

5.2.1 Effect of Varactor Loss on Gain. Using the basic form in (3.16) together with the lossless gain relation in (5.12), lower-sideband conversion gain in the presence of varactor loss becomes

$$\overline{G}_{r\ell} = \frac{4\rho_\ell}{(1-\rho_\ell)^2}\left(\frac{\overline{\omega}_\ell}{\overline{\omega}_r}\right)\left(\frac{g_S g_L}{g_r g_\ell}\right) \tag{5.21a}$$

where

$$\begin{aligned} g_r &= g_S + g_{dr} \\ g_\ell &= g_L + g_{d\ell} \end{aligned} \tag{5.21b}$$

and where

$$g_{dr} = \omega_r{}^2 C/\omega_d \qquad g_{d\ell} = \omega_\ell{}^2 C/\omega_d \tag{5.22}$$

Therefore, for finite gains, some increase in ρ_ℓ is required to overcome the loss factor $(g_S g_L/g_r g_\ell)$, but losses also influence ρ_ℓ. Following the procedure outlined above, we find that

$$\rho_\ell = \frac{g_L g_S}{g_\ell g_r}\left(\frac{\gamma_p{}^2}{g_L g_S}\right) = \frac{g_L g_S}{g_\ell g_r}\,\tilde{\rho}_\ell \tag{5.23}$$

where $\tilde{\rho}_\ell$ is ρ_ℓ in the absence of loss. Therefore, due to varactor loss, two increments of increase in $\tilde{\rho}_\ell$ are required to restore $\overline{G}_{r\ell}$. As a result, the sensitivity in (5.19) increases by

$$S_g = \sqrt{\frac{g_r g_\ell}{g_S g_L}}\;\tilde{S}_g \tag{5.24}$$

where $\tilde{S}_g$ is the sensitivity due to g_S and g_L alone.

5.2.2 Noise Figure. There are two basic contributions to excess noise figure in lower-sideband converters. The first is thermal noise from the parasitic input and output losses g_{dr} and $g_{d\ell}$, which will be assumed to have noise temperature T_d. The second is thermal noise from the output load g_L, which will again be assigned the noise temperature T_L. The effect of these two contributions can be determined from the general noise figure relation in (3.27), but first the gain ratio $(\overline{G}_{\ell\ell}/\overline{G}_{r\ell})$ and the noise bandwidth ratio $(B_{\ell\ell}/B_{r\ell})$ must be calculated. Here $\overline{G}_{\ell\ell}$ denotes the midband transducer gain by reflection at ω_ℓ which is defined in (3.25). However, the proper expression for $\overline{G}_{\ell\ell}$, corrected for varactor loss, can be obtained from (5.13) by a derivation similar to that yielding $\overline{G}_{r\ell}$ in (5.21). The result is

$$\overline{G}_{\ell\ell} = \left(\frac{2}{1-\rho_\ell}\right)^2 \left(\frac{g_L}{g_\ell}\right)^2 \tag{5.25}$$

so the gain ratio is

$$\frac{\overline{G}_{\ell\ell}}{\overline{G}_{r\ell}} = \frac{1}{\rho_\ell}\,\frac{\overline{\omega}_r}{\overline{\omega}_\ell}\,\frac{g_r g_L}{g_S g_\ell} \tag{5.26}$$

For large gains, where $\rho_\ell \approx 1$, the bandwidths of $G_{\ell\ell}$ and $G_{r\ell}$ are both given by (5.16), so (3.27) beomes

$$F_{r\ell} = 1 + \frac{g_{dr}T_d}{g_S T_o} + \frac{\overline{\omega}_r}{\overline{\omega}_\ell}\left[\frac{g_{d\ell}T_d + g_L T_L}{g_\ell T_o}\right]\frac{g_r}{g_S} \tag{5.27a}$$

$$= 1 + \frac{g_{dr}T_d}{g_S T_o} + \frac{\overline{\omega}_r}{\overline{\omega}_\ell}\,\frac{g_r T_\ell}{g_S T_o} \tag{5.27b}$$

where

$$T_\ell = \frac{g_{d\ell}T_d + g_L T_L}{g_{d\ell} + g_L} \tag{5.27c}$$

is the effective noise temperature of all conductance at the ω_ℓ terminals. Because the parasitic conductances are frequency sensitive, further study of $F_{r\ell}$ becomes an optimization problem, which can be summarized as follows.

First it is desirable for g_L to be much larger than $g_{d\ell}$ to efficiently utilize the large conversion gains that are possible when $\rho_\ell \approx 1$. Or, stated in other words, the efficiency factors

$$z = \frac{g_L}{g_\ell} = \frac{1}{1 + \dfrac{\omega_\ell{}^2 C}{\omega'_d\, g_S}} \tag{5.28a}$$

$$x = \frac{g_S}{g_r} = \frac{1}{1 + \dfrac{\omega_r{}^2 C}{\omega'_d\, g_S}} \tag{5.28b}$$

should be close to unity. Since ω_r and the varactor are often specified, x depends basically on the source conductance g_S. However, z depends basically on ω_ℓ and falls off at 12 db per

octave when $\omega_\ell > \omega_d g_L/C$. Below the latter frequency, $F_{r\ell}$ tends to decrease with ω_ℓ due to the factor $\bar{\omega}_r/\bar{\omega}_\ell$ in the second term. So extremely large $\bar{\omega}_\ell/\bar{\omega}_r$ ratios will be useful if g_L in (5.28a) is large. On the other hand, the pumping coefficient (γ_p/C) should be considered a constant, so g_S must decrease as g_L increases to keep $\rho_\ell \approx 1$. This decreases the input efficiency and raises the first term in (5.27). Therefore, the second term in (5.27) will dominate for small $\bar{\omega}_\ell$, while the first term is dominant for large $\bar{\omega}_\ell$. This suggests optimum values for $\bar{\omega}_r/\bar{\omega}_\ell$ and x, for a given pumping coefficient (k_p), varactor cut-off frequency (ω_d), signal center frequency ($\bar{\omega}_r$), and output efficiency (z). In Appendix A, these optimum values are shown to be

$$\left(\frac{\omega_r}{\omega\ell}\right)_{opt} = \frac{R_r}{1-z}\left[1 + \sqrt{1 + \frac{1-z}{R_r[1+z\,(t-1)]}}\right] \tag{5.29a}$$

$$\approx \sqrt{\frac{R_r}{(1-z)(1+z)(t-1)}} \quad ; \quad \text{if} \quad \frac{R_r}{1-z} << 1 \tag{5.29b}$$

and

$$(x)_{opt} = 1 - \frac{1}{1 + \sqrt{1 + \frac{1-z}{R_r[1+z\,(t-1)]}}} \tag{5.30a}$$

$$\approx 1 - \frac{1}{\sqrt{\frac{1-z}{R_r[1+z\,(t-1)]}}} \quad ; \quad \text{if} \quad \frac{R_r}{1-z} << 1 \tag{5.30b}$$

where[1]

$$R_r = \left(\frac{\bar{\omega}_r}{\omega_d}\right)^2 \left(\frac{C}{\gamma_p}\right)^2 = \left(\frac{\bar{\omega}_r}{\omega'_d}\right)^2 \tag{5.31a}$$

$$t = \frac{T_L}{T_d} \tag{5.31b}$$

---

[1]See footnote on p. 56 for a discussion of R_r and ω'_d.

The optimum noise figure in this case is

$$(F_{r\ell})_{opt} = 1 + 2R_r\left[\frac{1+z(t-1)}{1-z}\right]\sqrt{1 + \frac{1-z}{R_r[1+z\,(t-1)]}} \qquad (5.32a)$$

$$1 + 2\sqrt{R_r(1 + \frac{tz}{1-z})}\ ; \quad \text{if } \frac{R_r}{1-z} << 1 \qquad (5.32b)$$

The corresponding source and load conductances that must accompany this optimum noise figure are given by

$$\left(\frac{g_S}{\bar{\omega}_r C}\right)_{opt} = \frac{\omega_r}{\omega_d}\sqrt{1 + \frac{1}{R_r(1 + \frac{tz}{1-z})}} \qquad (5.33a)$$

$$\left(\frac{g_L}{\bar{\omega}_\ell C}\right)_{opt} = \left(\frac{z}{1-z}\right)\left(\frac{\bar{\omega}_\ell}{\omega_d}\right) \qquad (5.33b)$$

A universal plot of $(F_{r\ell})_{opt}$ is found in Appendix A.

Now to illustrate these noise figure relations, consider the following example.

(1) A signal at 3 kMc is to be converted to ω_ℓ with maximum gain and minimum noise figure.

(2) An output efficiency z = 0.5 will be tolerated.

(3) A varactor with cut-off frequency $\omega_d = 2\pi$ (100 kMc) is available, and it can be pumped so $\gamma_p/C = 0.3$.

(4) $T_L = T_d = T_o$.

Then t = 1, z = 0.5, and $R_r = 0.01$, which yields:

by (5.29)
$$\left(\frac{\bar{\omega}_r}{\bar{\omega}_\ell}\right)_{opt} = 0.02 \quad \left(1 + \sqrt{51}\right) = 1/6.1 \qquad (5.34a)$$

by (5.32)
$$\left(F_{r\ell}\right)_{opt} = 1 + 0.04 \quad \sqrt{51} = 1.29 \qquad (5.34b)$$

by (5.33)
$$\left(\frac{g_S}{\omega_r C}\right)_{opt} = (.03)\ \sqrt{51} = .21 \tag{5.34c}$$

$$\left(\frac{g_L}{\omega_\ell C}\right)_{opt} = 0.18 \tag{5.34d}$$

The last two values correspond to a terminal Q of 5 at each terminal, but $g_{d\ell} = g_L$ in this case, so Q_ℓ is actually 2.5. (The input loss $g_{dr} = g_S/6$ does not affect Q_r appreciably.) However, for optimum gain-bandwidth product the terminal bandwidths must be equal, which corresponds to $\omega_r Q_\ell = \omega_\ell Q_r$ when both terminal capacities are assumed equal. Hence, if $Q_r = 5$, then an optimum gain-bandwidth product occurs for $Q_\ell = 30$, but an optimum noise figure requires $Q_\ell = 2.5$. A proportionately narrower input bandwidth is required for optimum noise figures because input noise receives more amplification than output noise, if $\omega_r < \omega_\ell$, according to (5.26).

A brief comparison with upper-sideband noise figure will now be constructive. Using the same varactor, the same signal frequency and $R_r = 0.01$, Fig. 4.5 yields $F_{ru} = 1.38$ for the same pump frequency which is a somewhat larger value. However, if ω_p is reduced until ω_u occurs at the frequency where ω_ℓ was previously, then $F_{ru} = 1.28$ which is essentially the same as (5.34b).

5.3 Parametric Amplification

The application of lower-sideband conversion that has received the greatest prior attention is power gain by reflection. It provides a means for one-port amplification that is commonly termed parametric amplification. Therefore, the portion of Fig. 5.1 extending to the right of the line aa' constitutes a parametric amplifier, and has the driving point characteristic shown in Fig. 5.3a. The basic circuit configuration for parametric amplification is shown in Fig. 5.3b, and a typical gain characteristic of this circuit appears in Fig. 5.3c.

One of the drawbacks to the configuration in Fig. 5.3b is that both the source and the load intercept the reflected power. A common technique for overcoming this limitation, at least at microwave frequencies, is by using a circulator to isolate the source, the load, and the negative conductance port. Basically a circulator is a lossless device that permits nonreciprocal coupling between each pair of its three or more ports. In Fig. 5.4

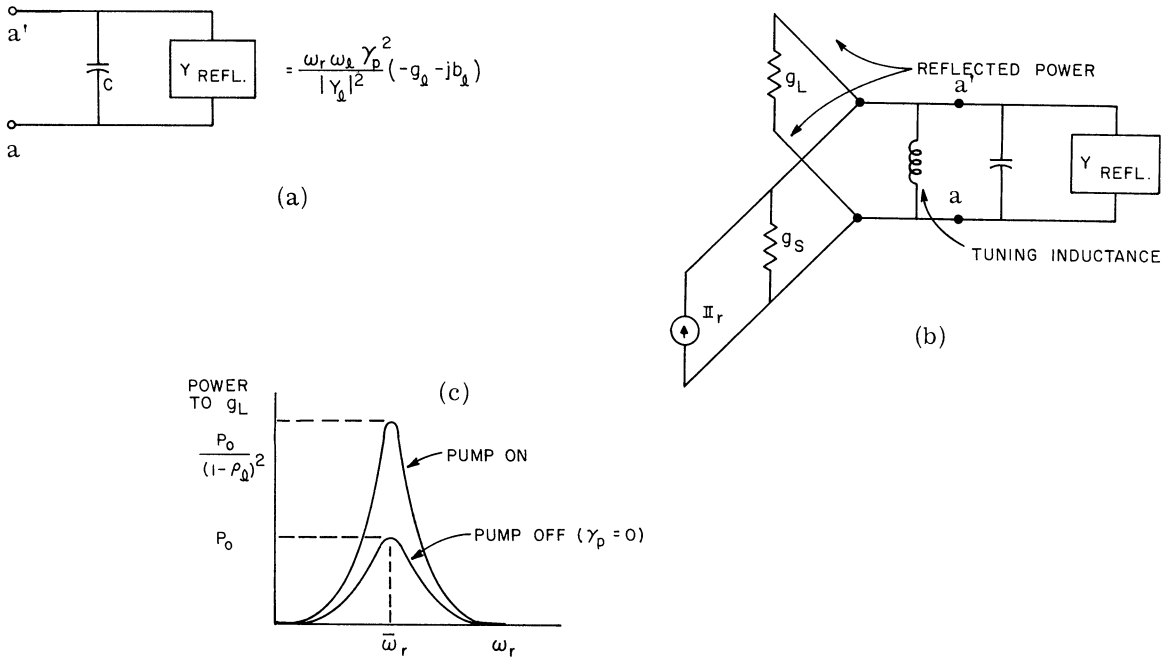

Fig. 5. 3. Power gain by reflection through parametric amplification. (a) shows the negative conductance generated by lower-sideband mixing, (b) shows a simple circuit for realizing reflector gain, and (c) shows a typical gain response.

a three-port circulator is shown which operates as follows: an incident signal at port A is coupled only to port B, where it impinges upon a parametric amplifier. The latter in turn reflects an amplified version of the signal back into port B, where it now passes entirely to port C. If g_L matches the circulator at port C, none of the reflected power will reach the source at port A, and the desired separation of source and load is achieved.

Usually the characteristic admittance is the same for each circulator port. Call this Y_o. Then if $g_S = g_L = Y_o$ the conductance seen by the parametric amplifier is no longer $g_S + g_L = 2Y_o$, but now $g_r = Y_o$. Therefore, in the presence of a circulator, the critical parameter ρ_ℓ in (5. 13) doubles its value. Alternately, a 30 percent reduction in γ_p can be achieved through the use of a circulator.[2] In addition, for equal values of ρ_ℓ, the circulator provides up to 3 db more gain (because the amplified signal is isolated from the source). A circulator also reduces the sensitivity of power gain to g_L and g_S.

---

[2]Parasitic losses are neglected in these comparisons.

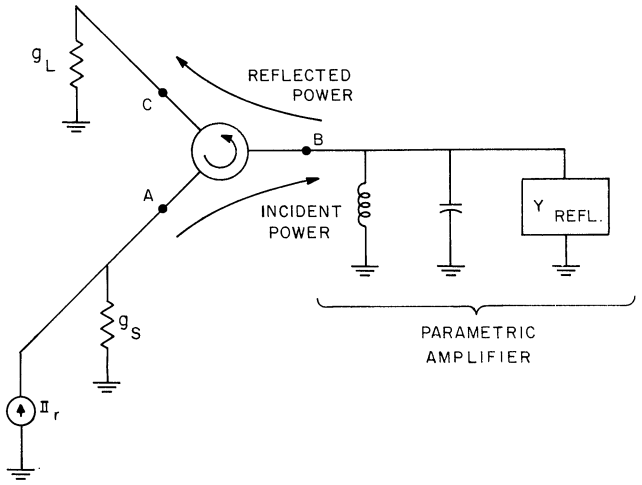

Fig. 5.4. A parametric amplifier with a circulator for improved performance.

In the high gain condition ($\rho_\ell \approx 1$), it can be shown that the noise figure of a parametric amplifier with a circulator is also given by (5.27). Hence, the subscripts r and ℓ on $F_{r\ell}$ in (5.27) can be ignored for the present. For parametric amplification, the load g_L at ω_ℓ can be zero since the actual load is attached the circulator at ω_r. At one time it was felt that additional loading at ω_ℓ could reduce the noise figure by being cooled, since this would reduce the effective lower-sideband noise temperature appearing in (5.27c). However, to keep $\rho_\ell \approx 1$, an added conductance at ω_ℓ calls for a reduction in the source conductance g_S, which in turn causes an unfavorable increase in g_{dr}/g_S in (5.27). This conclusion can also be noted from (5.32a) where variations in g_ℓ are equivalent to variations in z, and (5.32) is actually a minimum when z equals zero.[3] Therefore, the optimum noise figure of a parametric amplifier with circulator is

$$\left(F_{rr}\right)_{opt} = 1 + 2R_r\sqrt{1 + \frac{1}{R_r}} \tag{5.35a}$$

and it occurs for

$$\left(\frac{\omega_r}{\omega_\ell}\right)_{opt} = R_r\left[1 + \sqrt{1 + \frac{1}{R_r}}\right] \tag{5.35b}$$

---

[3]This is true even if $T_L < T_D$. Further discussion of this point is found in Appendix A.

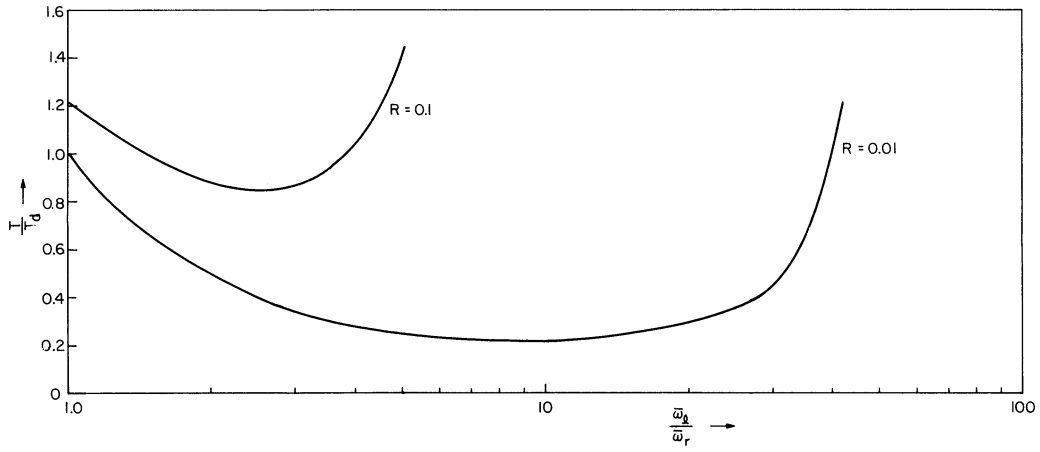

Fig. 5.5. Parametric amplifier noise temperature vs. frequency ratio, showing the optimum predicted by (5.35b).

Consider now an example similar to the one in the previous section, where ω_d = 100 kMc, $\bar{\omega}_r$ = 3 kMc, γ_p/C = 0.3, and $T_d = T_o$. In this case, a parametric amplifier at 3 kMc has a minimum noise figure of 1.2, which is smaller than the corresponding value in (5.34b). The smaller loading at ω_ℓ in the parametric amplifier accounts for its lower noise figure. A sketch of parametric amplifier noise temperature for arbitrary ω_r/ω_ℓ ratios is shown in Fig. 5.5. It illustrates the existence of an optimum pumping frequency, but it can be noted that a rather broad minimum occurs.

5.4 The Degenerate Parametric Amplifier

A special case of parametric amplification occurs when $\omega_r = \omega_\ell = \omega_p/2$. In this case, the basic analytical form in (5.1) reduces to a single equation

$$\mathrm{I\!I}_r = Y_r V_r + j\omega_r \gamma_p V_r^* \tag{5.36a}$$

whose solution is

$$V_r = \frac{Y_r^* \mathrm{I\!I}_r - j\omega_p \gamma_p \mathrm{I\!I}_r^*}{|Y_r|^2 - \omega_r^2 |\gamma_p|^2} \tag{5.36b}$$

Again, very large gains can occur, but now they are sensitive to the relative phase of the

pump γ_p and the source $\mathbb{I}_r$. At midband, with $Y_r = g_r$, maximum gain occurs for:

$$g_r = \overline{\omega}_r |\gamma_p| \tag{5.37a}$$

$$\text{phase } \gamma_p - 2(\text{phase } \mathbb{I}_r) = \pi/2 \tag{5.37b}$$

However zero gain occurs is

$$\text{phase } \gamma_p - 2(\text{phase } \mathbb{I}_r) = -\pi/2 \tag{5.38}$$

Therefore, if a degenerate parametric amplifier breaks into oscillation, the phase relation in (5.37b) can be anticipated.

To date, this form of parametric amplification has been regarded mainly as a novelty. However, a practical application of this principle will be discussed in Chapter X.

5.5 Conclusions

All effects in this chapter have been the result of a regenerative coupling between ω_r and the lower sideband, which has manifested itself as negative resistence. This effect has given rise to large conversion gains, but with small bandwidths and high sensitivities to parameter variations. In succeeding chapters, other frequency components will be introduced that will greatly extend the potentialities of single-sideband reactive mixing. Henceforth, Chapters IV and V will serve as convenient bases for comparing the newly found properties of double-sideband reactive mixers.

CHAPTER VI

STABILITY OF NETWORKS WITH PERIODICALLY VARYING REACTIVE ELEMENTS

It has been demonstrated in Chapter II that an analysis of the general reactive mixer in Fig. 1.3 can be accomplished by treating an alternate network; one that is linear, but time-varying. For example, the time-varying network in Fig. 2.1 was shown to be appropriate for treating the spectrum in Fig. 1.4. It thereby illustrated a linearizing procedure in which the pump and nonlinear element are replaced by a linear element that varies periodically at the fundamental pump frequency. Since this substitution has been shown to be valid for all first-order mixing, the circuit in Fig. 6.1 constitutes a first-order linear model for all reactive mixers.

The sinusoidal steady-state properties of two special cases of Fig. 6.1 were evaluated in Chapters IV and V. Several of these properties were suggestive of instability, which is discomforting since rigorous statements about stability normally originate outside the steady-state realm. The present chapter will consider, more rigorously, the stability of the circuit in Fig. 6.1. In particular, the relationship between true instability and that predicted by sinusoidal steady-state analysis will be considered, and it will be shown that knowledge of the sinusoidal steady-state response is sufficient to distinguish between stable and unstable solutions.

In Fig. 6.1, the time-varying capacitance is assumed to have period $2\pi/\omega_p$, and the source is assumed to be sinusoidal with period $2\pi/\omega$. Since the admittance of the time-varying portion of Fig. 6.1 can be written in the form

$$Y(j\omega) = \frac{\sum_{n=0}^{N} a_n (j\omega)^n}{\sum_{m=0}^{M-1} b_m (j\omega)^m} \tag{6.1}$$

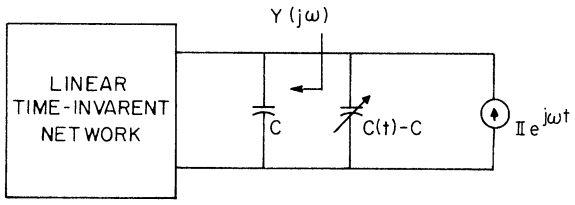

Fig. 6.1. An appropriate linear model for first-order interactions in reactive mixers. C denotes average value of C(t).

the entire circuit is described by the following linear differential equation:

$$\sum_{m=1}^{M} b_{m-1} \frac{d^m}{dt^m} \left\{ [C(t) - C]\, v(t) \right\} + \sum_{n=0}^{N} a_n \frac{d^n v(t)}{dt^n} = \sum_{m=0}^{M-1} b_m (j\omega)^m \Pi\, e^{j\omega t} \qquad (6.2)$$

However, (6.2) can also be written as a set of M first-order differential equations, of the form:

$$\frac{dx_i}{dt} + \sum_{j=1}^{N} \phi_{ij}(t) x_i = \theta_i \qquad (i = 1, 2, \ldots, M) \qquad (6.3)$$

In this set, the x_i are functions of v(t) or its derivatives, the ϕ_{ij} are periodic coefficients with period $2\pi/\omega_p$, and the θ_i have the period $2\pi/\omega$.

Given a typical circuit of the type shown in Fig. 6.1, there are several alternate methods by which sets in the form of (6.1) can be obtained. These all take the form of (6.3), but in each case the individual ϕ_{ij} depend upon how the x_i are chosen with respect to the circuit variables. In any case, the same stability characteristics will be predicted, so it is immaterial for now just how the set (6.3) is chosen. In Section 6.2, an example is given that shows how the set (6.3) can be obtained in a particular case.

6.1 Solutions of the Set (6.3)

From the well-known theory of linear differential equations with periodic coefficients (Ref. 33), the homogeneous portion of the set (6.3) has solutions of the form

$$x_i = e^{\mu t} y_i \qquad (6.4)$$

where the y_i are periodic in t with period $2\pi/\omega_p$. In general, there are M values of μ (although they need not all be distinct) that characterize (6.4), namely

$$\mu = \mu_k, \qquad (k = 1, 2, \ldots, M) \tag{6.5}$$

Since the y_i are periodic, the μ_k must determine the stability of this system and a necessary and sufficient condition for stable solutions is that

$$R_e(\mu_k) < 0 \qquad (k = 1, 2, \ldots, M) \tag{6.6}$$

If the μ_k are distinct, there are M linearly independent solutions of the form (6.4) and the general solution of the homogeneous portion of (6.3) is

$$x_i = \sum_1^M e^{\mu_k t} y_{ik}(t)\, \eta_k \tag{6.7}$$

where the η_k are, for the moment, arbitrary constants.

The solution of the inhomogeneous set (6.3) can now be found by the method of variation of parameters, which regards (6.6) as a transformation of the set x_i to the set η_k. When (6.7) is substituted into (6.3), the η_k are found to satisfy the relation

$$\sum_k e^{\mu_k t} y_{ik} \frac{d\eta_k}{dt} = \theta_i \tag{6.8}$$

Therefore, the solution of the inhomogeneous set (6.3) can be obtained by replacing the constant η_k in (6.7) by functions of time that satisfy (6.8). Solving this latter set for the derivatives of η_s, yields

$$\frac{d\eta_s}{dt} = \frac{\Delta s}{\Delta} \qquad (s = 1, 2, \ldots, M) \tag{6.9}$$

where Δ is the determinant of the coefficients of $d\eta_s/dt$,

$$\Delta = \left|y_{ik}\right| e^{\sum_k \mu_k t} \tag{6.10}$$

and Δ_s is the determinant Δ with its sth column replaced by the θ_i. Therefore

$$\frac{d\eta_s}{dt} = \frac{\begin{vmatrix} y_{11} \cdots \theta_1 \cdots y_{1M} \\ y_{21} \cdots \theta_2 \cdots y_{2M} \\ \\ y_{M1} \cdots \theta_M \cdots y_{MM} \end{vmatrix} e^{-\mu_s t}}{\left| y_{ik} \right|} \tag{6.11a}$$

$$= \frac{D_s}{D} e^{-\mu_s t} \tag{6.11b}$$

Since the y_{ik} all have period $2\pi/\omega_p$, and the θ_i have period $2\pi/\theta$, the ratio D_s/D will contain only those frequencies in the set

$$\omega_{mn} = m\omega_p + n\omega \qquad \begin{matrix} m = 0, \pm 1, \pm 2, \ldots \\ n = 0, \pm 1, \pm 2, \ldots \end{matrix}$$

Therefore,

$$\frac{D_s}{D} = \sum_{mn} N^s_{mn} e^{j\omega_{mn} t} \tag{6.12}$$

and

$$\eta_s = B_s + \int_0^t \frac{D_s}{D} e^{-\mu_s t} dt \tag{6.13a}$$

$$= B_s + \sum_{mn} N^s_{mn} \left[\frac{e^{(j\omega_{mn} - \mu_s)t}}{-\mu_s + j\omega_{mn}} - \frac{1}{-\mu + j\omega_{mn}} \right] \tag{6.13b}$$

$$= B_s + P_s(t) e^{-\mu_s t} - P_s(0) \tag{6.13c}$$

where B_s is the initial condition and $P_s(t)$ varies at the frequencies ω_{mn}. The final solution of the set (6.3) is now found to be

$$x_i = \sum_k e^{\mu_k t} y_{ik}(t) [B_k - P_k(0)] + \sum_k y_{ik}(t) P_k(t) \qquad (6.14)$$

The second term in (6.14) is the steady-state response. The first term is the transient response, and hence it is the part of the solution that is normally used to determine stability. A question of interest, however, is whether the interrelation between these two solutions is such that either can predict stability. To pursue this question, consider a typical set of characteristic roots for the circuit in Fig. 6.1, as shown in Fig. 6.2. In the absence of pumping (i.e., when C(t) - C is 0), these roots are simply the poles of impedance of the static network in Fig. 6.1. However, when the pump is applied, each root tends to move and may cross the imaginary axis. Assume that no root crosses the imaginary axis prior to μ_s, which will be assumed to cross at $j\omega_s$. Also, let ω in (6.11) be selected so that one of the ω_{mn} has the value ω_s. Then, by writing $\mu_s = -\delta + j\omega_s$, $\delta = 0$ will mark the boundary between stability and instability. In this case, the component of $P_s(t)$ [in (6.13)] at ω_s becomes

$$[P_s(t)]_{mn} e^{-\mu_s t} = \frac{N^s_{nm} e^{\delta t}}{\delta} \qquad (6.15)$$

which approaches infinity as δ approaches 0. However,

$$\lim_{\delta \to 0} \left[P_s(t) e^{-\mu_s t} - P_s(0) \right] = \frac{N^s_{nm}}{2\pi} t \qquad (6.16)$$

which is the familiar form of solution at resonance. Thus, when $\delta = 0$, the total solution remains bounded for all finite time, but its growth marks an instability threshold. However, the steady-state term in (6.14) itself becomes infinite when a characteristic root crosses the imaginary axis. Therefore, if one can obtain an accurate estimate of the sinusoidal steady-state response of a periodically varying system (hopefully even without solving the differential equations), the singular points of this estimate will determine the thresholds of instability. This result is well known in constant parameter linear systems, where the characteristic roots themselves can be calculated by a direct and simple algebraic method. In systems with time varying parameters, however, or even in those with periodically varying parameters, approximate (and often tedius) methods are required to locate the characteristic roots (see

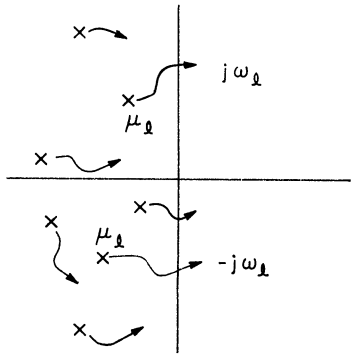

Fig. 6.2. A typical root locus for the circuit in Fig. 6.1 showing how the characteristic roots may shift when C(t) is applied.

Section 6.2 for a typical calculation). Therefore, the use of sinusoidal steady-state solutions to determine stability promises to be a significant aid to the study of systems with periodically varying parameters.

In Chapter II, the steady-state performance of several periodically varying networks were represented by characteristic matrix equations [i.e., (2.27) and (2.33)], so the singular points of these representations occur when the inverse fails to exist. For linear equations such as (2.27), the vanishing of the system determinant marks the threshold of instability. For semilinear equations, such as (2.23b), the same principle can be applied. For example, by rewriting (2.33b) in the form

$$[Y_A^*][\mathbb{I}] - [Y_B][\mathbb{I}^*] = \left\{[Y_A][Y_A^*] - [Y_B][Y_B^*]\right\}[V]$$

the vanishing of the determinant of the real matrix $[Y_A][Y_A^*] - [Y_B][Y_B^*]$ is seen to mark the threshold of instability.

6.2 Illustrative Calculation of Stability from Sinusoidal Steady-State Response

A steady-state analysis of the elementary lower-sideband reactive mixer was formulated in Chapter V. The basic assumption in this analysis, as depicted by the ideal circuit in Fig. 3.3, is that all frequencies except ω_r and ω_ℓ are short circuited. The remaining steady-state voltages, V_r and V_ℓ, can then be determined by (5.1). According to the rule established in the previous section, instability can be expected when V_r or V_ℓ be-

come unbounded, which occurs when the system determinant of (5. 1) vanishes,

$$Y_r Y_\ell^* - \omega_\ell \omega_r \gamma_p^2 = 0 \tag{6. 17}$$

An important special case occurs when the ω_r and ω_ℓ loads are synchronously tuned, so $\overline{\omega}_r = \omega_p - \overline{\omega}_\ell$. Then (6. 17) will vanish for the smallest possible value of γ_p, namely that given by:

$$g_r g_\ell - \overline{\omega}_\ell \overline{\omega}_r \gamma_p^2 = 0 \tag{6. 18}$$

This condition was previously noted in (5. 10) to yield infinite conversion gain. An important question that we now ask is, "How well does (6. 18) predict instability in a practical circuit?" To answer this question, a practical circuit will be tested by this method.

6. 2. 1 Synthesis of a Prototype Circuit. The simplest type of circuit for approximating a lower-sideband converter is the four-pole network (and attached time-varying capacitor) shown in Fig. 6. 3. For convenience, the frequency of the time-varying capacitor has been normalized to two rad/sec, so the basic period of this system is π seconds. The poles and zeros of impedance of the static portion of this network are shown in Fig. 6. 4, where the pole locations are denoted by

$$\begin{aligned} P_r &= -\sigma_r + j\Omega_r & P_\ell &= -\sigma_\ell + j\Omega_\ell \\ P_r^* &= -\sigma_r - j\Omega_r & P_\ell^* &= -\sigma_\ell - j\Omega_\ell \end{aligned} \tag{6. 19a}$$

and the zero locations are denoted by

$$\begin{aligned} Z_2 &= -k_2 & Z_1 &= -k_1 + j \\ & & Z_1^* &= -k_1 - j \end{aligned} \tag{6. 19b}$$

The choice (j) for the imaginary component of α_1 is arbitrary and is made only for convenience. If it is assumed that

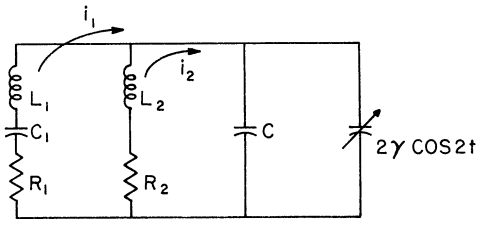

Fig. 6.3. A canonical realization of the lower-sideband mixer using a time-varying capacitor.

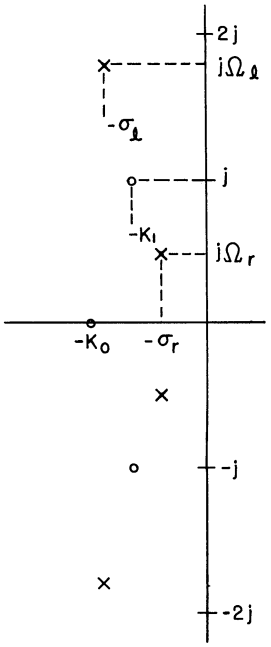

Fig. 6.4. The poles and zeros of the circuit in Fig. 6.3.

$$\left|\frac{\Omega_r}{\sigma_r}\right| >> 1, \qquad \left|\frac{\Omega_\ell}{\sigma_\ell}\right| >> 1 \tag{6.20}$$

the resonant frequencies of the static network will be very nearly equal to Ω_r and Ω_ℓ, and the condition for synchronous tuning will become simply

$$\Omega_r + \Omega_\ell = 2 \tag{6.21}$$

Figure 6.3 will then be viewed as a mixer from ω_r to $\omega_\ell = 2-\omega_r$, with midband frequencies

$\bar{\omega}_r$ and $\bar{\omega}_\ell$ that equal Ω_r and Ω_ℓ, respectively.

In view of the assumption in (6.20), the reactive portions of Fig. 6.3 will be synthesized first, and the resistors R_1 and R_2 will be added by perturbation. The synthesis yields the following element values

$$L_2C = \frac{1}{\Omega_r^2 \Omega_\ell^2} \tag{6.22a}$$

$$L_1C = \frac{1}{(1-\Omega_r^2)(\Omega_\ell^2-1)} \tag{6.22b}$$

$$\frac{C_1}{C} = (1-\Omega_r^2)(\Omega_\ell^2-1) \tag{6.22c}$$

When losses are introduced, by adding R_1 and R_2 as shown in Fig. 6.3, the poles and zeros move off the $j\omega$ axis. The real parts of the zero locations are then related to R_1 and R_2 by

$$k_1 = \frac{R_1}{L_1}, \qquad k_2 = \frac{R_2}{L_2} \tag{6.23}$$

while the real parts of the pole locations satsify the relations

$$\frac{k_1}{2} = \frac{e\sigma_r + f\sigma_\ell}{e+f} \tag{6.24a}$$

$$\frac{k_2}{2} = \frac{e\sigma_r + f\sigma_\ell}{e+f} \tag{6.24b}$$

where

$$e = \frac{\Omega_\ell^2}{1-\Omega_\ell^2} \qquad f = \frac{\Omega_r^2}{1-\Omega_r^2} \tag{6.24c}$$

The principle relating Fig. 6.3 and Fig. 3.3 can be stated as follows: Fig. 6.3 has been designed to support frequencies in the vicinity of $\omega = \Omega_r$ and $\omega = \Omega_\ell$, and to suppress (as effectively as possible) other mixing products. For approximate steady-state analysis, Fig. 3.3 would then be chosen to duplicate Fig. 6.3 in the vicinity of $\bar{\omega}_r = \Omega_r$ and $\bar{\omega}_\ell = \Omega_\ell$, and to give perfect suppression elsewhere. Therefore, if $Y(\omega)$ is the admittance of the static

portion of Fig. 6.3, then Fig. 3.3 would use the quantities $Y_r = Y(\omega_r)$ and $Y_\ell = Y(\omega_\ell)$.

In the present calculation, in which (6.18) is being tested, only the real part of $Y(\omega)$ is needed which can be written

$$\frac{g}{C}(\omega) = \frac{k_1(1-\Omega_r^2)(\Omega_r^2-1)}{k_1^2 + (\omega - \frac{1}{\omega})^2} + \frac{k_2\Omega_r^2\Omega_\ell^2}{k_2^2 + \omega^2} \tag{6.25a}$$

$$\approx \frac{k_1(1-\Omega_r^2)(\Omega_\ell^2-1)}{(\omega - \frac{1}{\omega})^2} + \frac{k_2\Omega_r^2\Omega_\ell^2}{\omega^2} \tag{6.25b}$$

The approximation above is valid if the poles and zeros are reasonably well separated. This will normally be the case in a practical converter. Within the ω_r and ω_ℓ bands, (6.25b) will be considered to have the constant values $g_r = g(\Omega_r)$ and $g_\ell = g(\Omega_\ell)$. Using these relations in (6.18) yields the following steady-state prediction for the instability threshold.

$$\left(\frac{\gamma_p}{C}\right)^2 = \frac{(\Omega_r^2-1)(\Omega_\ell^2-1)(k_1f-k_2e)(k_1e-k_2f)}{\Omega_r\Omega_\ell} \tag{6.26a}$$

which can be simplified to read

$$\left(\frac{\gamma_p}{C}\right)^2 = \frac{-4(e-f)^2\sigma_r\sigma_\ell\Omega_r\Omega_\ell}{ef} \tag{6.26b}$$

It will now be shown that (6.26) accurately predicts the pump level for which the characteristic roots of Fig. 6.3 cross the imaginary axis.

6.2.2 Analysis of Fig. 6.3. By writing the mesh equations, the differential equations for the circuit in Fig. 6.3 can be obtained as shown below.

$$\ddot{Q}_1 + k_1\dot{Q}_1 + Q_1 + \frac{Q_1 + Q_2}{L_1C}(1 - \alpha\cos 2t) = 0$$

$$\ddot{Q}_2 + k_1\dot{Q}_2 + \frac{Q_1 + Q_2}{L_2C}(1 - \alpha\cos 2t) = 0 \tag{6.27a}$$

where

$$Q_1 = \int i_1 dt \qquad Q_2 = \int i_2 dt$$

Here the assumption has been made that

$$\frac{1}{C + 2\left|\gamma_p\right| \cos 2t} \approx \frac{1}{C}\,(1-\alpha \cos 2t)$$

$$\alpha = 2\left|\frac{\gamma_p}{C}\right| \tag{6.27b}$$

Now let us consider a change in (6.27a) which will be explained later; namely to replace k_1 and k_2 by the quantities $s\alpha k_1$ and $s\alpha k_2$, respectively. We note that the condition $s = \alpha^{-1}$ restores the original set of equations in (6.25). These equations can now be put into normal form [i.e., that of (6.3)] by making the following substitutions.

$$\begin{aligned} x_1 &= Q_1 & x_3 &= Q_2 \\ x_2 &= Q_1 & x_4 &= Q_2 \end{aligned} \tag{6.27c}$$

which yields

$$\begin{vmatrix} x_1 \\ x_2 \\ x_3 \\ x_4 \end{vmatrix} = \begin{vmatrix} 0 & 1 & 0 & 0 \\ a_{21} & -s\alpha k_1 & a_{23} & 0 \\ 0 & 0 & 0 & 1 \\ a_{41} & 0 & a_{43} & -s\alpha k_2 \end{vmatrix} \begin{vmatrix} x_1 \\ x_2 \\ x_3 \\ x_4 \end{vmatrix} \tag{6.28}$$

where

$$\begin{aligned} a_{21} &= -(\Omega_r^2 + \Omega_\ell^2 - \Omega_r^2\,\Omega_\ell^2) + \alpha\,(1 - \Omega_r^2)(\Omega_\ell^2 - 1)\cos 2t \\ &= a_{21}^o + \alpha\, a'_{21} \\ a_{23} &= -(1 - \Omega_r^2)(\Omega_\ell^2 - 1)(1 - \alpha \cos 2t) \\ &= a_{23}^o + \alpha\, a'_{23} \\ a_{41} &= -\Omega_r^2\,\Omega_\ell^2\,(1 - \alpha \cos 2t) = a_{41}^o + \alpha\, a'_{41} \\ a_{43} &= -\Omega_r^2\,\Omega_\ell^2\,(1 - \alpha \cos 2t) = a_{43}^o + \alpha\, a'_{43} \end{aligned} \tag{6.29}$$

Equation (6.28) can be abbreviated as follows,

$$x_i = \sum_k a_{ik}x_k = \sum_k (a^o_{ik} + \alpha\, a'_{ik})x_k \quad (i = 1, \ldots, 4) \tag{6.30}$$

To test the stability condition predicted in (6.18), the characteristic roots of the system in (6.28) will be determined by perturbation methods. Realizing the form of the solution stated in (6.4) the substitution will be made

$$x_i = e^{\mu t}y_i \tag{6.31}$$

where it can be asserted that y_i is a function with period π. Equation (6.30) now becomes

$$y_i + \mu y_i = \sum_k a_{ik}y_k \qquad (i = 1, 2, 3, 4) \tag{6.32}$$

6.2.3 The Perturbation Method. In the present problem there are four characteristic roots, so $\mu = \mu_k$ where k = 1, 2, 3, 4. To obtain these roots by perturbation methods, let

$$\mu_k = \mu^o_k + \alpha\, \mu'_k + \alpha^2 \mu''_k + \ldots \tag{6.33a}$$

Corresponding to each root there will occur a periodic function Y_{ik} satisfying (6.31). Therefore, let

$$y_{ik} = y^o_{ik} + \alpha\, y'_{ik} + \alpha^2 y''_{ik} + \ldots \tag{6.33b}$$

where each term in (6.33b) is required to be periodic. Substituting (6.33a) and (6.33b) into (6.37), and collecting powers of α, yields the following schedule:

$$y^o_{ik} + \mu^o_k y^o_{ik} - \sum_\nu a^o_{i\nu}y^o_{\nu k} = 0 \tag{6.34a}$$

$$y'_{ik} + \mu^o_k y'_{ik} - \sum_\nu a^o_{i\nu}y'_{\nu k} = -\mu'_k y^o_{ik} + \sum_\nu a'_{i\nu}y^o_{\nu k} \tag{6.34b}$$

$$y''_{ik} + \mu^o_k y''_{ik} - \sum_\nu a^o_{i\nu}y'_{\nu k} = \mu''_k y^o_{ik} + \sum_\nu (a'_{i\nu} - \mu'_k)y'_{\nu k} \tag{6.34c}$$

Since the first equation above (6.33a) pertains to an analysis of Fig. 6.3 with $R_1 = R_2 = \gamma_p = 0$, the solutions y^o_{ik} are readily found. This unperturbed solution can then be applied as a forcing

function in (6.33b). The latter equation has constant coefficients, so it can be readily solved for y'_{ik}. However, only those terms in y'_{ik} with period π are of interest, so it will be found that such terms exist only for certain values of μ'_k. Thus the desired quantities: μ'_k and periodic y'_{ik} are obtained. In turn, these can be applied to (6.34c) to yield still higher approximations. A noteworthy feature of this method is that any one root can be approximated to an arbitrary degree, without carrying along any approximations to the other roots.

6.2.3.1 The Unperturbed Solution. Since the unperturbed solution is used to calculate higher approximations to the desired solution, it is expedient for y'_{ik} to be as simple as possible. Therefore, the resistors R_1 and R_2 will be added as perturbations, and the unperturbed roots will be located in the simplest possible position, namely on the imaginary axis. Therefore, the μ_k^o will be assigned as follows.

$$\mu_1^o = j\Omega_r, \quad \mu_2^o = -j\Omega_r, \quad \mu_3^o = j\Omega_\ell, \quad \mu_4^o = -j\Omega_\ell \tag{6.35}$$

It may be imagined that introducing two perturbing effects simultaneously would reduce the rate of convergence of the entire perturbation process. However, just the opposite is true in the present case, because the effect of γ_p is to move the characteristic roots into the unstable half-plane [as defined in (6.6)], while R_1 and R_2 tend to displace each root into the stable half-plane. Thus, for a given value of γ_p, there exists some value of s [in (6.28)] that causes the least change in the characteristic roots. When s is in this neighborhood, the most rapid convergence of (6.33a) will occur.

In the present analysis, the case of interest occurs when the characteristic roots in Fig. 6.3 have just crossed the imaginary axis. When the corresponding situation occurs in (6.28), the real part of the perturbed characteristic roots will vanish. This situation must occur for a certain value of s, say s_c. Therefore the threshold of instability in Fig. 6.3 will be marked by

$$\frac{\gamma_p}{C} = \frac{s_c}{2} \tag{6.36}$$

Because synchronous tuning has been assumed, it can be anticipated that there will be little root motion in the imaginary direction. Therefore, the value of s_c should lead to rapid convergence of (6.33a).

In the special case of constant coefficients, the y_{ik} in the general solution (6.7) are constants, so the unperturbed solution of (6.28) becomes

$$x_i^o = \sum_\nu c_{i\nu} e^{\mu_\nu^o t} \tag{6.37}$$

However, one of the constants associated with each root is arbitrary, so let $c_{1\ell} = 1$ for $\ell = 1, 2, 3,$ and 4. The remaining $c_{i\ell}$ can be found by substituting (6.37) into the unperturbed portion of (6.28), which yields

$$\left|c_{i\nu}\right| = \begin{vmatrix} j\Omega_r & -j\Omega_r & j\Omega_\ell & -j\Omega_\ell \\ e & e & f & f \\ j\Omega_r e & -j\Omega_r e & j\Omega_\ell f & -j\Omega_\ell f \end{vmatrix} \tag{6.38}$$

To simplify the perturbation method of solution, the dependent variable will now be transformed from x_i to y_i, according to (6.31). This transformation is made separately for each root μ_k, which yields

$$y_{ik}^o = \sum_\nu c_{i\nu} \eta_{\nu k}^o e^{(\mu_\nu^o - \mu_k^o)t} \tag{6.39}$$

where the $c_{i\nu}$ are as defined in (6.38) and the $\eta_{\nu k}^o$ are undetermined constants that will be used to distinguish those parts of (6.39) with period π.

Since this perturbation allows each μ_k root locus to be separately evaluated, the root μ_1 (with unperturbed value $j\Omega_r$) will be considered first. In this case

$\nu = 1$: $\mu_\nu^o - \mu_1^o = 0$	$\nu = 3$: $\mu_\nu^o - \mu_1^o = j(\Omega_\nu - \Omega_r)$
$\nu = 2$: $\mu_\nu^o - \mu_1^o = -2j\Omega_r$	$\nu = 4$: $\mu_\nu^o - \mu_1^o = -j(\Omega_\nu + \Omega_r)$

(6.40)

so two terms in (6.39) have period π. Therefore, letting $\eta_{12}^o = \eta_{13}^o = 0$, the unperturbed solution becomes

$$y_{i1}^o = c_{i1} \eta_{11}^o + c_{i4} \eta_{41}^o e^{-2jt} \tag{6.41}$$

where η_{11} and η_{41} remain to be determined.

6.2.3.2 First-Order Perturbations. The unperturbed solutions in (6.40) can now be substituted into (6.34b) to obtain the first-order solutions y'_{i1}. Note that the forms of the y'_{i1}, and of all higher order solutions, are quite similar because the homogeneous part of each equation in (6.34) has the characteristic roots given in (6.40). Therefore, the general solution of the unforced portion of (6.34b) is

$$y_{ik} = \sum_{\nu} c_{i\nu}\eta_{\nu k}\, e^{(\mu^o_\nu - \mu^o_k)t}$$

When the forcing function in (6.34b) is considered, solution by the method of variation of parameters yields the following first-order differential equation for the $\eta'_{\ell k}$

$$\frac{d\eta'_{\nu k}}{dt} = \frac{D_{\nu k}}{|c_{i\ell}|}\, e^{-(\mu^o_\nu - \mu^o_k)t} \tag{6.42}$$

Here, $D_{\nu k}$ is the determinant of $c_{i\nu}$ with the νth column replaced by the column

$$\theta_{ik} = \sum_{\nu} (a'_{i\nu} y^o_{\nu k}) + \mu'_k y^o_{ik} \tag{6.43}$$

Therefore, $D_{\nu k}$ has period π.

The solution of (6.42) has the same form as (6.13a), with the index n absent. Therefore,

$$\eta'_{\nu k} = B'_{\nu k} + \sum_{m} N'_{\nu k m}\, \mathrm{Re}\left[\frac{e^{(4\pi m j - \mu^o_\nu + \mu^o_k)t}}{4\pi m j - \mu^o_\nu + \mu^o_k}\right] \tag{6.44}$$

However, as previously illustrated in (6.16), $\eta'_{\nu k}$ exhibits a resonance type solution if $\exp(-\mu^o_\nu - \mu^o_k)t$ has period π. Therefore, two forms of (6.44) must be distinguished

a) $\mu^o_\nu - \mu^o_i = 2nj$:

$$\eta'_{\nu k} = \beta'_{\nu k} + P'_{\nu k}(t)\, e^{-(\mu^o_\nu - \mu^o_k)t} - P_{\nu k}(0) \tag{6.45a}$$

b) $\mu_\nu^o - \mu_k^o = 2nj$:

$$\eta'_{\nu k} = \beta'_{\nu k} + \frac{N'_{\nu kn} t}{2\pi} + Q'_{\nu k}(t) \tag{6.45b}$$

where $B'_{\nu k}$ is constant and $P'_{\nu k}(t)$ and $Q'_{\nu k}(t)$ have period π. Once the solutions for $\eta'_{\nu k}$ are obtained, they are to be substituted into (6.41) to obtain the y'_{ik}, but the latter are required to have period π. Therefore, the following conditions are necessary to insure that the y_{ik} have this period

$$[\text{in (6.45a)}] \qquad B'_{\nu k} - P'_{\nu k}(0) = 0 \tag{6.46a}$$

$$[\text{in (6.45b)}] \qquad \frac{N'_{\nu kn}}{2\pi} = 0 \tag{6.46b}$$

The condition in (6.46a) can always be met because $B'_{\nu k}$ is simply a constant of integration. However, (6.46b) requires that (6.42) have no constant terms when ν and k are such that $(\mu_\nu^o - \mu_k^o)$ is an integral multiple of 2j. This constraint will determine μ'_k.

When k = 1, the values of $\mu_\nu^o - \mu_k^o$ are given in (6.40). There are two values of ν for which the resonance solution in (6.45b) can occur, namely, $\nu = 1$ and $\nu = 4$. Therefore, from (6.42), μ'_k must be chosen so D_{11} and $D_{41}e^{-2jt}$ have no constant terms.

Setting these constant terms equal to zero yields two simultaneous equations in μ'_1 and η_{41}^o/η_{11}^o. Eliminating η_{41}^o/η_{11}^o yields the following expression for μ'_1 as a function of s.

$$\left[\mu'_1 + \frac{s(k_1 - \frac{f}{e}k_2)}{2(1 - \frac{f}{e})}\right]\left[\mu'_1 + \frac{s(k_1 - \frac{f}{e}k_2)}{2(1 - \frac{e}{f})}\right]$$

$$= \frac{1}{16\,\Omega_r\Omega_\ell(1 - \frac{f}{e})(1 - \frac{e}{f})} \tag{6.47}$$

The effect of pumping on μ_i can now be found by setting $s = \alpha^{-1}$, as noted on p. 89 . In general, values of μ_i with both positive and negative real parts will result, but the case of interest is for $s = s_c$ [see (6.36)], where the real part of μ_i vanishes. Assuming

that the imaginary part of μ_i also vanishes when $s = s_c$, then s_c occurs for $\mu_i = 0$ in (6.47) which yields

$$s_c^2 = \frac{-ef}{16(e-f)^2\sigma_r\sigma_\ell\Omega_r\Omega_\ell} \tag{6.48}$$

where (6.24) has been used to simplify this result. The fact that s_c^2 above is positive and real, shows the validity of the assumption that Im $(\mu_i) = 0$. Now, using (6.36), the stability condition becomes

$$\left(\frac{\gamma_p}{C}\right)^2 < \frac{-4(e-f)^2\sigma_r\sigma_\ell\Omega_r\Omega_\ell}{ef} \tag{6.49}$$

which agrees exactly with (6.26). Therefore, direct calculation of the characteristic roots of Fig. 6.3 has verified the much simpler stability prediction in (6.18), although the latter was derived from an idealized representation of Fig. 4.3 by steady-state analysis.

The main approximations that have been obtained in this first-order verification are these in (6.20) and (6.25b). If they were not satisfied a new formulation of the steady-state analysis could be made to account for these cases.

4.3 Conclusion

In this chapter the following theorem has been proven: The formal steady state response of a periodically varying system becomes unbounded if and only if one or more of the characteristic roots of the system is purely imaginary. The purpose of subsequent analysis has then been shown how approximate steady-state solutions can be used with this theorem to yield useful and accurate stability predictions. A secondary purpose has also been accomplished in showing the laborous procedure involved in obtaining the characteristic roots of a periodically varying system. In this way the practicality of the above stated theorem has been demonstrated.

CHAPTER VII

GENERAL CONSIDERATIONS OF REACTIVE MIXING INVOLVING SYMMETRICAL SIDEBAND PAIRS

The preceding chapters, summarizing single-sideband reactive mixers, have demonstrated two extremes in circuit properties. In the first case considered, only the upper sideband was present. A completely stable conversion gain was demonstrated, which was limited in magnitude to the ratio of output to input frequency. Lower-sideband mixing, on the other hand, demonstrated arbitrarily large conversion gains, but at the expense of an ever increasing threat of instability. Large, lower-sideband conversion gains are also accompanied by large input reflections. While the latter are useful, as a means of one-port (parametric) amplification, they are difficult to control and to exploit fully. Furthermore, single-sideband parametric amplification is limited to frequencies below the pump frequency.

In view of the striking differences between these two single-sideband cases (both with respect to their useful features and their limitations), the presence of sideband pairs causes the anticipation of interesting effects. The main effects that will be discussed are enumerated below:

1. Parametric amplification at frequencies higher than pump frequency, without relying upon effects from pump harmonics.
2. Conversion gains between ω_r and ω_u, well in excess of the output to input frequency ratio, and either with or without negative input resistance.
3. Amplification by phase modulation and detection.

In each of these cases, the added influence of the pump harmonic $2\omega_p$ will be considered. In most instances, it will be shown to provide still further improvement in mixer performance. The detailed realization of these effects will be the subject of later chapters, but the present chapter will discuss them from the point of view of the general energy relations. It will be shown that the latter predict each of the effects noted above.

7.1 Application of the General Energy Relations to Double-Sideband Reactive Mixers

When applied to double-sideband reactive mixers, the Manley-Rowe general energy equations in (2.9) reduce to the set in (3.2). But when the pump harmonic is added, they become

$$\frac{W_p + W_{2p}}{\omega_p} + \frac{W_u}{\omega_u} + \frac{W_\ell}{\omega_\ell} = 0 \tag{7.1a}$$

$$\frac{W_r}{\omega_r} + \frac{W_u}{\omega_u} - \frac{W_\ell}{\omega_\ell} = 0 \tag{7.1b}$$

Before going on, it is important to consider the artifice of restricting the Manley-Rowe relations to a particular set of frequencies. We note that the realization of a predicted energy distribution, without the influence of certain of the eliminated frequencies, is not guaranteed. For example, if the external circuitry reactively terminated a particular frequency, it would be eliminated from (7.1), but this frequency may still contribute internally to the conversion process. It may be a hidden mechanism behind effects that seem from (7.1) to be independent of this frequency. In other words, the Manley-Rowe equations only relate frequencies where real power flows.

Situations of this nature will be illustrated herein, particularly in connection with the first pump harmonic. For example, (7.1a) suggests nothing about the relative importance of the pump and its harmonic. It even suggests that they are interchangeable, which is rarely true. A further distinction between these two frequencies must come through a knowledge of their reactive power components. Therefore, the term W_{2p} in (7.1a) can be ignored for the present, if it is realized that reactive power at $2\omega_p$ (or other suppressed frequencies) may still be required to realize the effects predicted by (7.1).

Further study of (7.1) will be divided into two parts. Consider first the application of signals at ω_r and ω_p, with ω_ℓ and ω_u experiencing passively realizable loads only (in particular, loads whose resistive components are positive). Thus, W_ℓ and W_u are nonpositive and (7.1b) yields the following expressions for the up-conversion power gain from ω_r to ω_ℓ, or to ω_u.

$$P_{ru} = -\frac{W_u}{W_r} = \left(\frac{\omega_u}{\omega_r}\right)\left(\frac{1}{1 - X_{\ell u}}\right) \tag{7.2a}$$

$$P_{r\ell} = -\frac{W_\ell}{W_r} = \left(\frac{\omega_\ell}{\omega_r}\right)\left(\frac{X_{\ell u}}{1 - X_{\ell u}}\right) \tag{7.2b}$$

Similarly, the ratio of pump power to signal power is given by

$$\frac{W_p}{W_r} = \left(\frac{\omega_p}{\omega_r}\right)\left(\frac{1 + X_{\ell u}}{1 - X_{\ell u}}\right) \tag{7.2c}$$

where $X_{\ell u} = W_\ell \omega_u / W_u \omega_\ell$. To illustrate the remarks to follow, sketches of (7.2) are shown in Fig. 7.1. In the limit where ω_ℓ is short circuited ($W_\ell = 0$), P_{ru} has the previously discussed value ω_u/ω_r. However, P_{ru} increases as $X_{\ell u}$ is increased, and arbitrarily-large positive values of P_{ru} can be achieved in the vicinity of $X_{\ell u} < 1$. This suggests that large conversion gain is possible without reflecting negative input conductance at ω_r. For $X_{\ell u} > 1$, P_{ru} and $P_{r\ell}$ are negative. Hence, this condition defines a general region of potential instability in which parametric amplification is possible at ω_r. It is important to note that negative conversion gains do not necessarily imply the reflection of negative conductance at the input frequency terminals, although this was the case in the circuits discussed previously. The Manley-Rowe equations would also predict negative conversion gains if the input signal were completely absorbed at one terminal pair, amplified, and then expelled at the same frequency (along with other conversion frequencies) at another terminal pair. The realization of this effect (without using circulators) is one goal of this analysis.

The second case of interest is with signals applied at ω_p and ω_u, and where ω_r and ω_ℓ are terminated only in passive loads. In this case, with $X_{\ell r} = W_\ell \omega_r / W_r \omega_\ell$, (7.1) yields the following expressions, which are also plotted in Fig. 7.2.

$$P_{ur} = -\frac{W_r}{\omega_u} = \frac{\omega_r}{\omega_u}\left(\frac{1}{1 - X_{\ell r}}\right) \tag{7.3a}$$

$$\frac{W_p}{W_u} = \frac{\omega_p}{\omega_u}\left(\frac{2X_{\ell r} - 1}{1 - X_{\ell r}}\right) \tag{7.3c}$$

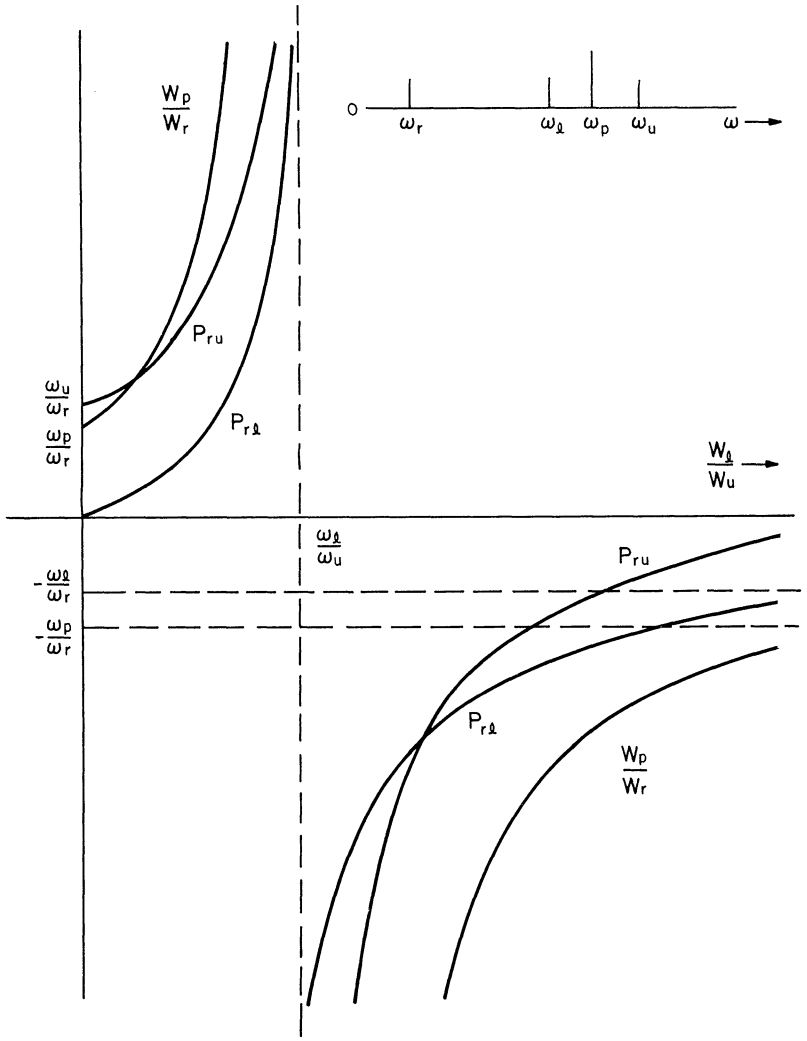

Fig. 7.1. Sketches of (7.2) showing the regions of positive and negative conversion gains from ω_r to ω_u and ω_ℓ vs. the ratio of output powers at ω_ℓ and ω_u. Pump power is applied at ω_p and W_p/W_r is the ratio of pump to signal power.

For $X_{\ell r} < 1/2$, P_{ur} and $P_{u\ell}$ are positive, but W_p/W_u is negative. Therefore, the pump circuit is unstable in this region and the signal at ω_u will act as the power source.[1] For $\omega_p/\omega_u < (X_{\ell r}) < 1$, P_{ur} is greater than unity, so this is a region of arbitrary down-conversion gain with positive input conductance. For $(X_{\ell r}) > 1$; P_{ur} and W_p/ω_u are negative. Thus, a region of potential instability exists at ω_u, which suggests that parametric amplification is possible at this frequency.

[1] See Section 3.1.2.

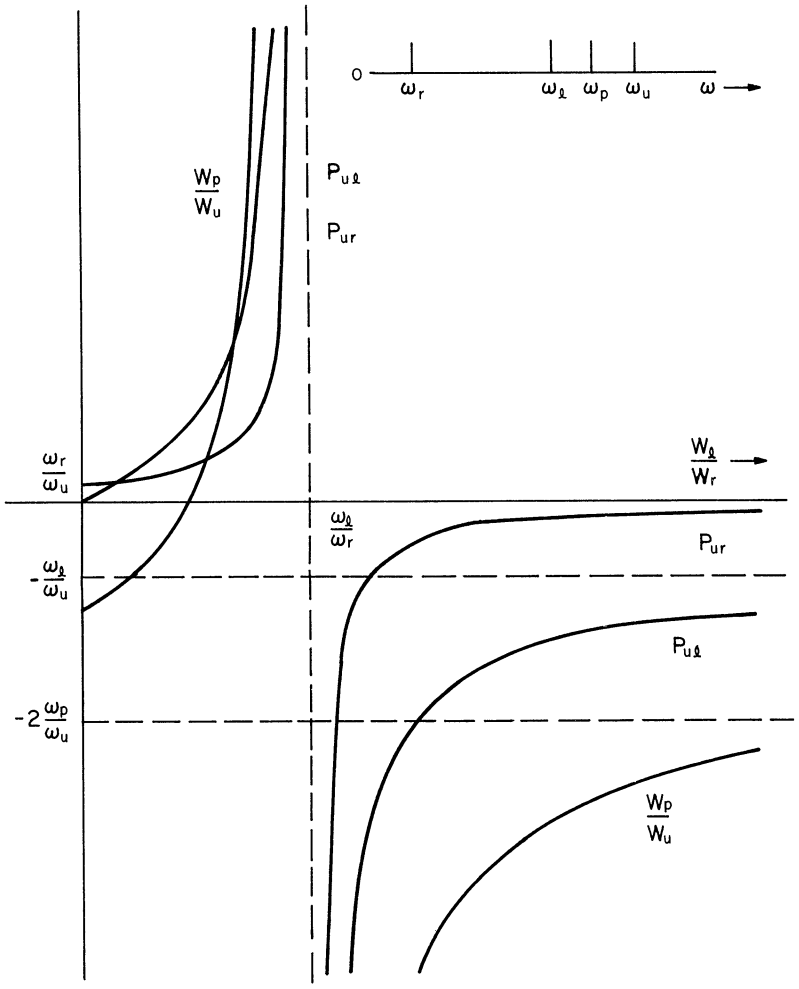

Fig. 7.2. Sketches of (7.3) showing the regions of positive and negative conversion gains from ω_u to ω_r and ω_ℓ vs. the ratio of output powers at ω_ℓ and ω_u. Pump power is applied at ω_p, and W_p/W_r is the ratio of pump to signal power.

Again, it should be noted that the Manley-Rowe equations do not guarantee that just any reactive element will yield the results above. For a particular element, only the trivial solution, $W_{mn} = 0$, may be possible. For example, it can be noted from Fig. 7.2 that parametric amplification at ω_u is predicted even in the limit where ω_r is short circuited ($W_r = 0$). But, applying the time-varying reactance model in Fig. 2.1, as described by (2.27) [a model that satisfies the Manley-Rowe equations in (7.1)], it can be shown that ω_u is completely decoupled when ω_r is suppressed, unless the pump harmonic γ_{2p} is present.

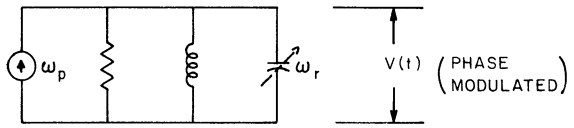

Fig. 7.3. An illustration of phase modulation by reactive mixing.

7.2 Application of the General Energy Relations to Phase Modulation

An important characteristic of reactive mixers is their tendency, under certain circumstances, to produce phase modulation. This effect is illustrated in Fig. 7.3, where a signal at ω_r varies the tuning of a resonant circuit and hence varies its phase shift. A true phase modulation spectrum, as shown in Fig. 7.4, is symmetrical in the sense in which the term is used here. (That is, the distribution of sidebands by frequency is symmetrical with respect to ω_p.) However, the spectrum in Fig. 7.4 has still a higher degree of symmetry, since $W_{mn} = W_{m,-n}$.

It will now be of interest to apply the Manley-Rowe equations to this configuration. This step is facilitated if (2.9b) is first written in the form

$$\frac{W_r}{\omega_r} + \sum_{n=0}^{\infty} \sum_{m=1}^{\infty} \left[\frac{nW_{mn}}{m\omega_p + n\omega_r} + \frac{nW_{-m,n}}{-m\omega_p + n\omega_r} \right] = 0 \qquad (7.4)$$

If (2.5b) is applied to the last term, (2.9b) can be further modified to read:

$$\frac{W_r}{\omega_r} + \sum_{n=0}^{\infty} \sum_{m=1}^{\infty} \left[\frac{nW_{mn}}{m\omega_p + n\omega_r} - \frac{nW_{m,-n}}{m\omega_p - n\omega_r} \right] = 0 \qquad (7.5)$$

But, in Fig. 7.4, $m = 1$ and $W_{mn} = W_{m,-n}$, so in this case

$$\frac{W_r}{\omega_r} = \sum_{n=1}^{\infty} \frac{2n^2 \omega_r W_{mn}}{\omega_p^2 + (n\omega_r)^2} \qquad (7.6)$$

Each sideband in Fig. 7.4 is passively terminated, so the right hand side of (7.6) must be negative, and hence W_r must also be negative. Therefore, the phenomenon of phase modulation by reactive elements is potentially unstable. Instability in this spectrum arises be-

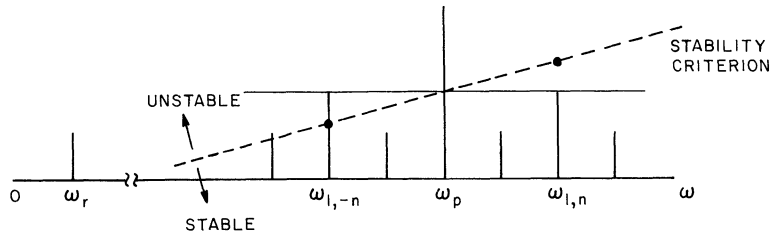

Fig. 7.4. A typical phase modulation spectrum and the associated stability criterion based on (7.7).

cause the lower sideband is dominant in each sideband pair in (7.5).

Further inspection of (7.5) shows that W_r is negative as long as

$$\frac{W_{mn}}{W_{m,-n}} < \frac{m\omega_p + n\omega_r}{n\omega_p - n\omega_r} \tag{7.7}$$

This relation defines the line shown dotted in Fig. 7.4, which is an envelope that separates stable and unstable spectral distributions. For example, if a line is drawn through the peaks of the power spectral components of any symmetrical pair of sidebands, then its slope, relative to the dotted line in Fig. 7.4, determines the influence of this pair on stability. If the slope is greater than the reference line, the pair will contribute positively to W_r and to stability. With lesser slope, the same sidebands contribute negatively to W_r and hence contribute to instability.

It will be of interest to now consider pump power. If the decomposition employed in (7.4) and (7.5) is applied to (2.9a), the following relation for pump power is obtained

$$\frac{W_p}{\omega_p} + \sum_{n=1}^{\infty}\sum_{m=1}^{\infty} m\left[\frac{W_{mn}}{m\omega_p + n\omega_r} + \frac{W_{m,-n}}{m\omega_p - n\omega_r}\right] = 0 \tag{7.8}$$

Applying this relation to the spectrum in Fig. 7.4, where $m = 1$, yields

$$\frac{W_p}{\omega_p} = -\sum_{n=1}^{\infty} \frac{2\omega_p W_{1n}}{\omega_p^2 + (n\omega_r)^2} \tag{7.9}$$

If this result is now compared with (7.6), a given sideband pair will be seen to receive pump

and signal power in the ratio

$$-\frac{\omega_p^2}{n^2\omega_r^2} \tag{7.10}$$

Therefore, nearly all sideband power is contributed by the pump, in the ratio of pump to signal frequency squared. This will be an important result later on.

7.3 A Generalization of the Double-Sideband Mixer

The reader will eventually see that the remainder of this study is essentially an investigation of the 3 X 3 matrix in (2.27). While this matrix was derived for the symmetrical mixing scheme in Fig. 1.4, it is of interest to note that an infinity of unsymmetrical mixer schemes are equally well described by (2.26) or (2.27). As proof, consider a general time-varying capacitor with components γ_{mp} at all pump harmonics $n\omega_p$, and consider further that the signal set includes any of the frequencies $m\omega_p \pm \omega_r$. It can be shown that the relation corresponding to (2.26) in this case is the following:

$$\begin{vmatrix} \\ -I^*_{4,-1}/j\omega_{4,-1} \\ -I^*_{3,-1}/j\omega_{3,-1} \\ -I^*_{2,-1}/j\omega_{2,-1} \\ -I^*_{\ell}/j\omega_{\ell} \\ I_r/j\omega_r \\ I_u/j\omega_u \\ I_{21}/j\omega_{21} \\ I_{31}/j\omega_{31} \\ \\ \end{vmatrix} = \begin{vmatrix} - & - & - & - & - & - & - & - & - & - \\ - & C & \gamma_p^* & \gamma_{2p}^* & \gamma_{3p}^* & \gamma_{4p}^* & - & - & - & - \\ - & \gamma_p & C & \gamma_p^* & \gamma_{2p}^* & \gamma_{3p}^* & \gamma_{4p}^* & - & - & - \\ - & \gamma_{2p} & \gamma_p & C & \gamma_p^* & \gamma_{2p}^* & \gamma_{3p}^* & \gamma_{4p}^* & - & - \\ - & \gamma_{3p} & \gamma_{2p} & \gamma_p & C & \gamma_p^* & \gamma_{2p}^* & \gamma_{3p}^* & \gamma_{4p}^* & - \\ - & \gamma_{4p} & \gamma_{3p} & \gamma_{2p} & \gamma_p & C & \gamma_p^* & \gamma_{2p}^* & \gamma_{3p}^* & - \\ - & - & \gamma_{4p} & \gamma_{3p} & \gamma_{2p} & \gamma_p & C & \gamma_p^* & \gamma_{2p}^* & - \\ - & - & - & \gamma_{4p} & \gamma_{3p} & \gamma_{2p} & \gamma_p & C & \gamma_p^* & - \\ - & - & - & - & \gamma_{4p} & \gamma_{3p} & \gamma_{2p} & \gamma_p & C & - \\ - & - & - & - & - & - & - & - & - & - \end{vmatrix} \begin{vmatrix} \\ V^*_{4,-1} \\ V^*_{3,-1} \\ V^*_{2,-1} \\ V^*_{\ell} \\ V_r \\ V_u \\ V_{21} \\ V_{31} \\ \\ \end{vmatrix} \tag{7.11}$$

It can be observed that the center 3 X 3 submatrix in (7.11) is identical to (2.26). Also, all other 3 X 3 submatrices along the main diagonal are equivalent to (2.26),

although each involves a different set of signal frequencies. Therefore, all signal frequency subsets that are defined by

$$\begin{aligned} -(\omega_p - \omega_r) &\pm n\omega_p \\ \omega_r &\pm n\omega_p \\ \omega_p + \omega_r &\pm n\omega_p \end{aligned} \tag{7.12}$$

are identical. Consequently, all properties in later chapters that are attributed to ω_r, ω_ℓ, and ω_u can also be realized with the mixing spectra in the table below, providing the indicated correspondence is followed.

Reference Set	ω_ℓ	ω_r	ω_u
All lower sideband equivalents	$2\omega_p - \omega_r$	$\omega_p - \omega_r$	ω_r
	$3\omega_p - \omega_r$	$2\omega_p - \omega_r$	$\omega_p - \omega_r$
	—	—	—
All upper sideband equivalents	ω_r	$\omega_p + \omega_r$	$2\omega_p + \omega_r$
	$\omega_p + \omega_r$	$2\omega_p + \omega_r$	$3\omega_p + \omega_r$
	—	—	—

Table of equivalent signal spectra.

7.4 Conclusion

The general energy relations have suggested some interesting effects associated with double-sideband reactive mixing. In particular, it has been seen that extracting power at the lower sideband, ω_ℓ, will increase the power transfer between ω_r and ω_u. Also, these same interactions can be attained with an infinite number of sets of three signal frequencies. The following chapters will now treat these individual cases by means of appropriate small signal analysis. In this way, the many improved circuit effects associated with double-sideband reactive mixing will be discovered.

CHAPTER VIII

DOUBLE-SIDEBAND, SINGLE-PUMP MIXING WITH INDEPENDENT SIDEBAND LOADING

A convenient first step towards investigating the advantages of double-sideband reactive mixers is provided by a simple combination of the two typical single-sideband cases. The single-pump frequency ω_p will be retained, but the signal frequency set will be extended to include ω_r, ω_ℓ, and ω_u simultaneously. The formulation for first-order mixing in this case is essentially in (2.27). The only modification required to make (2.27) applicable now is to set γ_{2p} to zero which yields:

$$\begin{bmatrix} \mathrm{I}_r \\ \mathrm{I}_u \\ \mathrm{I}_\ell \end{bmatrix} = \begin{bmatrix} Y_r & j\omega_r\gamma_p^* & j\omega_r\gamma_p \\ j\omega_u\gamma_p & Y_u & 0 \\ -j\omega\ \gamma_p^* & 0 & Y_\ell^* \end{bmatrix} \begin{bmatrix} V_r \\ V_u \\ V_\ell^* \end{bmatrix} \tag{8.1}$$

Again, γ_p will be assumed real. The effects incurred by neglecting γ_{2p} will be explained in Chapter 10.

An appropriate equivalent circuit for (8.1) is Fig. 2.1 (with $\gamma_{2p} = 0$), but in employing this figure ω_ℓ and ω_u will be assumed to be widely spaced in frequency. Ideal filtering can then be approximated reasonably well, and the sidebands can then be independently loaded. Hence Y_ℓ and Y_u can be regarded as arbitrary, positive-real admittances.

An alternate equivalent circuit can be formed by combining the equivalent circuits in Figs. 4.2 and 5.1, as shown in Fig. 8.1. Here, the ω_r terminals are simultaneously coupled to the ω_ℓ and the ω_u terminals, but the latter two frequencies have no direct coupling. By recalling the separate functions of the individual sidebands, the following operation of Fig. 8.1 can be visualized. The load at ω_u reflects positive conductance

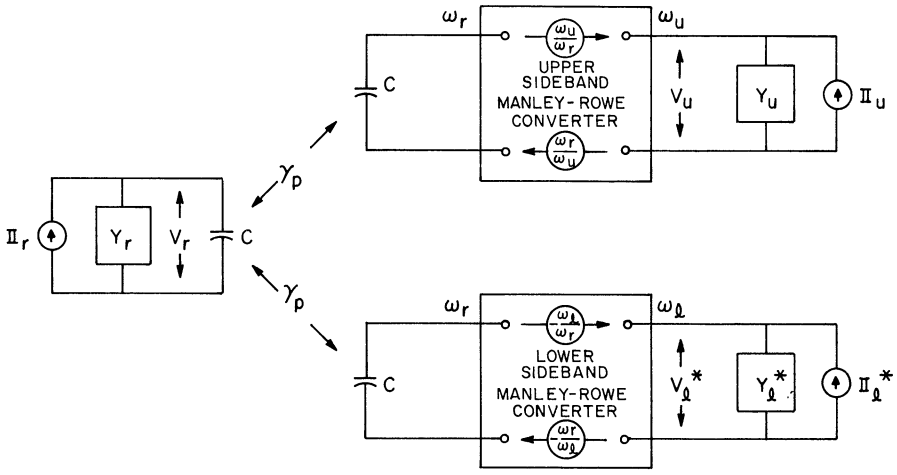

Fig. 8.1. A functional equivalent circuit of double-sideband conversion with a single pumping frequency.

into the ω_r terminals, while the load at ω_ℓ reflects negative conductance. The latter tends to enhance the input signal by parametric amplification. Therefore, any signal power that is converted to ω_u will be amplified before conversion. As a result, the transducer gain from ω_r to ω_u can greatly exceed the ratio of these frequencies. Ironically then, the extraction of power at ω_ℓ increases the power conversion to ω_u.

Figure 8.1 also suggests enhanced down-conversion gain from ω_u to ω_r, because the down-converted signal will receive parametric amplification before emerging from the ω_r terminals. However, this action at ω_r radically changes the input admittance at ω_u, even to the extent of reflecting negative conductance at this frequency. When this is the case, direct parametric amplification will occur at ω_u--a frequency higher than the true pump frequency. Note that this accomplishment is quite different from "parametric amplification by low frequency pumping," as reported by Bloom and Chang (Refs. 34, 35, 36), who used harmonic generation to make a low frequency pump produce capacitance variations at the normal pumping frequency. Basically their system is a conventional lower-sideband converter.

The question arises as to what benefits ω_u might bestow on conversion from ω_r to ω_ℓ. In short, this case appears to offer no advantage because the single-sideband case has already demonstrated arbitrary conversion gain between ω_r and ω_ℓ and the pre-

sence of ω_u simply introduces excess loading. Of course, in certain applications this loading may be useful for controlling stability, but the effect of ω_u on ω_ℓ appears to be less deserving of attention than the previously noted effects of ω_ℓ on ω_u. Therefore, the exploit of the present chapter will be limited to effects that can be derived at the ω_r and ω_u terminals.

Using the results of Chapters IV and V, the input admittances at each terminal in Fig. 8.1 can be written by inspection. At ω_r, the two reflected admittances appear in parallel, so by (4.10b) and (5.6) one obtains

$$Y_{r_{in}} = Y_r + \frac{\omega_r \omega_u \gamma_p^2}{Y_u} - \frac{\omega_r \omega_\ell \gamma_p^2}{Y_\ell^*} \tag{8.2}$$

To perform a similar calculation at ω_u, the load at ω_ℓ will first be reflected to ω_r according to (5.6) and then the parallel combination thus formed with Y_r will be reflected to ω_u. Upon adding this reflected admittance to Y_u, one obtains

$$Y_{u_{in}} = Y_u + \frac{\omega_r \omega_u \gamma_p^2}{Y_r - \frac{\omega_s \omega_\ell \gamma_p^2}{Y_\ell^*}} \tag{8.3}$$

Similarly, at ω_ℓ

$$Y_{\ell_{in}}^* = Y_\ell^* - \frac{\omega_r \omega_\ell \gamma_p^2}{Y_r + \frac{\omega_r \omega_u \gamma_p^2}{Y_u}} \tag{8.4}$$

It is generally desirable to have all frequencies synchronously tuned. In this case, (8.2) through (8.4) reduce to

$$g_{r_{in}} = g_r + \frac{\omega_r \omega_u \gamma_p^2}{g_u} - \frac{\omega_r \omega_\ell \gamma_p^2}{g_\ell} \tag{8.5a}$$

$$g_{u_{in}} = g_u + \frac{\omega_r \omega_u \gamma_p^2}{g_r - \frac{\omega_r \omega_\ell \gamma_p^2}{g_\ell}} \tag{8.5b}$$

$$g_{\ell_{in}} = g_\ell - \frac{\omega_r \omega_\ell \gamma_p^2}{g_r - \frac{\omega_r \omega_\ell \gamma_p^2}{g_u}} \tag{8.5c}$$

which are plotted, vs. γ_p, in Fig. 8.2.

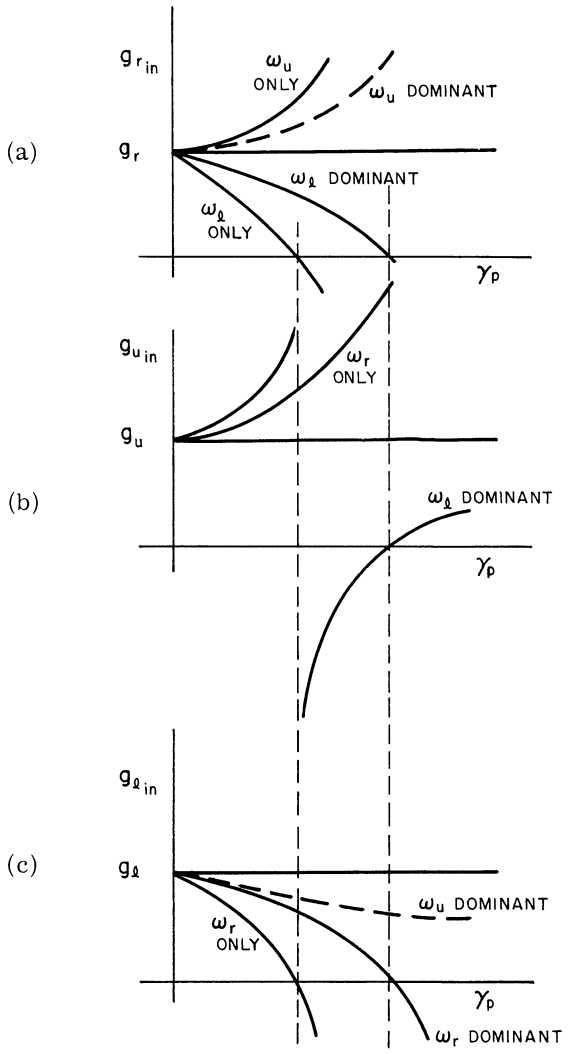

Fig. 8.2. The input conductance at resonance vs. γ_p, showing regions of apparent instability.

The important question of stability arises again in connection with Fig. 8.2. It can be seen that regions of negative input conductance appear at each of the individual terminals, but for different values of γ_p. For example, $g_{u_{in}}$ becomes negative for a smaller value of γ_p than $g_{\ell_{in}}$ or $g_{r_{in}}$, and so the stable regions of Fig. 8.2 are a matter of concern.

In a preliminary study of this problem by the author (Ref. 19), the range of stable operation was assumed to be determined by the negative conductance region that first appeared as γ_p increases. However, this assertion is inconsistent with the more rigorous criterion outlined in Chapter VI. For example, further examination of Fig. 8.2 shows that

the input conductance at the individual terminal pairs can become negative in two ways, either by going through zero or through infinity. According to the criterion just mentioned, only the latter instance is actually unstable. Thus the possible range of stable loadings in Fig. 8.2 is greater than once expected.

A more specific statement about the stability of double-sideband, single-pump mixers can be made directly from (8.1). It has been established that a sinusoidal, steady-state response must become infinite at thresholds of instability. Therefore, to the extent that (8.1) predicts the steady-state response in an actual mixer, the vanishing of a system determinant (Δ) will mark the instability thresholds. From (8.1),

$$\Delta = Y_r Y_\ell^* Y_u + \omega_r \gamma_p^2 \quad (\omega_u Y_\ell^* - \omega_\ell Y_u) \tag{8.6}$$

or, by (8.2),

$$\Delta = Y_\ell^* Y_u Y_{r_{in}} \tag{8.7}$$

which vanishes only when $Y_{r_{in}}$ vanishes. The fact that the input admittance at ω_r can be used to predict stability is important because there the influence of the individual sidebands can easily be distinguished through the representation in Fig. 5.2. In essence, the lower-sideband is the source of all instability, so it can be said that ω_ℓ is always regeneratively coupled to ω_r. By contrast, the upper-sideband is degeneratively coupled to ω_r, and a proper balance of these two feedback mechanisms will produce an interesting variety of circuit effects.

8.1 Gain and Bandwidth for Double-Sideband Conversion from ω_r to ω_u

It has been noted that the transducer gain from ω_r to ω_u increases significantly with the dissipation of power at ω_ℓ. To quantitatively evaluate this effect, the transducer gain from ω_r to ω_u can be calculated from (8.1) and (3.15b) which yields

$$G_{ru} = \frac{\omega_u}{\omega_r}\left(\frac{4 g_S g_L \omega_r \omega_u \gamma_p^2}{\left|Y_r Y_u + \omega_r\omega_u\gamma_p^2 - \omega_r\omega_\ell\gamma_p^2 Y_u/Y_\ell^*\right|^2}\right) \tag{8.8}$$

The most fundamental application of (8.8) occurs when the individual terminals are syn-

chronously tuned. Then, if each terminal admittance is equivalent to a simple resonant circuit, the latter can be approximated by

$$Y_r \approx g_r\left(1 + \frac{2j\delta}{\beta_r}\right) \tag{8.9a}$$

$$Y_u = g_u\left(1 + \frac{2j\delta}{\beta_u}\right) \tag{8.9b}$$

$$Y_\ell = g_\ell\left(1 - \frac{2j\delta}{\beta_\ell}\right) \tag{8.9c}$$

where $\omega_r = \overline{\omega}_r + \delta$, and β_r, β_ℓ, and β_u are the bandwidths in angular frequency of the ω_r, ω_ℓ, and ω_u terminals, respectively. The approximations in (8.11) are useful because the most significant circuit behavior occurs for values of 2δ that are less than the individual bandwidths. In this case, the terminal admittances are well represented by (8.9).

Substituting (8.9) in (8.8) yields the following expression for first-order dependence of transducer gain upon δ.

$$G_{ru}(\delta) \cong \frac{4\left(\frac{\overline{\omega}_u}{\overline{\omega}_r}\right)\left(\frac{g_S g_L}{g_r g_u}\right)\rho_u}{\left(1 + \frac{2j\delta}{\beta_r}\right)\left(1 + \frac{2j\delta}{\beta_u}\right) + \rho_u - \rho_\ell\left(\frac{1 + 2j\delta/\beta_u}{1 + 2j\delta/\beta_\ell}\right)^2} \tag{8.10}$$

Two additional approximations made in writing (8.10) are that

$$\frac{\omega_r \omega_u \gamma_p^2}{g_r g_u} \approx \frac{\overline{\omega}_r \overline{\omega}_u \gamma_p^2}{g_r g_u} = \rho_u \tag{8.11a}$$

$$\frac{\omega_r \omega_\ell \gamma_p^2}{g_r g_\ell} \approx \frac{\overline{\omega}_r \overline{\omega}_\ell \gamma_p^2}{g_r g_\ell} = \rho_\ell \tag{8.11b}$$

The midband value of (8.10) is

$$\overline{G}_{ru} = \frac{4\left(\frac{\overline{\omega}_u}{\omega_r}\right)\left(\frac{g_S g_L}{g_r g_u}\right)\rho_u}{(1 + \rho_u - \rho_\ell)^2} \tag{8.12}$$

which becomes arbitrarily large as $\rho_\ell \to 1 + \rho_u$.

In (8. 11) ρ_u depends on the input and output conductance, while ρ_ℓ is rather arbitrary. Therefore it is instructive to regard (8. 12) as a function of ρ_u, with ρ_ℓ as a parameter. It is apparent from (8. 12), that an optimum value of ρ_u exists. To further evaluate (8. 12), it will be rewritten as follows

$$\overline{G}_{ru} = \frac{\overline{\omega}_u}{\overline{\omega}_r} \frac{Nxy(1-x)(1-y)}{[1-\rho_\ell + N(1-x)(1-y)]^2} \tag{8.13}$$

$$N = \frac{\overline{\omega}_r \overline{\omega}_u \gamma_p^2}{g_{dr} g_{du}} = \frac{\rho_u}{(1-x)(1-y)} \tag{8.14a}$$

$$x = \frac{g_S}{g_r} \qquad y = \frac{g_L}{g_u} \tag{8.14b}$$

The quantities in (8. 14b) are the same input and output efficiency factors that were previously introduced in Section 4. 2. 3.

For a given varactor, a given ρ_ℓ, and for fixed frequencies, N will be constant in (8. 13) so $\overline{G}_{ru}$ can be optimized with respect to x and y. The result is expressed below in several alternate forms

if $\rho_\ell < 1$:

$$(\overline{G}_{ru})_{opt} = \left(\frac{\overline{\omega}_u}{\overline{\omega}_r}\right) \frac{\rho_u}{(1-\rho_\ell)^2} \tag{8.15}$$

which occurs for

$$x = y \tag{8.16a}$$

$$\rho_u = (2x-1)(1-\rho_\ell) \tag{8.16b}$$

if $\rho_\ell > 1$:

$$(\overline{G}_{ru})_{opt} = \infty \tag{8.17}$$

which occurs for

$$\rho_u = \rho_\ell - 1 \tag{8.18}$$

Therefore, the optimum gain depends on ρ_ℓ. If ρ_ℓ is varied, $\overline{G}_{ru}$ increases monotonically until (8.18) is satisfied. But if ρ_u is varied, the optimum gain can be either finite or infinite depending on ρ_ℓ.

To interpret the optimum gains above, note that (8.16) reduces to the previous result [in (4.35)] when $\rho_\ell = 0$. But in the latter case, optimum gain corresponded to a matched source and load. Therefore, it will be of interest to see if (8.16) retains this special significance in its more general application.

By (8.5a)

$$g_{r_{in}} = g_S + g_{dr} + g_r(\rho_u - \rho_\ell) \tag{8.19a}$$

$$= g_S + g_S\left[\frac{\rho_u - \rho_\ell + 1 - x}{x}\right] \tag{8.19b}$$

but the first term denotes the source itself. Therefore, the source will be matched when

$$\rho_u - \rho_\ell = 2x - 1 \tag{8.19c}$$

Similarly, by (8.5b), the load will be matched when

$$\left(\frac{\rho_u}{1-\rho_\ell}\right) g_u + g_{du} = g_L \tag{8.20a}$$

or

$$\frac{\rho_u}{1-\rho_\ell} = 2y-1 \tag{8.20b}$$

Since (8.20b) is identical to (8.16), it is evident that (8.19b) and (8.20b) cannot be satisfied simultaneously unless $\rho_\ell = 0$. Therefore, in the presence of the lower sideband, but with $\rho_\ell < 1$, optimum gain from ω_r to ω_u corresponds to the output load being matched, but not the source. Under these conditions the source is mismatched according to (8.19b), which yields

$$g_{r_{in}} = g_S + g_S(1 - 2\rho_\ell) \tag{8.20c}$$

The second term here is the conductance seen by the source, which cannot exceed g_S. Thus

the relationship between ρ_u and ρ_ℓ in (8.15) yields arbitrarily large gains with: (1) a matched output, and (2) an optimum compensation for varactor loss. However, as the gain becomes infinite in this case, ρ_u must become vanishingly small, which puts a severe restriction on the output load. When $\rho_\ell > 1$, alternate advantages accure because infinite gain can result for nonzero values of ρ_u. No optimization with respect to x or y occurs in this case because infinite gain is theoretically possible for any x or y.

8.1.1 Gain Improvement When $\rho_\ell < 1$. The optimum gain in (8.15) can be regarded as the simplest extension of the pure upper-sideband converter. Therefore, to obtain a better feeling for the influence of the lower sideband, the dependence of $(\overline{G}_{ru})_{opt}$ upon frequency will be calculated for this case. Combining the relations in (4.18c), (5.8), and (8.14 through 8.16), the following normalized gain expression can be obtained

$$(\overline{G}_{ru})_{opt} \left(\frac{\overline{\omega}_r}{\omega'_d}\right)^2 = \left(\frac{2x-1}{1-\rho_u}\right)\frac{\overline{\omega}_u}{\overline{\omega}_r} \left(\frac{\omega_r}{\omega'_d}\right)^2 \tag{8.21}$$

where

$$\frac{\overline{\omega}_u}{\overline{\omega}_r} \cdot \left(\frac{\overline{\omega}_r}{\omega'_d}\right) = \frac{(1-x)^2}{(2x-1)(1-\rho_\ell)} \tag{8.22}$$

Eliminating x from these two relations yields the curves in Fig. 8.3. These curves show that gain increases with ρ_ℓ even in the presence of varactor loss. However, a further limitation arises because ρ_ℓ depends on the varactor loss $g_{d\ell}$ at ω_ℓ. The maximum value of ρ_ℓ occurs when $g_\ell = g_{d\ell}$, which yields

$$(\rho_\ell)_{max} = \frac{\overline{\omega}_r \overline{\omega}_\ell \gamma_p^2}{g_r g_{d\ell}} = (1-x)\, N \frac{\overline{\omega}_\ell}{\overline{\omega}_u} \tag{8.23a}$$

Or, by (8.14) and (8.16),

$$(\rho_\ell)_{max} = \left(\frac{2x-1}{1-x}\right)\left[1-(\rho_\ell)_{max}\right]\left(\frac{\overline{\omega}_\ell}{\overline{\omega}_u}\right) \tag{8.23b}$$

Therefore

$$(\rho_\ell)_{max} = \frac{2x-1}{\frac{\overline{\omega}_u}{\overline{\omega}_\ell}(1-x) + (2x-1)} \tag{8.24a}$$

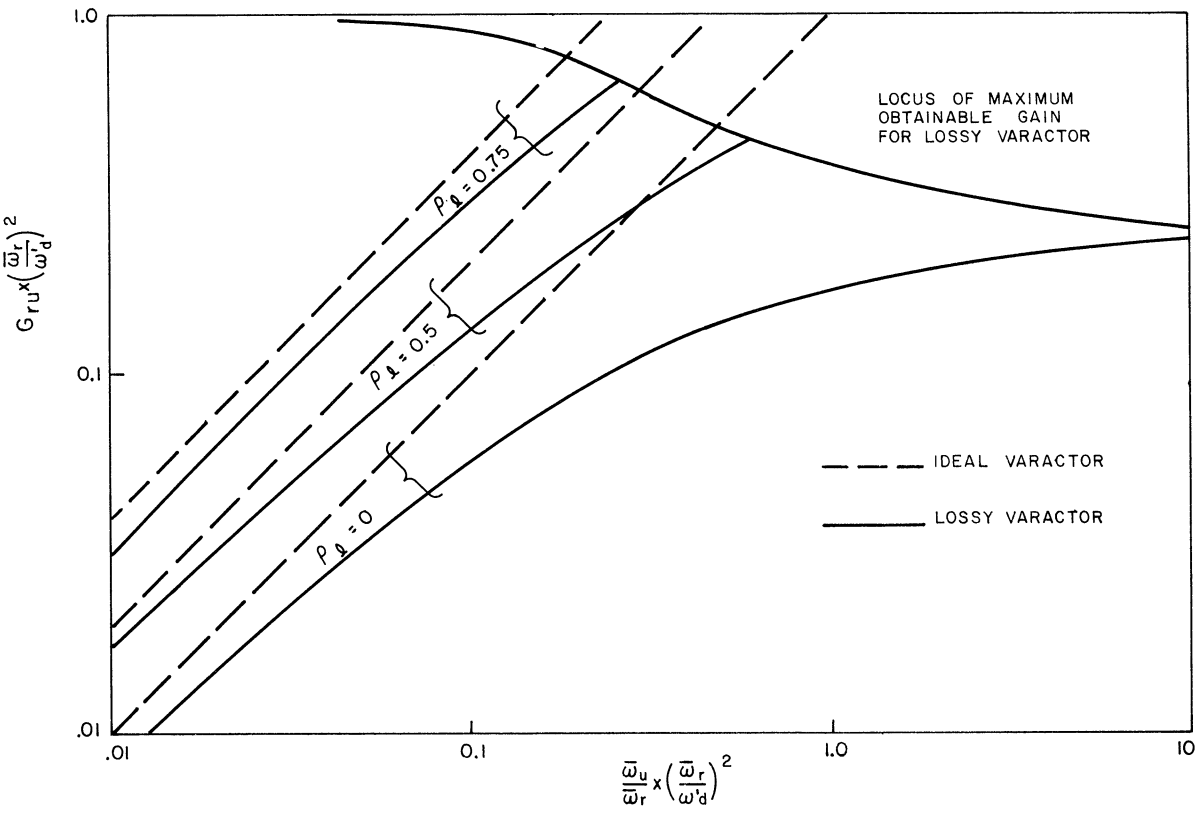

Fig. 8.3. Curves showing improved upper sideband up-conversion due to the introduction of the lower sideband. The parameter ρ_ℓ is a measure of the amount of parametric amplification due to the lower sideband. When $\rho_\ell = 1$, the lower sideband is coupled just as it would be in a simple lower-sideband converter with infinite gain.

which is less than

$$(\rho_\ell)_{max} \approx \frac{2x-1}{x} \qquad \text{if } \frac{\bar{\omega}_u}{\bar{\omega}_\ell} \approx 1 \tag{8.24b}$$

Substituting the latter value into (8.21) yields

$$(\bar{G}_{ru})_{max} \approx \left(\frac{\omega'_d}{\bar{\omega}_r}\right)^2 x^2 = \left(\frac{\omega'_d}{\bar{\omega}_r}\right)^2 \left(\frac{1}{2-\rho_\ell}\right)^2 \tag{8.25}$$

which means that the limiting case of $\rho_\ell = 1$ yields a maximum gain that is only four times larger than the maximum gain possible when $\rho_\ell = 0$. However, the larger gain occurs at a lower pump frequency, which offers additional advantages.

Therefore, for a given $\bar{\omega}_u/\bar{\omega}_r$ ratio, varactor loss will limit ρ_ℓ in (8.16b) to some value less than one. This limit is such that (8.15) can be improved by a factor of at most 4 (6 db) over the optimum value for $\rho_\ell = 0$. The maximum gain for a given ρ_ℓ, based on (8.24b), is also shown in Fig. 8.3. It should be noted that the error of approximation in (8.24c) is such that the curves in Fig. 8.3 are a slight overestimate of $\bar{G}_{ru}$.

8.1.2 Gain Improvement When $\rho_\ell > 1$. When $\rho_\ell > 1$, the condition in (8.18) will yield infinite gain. In this case, the double-sideband converter has essentially the same gain and bandwidth properties as the simple lower-sideband converter. The lower sideband now completely dominates in the circuit, so only the output frequency is different, being ω_u instead of ω_ℓ. The gain-bandwidth product is given by (8.37), which differs from (5.17) only by the factor ω_u/ω_ℓ. Not to be overlooked, however, is that now nearly identical outputs are available at two separate frequencies.

8.1.3 Bandwidth of G_{ru}. For a further description of double-sideband conversion, the bandwidth of (8.12) will be calculated. First, it will be noted that the input and output bandwidths must be equal to obtain maximum conversion bandwidth. Then it will be reasoned that if an additional signal frequency produces desirable effects, its presence will be desired over the entire conversion band. Therefore, a case of general interest occurs when the terminal bandwidths are equal, namely when $\beta_r = \beta_\ell = \beta_u = \beta$. In this case, (8.10) reduces to

$$G_{ru}(\delta) = \left(\frac{\bar{\omega}_u}{\bar{\omega}_r}\right) \frac{4xy\rho_u}{\left[1 + \rho_u - \rho_\ell + \left(\frac{2\delta}{\beta}\right)^2\right]^2 + 4\left(\frac{2\delta}{\beta}\right)^2} \tag{8.26}$$

The bandwidth of (8.21) is found to be

$$\frac{2\delta}{\beta}^{\frac{1}{2}} = \left[(A-2) + \sqrt{4 - 4A + 2A^2}\right]^{\frac{1}{2}} \tag{8.28}$$

$$\approx \frac{A}{2} \qquad \text{if } A << 1 \tag{8.29}$$

where:

$$A = 1 + \rho_u - \rho_\ell . \tag{8.30}$$

Thus, as $A \to 0$, $G_{ru} \to \infty$, while $\delta_{\frac{1}{2}} \to 0$. The significance of these limits can be conveniently demonstrated in terms of the gain-bandwidth product, which has the value

$$2\delta_{\frac{1}{2}} \sqrt{\overline{G}_{ru}} = 2\beta \sqrt{\left(\frac{\overline{\omega}_u}{\overline{\omega}_r}\right) xy\rho_u \left[\frac{(A-2) + \sqrt{4 - 4A + 2A^2}}{A^2}\right]} \qquad (8.31)$$

It appears from (8.31) that ρ_u should be large, but ρ_u is not independent of β. By rewriting ρ_u as follows

$$\rho_u = \frac{\overline{\omega}_r \overline{\omega}_u \gamma_p^2}{\beta_r \beta_u C_r C_u} \qquad (8.32)$$

and using $\beta_r = \beta_u = \beta$, then

$$\beta \sqrt{\rho_u} = \sqrt{\overline{\omega}_r \overline{\omega}_u} \left(\frac{\gamma_p}{\sqrt{C_r C_u}}\right) \qquad (8.33)$$

which is a constant for fixed frequencies. Therefore, (8.31) is not proportional to $\sqrt{\rho_u}$ as it appears. Using (8.33) in (8.31), the latter becomes

$$2\delta_{\frac{1}{2}} \sqrt{\overline{G}_{ru}} = 2\gamma_p \omega_u \sqrt{\frac{xy}{C_r C_u} \left[\frac{A-2 + \sqrt{4-4A + 2A^2}}{A^2}\right]} \qquad (8.34)$$

The expression in square brackets in (8.31) has maximum value $\frac{1}{2}$ which occurs for $A = 2$. For this value, a maximally flat bandpass results with a bandwidth $\sqrt{2\beta}$. The same result was noted for the pure upper-sideband converter ($\rho_\ell = 0$), in Table 3.1.

When the lower sideband is introduced, so ρ_ℓ increases from zero, the optimum bandwidth associated with $A = 2$ can be retained if ρ_u also increases. Therefore, one provision offered by introducing the lower sideband is the means of trading gain for bandwidth, while retaining an optimum gain-bandwidth product. The latter quantity can be found by setting

$$\rho_u = 1 + \rho_\ell$$

which makes A = 2. Then by (8.34)

$$2\delta_{\frac{1}{2}} \sqrt{\bar{G}_{ru}} = \omega_u \gamma_p \sqrt{\frac{2xy}{C_r C_u}} \tag{8.35}$$

which is optimum for a given pair of input and output efficiency factors x and y.

Comparing (8.34) with (8.16) shows that optimum gain-bandwidth and the (finite) optimum gain occur simultaneously only if $\rho_\ell = 0$. When (8.16) is satisfied

$$A = 2x(1-\rho_\ell) \leq 2 \tag{8.36}$$

which approaches zero for large gains. However, as $A \to 0$, the gain-bandwidth product in (8.34) approaches

$$2\delta_{\frac{1}{2}} \sqrt{\bar{G}_{ru}} = \omega_u \gamma_p \sqrt{\frac{xy}{C_r C_u}} \tag{8.37}$$

which is 30 percent less than the optimum value in (8.35). The complete dependence of gain-bandwidth on A is shown in Fig. 8.4. Also shown in this figure is a plot, vs. ρ_ℓ, of the gain relative to that at optimum gain-bandwidth. Since the minimum value of this curve corresponds to $A = 1 + \rho_u$, this minimum value will be greater than zero db if $\rho_u < 1$. The optimum gain-bandwidth product could not be realized in this case.

Of the two optimum gain cases cited in (8.16) and (8.18), the latter still seems preferable. Both yield slightly less than optimum gain-bandwidth product, but (8.18) yields infinite gain with more flexible conditions.

8.2 Noise Figure for Conversion From ω_r to ω_u

The up-conversion noise figure in the presence of ω_ℓ can be calculated and optimized directly from (3.27). However, two basic cases should be distinguished. The first is with the load matched, which has been shown to yield only finite gains in practical application. The second is with infinite gain, where both the source and load experience negative reflected conductance. In these two cases, (3.27) becomes

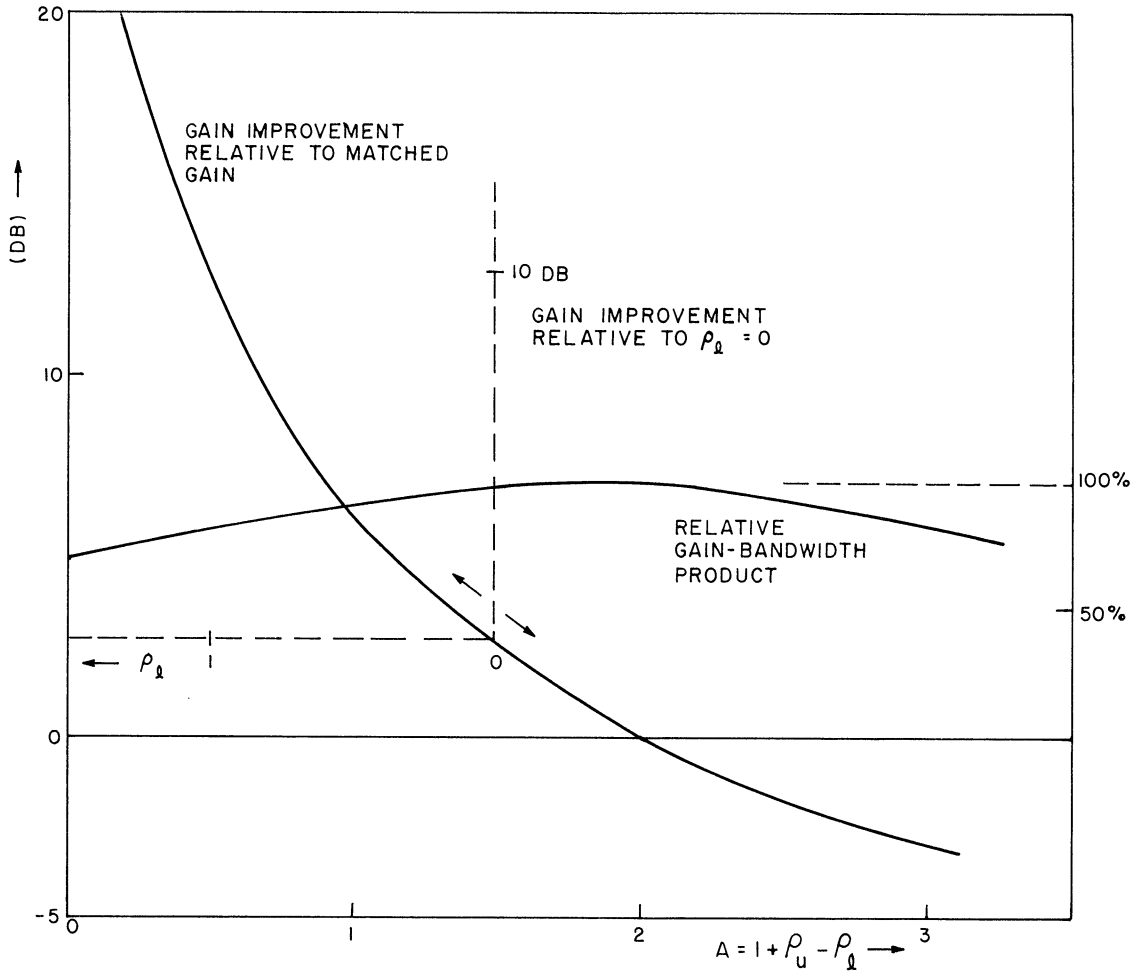

Fig. 8.4. Gain improvement and corresponding gain-bandwidth product for upper-sideband conversion in the presence of the lower sideband.

$$F_{ru} = 1 + \frac{g_{dr}\, T_d}{g_S\, T_o} + \frac{\overline{G}_{\ell u}\, T_\ell}{\overline{G}_{ru}\, T_o} + \begin{cases} \dfrac{\overline{G}_{uu}\, T_d\, g_{du}}{\overline{G}_{ru}\, T_o\, g_L} & \text{with output matched} \\ \dfrac{\overline{G}_{uu}\, T_u\, g_u}{\overline{G}_{ru}\, T_o\, g_L} & \text{with infinite gain} \end{cases} \tag{8.38}$$

The evaluation of F_{ru} will be simplified by employing the efficiency factors

$$x = \frac{g_S}{g_r} \qquad y = \frac{g_L}{g_u} \qquad z = \frac{\tilde{g}_\ell}{g_\ell} \tag{8.39}$$

and the noise temperature ratios

$$t = \frac{T_L}{T_d} \qquad s = \frac{\tilde{T}_\ell}{T_d} \tag{8.40}$$

Here $\tilde{g}_\ell$ denotes an external load at ω_ℓ with noise temperature $\tilde{T}_\ell$. Since $\tilde{g}_\ell$ is a dummy load, it will be adjusted to optimize F_{ru}.

The various factors in (8.38) can be expressed in terms of the normalized quantities in (8.39) and (8.40). For example, the gain ratios can be found by calculations similar to those leading to (8.12). This yields

$$\frac{G_{\ell u}}{G_{ru}} = \frac{\rho_\ell \overline{\omega}_r}{x\,\overline{\omega}_\ell} \tag{8.41a}$$

$$\frac{\overline{G}_{uu}}{\overline{G}_{ru}} = \frac{y\,\overline{\omega}_r(1-\rho_o)^2}{x\,\rho_u\,\overline{\omega}_u} \tag{8.41b}$$

Perhaps it should be noted that z does not appear in (8.41a) because, at a dummy terminal like ω_ℓ, g_ℓ is considered to be the source conductance, and not $\tilde{g}_\ell$. The noise temperature ratios are given by

$$\frac{T_\ell}{T_d} = \frac{g_{d\ell}\,T_d + \tilde{g}_\ell\,\tilde{T}_\ell}{(g_{d\ell} + g_L)\,T_d} = 1 + z(s-1) \tag{8.42a}$$

$$\frac{T_u}{T_d} = \frac{g_{du}\,T_d + g_L\,T_L}{(g_{du} + g_L)\,T_d} = 1 + y(t-1) \tag{8.42b}$$

which can be used to evaluate the bracketed terms in (8.38). For the two cases, it follows that

$$\frac{T_d\,g_{du}}{T_o g_L} = \frac{T_d}{T_o}\left(\frac{1-y}{y}\right) \qquad \text{matched output case} \tag{8.43a}$$

$$\frac{T_u g_u}{T_o g_L} = \frac{T_d}{T_o}\left(\frac{1-y}{y} + t\right) \qquad \text{infinite gain case} \tag{8.43b}$$

Therefore, the same form of (8.38) is appropriate for the infinite gain case and for the

matched output case. Setting t = 0, one obtains the second from the first. The following single expression for F_{ru} now results.

$$F_{ru} = 1 + \frac{T_d}{T_o}\left\{\frac{1-x}{x} + \frac{\omega_r \rho_\ell [1+z(s-1)]}{x\,\omega_\ell} + \frac{\overline{\omega}_r (1-\rho_\ell)^2 [1+y(t-1)]}{x\rho_u \overline{\omega}_u}\right\} \tag{8.44}$$

This expression will now be minimized subject to the various gain conditions previously cited.

8.2.1 Noise Figure for Infinite Gain. For the infinite gain case, the appropriate condition is

$$1 + \rho_u - \rho_\ell = 0 \tag{8.45}$$

which can be expressed in terms of the same fundamental quantities that appear in (8.44). With the aid of the identity in (8.14a), together with (3.29), ρ_u and ρ_ℓ are given by

$$\rho_u = \frac{\overline{\omega}_r (1-x)(1-y)}{\overline{\omega}_u R_r} \tag{8.46a}$$

$$\rho_\ell = \frac{\overline{\omega}_r (1-x)(1-z)}{\overline{\omega}_\ell R_r} \tag{8.46b}$$

The quantity R_r in (8.46) appeared previously in (4.32b). It has the value

$$R_r = \left(\frac{\overline{\omega}_r}{\omega_d}\right)^2 \left(\frac{C}{\gamma_p}\right)^2 \tag{8.47}$$

The high gain condition in (8.45) now becomes

$$\frac{\overline{\omega}_r}{\omega_\ell} = \frac{R_r}{(1-x)(1-z)} + \left(\frac{\overline{\omega}_\ell}{\overline{\omega}_u}\right)\left(\frac{1-y}{1-z}\right) \tag{8.48}$$

but $\omega_u = \omega_\ell + 2\omega_r$. Therefore, letting $\overline{\omega}_r / \overline{\omega}_\ell = a$, (8.48) becomes

$$a = \frac{R_r}{(1-x)(1-z)} + \left(\frac{1-y}{1-z}\right)\left(\frac{a}{1+2a}\right) \tag{8.49}$$

Before attempting to solve this equation exactly it should be noted that ω_ℓ and ω_u must be much larger than ω_r if small noise figures are to be obtained. Also, if the noise figures are not small, their optimization will not be of critical interest. Therefore, asserting that (a) is small, the following approximate solution for (8. 49) is obtained

$$a \approx \frac{R_r}{(1-x)(y-z)}, \qquad \text{if } a << 1 \tag{8.50}$$

Since the denominator of (8. 50) must be positive and cannot exceed one, two conditions are necessary for (8. 50) to be valid, namely $R_r << 1$ and $z < y$. However only the first is an approximation in this case, since $z < y$ is necessary for $\rho_\ell > 1$.

By (8. 46b), an alternate form for (8. 50) is

$$a = \frac{\rho_\ell R_r}{(1-x)(1-z)}$$

and therefore

$$\rho_\ell \approx \frac{1 - z}{y - z} \tag{8.51a}$$

$$\rho_u = \frac{\omega_\ell}{\omega_u}\frac{(1-y)}{(1-z)} \approx \frac{1-y}{y-z} \tag{8.51b}$$

The importance of (8. 50) and (8. 51) is that ρ_ℓ does not depend explicitly on x when (a) is small. Therefore the noise figure in (8. 44) can be written

$$F_{ru} = 1 + \frac{T_d}{T_o}\left\{\frac{1-x}{x} + \frac{\alpha}{x(1-x)}\right\} \tag{8.52a}$$

where

$$\alpha \approx R_r\left\{\frac{[1 + y(t-1)](1-y)}{(y-z)^2} + \frac{[1 + z(s-1)](1-z)}{(y-z)^2}\right\} \tag{8.52b}$$

Since (8. 52a) has the form of (A-5), its optimum value will be given by (A-7a) whenever ρ_ℓ, and hence α, are independent of x.

It is evident from Fig. A-1, that α should be as small as possible. Considering first the factor

$$\frac{1 + z\,(s-1)}{1-z}$$

its minimum value occurs for $z = 0$, which means $g_\ell = 0$. Hence any excess loading at ω_ℓ is harmful. When ρ_ℓ is given by (8.51), as it will be in most cases of interest, $z = 0$ also minimizes this factor. Therefore, the minimum value of the second term in (8.52b) is $(1/y)^2$ which occurs for $z = 0$. In this case,

$$\alpha = R_r \left[\frac{1+y(t-1)}{1-y} + \frac{1}{y^2} \right] \tag{8.53}$$

The latter quantity will be minimum with respect to y if

$$\frac{y^3}{(1-y)^2} = \frac{2}{t} \tag{8.54}$$

The solution of this equation is shown in Fig. 8.5. Also shown is the corresponding value of α/R_r. These values can be used in (A-7b) to find the effective noise temperature of the converter.

$$\frac{T_{ru}}{T_d} = 2\alpha\left[1 + \sqrt{1 + \frac{1}{\alpha}}\right] \tag{8.55}$$

However, it is convenient to relate this optimum noise temperature to the frequency ratio

$$\frac{\overline{\omega}_u}{\overline{\omega}_r} = 2 + \frac{1}{a} \tag{8.56}$$

Or, by (8.50)

$$R_r \frac{\overline{\omega}_u}{\overline{\omega}_r} = \left[2R_r + y(1-x)\right] \tag{8.57}$$

Eliminating α and R_r between (8.57), (8.55), and Fig. 8.5 yields the minimum noise temperature and optimum frequency ratio curves in Fig. 8.6. For $\overline{\omega}_u/\overline{\omega}_r > 2$, the accuracy of the approximation in Fig. 8.6 increases rapidly.

As an illustration in the use of these curves, when ω_u/ω_r is large

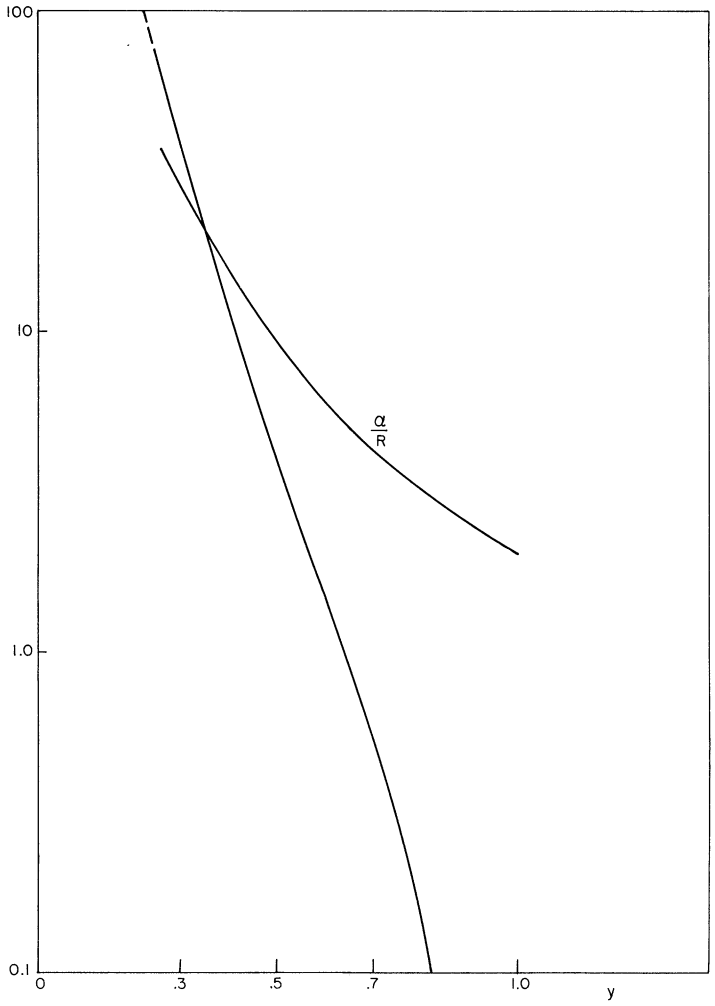

Fig. 8.5. Solutions of (8.54).

$$\left(\frac{T_{ru}}{T_d}\right)_{opt} \approx 2\sqrt{\alpha} \tag{8.58}$$

When t = 1, Fig. 8.5 yields y = 0.67 and $\alpha = 5R_r$, so

$$\left(\frac{T_{ru}}{T_d}\right)_{opt} \approx 2\sqrt{5R_r} \tag{8.59}$$

This result can be compared with the corresponding lower sideband converter. For the same output efficiency factor, z = 0.67, (5.32b) yields

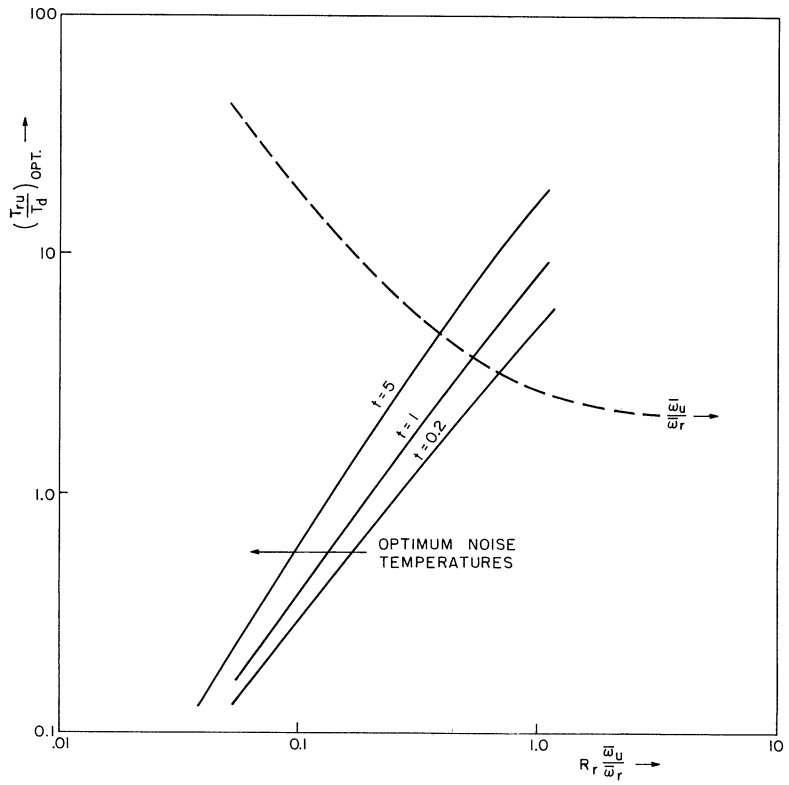

Fig. 8.6. Optimum noise temperatures corresponding to infinite conversion gain between ω_r and ω_u.

$$\left(\frac{T_{r\ell}}{T_u}\right)_{opt} = 2\sqrt{3R_r} \tag{8.60}$$

which is some 20 percent less for equal values of R_r.

On the other hand, comparing with the pure upper-sideband converter, Fig. 4.5 shows

$$\left.\begin{aligned} \frac{T_{ru}}{T_d} &= .34 \\ G_{ru} &= 6 \end{aligned}\right\} \quad \text{for } R_r = 0.01,\ \frac{\bar{\omega}_u}{\bar{\omega}_r} = 10$$

For the same R_r, (8.59) yields

$$\frac{T_{ru}}{T_d} = 0.43$$

but here G_{ru} is infinite. So this particular technique for adding the lower sideband greatly enhances G_{ru} with only a small increase in noise temperature.

There is another interesting difference that can be noted between the pure lower-sideband converter and the present case. The noise figure of the former decreases uniformly with the output efficiency factor, while the latter calls for a particular output efficiency according to Fig. 8.5. In practice, however, this distinction would probably disappear. In discussion conversion between ω_r and ω_ℓ in Chapter V, no effect from ω_u was assumed but with a real varactor, pure lower-sideband conversion is impossible. Considering only the varactor loss g_{du}, an increase in noise temperature would occur that would require a specific choice of output efficiency for minimization. Of course, it may be found that reactive detuning at ω_u reduces the effect of g_{ru}, but in any case ω_u will make some contribution to $T_{r\ell}$ such that the final comparison of lower and upper sideband conversion will yield nearly identical noise temperatures. Therefore, the most outstanding difference between these two cases is not their noise temperature, but rather their ease of realization. A precise adjustment at ω_ℓ is required to yield infinite gain from ω_r to ω_u, while that from ω_r to ω_ℓ is relatively insensitive to the suppression of ω_u.

8.2.2 The Noise Figure, Subject to (8.16). The noise figure relation in (8.44) can be optimized only when some constraint relates ρ_u and ρ_ℓ. In (8.16b), a constraint is given yielding optimum gain with a matched output, namely

$$\rho_u = (2x - 1)(1 - \rho_\ell)$$

In this case, it has already been noted that the noise figure is given by (8.44) if $t = 0$.

Therefore,

$$F_{ru} = 1 + \frac{T_d}{T_o}\left\{\frac{1-x}{x} + \frac{\overline{\omega}_r \rho_\ell [1+z(s-1)]}{\overline{\omega}_\ell x} + \frac{\overline{\omega}_r}{x\rho_u \omega_u}\right\} \tag{8.61}$$

But

$$\frac{\overline{\omega}_r}{x\rho_u \overline{\omega}_u} = \frac{R_r}{x(1-x)} \tag{8.62a}$$

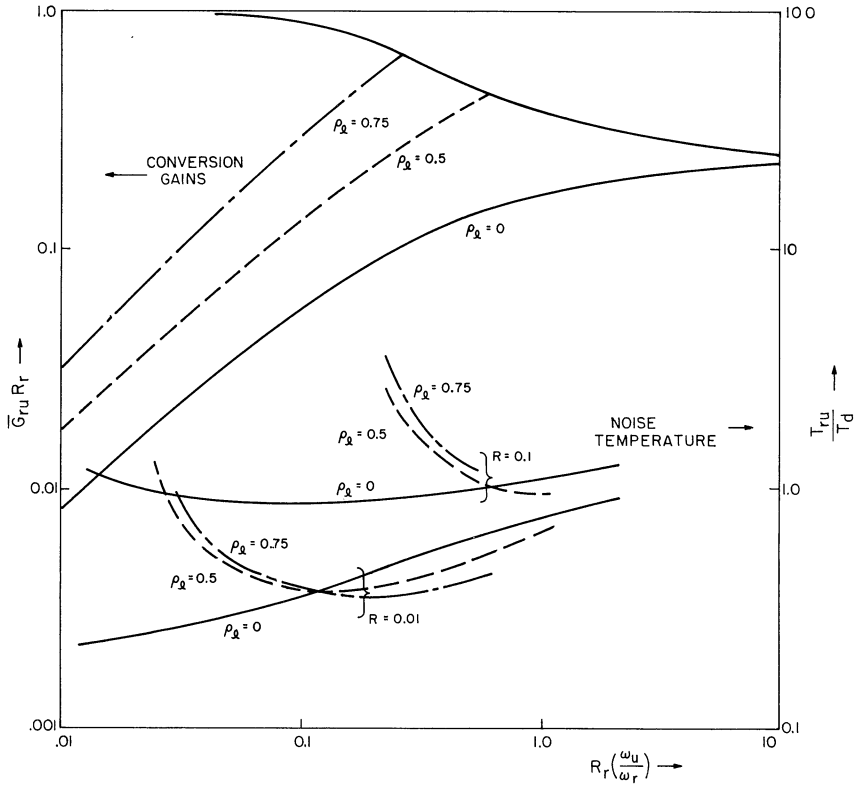

Fig. 8.7. Effects of the lower sideband on T_{ru} and G_{ru} in the matched output case.

and

$$\frac{\bar{\omega}_r \rho_\ell}{\bar{\omega}_\ell x} = \left(\frac{\bar{\omega}_r}{\bar{\omega}_u}\right)\left(\frac{\rho_\ell}{x}\right)\left(\frac{1}{1-2\frac{\bar{\omega}_u}{\bar{\omega}_r}}\right) \tag{8.62b}$$

which facilitates the evaluation of (8.61). Curves of T_{ru} are shown in Fig. 8.7. These were obtained by eliminating x between (8.61) and (8.62). An interesting aspect of these curves is that x increases with ρ_ℓ for fixed ω_r, ω_u, and ω'_d. In (8.61) this causes the first term to decrease with ρ_ℓ and the second two terms to increase with ρ_ℓ. As a result, improved noise figures occur over certain ranges of the abcissa. For example, if R = 0.01 and $\omega_u/\omega_r = 16$, $T_{ru} = .66$ for $\rho_\ell = 0$ but $T_{ru} = .57$ for $\rho_\ell = 0.5$. Yet, in the latter case, G_{ru} is some three times larger.

The noise temperature curves have been superimposed in the gain curves to show their correspondence. Because a maximum value of $(\omega_u/\omega_r)\, R_r$ exists whenever

$\rho_\ell \neq 0$, the range of R_r is limited. For $\rho_\ell = 0.5$, $R_r < 0.2$ is necessary. However, for some range below this value of R, an optimum noise temperature exists, that depends on ρ_ℓ.

8.3 Down-Conversion from ω_u to ω_r

In an earlier discussion, in Section 4.3, down-conversion from ω_u to ω_r was shown to be impractical, but the lower sideband was absent in that treatment. The lower sideband will now be introduced and it will be shown to greatly enhance down-conversion gain. The first step is to calculate G_{ur} from (8.1). With the aid of (3.15b), one obtains

$$G_{ur} = \frac{\omega_r}{\omega_u}\left[\frac{4\, g_S g_L\, \omega_r \omega_u\, \gamma_p{}^2}{Y_r Y_u + \omega_r\, \gamma_p{}^2 (\omega_u - \omega_\ell\, Y_u/Y_\ell{}^*)}\right] \tag{8.63}$$

By comparison with (8.8), it is interesting to observe that

$$G_{ur} = \left(\frac{\omega_r}{\omega_u}\right)^2 G_{ru} \tag{8.64}$$

The proportionality just noted means that both up- and down-conversion have the same bandwidth [see (8.27)]. Consequently, the down-conversion gain-bandwidth product is ω_r/ω_u smaller than that for up-conversion. Being less than one, this ratio is one of the disadvantages plagueing the down-conversion mode.

The result in (8.64) applies even with ω_ℓ shorted, and it was obtained for this case earlier. However, a point of interest arises because the derivation in Section 4.3 made use of a symmetry that does not exist when ω_ℓ is present. Without ω_ℓ, the basic equation for relating ω_r and ω_u is (4.1), which is symmetrical in these variables, but the more general expression is (8.1), which is not generally symmetrical in ω_r and ω_u. Therefore, though conversion gain obeys the scaling relationship in (8.64), other properties of up- and down-conversion may be found to differ by more than a simple scaling.

Using the notation of (8.11), (8.63) can be written

$$G_{ur} = \frac{\omega_r}{\omega_u}\left[\frac{4\, xy\rho_u}{(1 + \rho_u - \rho_\ell)^2}\right] \tag{8.65a}$$

where again

$$x = \frac{\tilde{g}_r}{g_r}, \quad y = \frac{\tilde{g}_u}{g_u}, \quad \text{and} \quad z = \frac{\tilde{g}_\ell}{g_\ell} \tag{8.65b}$$

However, the source and load are now interchanged (relative to their positions for up conversion) so it follows that $\tilde{g}_r = g_L$ and $\tilde{g}_u = g_S$, while $\tilde{g}_\ell$ is a dummy load.

As anticipated, G_{ur} is no longer limited to the frequency ratio ω_r/ω_u, but can be arbitrarily large if $\rho_\ell \to 1 + \rho_u$. Therefore, by introducing the lower sideband, one limitation of simple down-conversion is overcome, namely that of gain being less than unity. However, high gain again occurs at the expense of negative reflected conductance at each terminal, so no improvement in gain-bandwidth product results.

Another problem that previously characterized down-conversion was a high noise figure, so let us now consider the influence of ω_ℓ on the down-conversion noise figure. It will be sufficient to consider the noise figure associated with infinite gain, which (using the form of 2.48) can be expressed as follows:

$$F_{ur} = 1 + \frac{g_{du} T_d}{g_S T_o} + \frac{G_{\ell r} T_\ell}{G_{ur} T_o} + \frac{G_{rr} T_r g_r}{G_{ur} T_o g_L} \tag{8.66}$$

Here T_r is the effective noise temperature of the ω_r terminals, and by (8.40) it follows that

$$\begin{aligned} T_r &= [1 + x(t-1)]\ T_d \\ T_\ell &= [1 + z(s-1)]\ T_d \end{aligned} \tag{8.67}$$

Again using (8.1) it can be shown that

$$G_{\ell r} = 4 \frac{\omega_r}{\omega_\ell} \left[\frac{x \rho_\ell}{(1 + \rho_u - \rho_\ell)^2} \right] \tag{8.68a}$$

$$G_{rr} = \frac{4x^2}{(1 + \rho_u - \rho_\ell)^2} \tag{8.68b}$$

Therefore (8.66) becomes

$$F_{ur} = 1 + \frac{T_d}{T_o} \left[\frac{1-y}{y} + \frac{\omega_u \rho_\ell T_{\ell 1}}{\omega_\ell \rho_u T_d y} + \frac{\omega_u T_r}{\omega_r T_d} \left(\frac{1}{y \rho_u} \right) \right] \tag{8.69}$$

Two important aspects of (8.69) are the frequency ratios ω_u/ω_ℓ and ω_u/ω_r, which both exceed one. Because of these ratios, it will be shown that F_{ur} is invariably larger than F_{ru}.

Further examination of F_{ur} is aided by the following identities, which are obtained from (8.46)

$$\frac{\rho_\ell}{\rho_u} = \left(\frac{1-z}{1-y}\right) \frac{\omega_u}{\omega_\ell} \tag{8.70a}$$

$$\frac{\omega_u}{\rho_u \omega_r} = \frac{R_u}{(1-x)(1-y)} \tag{8.70b}$$

The quantity R_u is the same as previously defined in (4.38), namely

$$R_u = \left(\frac{\omega_u}{\omega_r}\right)^2 R_r = \left(\frac{\omega_u}{\omega'_d}\right)^2 \tag{8.70c}$$

R_u is useful for normalizing down-conversion noise figures because it only depends on: (1) input frequency, (2) the varactor, and (3) the pump level.

Using the identities in (8.70), F_{ur} in (8.69) now becomes

$$F_{ur} = 1 + \frac{T_d}{T_o}\left[\frac{1-y}{y} + \frac{\alpha}{y(1-y)}\right] \tag{8.71a}$$

where

$$\alpha = \left(\frac{\omega_u}{\omega_\ell}\right)^2 (1 - z)\,[1 + z(s-1)] + \frac{R_u}{1 - x}\,[1 + x(t-1)] \tag{8.71b}$$

As written, (8.71a) has the form treated in Appendix A (with the variable y substituted for x), but there α is assumed to be independent of y. Now, α depends on y, because z, y, and ω_u/ω_r are related by the high gain constraint $1 + \rho_u - \rho_\ell \approx 0$, which [by (8.46)] can be written in the following form:

$$(1 - z)\,\frac{\omega_u}{\omega_\ell} = \left(\frac{\omega_r}{\omega_u}\right)\left(\frac{R_u}{1 - x}\right) + (1 - y) \tag{8.72}$$

Therefore, the optimization of (8.71a) will differ from that of other noise figures, because the variation of α with y must be accounted for.

It will be expedient to assume that R_u, x, and t are specified, so the second

term in (8.71b) will be constant, that is

$$\frac{R_u}{1-x}\,[1 + x(t-1)] = N \tag{8.73}$$

First consideration will then be given to the case where all noise sources are at room temperature. Using (8.72) in (8.71b), the latter becomes:

s=t=1

$$\alpha = \frac{\omega_u}{\omega_\ell}\,(1-y) + \frac{R_u}{1-x}\left(\frac{\omega_p}{\omega_\ell}\right) \tag{8.74a}$$

and

$$F_{ur} = 1 + \frac{T_d}{T_o}\left[\frac{2\omega_p}{y\omega_\ell} - 1 + \frac{\left(\frac{R_u}{1-x}\right)\left(\frac{\omega_p}{\omega_\ell}\right)}{y(1-y)}\right] \tag{8.74b}$$

which is minimum for

$$y_{opt} = 1 - \frac{1}{1 + \sqrt{1 + \frac{2(1-x)}{R_u}}} \tag{8.75}$$

It is interesting to note that y_{opt} is independent of frequency ratio in this case, and therefore the optimum F_{ur} decreases with ω_p/ω_ℓ. Hence, for a given ω_u, the lowest noise figures will result if $\omega_r/\omega_u << 1$. In this case, the effective noise temperature depends on $R_u/(1-x)$ as shown in Fig. 8.8.

An interesting difference now arises over the previous noise figures considered, in that idler cooling can reduce the noise figure. To demonstrate, consider an extreme case where the external load at ω_ℓ is cooled to absolute zero (i.e., s = 0), and then

s=0, t=1

$$\alpha = (a + 1 - y)^2 + N; \quad a = \frac{\omega_r}{\omega_u}\,\frac{R_r}{1-x} \tag{8.76a}$$

from which

$$F_{ur} = 1 + \frac{T_d}{T_o}\left[\frac{2}{y}\,(1+a) - 2 + \frac{N + a^2}{y(1-y)}\right] \tag{8.76b}$$

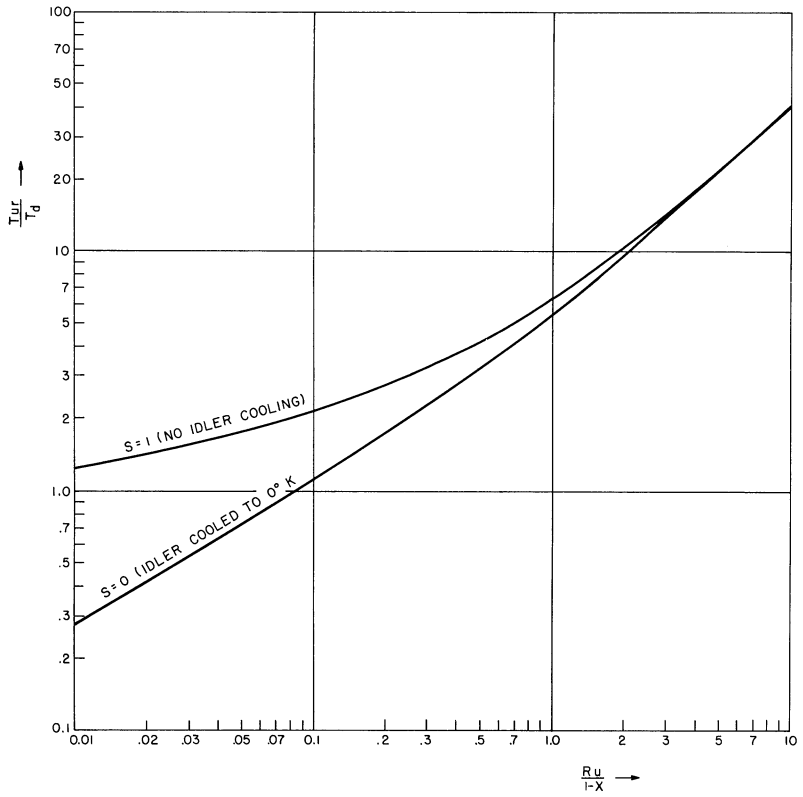

Fig. 8.8. Optimum noise temperatures for down-conversion from ω_u to ω_r, with and without idler load cooling (at ω_ℓ), and with a room temperature load. The basic requirement for these optimum noise temperatures is $\omega_r << \omega_u$.

The latter is minimum for

$$y_{opt} = 1 - \frac{1}{1 + \sqrt{1 + \frac{2(1+a)}{N + a^2}}} \tag{8.77}$$

Again the optimum noise figure increases monotonically with ω_r/ω_u, through the factor a.

If $a << 1$, then

s=0:

$$(F_{ur})_{opt} = 1 + \frac{T_d}{T_o}\left[\frac{2}{y_{opt}} - 2 + \frac{N}{y_{opt}(1 - y_{opt})}\right] \tag{8.78}$$

which is plotted in Fig. 8.8.

For other values of s and t, curves similar to those in Fig. 8.8 can be derived. In general, raising t moves all curves to the right, while s influences the lower portions of each curve.

Lower sideband cooling can improve the down-conversion noise figure because lower sideband noise is less amplified than output noise (at ω_r). The ratio of these two contributions is $\rho_\ell \omega_r/\omega_u$, which is less than one if ω_r/ω_u is small. Therefore, the optimization obtained here requires relatively heavy loading at ω_ℓ and ω_u, but light loading at the output frequency ω_r. Cooling the load at ω_ℓ will then reduce the noise figure. In practice, the input and idler frequency loadings are adjusted for high gain, while the output is loosely coupled to keep the noise figure down. This procedure would require that the output be followed by a power amplifier with high input impedance.

It is interesting to compare the optimum down-conversion noise figures with and without ω_ℓ, the latter being taken from Fig. 4.5. For the case where $R_u = 0.1$ and $\omega_u/\omega_r = 10$ are specified, the results are shown in the following table:

ω_ℓ shorted (Fig. 4.5)	ω_ℓ unshorted; x = 0.1	
	g_ℓ at room temp.	g_ℓ cooled to 0°K
$T_{ur} = 1.1$	$T_{ur} = 2.2$	$T_{ur} = 1.2$

The noise figures that accompany the introduction of ω_ℓ are somewhat larger than those without ω_ℓ, but it should be remembered that the former are accompanied by huge gains while the gain is less than one with ω_ℓ absent. In addition, cooling the ω_ℓ termination can reduce the difference between these two noise figures to something quite negligible.

Only one other technique has been considered in which infinite down-conversion gains are possible. This would be in the pure lower-sideband converter where $\omega_r > \omega_\ell$. The noise figure in this case is given by (5.27a) which has the optimum value in (5.32a). However, the latter optimum calls for the particular ω_r/ω_ℓ ratio in (5.29a). This ratio exceeds one only if $R_r/(1-z) > 0.2$. Therefore, the optimization leading to (5.32a) is not too practical for down conversion, since the latter often involves specified input and output frequencies. In this case, a definite minimum noise figure exists, which is

$$F_{r\ell} \geq 1 + \frac{T_d\, \omega_r}{T_o\, \omega_\ell} \tag{8.79}$$

Therefore, if the input frequency (ω_r) to output frequency (ω_ℓ) ratio is 10 to 1, as in the previous illustration, F_r will equal 11. It can be noted then that double sideband operation offers significant improvements in the down-conversion mode.

It is an interesting aspect of this down-conversion analysis that high ω_u/ω_r ratios, are required, which means that ω_u, ω_ℓ, and ω_p will become very closely spaced. Consequently, all three frequencies may fall within the same resonance. This would be a practical mode of operation, since it has been shown that ω_u and ω_ℓ require approximately the same loading when minimum noise figures are obtained. Further discussion of dependent sideband loading will be found in Chapter IX.

8.4 Conclusions

It has been shown that double-sideband reactive mixers have some advantages over single-sideband reactive mixers, two forms of up-conversion gain increase are possible, but both are accompanied by negative reflected conductance at the input. One form offers infinite gain and negative output conductance, while the other offers finite gains with a matched output. In the second case, an improvement in noise figure is possible, but in the first case a slight noise figure degradation occurs. In both cases, the gain-bandwidth product may reduce by about 30 percent with the gain increase, but it is possible to increase the gain by about 6 db without reducing gain-bandwidth product. One general advantage that can be cited is the opportunity to control gain between ω_r and ω_u by varying the loading at a dummy frequency ω_ℓ.

A significant improvement in down-conversion noise figure has been noted. Noise figures of slightly over 3 db are possible, with essentially infinite down-conversion gain, and for a wide selection of operating frequencies.

CHAPTER IX

DOUBLE-SIDEBAND MIXING WITH DEPENDENT SIDEBAND LOADING

In the configurations considered in previous chapters, up-conversion was found to be the most useful reactive mixer mode. An optimum sideband-to-signal frequency ratio was found to characterize this mode, but it varied according to varactor loss. For low signal frequencies or high varactor quality, the optimum frequency ratio is very large, with the result that the pump and sideband frequencies become very closely spaced. But an alternate limitation on frequency ratio then arises due to the difficulty in filtering. As an extreme case, the sidebands may fall within the pump resonance as illustrated in Fig. 9.1. When this occurs, Y_ℓ and Y_u are no longer independent quantities, and the character of double-sideband conversion changes radically.

At first glance, the configuration in Fig. 9.1 appears useless since sideband power would tend to be absorbed in pump internal conductance. However, as shown in Fig. 9.2a, the sidebands and the reflected pump signal can be separated from the pump generator with the aid of a circulator. The total reflected energy that emerges from the circulator thus constitutes a modulated signal. The useful properties of this signal will now be investigated.

For frequencies near ω_p, Fig. 9.2a is equivalent to the tuned circuit in Fig. 9.2b, which will be assumed resonant at ω_p for the case of basic interest. Then ω_ℓ and ω_u will be equally detuned so that

$$Y_u = Y_\ell^* \tag{9.1a}$$

$$\approx g_p \left(1 + j \frac{\omega_r}{\beta_p}\right) \tag{9.1b}$$

where

$$g_p = \tilde{g}_p + g_{dp} .$$

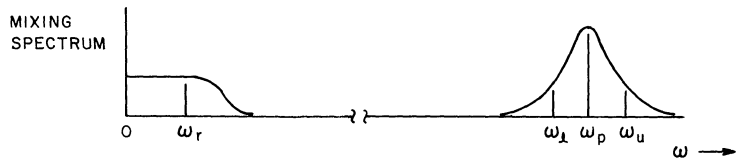

Fig. 9.1. A limiting case of double-sideband mixing that occurs for $\omega_r/\omega_p << 1$.

It is assumed in writing (9.1) that $\tilde{g}_p$ is the characteristic admittance of the circulator, so the varactor will see $\tilde{g}_p$ at the circulator terminals.

The first step in evaluating this special case will be to determine the type of modulation produced by the ω_ℓ and ω_u sidebands. In general, the total modulated waveform can be written in the form

$$V_m(t) = \text{Re}\left\{V_p e^{j\omega_p t}\left[1 + \frac{V_u}{V_p} e^{j\omega_r t} + \frac{V_\ell}{V_p} e^{-j\omega_r t}\right]\right\} \tag{9.2}$$

where the sideband voltages can now be found from (8.1) and (9.1). By direct calculation, the latter yields

$$V_u = \frac{-j\omega_u \gamma_p V_r}{Y_u} \tag{9.3a}$$

$$V_\ell = \frac{-j\omega_\ell \gamma_p V_r^*}{Y_u} \tag{9.3b}$$

But, recalling from (2.24b) that $\gamma_p = a_2 V_p/2$, the sideband voltages can be alternately expressed in the form

$$\frac{V_u}{V_p} = -j\omega_u M \qquad \frac{V_\ell}{V_p} = -j\omega_\ell M^* \tag{9.4a}$$

where

$$M = \frac{a_2 V_r}{2Y_u} = |M| e^{j\phi_M} . \tag{9.4b}$$

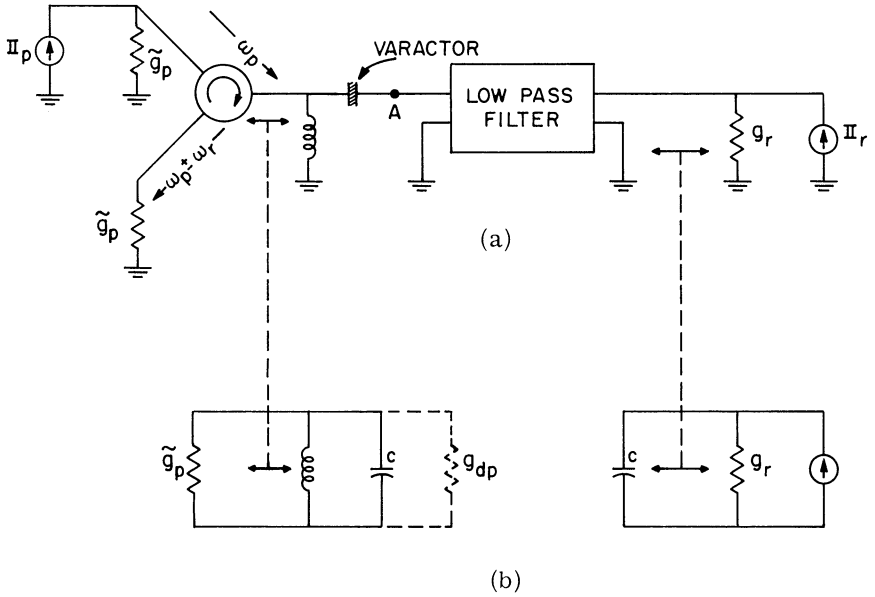

Fig. 9.2. (a) A basic technique for isolating the sidebands from the pump in Fig. 9.1; (b) the high and low frequency equivalent circuits of (a).

Substituting (9.4) in (9.2) now yields

$$V_m(t) = |V_p| \left[(1 + 2\omega_r|M|\sin\theta)^2 + (2\omega_p|M|\cos\theta)^2\right] \cos(\omega_p t + \phi + \phi_p) \quad (9.5a)$$

where $$\theta = \omega_r t + \theta_M \quad (9.5b)$$

$$\phi = -\tan^{-1}\left[\frac{2\omega_p|M|\cos\theta}{1 + 2\omega_r|M|\sin\theta}\right] \quad (9.5c)$$

$$V_p = |V_p| e^{j\phi_p} . \quad (9.5d)$$

Since M is proportional to the signal voltage, a small signal assumption can be used to make $|M|$ arbitrarily small. Also, $\omega_p >> \omega_r$ will be assumed, and together these assumptions render the fundamental nature of (9.5a) and (9.5c) observable by reducing them to the following simplified expressions:

$$\phi \approx -2\omega_p|M|\cos(\omega_r t + \phi_M) \quad (9.6a)$$

$$V_m(t) \approx |V_p|\cos[\omega_p t + \phi_p - 2\omega_p|M|\cos(\omega_r t + \phi_M)] . \quad (9.6b)$$

Three observations can now be made:

(1) The first-order effect of the signal at ω_r is to phase or angle modulate the pump voltage.

(2) The angular deviation of this modulation is

$$2\omega_p|M| = 2\omega_p\left|\frac{a_2 V_r}{2Y_u}\right| \tag{9.7a}$$

$$= \frac{\omega_p|\gamma_r|}{\beta_p C_p}\left[1 + 4\frac{\omega_r^2}{\beta_p^2}\right]^{-1} \tag{9.7b}$$

where $2\gamma_r = a_2 V_r$ is the amplitude of equivalent time varying capacity at ω_r. [See (2.30b).]

(3) The maximum angular deviation occurs as ω_r approaches zero.

Returning to the expressions for the sideband voltages in (9.3), the origin of phase modulation can be attributed to the common factor j. However, the fact that angular deviation is proportional to the signal voltage through the term γ_r suggests a physical explanation for this effect. The signal voltage, however small, will vary the capacity of the nonlinear element; and if this element is part of a resonant circuit tuned to ω_p, these capacity variations will phase modulate the pump voltage. It would seem perhaps that this effect should be masked by nonlinear effects from the larger pump signal, but the analysis in Chapter II refutes this notion. As stated in Section 2.4, first-order mixing can be alternately regarded as pump acting on signal, or signal acting on pump. For double-sideband configurations, the latter case is depicted by (2.33a) with $\gamma_{2p} = 0$, and since the pump is the only source in this case, (2.33a) becomes

$$\begin{bmatrix} 0 \\ \mathbb{I}_p \\ 0 \end{bmatrix} = \begin{bmatrix} Y_2 & j\omega_\ell \gamma_r & 0 \\ j\omega_p \gamma_r & Y_p & j\omega_p \gamma_r \\ 0 & j\omega_u \gamma_r & Y_u \end{bmatrix} \begin{bmatrix} V_\ell \\ V_p \\ V_u \end{bmatrix} \tag{9.8}$$

which attributes all modulation to time-varying capacitance at ω_r.

The formulations in (9. 8) and (8. 1) are effectively equivalent because

$$\frac{V_r}{V_p} = \frac{\gamma_r}{\gamma_p} \tag{9.9}$$

but they express the mixing process in different terms. The relative advantage of these two methods depends upon how the sidebands are used to form the output. For example, in the analysis in Chapter VIII, the output signal was a single-sideband filtered from the pump, so no advantage would result from retaining the pump in electrical form in this case. However, when the pump and sidebands together form the useful output, as in the present chapter, the formulation in Section 2. 4 is more convenient.

When the constraint in (9. 1) is included in (9. 8), the sideband voltages are identical to those in (9. 4) as expected. In addition, however, (9. 8) yields the effect of signal on pump directly, through the relation

$$Y_{p_{in}} = \frac{I_p}{V_p} = g_p \left[1 + 2\omega_p{}^2 |M|^2 \left(1 - j \frac{\omega_r{}^2}{\omega_p \beta_p}\right)\right] . \tag{9.10}$$

The corresponding relation from (8. 1) is

$$Y_{r_{in}} = Y_r + \frac{2\omega_p{}^2 |\gamma_p|^2}{Y_u} \tag{9.11}$$

which is a special case of (8. 2). It indicates the effect of pump on signal under the conditions in (9. 1). In (9. 10), the term

$$2\omega_p{}^2 |M|^2 g_p = (g_p)_{refl} \tag{9.12a}$$

is the reflected conductance at ω_p due to the modulating signal at ω_r, while the corresponding reflected conductance in (9. 11) is

$$(g_r)_{refl} = \frac{2\omega_r{}^2 |\gamma_p|^2}{|Y_u|^2} g_p = 2\omega_r{}^2 \left|\frac{V_p}{V_r}\right|^2 |M|^2 g_p . \tag{9.12b}$$

Therefore, in this mixing process the relative power contributions by the pump and signal are given by the ratio

$$\frac{\text{pump power}}{\text{signal power}} = \left|\frac{V_p}{V_r}\right|^2 \frac{(g_p)_{refl}}{(g_r)_{refl}} = \frac{\omega_p^2}{\omega_r^2} \quad . \tag{9.13}$$

In view of this enormous potential gain, it can be anticipated that immediate phase detection of the waveform in (9.6b) will recover a well-amplified version of the original signal. This point will be discussed further in Section 9.1, but first another curious aspect of this phase-modulation process should be noted.

In (9.4), the two sidebands have slightly different amplitudes such that

$$\left|\frac{V_u}{V_\ell}\right| = \frac{\omega_u}{\omega_\ell} \approx 1 + \frac{2\omega_r}{\omega_p} \quad . \tag{9.14}$$

Since this asymmetry vanishes as ω_r approaches zero, it is apparently responsible for the terms in (9.5) that involve ω_r. One such term appears as incidental AM and the other appears as phase distortion. Both of these distortions are negligible when $\omega_r << \omega_p$.

The sideband asymmetry noted in (9.14) has its greatest influence at ω_r. In Section 7.2, the Manley-Rowe equations were applied to phase-like modulation and there the tendency toward instability was found to be very sensitive to sideband asymmetry. In the present case, the ratio of the two sideband powers is

$$\frac{W_u}{W_\ell} = \left(\frac{\omega_u}{\omega_\ell}\right)^2 \tag{9.15}$$

which satisfies the stability condition in (7.7). In fact, using (7.5) and (9.15) together, one obtains the following sideband-to-signal power ratio

$$-\frac{(W_u + W_\ell)}{W_r} = \frac{\omega_p^2 + \omega_r^2}{\omega_r^2} \approx \frac{\omega_p^2}{\omega_r^2} \tag{9.16}$$

which is just the negative of the unstable ratio corresponding to pure phase modulation. Therefore, while the sideband asymmetry noted in (9.14) has a more or less negligible influence on distortion, it has a useful influence on stability. Further evidence of this appears in the derivation of $Y_{r_{in}}$ in (9.11), where the sideband asymmetry is seen to be just sufficient for the positive reflected conductance from the upper sideband to just overcome the negative conductance from the lower sideband. The net reflected conductance in (9.11) is positive, but small.

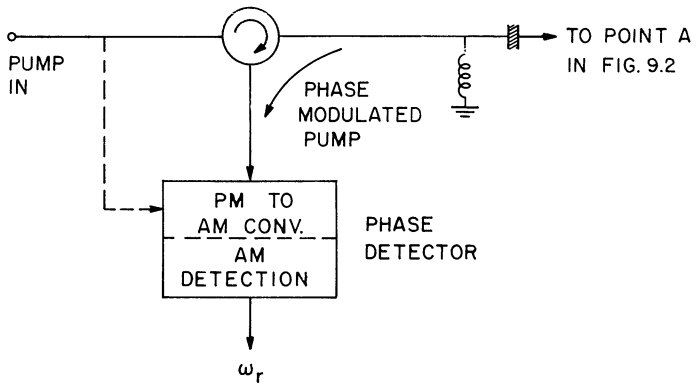

Fig. 9.3. A detection system for recovering an amplified version of the modulating signal.

9.1 Circuit Properties

It is now evident that a phase-modulated signal emerges from the circulator in Fig. 9.2. Hopefully, an amplified version of the modulating signal can be recovered by placing a phase detector at its output port, which is illustrated in Fig. 9.3. Since (9.16) suggests power gains in proportion to pump frequency squared for this case, it differs considerably from the cases previously studied, where power gain was proportional to only the first power of pump frequency. In deriving (9.16), the sideband powers were added as if they were incoherent signals. This step is satisfactory for merely estimating the power gain, but once it is recognized that the sidebands add coherently to form a phase-modulated signal, a more precise measure of gain is required.

Helpful in this respect is the classical view that the two sideband voltages can be regarded as vectors rotating with respect of V_p at angular frequency ω_r. The phase envelope is then formed by the total projection of V_u and V_ℓ in quadrature with V_p so the peak of the phase envelope will occur whenever the sidebands are in phase. Hence, a transducer gain for phase modulation can be defined by

$$G_{PM} = \frac{1}{2} \frac{\left(\begin{array}{c}\text{Maximum quadrature component} \\ \text{of } V_u + V_\ell \text{ with respect to } V_p\end{array}\right)^2}{\left(\begin{array}{c}\text{Available source power} \\ \text{at } \omega_r\end{array}\right)} g_p \cdot \qquad (9.17a)$$

Or, in the manner of (3.15b),

$$G_{PM} = \frac{4 g_r g_p}{\left|Y_{r_{in}}\right|^2} \left|\frac{V_p}{V_r}\right|^2 \left(\begin{array}{c}\text{Maximum imaginary component} \\ \text{of } (V_u + V_\ell)/V_p\end{array}\right)^2 \cdot \qquad (9.17b)$$

The phase of $(V_u + V_\ell)/V_p$, as found from (9.4), is somewhat arbitrary since the phase of V_r is arbitrary. However its maximum possible imaginary component is

$$(\omega_u + \omega_\ell)\,|M| = 2\omega_p\,|M| \tag{9.18}$$

which occurs when the instantaneous phases of V_r and Y_u are equal. As could be expected, (9.18) equals the angular deviation in (9.7a).

Using (9.4b), (9.9), and (9.11) in (9.17b), the conversion gain by phase modulation becomes

$$G_{PM} = \frac{16\, g_r g_p\, \omega_p^{\,2} |\gamma_p|^2}{\left|Y_r Y_u + 2\omega_r^{\,2} |\gamma_p|^2\right|^2} \cdot \tag{9.19}$$

Of course this gain will be useful only if the phase modulation sidebands can be converted back to ω_r efficiently, which calls for a good phase detector. But it will be shown that phase detection invariably introduces loss, so if η^2 is the fraction of phase envelope power that is actually converted back to ω_r, the over-all transducer gain will then be

$$G_r = \eta^2 G_{PM} \tag{9.20}$$

The numerical value of η^2 will be discussed later, but for now it can be stated that $0.1 < \eta^2 < .5$. A more detailed discussion of phase detection efficiency will be taken up in Section 9.3.

For a given source and load conductance, both (9.19) and (9.20) are maximum for $\omega_r = 0$. Therefore, an untuned input will be assumed having the form

$$Y_r = g_r \left(1 + j\,\frac{\omega_r}{\beta_r}\right) \tag{9.21}$$

where $\beta_r = g_r/C_r$ is the bandwidth and C_r is the total input capacity at ω_r (i.e., $C_r = C +$ stray). A low pass amplifier characteristic now results with the following amplifier characteristic

$$G_r(\omega_r) = \frac{8\eta^2 k_p^{\,2} \left(\dfrac{\omega_p^{\,2}}{\beta_r \beta_p}\right)\left(1 + \dfrac{\omega_r^{\,2}}{\omega_p^{\,2}}\right)}{\left|1 + (k_p^{\,2} - 1)\left(\dfrac{\omega_r^{\,2}}{\beta_r \beta_p}\right)^2 + j\omega_r\left(\dfrac{1}{\beta_r} + \dfrac{1}{\beta_p}\right)\right|^2} \tag{9.22}$$

where k_p^2 is the pumping coefficient and in this case

$$k_p^2 = \gamma_p^2 / C_r C_p \ .$$

There is a resemblance between the transducer gains in (9. 19) and (9. 22) and the power gain in (9. 16), since both are proportional to ω_p^2, but the former two remain finite as ω_r approaches zero. This difference occurs because the reflected input conductance at ω_r vanishes with ω_r, so no signal power can enter the converter when $\omega_r = 0$. Still, the maximum transducer gain occurs when $\omega_r = 0$ and has the value

$$\overline{G}_r = \frac{8\eta^2 k_p^2 \omega_p^2}{\beta_r \beta_p} \ . \tag{9.23}$$

9. 1. 1 Bandwidth and Gain-Bandwidth Product. To calculate the bandwidth (β) of the gain in (9. 20) it will be assumed that ω_r is much less than ω_p within the pass band β (i. e., $\beta << \omega_p$). Direct calculation then yields

$$\beta = \sqrt{\beta_r \beta_p} \left[\frac{-D + \sqrt{D^2 + 1}}{1 - k_p^2} \right]^{1/2} \tag{9.24a}$$

where

$$D = \frac{1}{2(1-k_p^2)} \left[\left(\frac{\beta_r}{\beta_p} + \frac{\beta_p}{\beta_r} \right)^2 - 1 \right] \tag{9.24b}$$

Inspection of these relations shows that

$$\beta \approx \left[\frac{1}{\beta_r} + \frac{1}{\beta_p} \right]^{-1} \tag{9.25a}$$

if

$$\left| \beta_p - \beta_r \right| >> 0 \tag{9.25b}$$

The maximum error in (9. 25a) is less than 30 percent, and it occurs when $\beta_r = \beta_p$ and $k_p^2 \approx 0$. Exact solution of (9. 26) are plotted in Fig. 9. 4 for $k_p^2 = 0$ and 1. For other values of k_p^2, β lies between the two curves plotted.

Since the two curves in Fig. 9. 4 are separated by no more than 30 percent, it can be concluded that the conversion bandwidth is roughly equal to the lesser of the two termin-

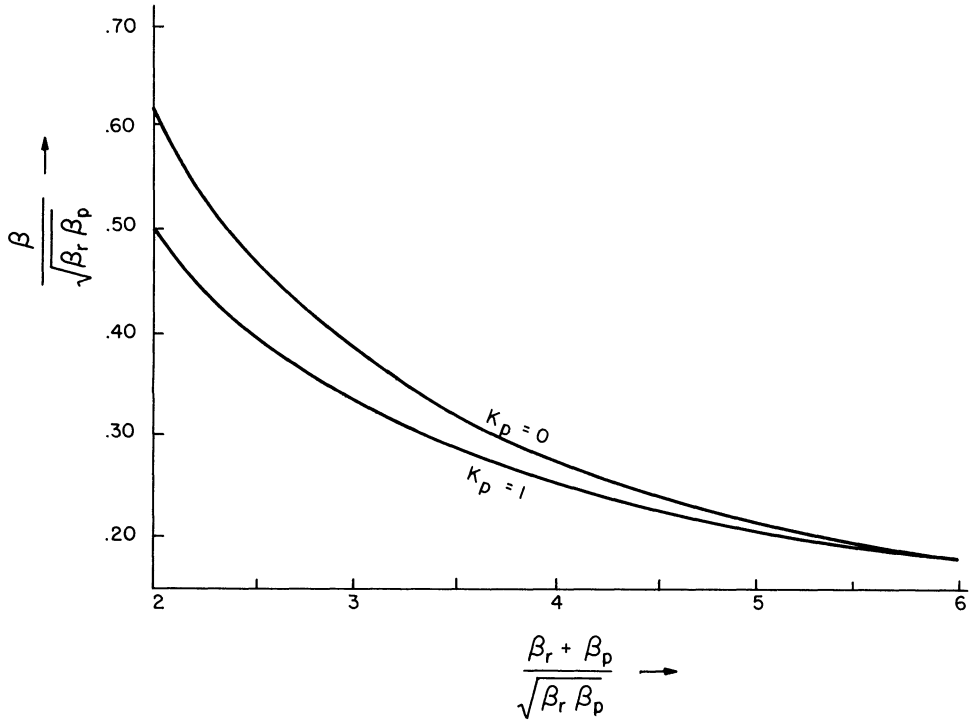

Fig. 9.4. The bandwidth of G_r vs. the sum of the circuit bandwidths, normalized to $\beta_r\beta_p$. The two curves shown are upper and lower bounds.

al bandwidths.[1] This result can be explained by considering the input and output admittances. The former was given in (9.11) and the latter can be found by substituting (9.1) into (8.3) and (8.4), which yields

$$Y_{u_{in}} = Y_u + \frac{\omega_r \omega_u |\gamma_p|^2 Y_u}{Y_r Y_u - \omega_r \omega_\ell |\gamma_p|^2} \tag{9.26a}$$

$$Y_{\ell_{in}} = Y_\ell - \frac{\omega_r \omega_\ell |\gamma_p|^2 Y_u}{Y_r^* Y_u + \omega_r \omega_u |\gamma_p|^2} \quad . \tag{9.26b}$$

From the point of view of bandwidth, the importance of these admittance relations is the ratio of the second term to the first, which shows the ratio of reflected to fixed admittance. In (9.11), the reflected admittance at ω_r has the components:

$$(g_r + jb_r)_{refl} = \frac{\omega_r^2 k_p^2}{\beta_r \beta_p \left(1 + \omega_r^2/\beta_p^2\right)} \left[g_r + j \left(\frac{\beta_r}{\beta_p}\right) b_r \right] . \tag{9.27}$$

[1] Note that β is actually half the bandwidth of the pump tank, but it is referred to here as the pump bandwidth.

The key factor here is k_p^2 which, in Section 9.1.3, will be shown to be much less than one. Therefore $(g_r)_{refl}$ and $(b_r)_{refl}$ are much smaller than g_r and b_r respectively, and the bandwidth of the ω_r terminals (g_r/C_r) changes very little when the pump is applied.

Investigation of the sideband admittance in (9.26a) and (9.26b) shows the same general trend, that

$$Y_{u_{in}} \approx Y_u \tag{9.28a}$$

$$Y_{\ell_{in}} \approx Y_\ell \, . \tag{9.28b}$$

However, it should be noted that $Y_{u_{in}} \neq Y^*_{\ell_{in}}$ even though $Y_u = Y^*_\ell$. In fact (9.26) shows

$$Y_{u_{in}}(\omega_r) = Y^*_{\ell_{in}}(-\omega_r) \, . \tag{9.29}$$

Some confusion may arise about the significance of $Y_{u_{in}}$ and $Y_{\ell_{in}}$, when they are part of the same resonance, but they apply on different sides of resonance, so they can be regarded as separate quantities. As one consequence of (9.29), frequencies above ω_p experience positive reflected conductance while those below see negative conductance. Nevertheless, these reflected conductances are numerically small compared to g_p, so their asymmetry is relatively unimportant.

Now that the bandwidth has been determined, a related quantity of basic importance is gain-bandwidth product. By (9.23)

$$\sqrt{G_r}\,\beta = 2\sqrt{2}\omega_p k_p \eta \, \frac{\beta}{\sqrt{\beta_r \beta_p}} \, . \tag{9.30}$$

It is of interest to optimize (9.30) but a number of practical factors can influence the result. For example, if the varactor is lossless, β_p can be chosen independently of ω_p. Then by Fig. 9.4, $\beta/\sqrt{\beta_r \beta_p}$ is maximum when $\beta_r = \beta_p$ which leads to the relation

$$\sqrt{\bar{G}_r}\,\beta \approx 1.83\,\omega_p k_p \eta\,(1 - 0.283\,k_p + \ldots)\,; \; k_p < 1 \, . \tag{9.31}$$

Since this gain-bandwidth product is proportional to ω_p, the lossless case emphasizes the

value of a high pump frequency. However, varactor loss eventually limits the usefulness of raising the pump frequency, as will be shown in Section 9.1.4.

9.1.2 A Numerical Example. To illustrate the great promise afforded by this double-sideband configuration, a numerical example will now be considered. Since the gain-bandwidth product in (9.29) is proportional to pump frequency, this suggests that the highest possible pump frequency should be selected. Today, it is well within the state-of-the-art for varactors to be pumped at 10 kMc, which means that a gain-bandwidth product of 1000 Mc is possible if ηk_p can be made made as large as $0.1/1.83 = 0.055$. Later it will be shown that $\eta k_p = 0.055$ is easily realized, so let us continue the present example by designing an amplifier with the following characteristics:

$$\text{Midband Gain,} \quad \overline{G}_r = 20 \text{ db} \tag{9.32a}$$

$$\frac{\text{Bandwidth}}{2\pi}, \quad \frac{\beta}{2\pi} = 100 \text{ Mc} \qquad \text{(dc to 100 Mc)} \tag{9.32b}$$

Together these correspond to a gain-bandwidth product of 1000 Mc, which in the present case requires

$$\eta k_p = 0.055 . \tag{9.33}$$

Now, assuming $\beta_r = \beta_p$ as suggested above, and $k_p^2 << 1$ as will be justified in the next section, Fig. 9.4 yields

$$\beta_s = \beta_p = \frac{\beta}{0.64} = 1.56\,\beta = 2\pi\,(156 \text{ Mc}) \tag{9.34}$$

for the pump and signal bandwidths. As expected, neither the pump nor signal terminal admittances are much affected by pumping. For example, applying (9.27) to the present case gives

$$(Y_r)_{refl} \leq \frac{k_p^2}{2}\, Y_r = \left(\frac{0.055}{\eta}\right)^2 \frac{Y_r}{2} = 0.012\, Y_r \tag{9.35}$$

where $\eta^2 = 1/8$ has been assumed. Therefore, the input admittance is essentially that of the varactor itself, which is purely capacitive for frequencies in the ω_r band.

It is evident that double-sideband reactive mixing provides a technique for dc amplification with extremely wide bandwidths, from dc to UHF. Although no standard termi-

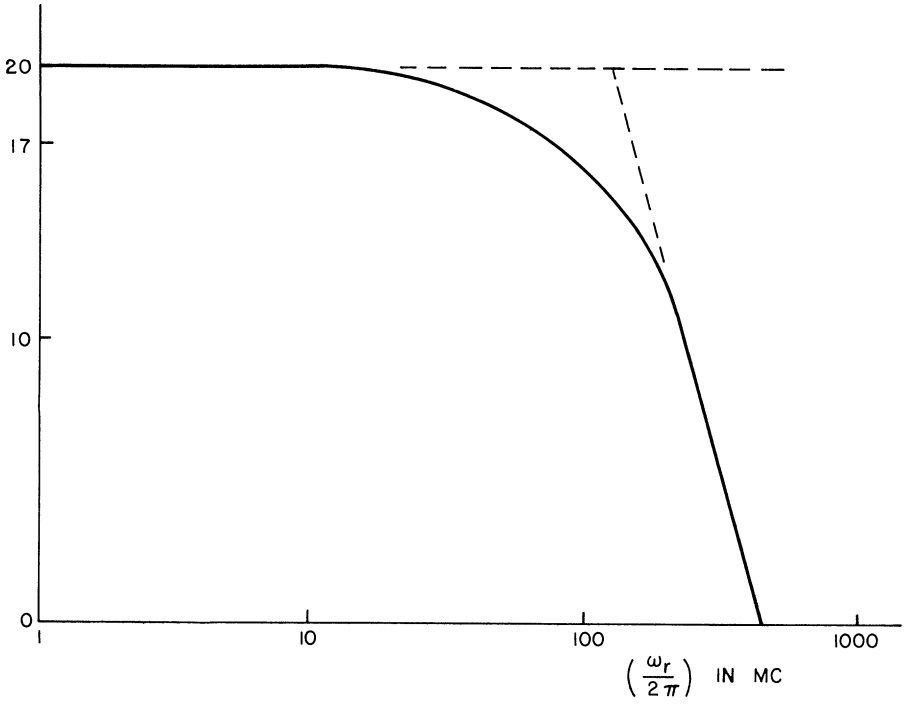

Fig. 9.5. Gain characteristic of the example amplifier in Section 9.1.2.

nology exists for this broad range of frequencies, it will be termed an extended video range and the configuration under discussion will henceforth be termed an ultra-wideband video amplifier. The frequency response of the amplifier in this example is shown in Fig. 9.5.

9.1.3 Physical Limitations on k_p^2. By (9.31), the gain-bandwidth product is proportional to k_p, so it is important to consider possible limitations on this quantity. According to the definition in (9.32)

$$k_p^2 = |\gamma_p|^2 / C_r C_p \tag{9.36}$$

where C_r and C_p are the total circuit capacities at ω_r and ω_p respectively. Therefore, in the notation of the general Taylor expansion in (2.11),

$$C_p = a_1 + \text{stray or filter capacity}$$

and $\gamma_p = \frac{a_2 V_p}{2}$, for which

$$k_p^2 < \left|\frac{a_2 V_p}{2a_1}\right|^2 . \tag{9.37}$$

However, this relation is valid only over a range where the varactor capacity varies linearly about the bias point, and typically this is true only when $V_p \div V < \frac{1}{2}$, where V is the bias voltage.

As previously noted in (2.10), varactors are characterized by relations in the form

$$q(v) = Q(1 - v/A)^{1-\sigma}; \qquad 0 < \sigma < 1 . \tag{9.38}$$

In this case, (9.37) becomes

$$k_p^2 < (\tfrac{\sigma}{2})^2 \left(\frac{|\overline{V}_p|}{A}\right)^2 \left(1 + \frac{\overline{V}}{A}\right)^{-2} \approx (\tfrac{\sigma}{2})^2 \left(\frac{\overline{V}_p}{2}\right)^2 \tag{9.39}$$

where the latter approximation is valid when A, the contact potential, is small compared to $|V_p|$ and V.

An upper limit on $|V_p|$ also arises because a varactor is basically a diode and excessive conduction takes place when $|V_p| = V + A \approx V$. Therefore, the upper limit on k_p^2, as predicted by (9.39), is $(\sigma/2)^2$. In a typical case, $\sigma = 1/2$, and then $k_p^2 \leq 0.06$.

However, for $|V_p| \approx \overline{V}$, the accuracy of (9.39) deteriorates because the formulation behind this relation is only concerned with first-order interactions. When $|V_p|$ is large, higher-order interactions also contribute to the circuit effects being observed, but this can be partially accounted for by replacing γ_p by the Fourier component of time-varying capacity at ω_p.

$$\gamma_p = \frac{1}{\pi} \int_0^{2\pi} \left.\frac{dq}{dv}\right|_{v_o} \epsilon^{j\omega_p t} \, d(\omega_p t) \tag{9.40a}$$

where:

$$v_o = V + \mathrm{Re}(V_p \epsilon^{j\omega_p t}) .$$

This expression for γ_p is proportional to V_p for small V_p/V, but deviates from proportionality as the latter increases. Similarly, with large pumping signals the average varactor capacity deviates from the bias value, and is given by the relation

$$C = \frac{1}{2\pi} \int_0^{2\pi} \left[\left(\frac{dq}{dv}\right)_{v_o} d(\omega_p t)\right] . \tag{9.40b}$$

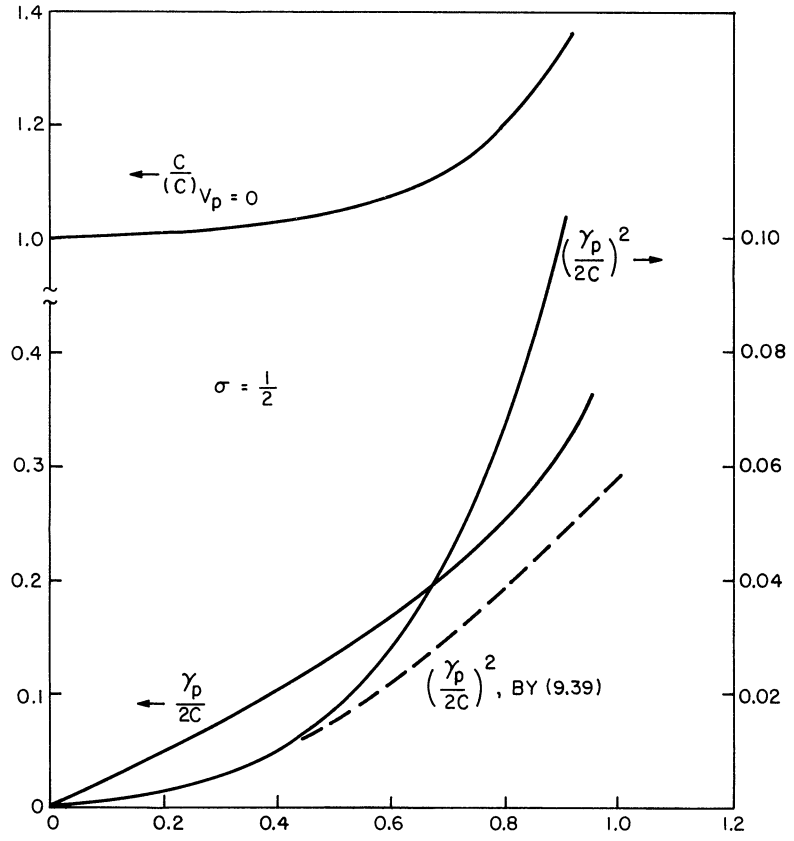

Fig. 9.6. Estimates of C, γ_p, and k_p^2 by Fourier analysis.

The integrals in (9.40) have been evaluated in Ref. 37 and the results are shown in Fig. 9.6 for $\sigma = 1/2$. Also plotted is the upper limit on k_p^2, namely $(\gamma_p/2C)^2$. Based on Fig. 9.6, the value 0.1 will be taken as a practical upper limit on k_p^2, in the sense that $k_p^2 = 0.1$ should be approachable with large pump signals and minimum stray or auxiliary capacity across the varactor.

Of course, filter of bypass capacity that may shunt the varactor at one or more of the operating frequencies will reduce both k_p^2 and the circuit bandwidth, and these reductions produce opposite effects on the gain $\overline{G}_r$. To illustrate this point, consider a case where the input signal is available from a 100 ohm source and the effective varactor capacitance (C) is 1 pf, so (neglecting any bypass capacity) $\beta_r/2\pi = 1600$ Mc. If the desired amplifier bandwidth is significantly smaller than 1600 Mc, the extra input circuit bandwidth in this case would unnecessarily reduce G_r; but if β_r is reduced by adding extra capacity in the video

circuit, k_p^2 would reduce simultaneously to nullify the possible advantage to be derived from this β_r reduction. Therefore, to make optimum use of a varactor for phase modulation, the video bandwidths must be controlled by inductive source transformations.

To continue the illustrations above, a stray capacity of 1 pf will be allowed for, making C_r = 2 pf, and a broadband 2:1 step-up transformer will be assumed to change the source impedance to 400 ohms. Then $\beta_r/2\pi$ is reduced to 200 Mc, with an accompanying transducer gain improvement of 6 db. (Note: the reduction in β_r accounts for 9 db, while the reduction in k_p^2 accounts for -3 db.) In this case, the importance of a high source impedance arises because the video input impedance is large, as a result of ω_r being much less than ω_p. Thus, phase modulation is particularly useful for wideband amplification with high impedance sources such as solid-state particle detectors or various photoelectric devices.

9.1.4 The Effect of Varactor Loss. As shown in (3.30), varactor loss can be represented by a frequency-sensitive shunt conductance. At ω_p it has the value

$$g_{dp} \cong \frac{\omega_p^2 C}{\omega_d} \tag{9.41}$$

and therefore

$$g_p = \tilde{g}_p + g_{dp} \tag{9.42}$$

where $\tilde{g}_p$ is the sum of all external conductance. As previously noted $\tilde{g}_p$ would typically be the characteristic admittance of the circulator.

The half-bandwidth of the pump tank now becomes

$$\beta_p = \frac{\tilde{g}_p + g_{dp}}{2C} = \tilde{\beta}_p + \beta_{dp} \tag{9.43a}$$

where

$$\tilde{\beta}_p = \frac{\tilde{g}_p}{2C}; \quad \beta_{dp} = \frac{g_{dp}}{2C} \quad . \tag{9.43b}$$

Therefore, the minimum possible value of β_p is

$$(\beta_p)_{min} = \beta_{dp} = \frac{\omega_p^2}{2\omega_d} \tag{9.44}$$

which occurs in the absence of external loading.

The expression in (9.23) for midband gain can be similarly modified to exclude sideband power lost in the varactor, which yields

$$\overline{G}_r = \frac{8\eta^2 k_p{}^2 \omega_p{}^2}{\beta_r \beta_p} \left[\frac{\tilde{g}_p}{\tilde{g}_p + g_{dp}} \right]^2 \tag{9.45a}$$

or by (9.43)

$$\overline{G}_r = \frac{16\eta^2 k_p{}^2 \omega_d}{\beta_r} \times \frac{\tilde{\beta}_p \beta_{dp}}{(\tilde{\beta}_p + \beta_{dp})^2} \quad . \tag{9.45b}$$

Since the last expression is maximum for $\beta_p = \beta_{dp}$, varactor loss is best compensated for by choosing $g_{dp} = g_p$, which matches the varactor to the circulator and yields

$$\overline{G}_r = \frac{4\eta^2 k_p{}^2 \omega_d}{\beta_r} \quad . \tag{9.46}$$

Without a circulator,

$$\tilde{g}_p = g_s + g_L \tag{9.47}$$

and then (9.46) must be reduced by the fraction of $\tilde{g}_p$ that constitutes the output load, namely g_L/g_p. However, this step will not alter the significance of (9.46).

A final step in optimizing $\overline{G}_r$ is to minimize β_r in (9.46). Using the approximation in (9.25a),

$$\frac{1}{\beta} \approx \frac{1}{\beta_r} + \frac{1}{\beta_p} = \frac{1}{\beta_s} + \frac{1}{\tilde{\beta}_p + \beta_{dp}} \tag{9.48}$$

it suggests that ω_p be increased until β_{dp}, and hence β_p, are much greater than β_r. Then β_r will have the minimum value β and the corresponding optimum dc gain will be

$$\left(\overline{G}_r\right)_{max} = \frac{4\eta^2 k_p{}^2 \omega_d}{\beta} \tag{9.49}$$

which occurs for $\omega_p{}^2 >> \beta\omega_d$. The maximum gain-bandwidth product is now

$$\sqrt{\overline{G}_r}\ \beta = 2\eta k_p \sqrt{\omega_d \beta} \quad . \tag{9.50}$$

By comparing (9.50) with (9.31), the effect of varactor loss is quite evident. For example, if $\omega_p = N\sqrt{\beta\omega_d}$, then ηk_p must be at least N times larger with varactor loss then without to yield the same gain-bandwidth product. Considering again the example in Section 9.1.2, a varactor with $\omega_d = 2\pi(10^5\ \text{Mc})$ will be assumed. To retain 100 Mc bandwidth with minimum pumping, let

$$\omega_p = 3\sqrt{\beta\omega_d} = 2\pi(10^4\ \text{Mc}) \ . \tag{9.51}$$

Then by (9.44)

$$\beta_{dp} = 2\pi(500\ \text{Mc}) \tag{9.52}$$

and if $\beta_p = \beta_{dp}$, then

$$\beta_p = 2\beta_{dp} = 2\pi(1000\ \text{Mc}) \ . \tag{9.53}$$

By (9.48)

$$\frac{2\pi}{\beta_r} = \frac{1}{100\ \text{Mc}} = \frac{1}{1000\ \text{Mc}} = \frac{1}{110\ \text{Mc}} \tag{9.54}$$

So by (9.46)

$$\begin{aligned} \overline{G}_r &= 4\eta^2 k_p{}^2 \left(\frac{10^5}{110}\right) \\ &= 50\ (17\ \text{db}) \text{ for } \begin{cases} k_p{}^2 = 0.1 \\ \eta^2 = 1/8 \end{cases} \ . \end{aligned} \tag{9.55}$$

Therefore, a gain-bandwidth product of 700 Mc seems to be the upper limit when varactor loss is considered in this case. Still, it must be noted that the optimum gain-bandwidth product in (9.50) is proportional to $\sqrt{\beta}$. Therefore, if the bandwidth is extended to 200 Mc, $\sqrt{\overline{G}_r}\ \beta$ will equal 1000 Mc for the same ω_d, η^2, and $k_p{}^2$, but the gain in this case is $\overline{G}_r = 25 = 14$ db. Also, it will be shown that η^2 can be as large as 1/2, which would add 6 db to (9.55).

A summary of how optimum gain varies with pump frequency is shown in Fig. 9.7. It assumes the case where a definite bandwidth β is required. When the pump frequency is low, the condition $\beta_{dp} = \widetilde{\beta}_p$ yields insufficient pump bandwidth, so $\widetilde{\beta}_p$ must be increased.

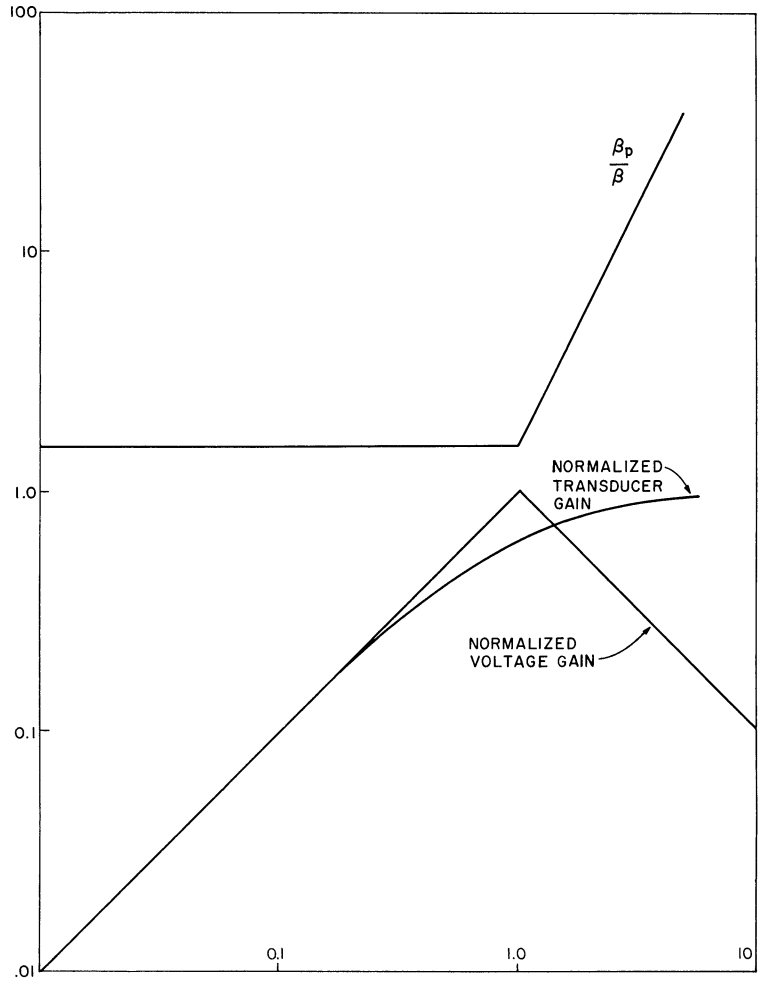

Fig. 9.7. A comparison of optimum $\sqrt{\overline{G_r}}$ and voltage gain for fixed bandwidth and varactor resistance vs. pump frequency. G_r is normalized to $4k_p\eta\omega_d$ and the voltage gain is normalized to $2(\gamma_p/C)\sqrt{\omega_d/1.56}$.

The optimum choice in this case is

$$\beta_r = \tilde{\beta}_p + \beta_{dp} = 1.56\,\beta \tag{9.56}$$

as noted in (9.34). However, as ω_p increases, β_{dp} increases in proportion to ω_p^2 and reaches the value $(1.56\beta/2)$ when $\omega_p = \sqrt{1.56\beta\omega_d}$. The latter is the highest pump frequency at which equal pump and signal bandwidths are optimum. For still higher pump frequencies, $\beta_{dp} = \tilde{\beta}_p$ must be satisfied for optimum efficiency, but then β_p increases in proportion to ω_p^2.

By (9. 18), the midband voltage gain is

$$\text{voltage gain} = \frac{2\omega_p |\gamma_p|}{\beta_p C} \tag{9. 57}$$

which is an increasing function of ω_p as long as β_p is constant. However, for $\omega_p > \sqrt{1.56\beta\omega_d}$, β_p increases faster than ω_p which reduces the voltage gain. At the same time, g_p increases in proportion of ω_p^2, so the output power remains constant for $\omega_p > \sqrt{1.56\beta\omega_d}$ even though the voltage falls off. Therefore, the main advantage to be gained from increasing ω_p beyond the point where varactor loss can account for half the pump bandwidth is that β_r can be reduced from 1.56β to β. In this region $\overline{G}_r$ increases asymptotically toward the value $4k_p\eta\omega_d$.

9. 1. 5 Noise Figure. A calculation of the noise figure associated with the phase modulation gain G_{PM}, or the detected gain G_r, follows the general procedure outlined in Section 3. 4. 2, which requires the specification of each external noise source. The main type of noise source that can be anticipated is that due to parasitic loss, which would be thermal in origin. In the ω_r band, excess noise will originate primarily in cables and transformers, etc., since varactor loss can be neglected in the video range (e.g., below 100 Mc, microwave varactors have Q's greater than 1000). It is actually in the pump tank that the varactor makes a fundamental noise contribution particularly when varactor loss is a significant fraction of the total pump tank loss. Therefore excess noise figures due to thermal noise sources in the pump tank will now be calculated, and the result used as a guide for determining when other, more arbitrary noise contributions, are significant.

The effective noise temperature in the pump tank is

$$T_p = \frac{T_d g_{dp} + \tilde{T}_p \tilde{G}_p}{\tilde{g}_p + \tilde{g}_{pd}} \tag{9. 58}$$

where T_d and $\tilde{T}_p$ are the noise temperatures of the varactor and the auxiliary pump circuitry, respectively. Therefore, considering the pump pass band as drawn in Fig. 9. 8, each increment $d\omega$ will experience an (incoherent) noise source

$$di_N = \sqrt{\frac{4kT_p g_p d\omega}{2\pi}} \quad . \tag{9. 59}$$

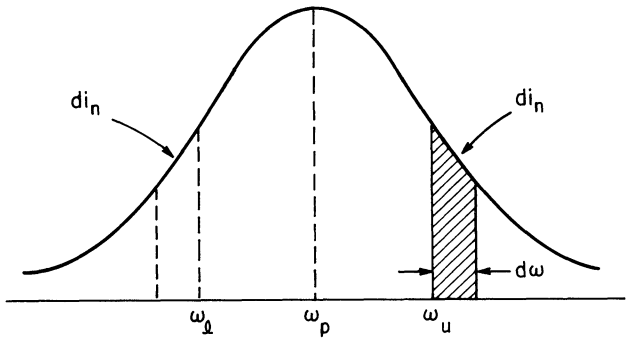

Fig. 9.8. Noise contributions from pump circuit conductance.

Consider first the increment lying between ω_u and $\omega_u + d\omega$. Two output noise contributions will arise in this band; one due to noise reflected from di_N and the other due to noise converted from the image band which lies between ω_ℓ and $\omega_\ell - d\omega$. To evaluate these two noise contributions let

$$Y_{u_{in}} = \text{total tank admittance at } \omega_u$$

$$Y_{\ell_{in}} = \text{total tank admittance at } \omega_\ell$$

$$Y_{u\ell} = \text{transfer admittance from } \omega_\ell \text{ to } \omega_u$$

$$Y_{\ell u} = \text{transfer admittance from } \omega_u \text{ to } \omega_\ell .$$

The total output noise power in the original increment now becomes

$$P(\omega_r)\, d\omega = \frac{|di_N|^2 g_p}{|Y_{u_{in}}|^2} + \frac{|di_N|^2 g_p}{|Y_{u_{i\ell}}|^2} \tag{9.60}$$

which expresses the output noise power distribution over the right half of Fig. 9.8. But, as previously noted in (9.29)

$$Y_{u_{in}}(\omega_r) = Y^*_{\ell_{in}}(-\omega_r) . \tag{9.61}$$

Similarly, it can be shown that

$$Y_{u\ell}(\omega_r) = Y^*_{\ell u}(-\omega_r) \tag{9.62}$$

so (9.55) is equally valid over the left half of Fig. 9.8 by letting ω_r be negative.

The total noise power delivered to g_p, which will be called P_p, is found by integrating (9.60) over the complete range $-\infty < \omega_r < \infty$. If $\omega_r << \omega_p$ and $k_p^2 << 1$, it is shown in Appendix B that P_p can be expressed approximately by

$$P_p = \int_{-\infty}^{\infty} d\omega_r \left[\frac{4k_p^2 T_p}{2\pi}\right]\left[\frac{1}{1+\left(\frac{\omega_r}{\beta_p}\right)^2}\right]\left[1 + \frac{\frac{1}{2}\left(\frac{k_p^2 \omega_r \omega_p}{\beta_r \beta_p}\right)^2}{\left(1 - \frac{\omega_r^2}{\beta_r \beta_p}\right)^2 + \omega_r^2\left(\frac{1}{\beta_r} + \frac{1}{\beta_p}\right)^2}\right]. \quad (9.63)$$

The effects of pumping on load noise are now evident through the term in P_p containing k_p^2, which vanishes in the absence of pumping. Hence this excess noise must be held against the amplifier even though it is partly due to the output load.

The quantitative evaluation of (9.63) is carried out in Appendix B for the condition $\beta_p \geq \beta_r$, because it includes each of the optimum gain cases that have been treated so far. Denoting the total noise power reaching the external conductance $\tilde{g}_p$ by $\tilde{P}_p$, then

$$\tilde{P}_p = \frac{\tilde{g}_p}{g_p}\left[4kT_p\left(\frac{2\beta_p}{2\pi}\right)\left(\frac{\pi}{2}\right)\left(1 + \frac{k_p^4 \omega_p^2}{4\beta_p\sqrt{\beta_r \beta_p}}\right)\right] \quad (9.64)$$

and the excess noise power reaching $\tilde{g}_p$ is

$$\left(\tilde{P}_p\right)_{\text{excess}} = \frac{\tilde{g}_p}{g_p}\left(4kT_p B_{pn}\right)\left(\frac{k_p^2}{32}\right)\left(\frac{\bar{G}_r}{\eta^2}\right)\sqrt{\frac{\beta_p}{\beta_r}} \quad (9.65a)$$

where

$$B_{pn} = \left(\frac{\pi}{2}\right)\left(\frac{\beta_p}{\pi}\right) \quad (9.65b)$$

is the noise bandwidth of the pump circuit in cps.

The noise figure due to varactor loss can now be found by referring (9.65a) to the input in the manner of (2.39), which yields

$$F = 1 + \frac{(P_p)_{excess}}{4k\, T_o\, B_{pn}\left(\frac{G_r}{\eta^2}\right)} \tag{9.66a}$$

$$= 1 + \frac{k_p^{\,2}}{32}\sqrt{\frac{\beta_p}{\beta_r}}\;\frac{T}{T_o} \quad . \tag{9.66b}$$

Therefore, for the high gain case where $k_p^{\,2} = 0.1$, $\beta_p = \beta_r$ and $T_p = T_o$,

$$F = 1.003 = 0.01 \text{ db}$$

which is negligably small. It can therefore be concluded that sources of noise other than the varactor itself will determine the noise figure of the configuration under study.

Measured noise figures will undoubtedly exceed the numerical values predicted above, so experiments will have to determine the source of additional noise contributions, although several can be anticipated. For example, the varactor can be assumed to be at room temperature ($T_d = T_o$), but the load temperature $\tilde{T}_p$ may be much larger, particularly if pump oscillator noise contributes to $\tilde{T}_p$. If this effect is large, pump oscillator padding will be required to reduce $\tilde{T}_p$. Other forms of load noise should be small if a circulator is employed. Finally, the magnitude of input circuit noise must be estimated in an actual circuit, so it can be included in (9.66). However, these extraneous effects are largely under the control of the circuit designer so very low noise figures can generally be expected.

9.2 Design Considerations

The principle of amplification by phase modulation is quite simple, but the optimum usage of this principle will involve a number of further considerations. As depicted in Fig. 9.3 this process contains three basic steps:

1. phase modulation (PM)
2. PM to AM conversion
3. AM detection .

The last two steps together constitute phase detection but they have been separated to indicate the important fact that all phase detectors are really amplitude detectors preceded by phase to amplitude conversion networks.

So far, only step 1 has been treated in detail, but the factor η has been reserved for the gain reductions due to steps 2 and 3. The fact that loss must be incurred in steps 2 and 3 is fundamentally true, even though detectors can be built employing either nonlinear reactive or nonlinear resistive elements. Reactive demodulators must be ruled out because they incur losses proportional to the ratio of output to input frequency squared, or just the inverse of the modulation gain [see (7.6)]. Resistive demodulators also incur loss, but more or less independently of frequency. Therefore, demodulation must be by resistive elements, with care being taken to minimize loss.

The statement that reactive mixer demodulators have high loss does not contradict the conclusions of Chapters V and VIII. There, high-gain down-converters were described, but because they employed indpendently loaded sidebands they would be unsuitable for video demodulation. Nevertheless, such converters could be used for secondary amplification prior to demodulation.

Phase detectors operate by adding a second signal to a phase modulated signal in such a way that phase variations become at least partially converted to amplitude variations. The second signal may be generated actively or passively through filter action, but in either case a conventional AM detector does the final demodulation.

For small angular deviations, the added signal will properly contain a quadrature carrier component. Therefore, taking the case of (9.6a), where $2\omega_p M$ is small, the general signal

$$B \sin(\omega_p t + \phi_B) \tag{9.67}$$

will be added to (9.6b) to yield the sum

$$N(t) \cos [\omega_p t + \psi(t)] \tag{9.68a}$$

where

$$N^2 = |V_p|^2 + B^2 + 2B|V_p| \sin[\phi_B - \phi_p - \theta(t)] \tag{9.68b}$$

$$\psi(t) = -\tan^{-1} \left\{ \frac{V_p \sin[\theta(t) + \phi_p] - B \cos \phi_B}{V_p \cos[\theta(t) + \phi_p] + B \sin \phi_B} \right\} . \tag{9.68c}$$

Two significant cases can be isolated from (9.68) and these are illustrated in Fig. 9.9. The first is where the two carriers are precisely in quadrature, which yields an enhanced carrier and corresponds to $(\phi_B - \phi_p) = 0$. The second is for $(\phi_B - \phi_p) > 0$, which yields a partially suppressed carrier.

However, each detection system will be further characterized by the degree of isolation that can be achieved between the varactor, the pump, and the detector. Isolation between the pump and detector is particularly desirable when the reference signal for phase detection is also taken from the pump generator, since the reference signal needs to be pure in frequency (and phase). There are two basic isolation techniques that can be considered. One is isolation by active circuitry through secondary amplification. The other is isolation by passive circuitry such as circulators. Of course the former gives an added advantage of increased gain, but it calls for an extra active stage which will be considered undesirable for the present analysis. Instead, our interest will be restricted to techniques in which the pump oscillator is the only active component, and secondary amplification will be regarded only as a potential means for extending each method discussed.

9.2.1 Quadrature or Slope Detection ($\phi_B = \phi_p$). For this case, (9.68b) yields

$$N(t) = \sqrt{|V_p|^2 + B^2} \left[1 \pm \frac{2\omega_p B|V_p M| \cos\theta(t)}{|V_p|^2 + B^2}\right]^{1/2} \tag{9.69a}$$

$$\sqrt{|V_p|^2 + B^2} \left[1 \pm \frac{\omega_p B|V_p M| \cos\theta(t)}{|V_p|^2 + B^2}\right] \tag{9.69b}$$

while by (9.68c),

$$\psi(t) = \tan^{-1}\left[\frac{B}{|V_p|} - 2\theta_p|M| \cos\theta(t)\right] \tag{9.70}$$

so the modulation now appears partly in the envelope and partly in the phase is depicted in Fig. 9.9a. Since $(2\omega_p|M|)$ is the original angular deviation, the index for amplitude variations in (9.69b) is

$$\left(\frac{B|V_p|}{|V_p|^2 + B^2}\right) \text{(angular deviation)} \tag{9.71}$$

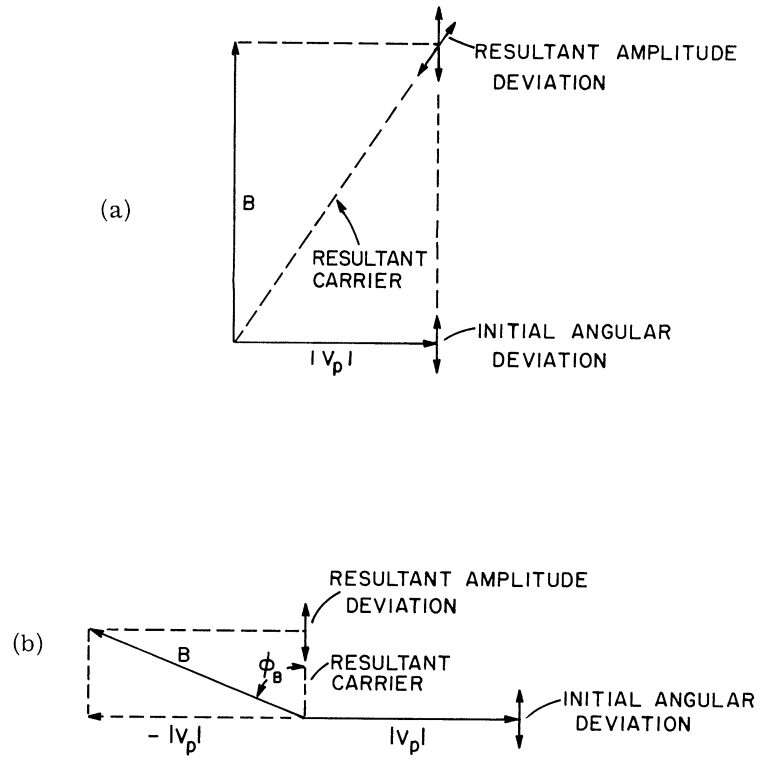

Fig. 9.9. Two examples of adding a carrier for phase detection. Case (a) corresponds to slope detection, while Case (b) is basically a suppressed carrier system.

Hence the maximum AM index occurs for $B = |V_p|$ and equals half the angular deviation, which means that only one-fourth of the coherent sideband power is made available for detection.

Of course the latter fraction can be increased to unity if $B >> |V_p|$, but this would represent an extravagant usage of pump power. It follows from (9.69b) that the greatest efficiency from the standpoint of pump power also occurs for $B = |V_p|$, and thus just doubles the original pump power requirement. Hence, for quadrature detection systems, the maximum available AM sideband power is 1/8 (-9 db) that possible as pure PM, for a given pump power. However, other detection systems will be shown to give better performance when they are usable.

There are several ways in which the quadrature signal in Fig. 9.9a can be generated, but each of these methods are equivalent to splitting the original pump signal and

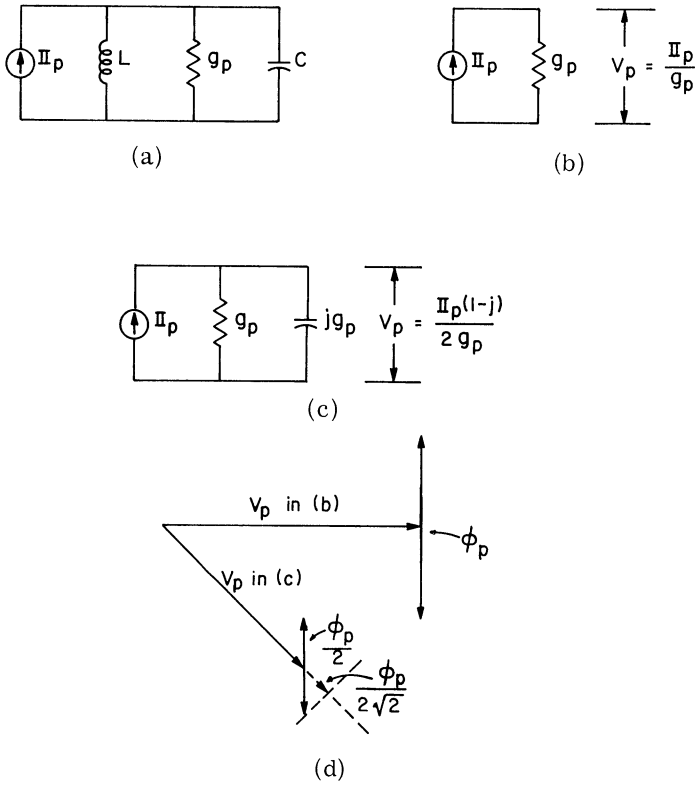

Fig. 9.10. A means for direct quadrature detection using the slope of the pump tank: (a) shows the basic pump tank; (b) is the same tank at resonance; (c) the same tank at its half power point, and (d) shows the corresponding pump phasors.

applying part to the varactor and part to the detector. To this end, let us consider the circuits in Fig. 9.10. It is evident that adding a susceptance jg_p to the conductance g_p introduces a quadrature component of voltage. However, this configuration is equivalent to operating a tuned circuit at its half power point. Thus, phase detection by the addition of a quadrature pump signal is equivalent to the well-known technique of slope detection.

Slope detection can be accomplished directly if the pump circuit is tuned as shown in Fig. 9.10c. This appears to be the most effective detection method whenever detector isolation is impractical. However, detuning the pump tank does cause a small reaction at the video input, which will be discussed in Section 9.2.4.

Figure 9.10 further illustrates the 9 db PM to AM conversion efficiency previously cited. Tuning to the half power point reduces $|V_p|$ by $1/\sqrt{2}$, but the sidebands are

doubly effected; first because they are proportional to $|V_p|$ and second because they are detuned, which yields a net sideband reduction of $(1/\sqrt{2})^2$ or -6 db. Finally, only half the sideband power appears in the AM envelope which introduces another -3 db loss, making (-9 db) in all.

Some improvement in the above system can be obtained using the balanced modulator configuration shown in Fig. 9.11, since it gives a better utilization of the extra pump power demanded by slope or quadrature detection. Two varactors are used and they are tuned so the upper half-power point of one coincides with the lower half-power point of the other. Hence, the pump sees a purely resistive load to which it can be matched, but it produces a dc envelope on each varactor equal to $|V_p|/\sqrt{2}$. When a modulating signal is applied simultaneously in each circuit, a balanced output results from the two detectors, and the resulting AM envelope in each detector is the same as that for a single detector in an unbalanced system. Therefore, for a given pump power, the maximum AM sideband power from a balanced modulator is 1/4 (-6 db) that possible as pure PM. Note, however, that the 3 db improvement in going from an unbalanced to a balanced system is due to pump matching and not to better handling of the sidebands. Hence η^2 is the same for both cases.

9.2.2 Detection of Double-Sideband, Suppressed Carrier Signals ($\phi_B - \phi_p > 0$).

A still more efficient detection method is depicted in Fig. 9.12, which shows the sidebands being completely converted to AM by employing a second signal with both quadrature and out-of-phase components. The out-of-phase component will just cancel the carrier if

$$\frac{B}{|V_p|} = -\frac{\cos \phi_p}{\sin \phi_B} \quad . \tag{9.72}$$

Hence this will be termed a suppressed carrier method. For convenience, ϕ_p will be set equal to zero and then (9.69) and (9.72) yield

$$N = |V_p| \operatorname{ctn} \phi_B [1 + 2\theta(t) \tan \phi_B]^{1/2} \tag{9.73a}$$

$$\approx |V_p| \operatorname{ctn} \phi_p [1 + \theta(t) \tan \phi_B] \quad . \tag{9.73b}$$

In this case, the AM index equals ($\tan \phi_B$) times the angular deviation, which gives 100 percent PM to AM efficiency for $\phi_B = \pi/4$.

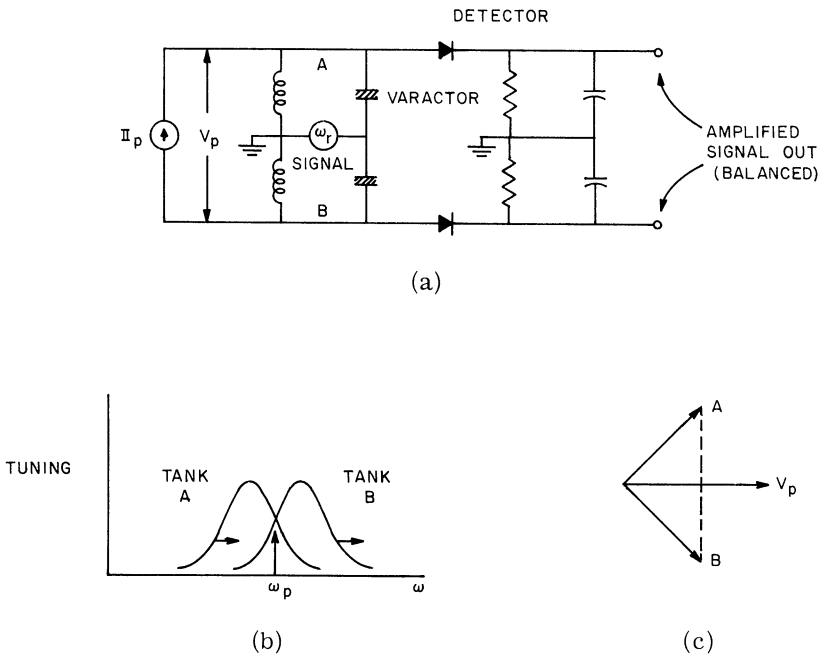

Fig. 9.11. A balanced modulator configuration, (a) for improving the pump power efficiency in the case of slope detection. The effect of a signal, as shown in (b), is to detune both tanks in the same direction. Figure (c) compares the individual tank voltages to the total pump voltage.

A suppressed carrier modulation is easily obtained when the varactor is matched to the pump, since the sidebands are all that emerge from the varactor in this case and a circulator can be used to isolate the sidebands from the pump generator. Since this is just the case depicted in Fig. 9.3, the latter with the circulator $\tilde{g}_p$ matched to the varactor loss g_{dp} is equivalent to Fig. 9.9b with $B = -|V_p|$.

Efficient detection can now be accomplished by adding a second carrier at the output port that is in quadrature with the original pump signal. However, this added signal can now be relatively small, perhaps an order of magnitude greater than the sidebands themselves, since it only needs to be large enough for linear detection. Figure 9.12 summarized this detection process, which for the same pump power yields nearly the same AM sideband power as can be obtained in pure PM. To illustrate this conclusion, consider a case where 100 milliwatts of pump power yields a phase modulation gain of 100. Then 10 microwatts of available signal power would produce 0.25 milliwatts in each sideband and a total coherent PM power of 1 milliwatt. But with a circulator this modulation can be completely converted

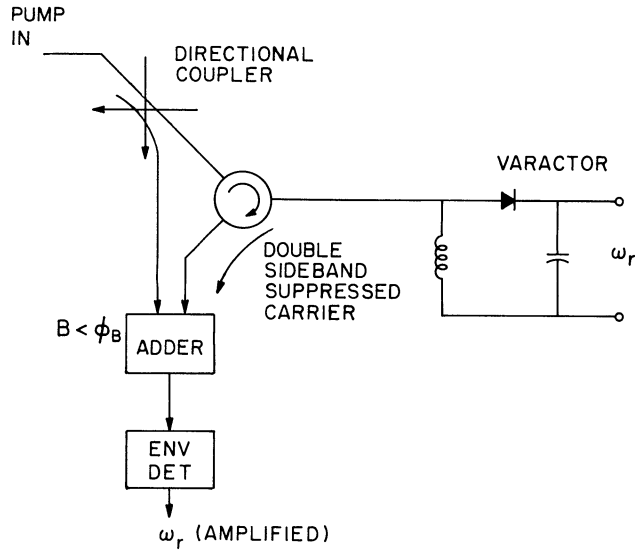

Fig. 9.12. A realization of the detection scheme in Fig. 9.9b.

to AM if a second signal, at about a 10-milliwatt level, is supplied.

9.2.3 Upper Limits on η^2. Returning now to the factor η^2, it should be noted that only the sideband power losses incurred during detection are included in η^2 and not pump power demands. The factor η^2 expresses the product (PM to AM efficiency) times (AM detection efficiency) and the preceding discussion has shown that the first factor varies from 1/8 to 1, depending on technique.

The second factor η^2, the detection efficiency, is even less tangible because it depends upon detector diode quality. In fact, one is suprised to find that detection efficiency is relatively undiscussed in standard engineering texts. Although matched detectors are easily made at microwave frequencies, they can be relatively inefficient unless care is taken. At lower frequencies 50 percent efficiencies can be easily obtained, so there is reason to expect efficiencies of this order at microwave frequencies too, but further study of this question is still in progress. Therefore, by using a circulator, so the sole contribution to η^2 will be from envelope detection, and using efficient diodes, η^2 can be as large as 1/2 in this case. Without a circulator, or other means of isolation, direct slope detection should be used which yields $\eta^2 = (1/4)(1/2) = 1/8$.

9.2.3 The Effect of Direct Slope Detection on Circuit Properties. The pump tank can be tuned for direct amplitude modulation by placing ω_p at one of the half-power frequencies, but then a new constraint must replace (9.1). Using upper and lower signs ($\pm$) to denote tuning to the upper and lower half-power points respectively, then

$$Y_u \cong g_p\left[1 \pm j(1 \pm \omega_r/\beta_p)\right]$$

$$Y_\ell \cong g_p\left[1 \pm j(1 \mp \omega_r/\beta_p)\right] . \qquad (9.74)$$

The approximations above are excellent for $\omega_r < Q_p\beta_p$, which will be an ample range if $Q_p \geq 3$.

The effect of slope detection is demonstrated most clearly by the input admittance at ω_r. In this case, (8.2) yields

$$Y_{r_{in}} = Y_r + \frac{\omega_r\omega_p|V_p|^2}{g_p}\left[\frac{\mp\frac{\omega_r}{\beta_p} \mp j\left(1 - \frac{\omega_r^2}{2\beta_p^2}\right)}{1 + \left(\frac{\omega_r^2}{2\beta_p^2}\right)^2} + \mathcal{O}\left(\frac{\omega_r}{\omega_p}\right)\right] \qquad (9.75)$$

which has several interesting properties. Considering first the case where ω_r is small, the main effect of pumping is the reflection of an input capacity

$$\mp \frac{\omega_p|\gamma_p|^2}{g_r} . \qquad (9.76)$$

Therefore, when the pump is tuned to the upper half-power point, the reflected input susceptance tends to cancel the nominal input susceptance $\omega_r C_r$. Just the reverse occurs at the lower sideband. One other effect is a reflected conductance

$$\mp \frac{\omega_r^2\omega_p|V_p|}{g_p} \qquad (9.77)$$

which is negative when tuning is to the upper half-power point. Together these effects yield a useful variety of circuit properties.

To study the input circuit properties in this case it is convenient to rewrite (9.37) as follows:

$$Y_{r_{in}} = g_r \left[1 \mp \frac{\mu\lambda^2}{1 + (\frac{\lambda}{2})^2} + j\frac{\lambda}{\nu}\left(1 \mp \frac{\mu\nu}{1 + (\frac{\lambda}{2})^2} \right) \right] \tag{9.78a}$$

$$\lambda = \omega_r/\beta_p \qquad \nu = \beta_r/\beta_p \qquad \mu = \frac{\omega_p k_p^2}{\beta_r} \quad . \tag{9.78b}$$

Perhaps the most interesting situation occurs at the upper half-power point, where increased bandwidth is possible. Study of this relation shows how input capacity is cancelled in proportion to the product $\mu\nu$. However, when $\lambda \approx 1$, a peak negative conductance appears which threatens stability. Therefore, to insure stability, a compromise must be made between suppressing capacity and introducing negative conductance.

The normal input bandwidth in the absence of pumping is $\lambda_{1/2} = \nu$. Therefore, if $\nu \leq 1/2$, the input bandwidth could be doubled and still the sidebands would remain in a region of linear slope on the pump resonance. By some experimentation with (9.18), it can be shown that $\mu\nu = 1/2$ approximately doubles the input bandwidth if $\nu \leq 1/2$, with a fairly safe stability margin.

In contrast, if $\mu\nu = 1$, the input susceptance is nearly zero over the entire linear slope of the pump tank ($0 < \lambda < 1$), but negative reflected conductance will produce instability for $1/\mu < \lambda < 1$. Therefore, operating at the upper half-power point provides a safe increase in bandwidth, up to a factor of about two, such that

$$(\beta_r)_{effective} \approx 2\,\beta_r \quad . \tag{9.79}$$

The asymmetry demonstrated in (9.78), with respect to the side of resonance being used, can be attributed to sideband distortion. At the upper half-power point, the lower sideband is enhanced at the expense of the upper sideband, so the negative conductance from the lower sideband is no longer balanced out by positive conductance reflected by the upper sideband. Just the reverse situation occurs on the lower side of resonance.

It is interesting to also examine the effect of sideband asymmetry on conversion gain. The gain relation corresponding to (9.17) in the case of direct slope detection is

$$G_{AM} = \frac{4\, g_r g_p}{\left|Y_{r_{in}}\right|^2} \left|\frac{V_p}{V_r}\right| \left[\begin{array}{l}\text{maximum real com-}\\ \text{ponent of } (V_u + V_\ell)/V_p\end{array}\right] \tag{9.80}$$

where voltage ratios needed above can be found by repeating the derivation of (9.3), but using (9.74) instead of (9.1). Now

$$\frac{V_u}{V_p} = \frac{-j\omega_u \gamma_r}{g_p[1 \pm j(1 \pm \lambda)]} \quad ; \quad \frac{V_\ell}{V_p} = \frac{-j\omega_\ell \gamma_r^*}{g_p[1 \pm j(1 \mp \lambda)]} \tag{9.81}$$

and hence

$$\left[\begin{array}{l}\text{maximum real component}\\ \text{of } (V_u + V_\ell)/V_p\end{array}\right] \approx \frac{1}{2}\left(\frac{\omega_p \left|\gamma_r\right|}{g_p}\right) F(\lambda) \tag{9.83}$$

where

$$F(\lambda) = \left[\frac{1}{1 + (1 \pm \lambda)^2} + \frac{1}{1 + (1 \mp \lambda)^2}\right] \tag{9.83}$$

Since $F(\lambda)$ is symmetrical in λ, it is independent of the choice of operating slope, and so the only asymmetry in G_{AM} with respect to side-of-resonance will be that due to $Y_{r_{in}}$. $F(\lambda)$ is plotted in Fig. 9.13 showing that it is essentially constant for $\lambda < 2.2$. Therefore, the effective half-bandwidth of the pump tank is

$$(\beta_p)_{\text{effective}} = 2.2\, \beta_p \ .$$

Because $F(\lambda)$ is essentially $\leq F(0)$ always, the midband gain can be taken at $\lambda = 0$, which yields

$$\overline{G}_{AM} = \frac{4\, \omega_p^2 \left|\gamma_p\right|^2}{g_r g_p} = \frac{2k_p^2 \omega_p^2}{\beta_r \beta_p} \tag{9.84}$$

By comparison with (9.23), $\overline{G}_{AM}$ is 1/4 as large as $\overline{G}_{PM}$ for the same γ_p, and hence 1/8 as large for the same pump power.

While these conclusions regarding gain reduction are consistent with the observations in Section 9.2.1, the latter suggest nothing about the bandwidth improvement. Because both β_r and β_p are effectively doubled with direct slope detection, β_r and β_p need

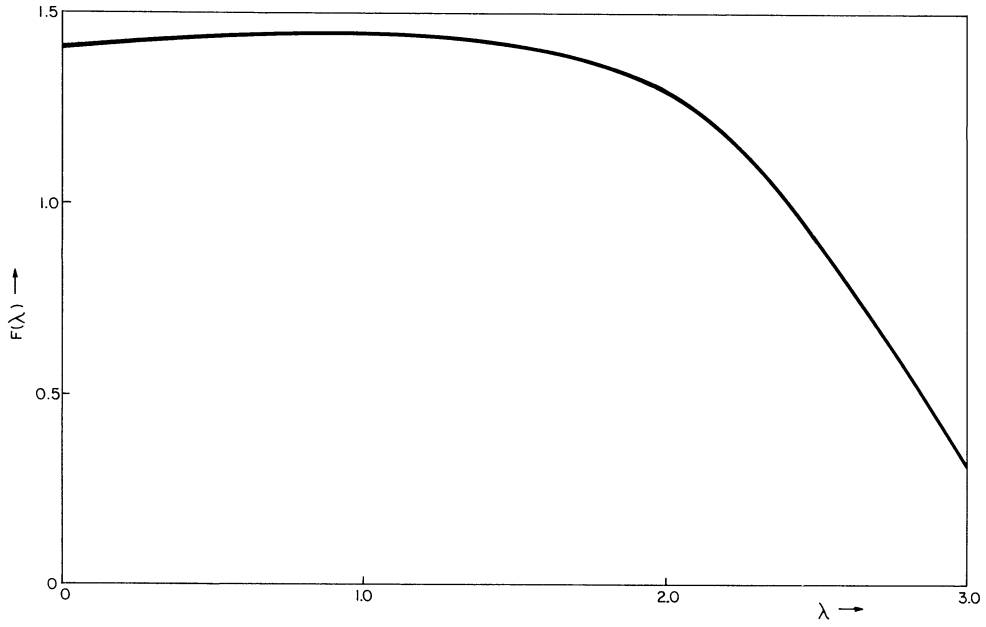

Fig. 9.13. $F(\lambda)$ in (9.38).

be only half as large in (9.84) as in (9.23). Therefore, for a given bandwidth and pumping coefficient, $\overline{G}_{AM}$, and $\overline{G}_{PM}$ can be equally large, but for different circuit adjustments.

However, in spite of this theoretical conclusion, direct slope detection will be less preferable in practice because of its greater sensitivity to adjustment. Without good detector isolation, such as that achieved with a circulator, the tuning adjustments for gain and detection are dependent on one another, which makes them more critical. Also, with the appearance of negative resistance at the input terminals, stability will be more critically dependent on pump tuning with direct slope detection.

9.3 Conclusions

The form of double-sideband reactive mixing that has been treated in this chapter yields an immediate practical application, namely the construction of an ultra-wideband video amplifier. This technique uses a form of reactive mixing to phase modulate a pump or carrier. The, when the latter is detected, an amplified video signal will result. The treatment of this problem has considered first the modulation process, and secondly the detection process. The optimization of both has been discussed, with the result that gain-bandwidth products of the order of 1000 Mc are possible. Much experimental work has been done in connection with this principle, which the reader will find discussed in Chapter XI.

The application of varactors to wideband video amplifiers is original with the present writer, as far as he knows, but the principle used here can be traced back several decades (Ref. 2). Nearly all prior attention to this concept can be found in the field of magnetic amplifiers, but there, little attention is given to ultra-wideband systems, mainly due to the type of material used. It can be said that the advent of microwave varactors has lead to wideband generalizations of basic magnetic amplifier principles. However, the customary form of analysis in reactive mixer circuits tends to obscure these relationships. Hopefully, the present analysis has bridged this gap.

CHAPTER X

DOUBLE-SIDEBAND MIXING WITH HARMONIC PUMPING

Several improvements have been demonstrated by the comparison of double-sideband reactive mixing in Chapter VIII with single-sideband conversion. The most noteworthy improvements were with respect to the upper sideband, and were due to negative resistance being reflected from ω_ℓ. Such negative resistance increased the conversion gain and also made possible parametric amplification at ω_u. However, the scope of these improvements was limited because the negative resistance increased the sensitivity to external circuitry at the input and output terminals. It will now be shown that the above limitations can be further relaxed by adding the pump harmonic.

One characteristic of the configuration treated in Chapter VIII is the lack of a direct coupling between ω_ℓ and ω_u. However this limitation can be overcome by adding the pump harmonic. With this added coupling, each pair of signal frequencies interacts in two ways. For example, a signal at ω_u is coupled directly to ω_r by the pump fundamental. It is also indirectly coupled to ω_r through ω_ℓ, by first mixing with the pump harmonic to yield ω_ℓ, which in turn mixes with ω_p to yield ω_r.

The scope of the present chapter will be to study the properties associated with this greater coupling flexibility. These properties can be divided into two categories according to whether the sidebands are independently or dependently loaded. In the former category, the following properties will be noted:

(1) Unilateral up- or down-conversion between any two of the three signal frequencies ω_r, ω_ℓ, and ω_u.

(2) Simultaneous unilateral conversion from ω_r to ω_ℓ and from ω_u to ω_ℓ, and vice versa.

(3) Arbitrarily large conversion gains between ω_r and ω_u with gain independent matching at the input and output terminals.

(4) Gain-bandwidth products and noise figures that compare favorably with those in conventional reactive mixers.

In the case of dependent sideband loading it will be shown that considerable improvement in gain-bandwidth product can result from harmonic pumping. It therefore provides a means for cascading phase modulation amplifiers, as described in Chapter IX, without using interstage phase detection. This point will be further expounded in Section 10.4, but since the case of independent sideband loading is the more general of the two, it will be treated first, and than dependent loading taken as a special case.

10.1 Basic Analysis of Harmonic Pumping

Mathematically, the first-order coupling of ω_r, ω_ℓ, ω_u, ω_p, and $2\omega_p$ is described by (2.27), which is already familiar through the special cases treated in previous chapters. In fact, relative to the treatment in Chapter VIII, all that is necessary to restore (2.27) to its most general form is to account for the pump harmonic by adding γ_{2p}. The formal solution of (2.27) is straightforward, but there are ten or more independent parameters in this equation, so more than a formal solution is required to understand all of the effects involved. The equivalent circuit for this configuration is Fig. 1.2.

In analyzing (2.27), no assumptions will be made regarding the relative phases of γ_p and γ_{2p}, so a phase parameter ξ will be introduced. It is convenient to define ξ by the relation

$$\frac{\gamma_p^{\,2}\,\gamma_{2p}^{*}}{|\gamma_p^{\,2}\,\gamma_{2p}|} = \epsilon^{j\xi} \tag{10.1a}$$

Another helpful variable change is to introduce the following set of normalized admittances

$$\tau_r = \frac{Y_r|\gamma_{2p}|}{\omega_r|\gamma_p|^2} = \tau_r' + j\tau_r'' \tag{10.1b}$$

$$\tau_u = \frac{Y_u}{\omega_u|\gamma_{2p}|} = \tau_u' + j\tau_u'' \tag{10.1c}$$

$$\tau_\ell = \frac{Y_\ell^{*}}{\omega_\ell|\gamma_{2p}|} = \tau_\ell' + j\tau_\ell'' \tag{10.1d}$$

They are proportional to the actual terminal admittances for constant pump level. In the present application of (10.1), no restrictions on sideband loading are imposed, so τ_r, τ_u, and τ_ℓ are independent parameters.

As an illustration of their usefulness, the normalized admittances reduce the system determinant of (2.27) to the following expression:

$$\Delta = \omega_r \omega_\ell \omega_u |\gamma_{2p}|^2 \gamma_{2p} \tilde{\Delta} \tag{10.2a}$$

where

$$\tilde{\Delta} = \tau_r \tau_\ell \tau_u + \tau_\ell - \tau_r - \tau_u + 2j\cos\xi \tag{10.2b}$$

This determinant is particularly important in applying the stability criterion of Chapter VI. The latter predicts that the region of validity of all steady-state solutions can be determined by the vanishing of Δ, and all solutions must eventually be tested in this way. For example, if a set of terminal admittances and pump levels are chosen to yield a certain circuit effect, then Δ must not vanish even as the pumps are brought up to the required level. In the absence of pumping

$$\Delta = Y_r Y_u Y_\ell^* \tag{10.2c}$$

The formal solution of (2.27) is achieved through the inversion of its admittance matrix $[Y]$. Using the notation in (10.2), it becomes

$$[Y]^{-1} = \frac{1}{\tilde{\Delta}} \begin{bmatrix} \dfrac{|\gamma_{2p}|(\tau_u\tau_\ell - 1}{\omega_r |\gamma_p|^2} & \dfrac{\tau_\ell + j\epsilon^{j\xi}}{j\omega_u \gamma_p} & \dfrac{\tau_u - j\epsilon^{-j\xi}}{j\omega_\ell \gamma_p^*} \\ \dfrac{\tau_\ell + j\epsilon^{-j\xi}}{j\omega_r \gamma_p^*} & \dfrac{\tau_r\tau_\ell - 1}{\omega_u |\gamma_{2p}|} & \dfrac{\tau_r - j\epsilon^{j\xi}}{j\omega_\ell \gamma_{2p}^*} \\ \dfrac{-\tau_u + j\epsilon^{+j\xi}}{j\omega_r \gamma_p} & \dfrac{-\tau_r + j\epsilon^{-j\xi}}{j\omega_u \gamma_{2p}} & \dfrac{\tau_r\tau_u + 1}{\omega_\ell |\gamma_{2p}|} \end{bmatrix} \tag{10.3}$$

The diagonal terms in (10.3) are of particular interest because they are the input impedance as experienced by an ideal source at each terminal in Fig. 2.1. In the cases treated previously, with $\gamma_{2p} = 0$, the various network effects have often been strongly dependent on negative terminal resistance, so it is important to see if this would again be the case. However, more convenient expressions result from considering the input admittance as given by the reciprocal of each diagonal element in (10.3). The result is

$$Y_{r_{in}} = \frac{\omega_r |\gamma_p|^2}{|\gamma_{2p}|} \tau_{r_{in}} \quad ; \quad \tau_{r_{in}} = \tau_r + \frac{\tau_\ell - \tau_u + 2j\cos\xi}{\tau_u \tau_\ell - 1} \tag{10.4a}$$

$$Y_{u_{in}} = \omega_u |\gamma_{2p}| \tau_{u_{in}} \quad ; \quad \tau_{u_{in}} = \tau_u + \frac{\tau_\ell - \tau_r + 2j\cos\xi}{\tau_r \tau_\ell - 1} \tag{10.4b}$$

$$Y_{\ell_{in}} = \omega_\ell |\gamma_{2p}| \tau_{\ell_{in}} \quad ; \quad \tau_{\ell_{in}} = \tau_\ell + \frac{\tau_r + \tau_u - 2j\cos\xi}{\tau_r \tau_u + 1} \tag{10.4c}$$

Again the normalized notation of (10.2) has been used, but the first term in each expression above can be identified with the terminal admittance in the absence of pumping, while the second term denotes the admittance reflected by pumping. The appearance of both the terminal and the reflected admittance in one expression makes this definition of input admittance particularly convenient for comparisons.

10.2 General Physical Interpretations

The physical significance of (10.4) can be seen by calculating the normalized image admittance relating each pair of frequencies. If ω_1 and ω_2 denote a general pair of frequencies, then the image admittance is

$$Y_{12} = \sqrt{Y_{1(s)}\, Y_{1(o)}} \tag{10.5}$$

where $Y_{1(s)}$ and $Y_{1(o)}$ denotes the reflected admittance at ω_1 due to a short or open respectively at ω_2. By applying this concept to (10.4), the following image admittances result:

between ω_r and ω_u: $\quad Y_{ru} = \dfrac{\omega_r |\gamma_p|^2}{|\gamma_{2p}|} \tau_{ru} \quad ; \quad Y_{ur} = \omega_u |\gamma_{2p}| \tau_{ur}$

(10.6a)

$$\tau_{ru} = \pm \tau_{ur} = \sqrt{\frac{\tau_\ell + 2j\cos\xi}{\tau_\ell}}$$

between ω_r and ω_ℓ:

$$Y_{r\ell} = \frac{\omega_r |\gamma_p|^2}{|\gamma_{2p}|}\,\tau_{r\ell}\ ; \qquad Y^*_{\ell r} = \omega_\ell |\gamma_{2p}| \tau_{\ell r} \tag{10.6b}$$

$$\tau_{r\ell} = \pm \tau_{\ell r} = \sqrt{\frac{\tau_u - 2j\cos\xi}{\tau_u}}$$

between ω_ℓ and ω_u:

$$Y^*_{\ell u} = \omega_\ell |\gamma_{2p}| \tau_{\ell u}\ ; \qquad Y_{u\ell} = \omega_u |\gamma_{2p}| \tau_{u\ell} \tag{10.6c}$$

$$\tau_{\ell u} = \pm \tau_{u\ell} = \sqrt{\frac{\tau_r - 2j\cos\xi}{\tau_r}}$$

Since the expressions above are somewhat foreign looking, a useful interpretation is provided by transmission line theory, where image admittance is equivalent to characteristic admittance. This identification is convenient in the present case because the magnitudes of the normalized image admittances are independent of direction, and therefore the set (10.6) gives rise to the informative representations in Fig. 10.1.

The second transmission line characteristic of interest is the propagation constant θ, which is generally defined by

$$\theta_{12} = \ln\left(\frac{V_2}{V_1}\sqrt{\frac{Y_{12}}{Y_{21}}}\right) \tag{10.7}$$

To make the propagation constant more informative, it will be applied only to the transmission line portions of Fig. 10.1, which yields

$$\epsilon^{\theta_{ru}} = \frac{-j\gamma_p}{|\gamma_{2p}|}\,\frac{\tau_\ell + j\epsilon^{-j\xi}}{\tau_u\tau_\ell - 1} \quad (a); \qquad \epsilon^{\theta_{ur}} = \frac{-j\gamma_p|\gamma_{2p}|}{|\gamma_p|^2}\,\frac{\tau_\ell + j\epsilon^{j\xi}}{\tau_r\tau_\ell - 1} \quad (b)$$

$$\epsilon^{\theta_{r\ell}} = \frac{-j\gamma_p}{|\gamma_{2p}|}\,\frac{-\tau_u + j\epsilon^{j\xi}}{\tau_u\tau_\ell - 1} \quad (c); \qquad \epsilon^{\theta_{\ell r}} = \frac{-j\gamma_p|\gamma_{2p}|}{|\gamma_p|^2}\,\frac{\tau_u - j\epsilon^{-j\xi}}{\tau_r\tau_u + 1} \quad (d) \tag{10.8}$$

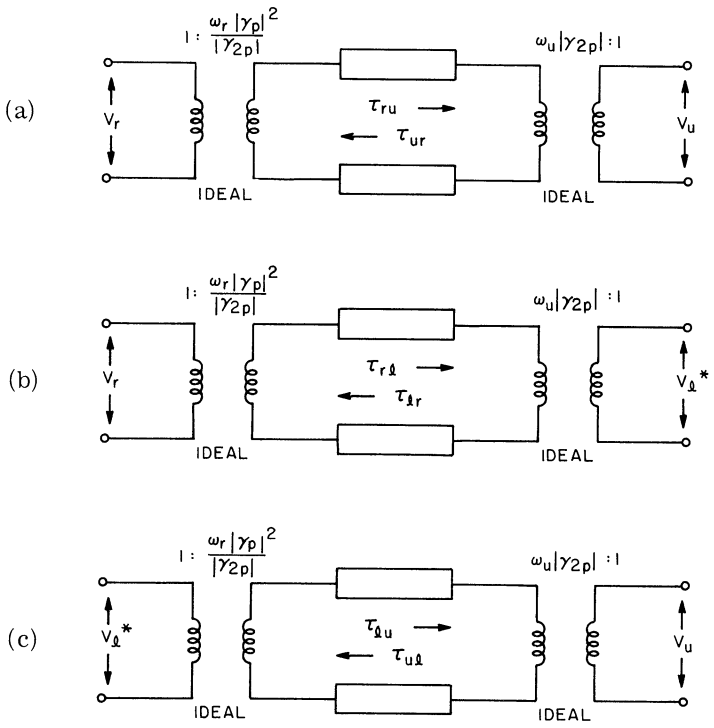

Fig. 10.1. Transmission line representations of the three possible conversions between ω_r, ω_ℓ, and ω_u.

$$\epsilon^{\theta_{\ell u}} = \frac{-j\gamma_{2p}}{|\gamma_{2p}|}\ \frac{\tau_r - j\epsilon^{j\xi}}{\tau_r\tau_u + 1}\quad \text{(e)}; \qquad \epsilon^{\theta_{u\ell}} = \frac{-j\gamma_{2p}}{|\gamma_{2p}|}\ \frac{-\tau_r + j\epsilon^{-j\xi}}{\tau_r\tau_\ell - 1}\quad \text{(f)} \tag{10.8}$$

In studying these relations, we first note that

$$\theta_{ij} \neq \theta_{ji} \qquad (i, j = r, \ell, u) \tag{10.9}$$

and hence the transmission lines in Fig. 10.1 are nonreciprocal. In fact, they can even be unilateral.

To illustrate the latter point, the numerator of (10.8a) can be written

$$\tau_\ell + (\sin\xi + j\cos\xi) \tag{10.10}$$

and therefore if

$$\tau_\ell = |\sin\xi| - j\cos\xi; \qquad \pi < \xi < 2\pi \tag{10.11}$$

(10.10) will vanish. There is no transmission from ω_r to ω_u in this case.

In contrast, the numerator of (10.8b) can be written

$$\tau_\ell + (-\sin\xi + j\cos\xi) \tag{10.12}$$

which does not vanish but equals $2|\sin\xi|$ when (10.11) is satisfied. However, the vanishing of $e^{\theta_{ur}}$ and $e^{\theta_{ru}}$ reverses when $0 < \xi < \pi$. Hence, between each terminal pair in Fig. 2.1, a state of unilateral conversion can be set up, whose conversion direction depends only on the relative phase of the pump and its harmonic.

Further inspection of (10.9) yields the following general conditions under which unilateral conversion is possible:

$$\text{between } \omega_r \text{ and } \omega_u; \qquad \text{if } \tau = \tau_o^* \tag{10.13a}$$

$$\text{between } \omega_r \text{ and } \omega_\ell; \qquad \text{if } \tau_u = \tau_o \tag{10.13b}$$

$$\text{between } \omega_\ell \text{ and } \omega_u; \qquad \text{if } \tau_r = \tau_o \tag{10.13c}$$

where

$$\tau_o = |\sin\xi| + j\cos\xi \tag{10.14a}$$

$$|\tau_o| = 1$$

Hence, unilateral conversion between each pair of frequencies depends only on the termination at the third frequency. The direction of unilateral conversion depends on the sign of $\sin\xi$.

The characteristic admittances also take on interesting values under (10.13). These are noted below:

$$\text{if } \tau_\ell = \tau_o^*: \qquad \tau_{ru} = -\tau_o = \tau_{ur} \tag{10.15a}$$

$$\text{if } \tau_u = \tau_o: \qquad \tau_{r\ell} = \tau_o = -\tau_{\ell r} \tag{10.15b}$$

$$\text{if } \tau_r = \tau_o: \qquad \tau_{u\ell} = \tau_o = -\tau_{\ell u} \tag{10.15c}$$

The sign of each characteristic admittance cannot be determined directly from (10.6), but it must be found from the corresponding input admittance in (10.4). For example, setting $\tau_\ell = \tau_o^*$ in (10.4a) yields

$$\tau_{r_{in}} = \tau_r + \frac{\tau_o - \tau_u}{\tau_u \tau_o^* - 1} \tag{10.16a}$$

which seems to depend on τ_u. However, by (10.14b), $\tau_o^* = 1/\tau_o$, so (10.15) reduces to

$$\tau_{r_{in}} = \tau_r - \tau_o \tag{10.16b}$$

which agrees with (10.15a). It is reasonable that each input admittance would be independent of the output load in the unilateral condition, since unilatarity depends only on the loading at the third frequency in each case. Therefore, a result similar to (10.16b) is found for the other input admittances as summarized in Table 10.1.

Direction of Zero Conversion Gain	Conditions		Image Admittance (Normalized)
	Critical Load	Sin ξ	
$\omega_r \rightarrow \omega_u$	$\tau_\ell = \tau_o^*$	< 0	$-\tau_o$
$\omega_u \rightarrow \omega_r$		> 0	$-\tau_o$
$\omega_r \rightarrow \omega_\ell$	$\tau_u = \tau_o$	< 0	τ_o^*
$\omega_\ell \rightarrow \omega_r$		> 0	$-\tau_o^*$
$\omega_u \rightarrow \omega_\ell$	$\tau_r = \tau_o$	< 0	τ_o^*
$\omega_\ell \rightarrow \omega_u$		> 0	$-\tau_o^*$

Table 10.1. A summary of conditions associated with unilateral conversion gains.

It is important to observe that the critical parameter τ_o is real when $\xi = \pm \pi/2$, which corresponds to γ_{2p} being 90^o out of phase with γ_p. Therefore, the original assumption of arbitrary pump phase is crucial to the main conclusions of this chapter. It is noteworthy that the least rewarding case occurs when the pumps are in phase, although this case might have been chosen initially for analytical reasons. Had this case been assumed, the

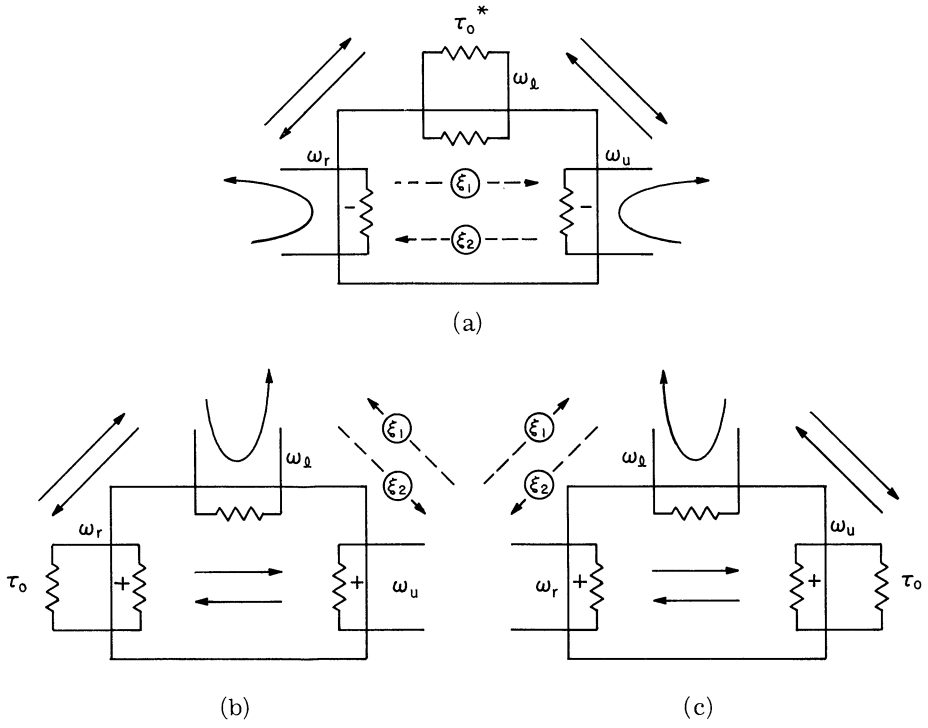

Fig. 10.2. The three basic configurations for unilateral conversion.
Key: $\pi < \xi_1 < 2\pi$; $0 < \xi_2 < \pi$; ⟶ nonvanishing conversion;
----ξ--→ unilateral conversions, vanishing for $\xi \overset{k}{=} \xi_k$.

unique features of harmonic pumping would have been missed. Further consequences of the choice of ξ will become evident later, but in general the more ξ differs from $\pi/2$, the harder it is, for practical reasons, to achieve unilateral conversion.

Continuing our evaluation by transmission line terminology, two important facts can now be noted about (10.8) and (10.15).

(1) The transfer functions in (10.8) dealing with conversions that originate at either ω_r or ω_u have singular points when $\tau_\ell = 1/\tau_u$ or $1/\tau_r$, respectively, and hence large conversion gains can occur in these cases.

(2) The transmission lines in Fig. 10.1 can have negative as well as positive characteristic admittances so reflection gains can be obtained at any frequency.

These remarks are depicted in Fig. 10.2, where three-port networks are used to illustrate the three conditions of unilateral conversion.

It is interesting to note the similarity between the (b) and (c) parts of Fig. 10.2. In fact, the symmetry with respect to ω_r and ω_u has been apparent in each expression derived so far, particularly where the normalized factors are concerned. Therefore, unilateral conversion can be treated in two cases rather than three. The first is depicted by Fig. 10.2a, which corresponds to (10.13a). In this case, the coupling between ω_r and ω_ℓ resemble a conventional lower-sideband converter, but in addition ω_ℓ and ω_u are regeneratively coupled so amplification by reflection can take place at ω_u. However, the most unusual feature of this configuration is the nonreciprocal conversion between ω_r and ω_u, which provides a means for unilateral conversion with large forward gain. Also, the forward direction can be changed by varying the relative phase of the two pumps.

The second case that will be separated from Fig. 10.2 is a combination of the configurations in (b) and (c). If $\tau_r = \tau_o$, as depicted in (b), then $\tau_u = \tau_r$ produces a conjugate match at ω_u, which corresponds to (c). Therefore, both (b) and (c) can exist simultaneously, and the resulting configuration is shown in Fig. 10.3. It yields two unilateral couplings, so the only transmission between ω_r and ω_u in this case is by the direct path. Coupling through ω_ℓ goes only one way. As a result, the conjugate match at ω_r and ω_u is independent of τ_ℓ, the normalized load at ω_ℓ. Since this second case (in Fig. 10.3) is more novel than the first (in Fig. 10.2a), it will receive the major attention of the remainder of this chapter.

10.3 Circuit Properties of Fig. 10.3

The basic properties that distinguish Fig. 10.3 from other circuits are gain, bandwidth, stability, parameter sensitivity, and noise figure. These can all be obtained systematically from (10.3), which will now be done in such a way that the results can be easily compared with those of the other configurations previously treated.

10.3.1 Gain and Bandwidth.

The first circuit property of interest will be the conversion gain between each pair of terminals. Although the general gain definition in (3.15a) will again be used, in the present analysis it is convenient to note that

$$G_{ij} = 4\, g_S g_L \left| [Y^{-1}]_{ji} \right|^2 ; \quad i,j = r, \ell, u \tag{10.17}$$

where $[Y^{-1}]_{ji}$ denotes the diagonal element of (10.3), and where g_S and g_L are the source

and load conductance at either terminal. Therefore, when the constraint $\tau_r = \tau_u = \tau_o$ is introduced, the gain expressions in Table 10.2 result. It is particularly interesting to note, due to the signs in Table 10.2, that only the denominators vanish. In addition, the following basic properties can also be observed for this case.

Gain Function	Sin $\xi > 0$	Sin $\xi < 0$
$\overline{G}_{ru}$	$\dfrac{\omega_u[(\tau'_\ell + \sin\xi)^2 + (\tau''_\ell + \cos\xi)^2]}{\omega_r[(\tau'_\ell - \sin\xi)^2 + (\tau''_\ell + \cos\xi)^2]}$	$\dfrac{\omega_u}{\omega_r}$
$\overline{G}_{ur}$	$\dfrac{\omega_r}{\omega_u}$	$\dfrac{\omega_r[(\tau'_\ell - \sin\xi)^2 + (\tau''_\ell + \cos\xi)^2]}{\omega_r[(\tau'_\ell + \sin\xi)^2 + (\tau''_\ell + \cos\xi)^2]}$
$\overline{G}_{r\ell}$	$\dfrac{4\,\omega_\ell\,\tau'_\ell \sin\xi}{\omega_r[(\tau'_\ell - \sin\xi)^2 + (\tau''_\ell + \cos\xi)^2]}$	0
$\overline{G}_{\ell r}$	0	$\dfrac{4\,\omega_r\tau'_\ell \sin\xi}{\omega_\ell[(\tau'_\ell + \sin\xi)^2 + (\tau''_\ell + \cos\xi)^2]}$
$\overline{G}_{\ell u}$	$\dfrac{4\,\omega_u\tau'_\ell \sin\xi}{\omega_\ell[(\tau'_\ell - \sin\xi)^2 + (\tau''_\ell + \cos\xi)^2]}$	0
$\overline{G}_{u\ell}$	0	$\dfrac{4\,\omega_\ell\,\tau'_\ell \sin\xi}{\omega_u[(\tau'_\ell + \sin\xi)^2 + (\tau''_\ell + \cos\xi)^2]}$

Table 10.2. Conversion gains when $\gamma_1 = \gamma_2 = \gamma_r$.

1. With $\tau''_\ell = \cos\theta$, arbitrarily large gains can be obtained between each frequency pair as $\tau'_\ell \to \sin\theta$. (Note: $\tau_\ell = \tau'_\ell + j\tau''_\ell$)
2. With sources at ω_r or ω_u, the input terminals are conjugately matched independently of gain, and therefore input circulators are never needed.
3. Unilateral gain is possible between ω_r and ω_ℓ, and between ω_u and ω_ℓ, for any value of forward gain.

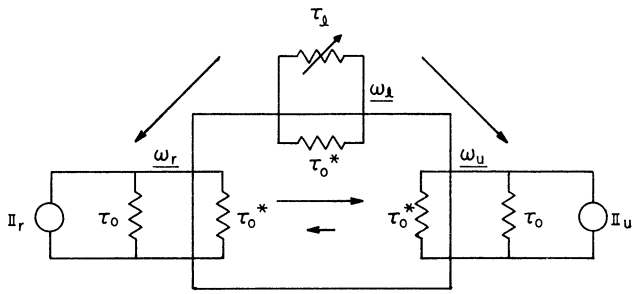

Fig. 10.3. Matched-up conversion from ω_r to ω_u, for $\tau_r = \tau_u = \tau_o$. Solid arrows depict the direction and relative magnitude of conversion gain for $0 < \xi < \pi$. All arrows reverse for $\pi < \xi < 2\pi$.

4. Although conversion between ω_r and ω_u is not unilateral, the ratio of forward to backward gain is proportional to forward gain, and hence can be made arbitrarily large.

The variable gain functions in Table 10.2 are large only when their denominators are small, and hence when $\Delta \approx 0$. Therefore, the bandwidths of each conversion depend solely on $\widetilde{\Delta}$, which is proportional to Δ. By (10.2b) and (10.4c)

$$\widetilde{\Delta} = (\tau_r \tau_u + 1)\, \tau_{\ell_{in}} \tag{10.18a}$$

which in the present case becomes

$$\widetilde{\Delta} = (2\tau_o + 1)\, \tau_{\ell_{in}} \tag{10.18b}$$

where the first factor is a constant. Therefore, the conversion bandwidth depends only on the bandwidth at the lower sideband terminals.

To calculate this large-gain bandwidth, let $\tau''_\ell = -\cos\xi$ at midband ($\overline{\omega}_\ell$) and let $\omega_\ell = \overline{\omega}_\ell(1 + \delta)$, where $|\delta| << 1$. Then by (10.4c)

$$\tau''_\ell \approx \frac{2C_\ell}{|\gamma_{2p}|} \left[\delta - \frac{|\gamma_{2p}|}{2C_\ell} \cos\xi\right] \tag{10.19}$$

where C_ℓ is the total fixed capacity at ω_ℓ. The bandwidth β can then be determined from the value of δ that yields

$$(\tau''_\ell + \cos\xi)^2 = (\tau'_\ell - \sin\xi)^2 \tag{10.20}$$

The result is

$$\beta = \frac{\overline{\omega}_\ell |\gamma_{2p}|(\tau'_\ell - |\sin\xi|)}{C_\ell - \frac{1}{2}|\gamma_{2p}\cos\xi|} \tag{10.21}$$

For large gains, $\tau'_\ell \approx |\sin\xi|$, and therefore the gain-bandwidth product for conversion between ω_r and ω_u is given by (i, j = r or u)

$$\sqrt{\overline{G}_{ij}}\ \beta = \sqrt{\frac{\overline{\omega}_j}{\overline{\omega}_i}}\ \frac{2\overline{\omega}_\ell |\gamma_{2p}\sin\xi|}{C_\ell - \frac{1}{2}|\gamma_{2p}\cos\xi|} \tag{10.22}$$

It is evident that $\xi = \pm\frac{\pi}{2}$ is optimum in this case, which can be explained by noting, in the basic condition $\tau_r = \tau_u = \tau_o$, that detuned terminals are required whenever $\xi \neq \pm\frac{\pi}{2}$. That is, in the absence of pumping, each terminal must be detuned in proportion to $\cos\xi$, so when the pumps are applied the reflected susceptance yields the required tuning. But, in addition to being inconvenient from a practical point of view, $\xi = \pm\frac{\pi}{2}$ yields reduced bandwidth. In the limit of in-phase pumps ($\xi = 0$), the gain-bandwidth product vanishes.

It is interesting to compare the gain-bandwidth product in (10.22) with that of a conventional upper-sideband up-converter. Assuming the optimum case, where $\xi = \pm\frac{\pi}{2}$, and defining the coefficient of harmonic pumping as

$$k_{2p} = \frac{\gamma_{2p}}{C_\ell} \tag{10.23}$$

then (10.22) yields

$$\sqrt{\overline{G}_{ru}}\ \beta = 2k_{2p}\sqrt{\frac{\overline{\omega}_\ell{}^2\omega_u}{\omega_r}} \approx 2k_{2p}\frac{\omega_p^{3/2}}{\omega_p^{1/2}} \tag{10.24a}$$

while from Table 3.1, in the conventional case,

$$\sqrt{\overline{G}_{ru}}\ \beta = 2k_p\omega_u \approx 2k_p\omega_p \tag{10.24b}$$

Therefore, by adding the pump harmonic, the gain-bandwidth product can increase by

$$\frac{k_{2p}}{k_p}\sqrt{\frac{\omega_p}{\omega_r}} \tag{10.24c}$$

When $\xi = \pm\frac{\pi}{2}$, $g_r = \omega_r|\gamma_p|^2/|\gamma_{2p}|$ while $g_u = \omega_u|\gamma_{2p}|$. Therefore, (10.24c) calls for $g_u >> g_r$. This is quite different from the simple upper-sideband converter described by (10.24b), which calls for $g_u \approx g_r$. An important advantage in the double-pump case is that β is independent of the bandwidths at the ω_r and ω_u terminals, which means greater flexibility in realizing the gain-bandwidth product in (10.24a).

10.3.2 Stability. Since it has been noted that the high gains in Table 10.2 are associated with Δ approaching zero, the question of stability arises. For $\tau_r = \tau_u = \tau_o$, Δ can be regarded as a function of τ_ℓ, and it vanishes only when $\tau_\ell = \tau_o^*$. Therefore, a sufficient condition for stability is $\tau'_\ell > |\sin\xi|$. However, the normalization that has been introduced in the τ parameters somewhat obscures the effect of pump variation on stability. Therefore let us consider the case where $\xi = \pm\frac{\pi}{2}$, such that $\tau_r = \tau_u = \tau_o = 1$ are appropriate conditions for realizing Fig. 10.3. By (10.2), $\tau_r = \tau_u = 1$ yields

$$g_r = \frac{\bar{\omega}_r|\bar{\gamma}_p|^2}{|\bar{\gamma}_{2p}|^2}\ ; \qquad g_u = \bar{\omega}_u|\bar{\gamma}_{2p}| \tag{10.25}$$

where $\bar{\gamma}_p$ and $\bar{\gamma}_{2p}$ denote the final operating values of γ_p and γ_{2p}, respectively. That is, γ_p and γ_{2p} equal $\bar{\gamma}_p$ and $\bar{\gamma}_{2p}$ when the pumps are warmed up. Then at midband

$$\Delta = \bar{\omega}_r\bar{\omega}_\ell\bar{\omega}_u|\bar{\gamma}_{2p}|\left\{|\gamma_{2p}|^2\left(\frac{g_\ell}{\bar{\omega}_\ell|\gamma_p|}-1\right)+|\bar{\gamma}_p|^2\frac{g_\ell}{\omega_\ell|\gamma_{2p}|}-\left(\frac{|\gamma_{2p}|}{|\bar{\gamma}_{2p}|}\right)^2\right\} \tag{10.26}$$

which is positive for $\tau_\ell = g_\ell|\bar{\omega}_\ell|\gamma_{2p}| >$ as long as $|\gamma_{2p}|$ does not exceed its specified value $|\bar{\gamma}_{2p}|$. Of course the latter condition only arises because the entire gain is due to a negative conductance proportional to $|\gamma_{2p}|$, which is reflected at the ω_ℓ terminals. Therefore, the basic configuration in Fig. 10.3 yields arbitrarily large conversion gains, but with stability that is independent of how the pumps are brought up to their desired levels.

10.3.3 Sensitivity. Sensitivity is another circuit property that is closely related to stability. Referring to the discussion in Section 5.1, the sensitivity of a circuit

property Z to a parameter X is defined as the ratio of the percentage change in Z to the percentage change in X, when the latter is small. In the negative resistance amplifiers and converters treated prior to the present chapter, gain was very sensitive to important external parameters, such as load conductance, source conductance, and pump level.

In the cases of present interest, however, the gain sensitivity vanishes both with respect to the load and to the source conductance. These and all other gain sensitivities are recorded in Table 10.3 for the circuit configuration in Fig. 10.3. The entries in Table 10.3 have been found from the general gain formula in (10.17) by using the following expression for the gain sensitivity from ω_i to ω_j,

$$S_X(G_{ij}) = \frac{4X_o}{G_{ij}(X_o)} \left[|Z_{ji}|^2 \frac{\partial(g_i g_i)}{\partial X} + 2g_i g_i R_e \left(Z_{ji}^* \frac{\partial Z_{ji}}{\partial X} \right) \right] X = X_o \qquad (10.27)$$

where X denotes a parameter with normal value X_o.

It is evident from Table 10.3 that $\xi = \pm \frac{\pi}{2}$ is optimum from the standpoint of sensitivity, which is interesting because this same condition yields optimum gain-bandwidth product. For this optimum case, the only nonvanishing gain sensitivities are those with respect to g_ℓ and γ_p; but this is consistent with the gain formulas themselves, which depend explicitly on the gain control parameter

$$\tau'_\ell = \frac{g_\ell}{\omega_\ell |\gamma_{2p}|} \qquad (10.29)$$

It is interesting to note that circuit properties other than gain can also have high sensitivities. However, these other properties may be sensitive to a different set of parameters than the gain. For example, the reflected input admittance is sensitive to the output load according to the relation

$$S_{\tau_u}(Y_{\gamma_{in}} - Y_\gamma) = \left(\frac{\tau_u}{\tau_{in} - \tau_\gamma} \right) \left(\frac{\partial \tau_{\gamma_{in}}}{\partial \tau_u} \right)_{\tau_u = \tau_o} = |\tau_o|^2 \left(\frac{1 + \tau_\ell}{1 - \tau_\ell} \right) \qquad (10.30)$$

Also, the sensitivity of the output admittance to the source obeys the same relation. However, the sensitivity of the reflected admittance at ω_ℓ to the source and load admittance is zero.

Parameter X	Normal Value X_o	Gain Sensitivity ω_i to ω_i $S_X(G_{ij})$
$\lvert\gamma_p\rvert$	arbitrary	ctn ξ
$\lvert\gamma_{zp}\rvert$	arbitrary	$\sqrt{\frac{\omega_i}{\omega_j}\, G_{ij}}$
ξ *	arbitrary	ctn $\xi \sqrt{\frac{\omega_i}{\omega_j}\, G_{ij}}$
g_ℓ	arbitrary	$\sqrt{\frac{\omega_i}{\omega_j}\, G_{ij}}$
g_γ	$\lvert\sin\xi\rvert \frac{\omega_\gamma \lvert\gamma_p\rvert}{\lvert\gamma_{zp}\rvert^2}$	0
g_u	$\lvert\sin\xi\rvert\omega_u\lvert\gamma_{zp}\rvert$	0
b_r, b_u, and b_ℓ	cos ξ	0

*Since ξ is an angle, the sensitivity to ξ is measured with respect to absolute changes in ξ (say $\Delta\xi$) rather than to relative changes in $\xi(\Delta\xi \mid \xi)$.

Table 10.3. Gain sensitivities for the circuit depicted by Fig. 10.3.

In the ideal case, where $\tau_u = \tau_o$, the input admittance is independent of τ_ℓ, and hence of gain. But, if $\tau_u \neq \tau_o$, the input admittance becomes quite sensitive to gain, as was shown in Fig. 10.4 for the case where $\xi = \pm \frac{\pi}{2}$. Yet, the circuit action is such that admittance variations at either the input or the output have no first-order effects on gain. Nevertheless, it can be anticipated that admittance variations can have an influence on noise figure. If the input is improperly coupled, negative resistance will appear at the output and will amplify the output noise. Further discussion of this point will appear in the next section.

Therefore, as far as sensitivity is concerned, the main advantage of double pumping is that no gain takes place at the input or output terminals. Consequently, the gain

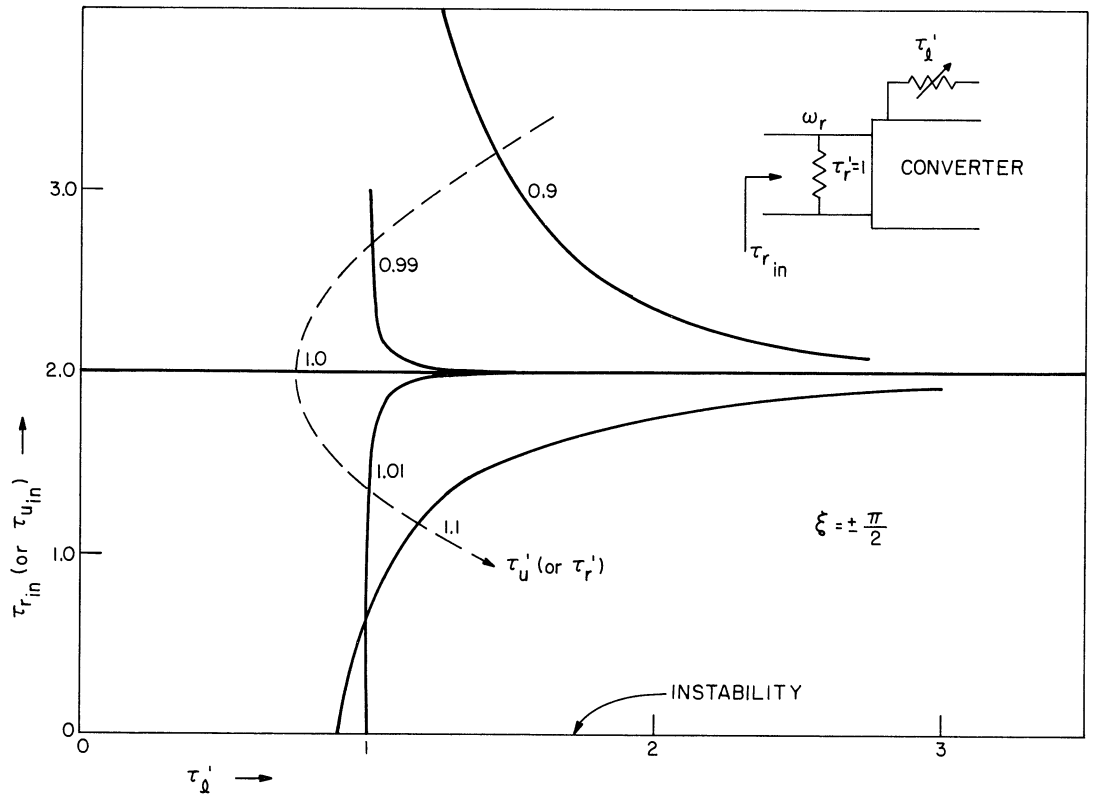

Fig. 10.4. Variation of the normalized input (or output) admittance with the gain parameter τ_ℓ', for various output (or input) loads. The ideal case is for $\tau_\ell' = 1$.

is not sensitive to imperfections in termination, even though some negative resistance may result from such. To illustrate these observations, consider up-conversion from ω_r to ω_u and let us assume that a 10 percent variation in source conductance is possible, but that the output load is constant. Thus, assuming $\xi = \frac{\pi}{2}$, the proper output load will correspond to $\tau_u' = 1$, so

$$G_{ru} = \frac{\omega_u}{\omega_r} \left[\frac{2}{\tau_\ell' - 1}\right]^2 \tag{10.31}$$

But when $\tau_r' = 1 \pm 0.1$, the reflected output conductance at ω_u can go negative if $\tau_\ell' < 1.1$. Therefore, by arbitrarily choosing $\tau_\ell' = 1.1$, G_{ru} will equal (26 db + 10 log ω_u/ω_r) with negligible fluctuation. However, from Fig. 10.4, the output conductance will fluctuate between an open circuit and about twice the load conductance. As a result, one obtains a high-

gain circuit that remains very stable in spite of mismatch fluctuation.

10.3.5 The Effects of Varactor Loss. According to the method outlined in Section 3.4.3, varactor loss can be introduced as frequency-dependent shunt conductance at each sideband terminal. As a result, the normalized terminal conductances have two components; one due to loss and one due to the externally applied conductance. For example,

$$\tau'_r = \tilde{\tau}'_r + \tau'_{rd} = \frac{|\gamma_{2p}|}{\omega_r |\gamma_p|^2} (\tilde{g}_r + g_{rd}) \tag{10.32}$$

where g_r is the external source or load conductance at ω_r, and g_{rd} is the loss conductance. Several interesting consequences of varactor loss will now be examined with the aid of this notation.

Perhaps the most outstanding feature introduced by double pumping is unilateral conversion, but the latter requires a critical value for each normalized admittance, according to Table 10.1. Therefore, when loss is introduced, unilateral conversion can only be retained by reducing the external conductances until Table 10.1 is again satisfied, but then varactor loss appears as a mismatch. One can compensate for this mismatch by deviating somewhat from perfect unilateral conversion.

For example, in the presence of loss, Fig. 10.3 can yield a match at ω_r and ω_u, or can yield perfect isolation between the pairs (ω_r, ω_ℓ) or (ω_ℓ, ω_u), but not both. Also, the conditions for isolation are still gain independent, but not those for match. It will be shown, however, that the conditions for match approach those for isolation as the gain increases, and therefore the imperfections due to loss are not serious.

To examine the conditions for simultaneous match with loss, consider the circuit in Fig. 10.3, and let us assume all terminals synchronously tuned with $\xi = \pi/2$. If x is the efficiency factor at ω_r ($x = \tilde{\tau}_r/\tau_r$) then match will occur if

$$\tau'_r = \tau'_{rd} + \frac{\tau'_\ell - \tau'_u}{\tau'_\ell \tau'_u - 1} \tag{10.33}$$

or

$$(2x - 1)\, \tau'_r = \frac{\tau'_\ell - \tau'_u}{\tau'_\ell \tau'_u - 1} \tag{10.34a}$$

Similarly, if y is the efficiency factor at ω_u, match will occur at ω_u if

$$(2y - 1)\,\tau'_u = \frac{\tau'_\ell - \tau'_r}{\tau'_\ell \tau'_r - 1} \tag{10.34b}$$

Although it is rather tedious to solve equations (10.34) simultaneously, a significant special case can easily be treated. If τ'_r and τ'_u are approximately unity when the ω_r and ω_u terminals are matched, then (10.34) can be approximated by

$$(2x - 1)\,(\tau'_r - 1) = \frac{1 + \tau'_\ell}{1 - \tau_\ell}\,(\tau'_u - 1) + 2(1 - x) \tag{10.35a}$$

$$(2y - 1)\,(\tau'_u - 1) = \frac{1 + \tau'_\ell}{1 - \tau'_\ell}\,(\tau'_r - 1) + 2(1 - y) \tag{10.35b}$$

Therefore, with high gain (i.e., with $\tau'_\ell \approx 1$)

$$\tau'_r - 1 = 2(y - 1)\left(\frac{(1 - \tau'_\ell)}{1 + \tau'_\ell}\right) \tag{10.36a}$$

$$\tau'_u - 1 = 2(x - 1)\left(\frac{1 - \tau'_\ell}{1 + \tau'_\ell}\right) \tag{10.36b}$$

which both approach zero as τ'_ℓ goes to one. Therefore, varactor loss causes very little mismatch in the unilateral conversion mode, if the gain is high.

The process described by (10.35) can be visualized with the aid of Fig. 10.4. If we start with $\tilde{\tau}'_u = 1$, and then introduce loss at ω_u, the resulting increase in τ'_u reflects a small negative conductance at ω_r, which reduces $\tau'_{r_{in}}$. But at high gain, the latter reduction actually overcompensates for the loss conductance at ω_r, so $\tilde{\tau}'_u$ can be reduced until τ'_r is only slightly greater than 1. Similarly, $\tilde{\tau}'_r$ is reduced until the loss at ω_u is cancelled, which occurs for $\tilde{\tau}'_r$ 1. In this case, the worst mismatch occurs at low gain, and then the input reflection coefficient is (1 - x). However, the latter vanishes as the gain increases.

10.3.4.1 Up-Conversion Noise Figure. The most significant effect of varactor loss in multiply-pumped circuits will undoubtedly be the influence on noise figure. However, it will be of interest to see what noise figure benefits accompany the rather unique

circuit properties that have come to light through double pumping. The basic circuit that will be treated for noise figure is Fig. 10.3, so let us first consider the noise figure for up conversion from ω_r to ω_u. The general noise figure expression in (3.27) can again be applied, but it takes on a simpler form in this case. The third term in (3.27) is the noise figure contribution by the output load, which would be due to an output mismatch. This term will be negligible if the output mismatch is small, which is the case in Fig. 10.3. Ideally, the output of Fig. 10.3 is perfectly matched, so mismatch only arises as a result of varactor loss. However, the influence of varactor loss has been shown to diminish when conversion gain increases. Therefore, a case of basic interest will be the noise figure for high gain under the conditions of unilateral conversion, namely $\tau_r = \tau_u = \tau_o$.

By (3.27), the up-conversion noise figure can be written

$$F_{ru} = 1 + \left(\frac{1 - x}{x}\right) \frac{T_d}{T_o} + \frac{G_{\ell u}\, T_\ell}{G_{ru}\, T_o} \tag{10.37}$$

where x is again the input efficiency factor (at ω_r in this case). Also, in writing (10.37), the bandwidths of $G_{\ell u}$ and G_{ru} have been assumed equal according to the argument of Section 10.1. By (10.17) and (10.3), the gain ratio in (10.37) becomes

$$\frac{G_{\ell u}}{G_{ru}} = \left(\frac{\omega_r}{\omega_\ell}\right)\left(\frac{\tau'_\ell}{x\tau'_r}\right) \left| \frac{\tau_r - je^{j\xi}}{\tau_\ell + je^{-j\xi}} \right|^2 \tag{10.38}$$

which depends on ξ. Since optimum up-conversion bandwidth and sensitivity occurs under the following conditions

$$\xi = \pi/2 \tag{10.39a}$$

$$\tau_r = \tau_u = 1 \tag{10.39b}$$

$$\tau_\ell = \tau'_\ell \text{ (i.e., real)} \tag{10.39c}$$

the latter will be assumed in calculating the noise figure. Now (10.38) becomes

$$\frac{G_{\ell u}}{G_{ru}} = \left(\frac{\omega_r}{\omega_\ell}\right)\left(\frac{\tau'_\ell}{x}\right)\left(\frac{2}{\tau'_\ell + 1}\right)^2$$

in which case

$$F_{ru} = 1 + \frac{T_d}{T_o}\left\{\frac{1-x}{x} + \left(\frac{a\omega_r}{x\omega_\ell}\right)[1 + z(s-1)]\right\} \tag{10.40}$$

where

$$T_\ell = T_d[1 + z(s-1)] \tag{10.41a}$$

$$z = \tilde{g}_\ell/g_\ell\,; \quad s = \tilde{T}_\ell/T_d \tag{10.41b}$$

$$a = \frac{4\,\tau'_\ell}{(\tau'_\ell + 1)^2} \tag{10.41c}$$

The noise temperature expression in (10.41a) is equivalent to (5.27c), but it has been written in the form used in Appendix A. Further evaluation of (10.40) is possible by using the constraints in (10.37a). In particular, if varactor loss is the only parasitic noise source, then by (3.30)

$$g_r = xg_r + \frac{\omega_r^{\,2} C}{\omega_c} = \omega_r\left|\frac{\gamma_p^{\,2}}{\gamma_{2p}}\right| \quad . \tag{10.42}$$

Hence

$$x = 1 - \sqrt{R_r}\,p \tag{10.43a}$$

where

$$p = \left|\frac{\gamma_{2p}}{\gamma_p}\right| \tag{10.43b}$$

$$R_r = \left(\frac{\omega_r C}{\omega_c|\gamma_p|}\right)^2 \quad . \tag{10.43c}$$

Similarly

$$g_\ell = z\,g_\ell + \frac{\omega_\ell^{\,2} C}{\omega_c} = \omega_\ell \gamma_{2p} \tag{10.44}$$

and therefore

$$\frac{\omega_r}{\omega_\ell} = \left(\frac{1}{p}\right)^2 \left(\frac{1-x}{1-z}\right) \quad . \tag{10.45}$$

A final observation before calculating the noise figure is that $a \approx 1$ in (10.41c) when $\tau'_\ell \approx 1$, and therefore choosing $a = 1$ corresponds to high gain. The noise figure for unilateral conversion with high gain now becomes

$$F_{ru} = 1 + \frac{T_d}{T_o}\left(\frac{\sqrt{R_r}\,p}{1 - \sqrt{R_r}p}\right)\left[1 + \frac{1}{p^2}\left(\frac{1 + z(s-1)}{1-z}\right)\right] \tag{10.46}$$

The three parameters in (10.46) have important physical significance, so they will be reviewed below:

$\frac{1}{\sqrt{R_r}}$ = the dynamic quality factor of the varactor. It is a measure of varactor quality and the degree of pumping, and is the same factor that appeared in (4.32b).

p = the ratio of the two pump components.

z = a measure of the external loading at the dummy terminal ω_ℓ.

Therefore p and z are parameters that can be varied to optimize the noise figure. However, R_r is an independent parameter that all reactive mixers, using the same varactor and pump, will have in common.

One other constraint that must be considered in optimizing (10.46) is the output condition $\tau_u = 1$. When considered together with the high gain condition $\tau_\ell = 1$, one obtains the relation

$$\frac{\omega_u}{\omega_\ell} = \frac{1 - y}{1 - z} \tag{10.47}$$

where y is the output efficiency factor. Now it is clear that y must be less than z, so z cannot equal zero in this case.

Now, to proceed with the minimization of (10.46), let

$$f = \frac{1 + z(s-1)}{1 - z} \tag{10.48}$$

and then

$$(p)_{opt} = -f\sqrt{R_r} + \sqrt{R_r f^2 + f} \tag{10.49}$$

from which

$$(F_{ru})_{opt} = 1 + \frac{2T_d\sqrt{R_r f}}{T_o}\left[\sqrt{R_r f} + \sqrt{1 + R_r f}\right] \qquad (10.50a)$$

or

$$(T_{ru})_{opt} = 2\sqrt{R_r}\ T_d/(p)_{opt} \ . \qquad (10.50b)$$

The smallest value of (10.50) occurs when f has its minimum value of one. However, (f) must exceed one in all practical cases because (z) must exceed zero to satisfy (10.47). Therefore to obtain low noise figures, the output efficiency (y) must be low so (z) can be small, which in turn makes (f) small in (10.50). An additional help in this case would be idler cooling to reduce f by reducing s.

It is interesting to observe that (10.50) is identical to the formula for optimum noise figure of a lower-sideband converter, as given by (A-10) in Appendix A. Therefore, Fig. A.1 with $\alpha = fR_r$ is a plot of the equivalent noise temperature in (10.50b). Actually, it is not unreasonable to find that these two converters have identical optimum noise figures, since they have the same noise sources--namely loss at the ω_r and ω_ℓ terminals. However, the value of harmonic pumping is not reduced by this conclusion. The point of interest is that multiple pumping offers such circuit advantages as increased stability and increased gain-bandwidth product, without an increased noise figure.

A further comparison of double-pumping noise figure can be based on the conventional upper-sideband converter (which also operates between ω_r and ω_u). By (4.35f), the optimum noise figure of the latter is given by (10.50) with f = 1, but the conversion gain is less than one in this case. Therefore, to obtain gain in the conventional upper-sideband up-converter, one must operate with less than optimum noise figure and hence must trade gain for noise figure. The corresponding result for the doubly-pumped converter is the necessity for trading output efficiency for noise figure. This point is summarized in Fig. 10.5, which shows the absolutely minimum noise temperature of a double-pump converter and the corresponding noise temperature of a single-pump converter operating at the same frequency. Also shown is a curve of idler efficiency (z) for which both converters have the same noise figure. Therefore, by accepting a low output efficiency, one can obtain lower noise figures

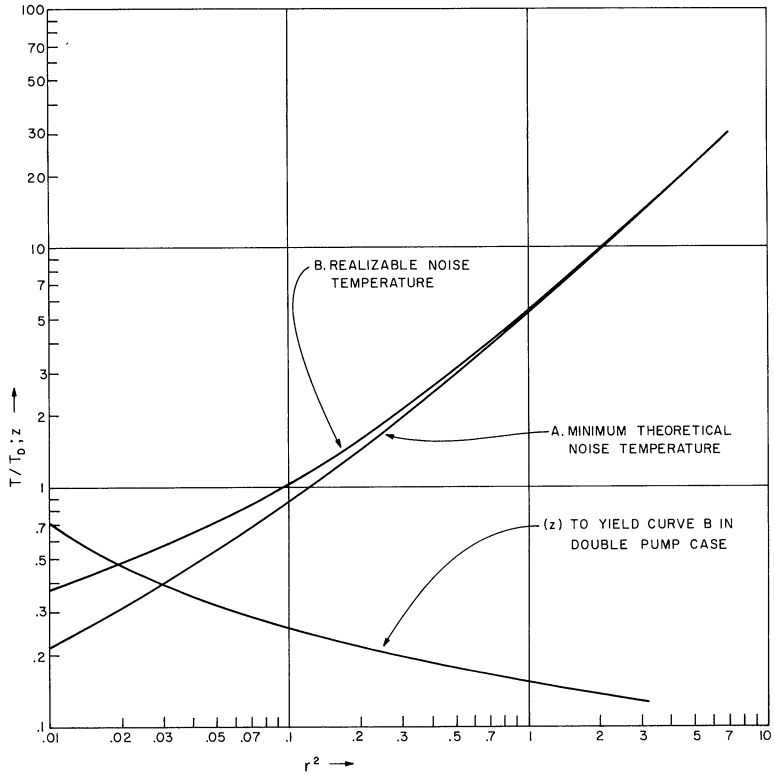

Fig. 10. 5. A comparison of upper-sideband noise temperatures for single- and double-pump up-converters. Curve A is a theoretical limit for two cases: (1) single pump with zero gain, and (2) double pump with zero efficiency (i. e., z = 0 at $[\omega_u/\omega_r]_{opt}$). Curve B is the noise temperature for: (1) the single-pump converter operating at the $[\omega_u/\omega_r]_{opt}$ for the double-pump case, or (2) the double-pump converter with the z indicated. Therefore, with Curve B both converters have the same frequencies, the same noise temperature, and the same external stability, but the one with two pumps has essentially infinite gain.

in a double-pump, rather than in the single-pump, upper-sideband converter.

10. 3. 4. 2 Down-Conversion Noise Temperatures. In the previous discussions of down-conversion, in Sections 4.3 and 8.3, the gain-bandwidth products and noise figures were considerably inferior to those of up-conversion. This result is basic to all reactive mixer configurations, but down-conversion is still of practical interest. There are many applications where even modest down-conversion gain-bandwidth products are useful, if their noise figures are reasonably low. Therefore, any method for reducing down-conversion noise figures is of interest, even if the same configuration yields better noise figures as an up-converter. One technique that falls in this category is harmonic pumping.

Following the procedure of the last section, the down-conversion noise figure becomes

$$F_{ur} = 1 + \left(\frac{1-y}{y}\right) \frac{T_d}{T_o} + \frac{G_{\ell r}}{G_{ur}} \frac{T_\ell}{T_o} \quad . \tag{10.51}$$

By (10.17) and (10.3)

$$\frac{G_{\ell r}}{G_{ur}} = \left| \frac{\tau_u - je^{-j\xi}}{\tau_\ell + je^{j\xi}} \right|^2 \left(\frac{\omega_u}{\omega_\ell}\right) \left(\frac{\tau_\ell}{y\tau_u}\right) \tag{10.52}$$

so again ξ must be selected. In comparison with (10.39), optimum down-conversion occurs for

$$\xi = -\pi/2 \tag{10.53a}$$

$$\tau_r = \tau_u = 1 \tag{10.53b}$$

$$\tau_\ell \text{ real } (= \tau'_\ell) \quad . \tag{10.53c}$$

In this case, (10.52) becomes

$$\frac{G_{\ell r}}{G_{ur}} = \frac{\omega_u}{\omega_\ell} \left(\frac{2}{\tau'_\ell + 1}\right)^2 \left(\frac{\tau'_\ell}{y}\right) \tag{10.54}$$

and, using the notation in (10.41), (10.51) reduces to

$$F_{ur} = 1 + \frac{T_d}{T_o} \left\{ \frac{1-y}{y} + \frac{a\omega_u}{y\omega_\ell} \left[1 + z(s-1)\right] \right\} \quad . \tag{10.55}$$

For high gain, $a \to 1$, and

$$\frac{\omega_u}{\omega_\ell} \to \frac{1-y}{1-z} \quad .$$

Therefore, the minimum noise figure occurs for $y \approx 1$, which yields

$$(F_{ur})_{min} = 1 + \frac{\omega_u}{\omega_\ell} \frac{T_d}{T_o} \quad . \tag{10.56}$$

Thus the minimum noise temperature equals the lower-sideband noise temperature T_ℓ, and this occurs for $\omega_r << \omega_u$. In this case (10.55) requires $z \approx y \approx 1$, which means heavy idler loading.

However, the condition $y \approx 1$ is not always possible. By (10.43a)

$$x = 1 - \sqrt{R_r\, p} \tag{10.57a}$$

and by a similar derivation

$$y = 1 - \sqrt{R_u/p} \tag{10.57b}$$

where[1]

$$R_u = \left(\frac{\omega_u\, C}{\omega_d\, \gamma_p}\right)^2 = \left(\frac{\omega_u}{\omega_r}\right)^2 R_r\,. \tag{10.57c}$$

Therefore, eliminating ρ yields

$$y = 1 - \frac{\sqrt{R_r R_u}}{1 - x} = 1 - \frac{\omega_r\, R_u}{\omega_u (1 - x)}\,. \tag{10.58}$$

In a typical down-converter application, ω_u and R_u would be specified. Therefore y will depend on the possible choices for ω_r and x. The smaller the latter are, the greater y can be. This point is illustrated in Fig. 10.6, which shows the conversion noise figures that accompany harmonic pumping.

It is apparent that the greater parameter flexibility offered by harmonic pumping is advantageous. For example, even if the figure of merit at ω_u (i.e., $1/\sqrt{R_u}$) is small, y can approximate one if $p = |\gamma_{2p}/\gamma_p|$ is large. Therefore, the pump harmonic (γ_{2p}) is useful for reducing the down-conversion noise figure, particularly if R_u is large. This result is also illustrated in Fig. 10.6, which shows the high-gain down-conversion noise figure for both the double and single pump cases. The latter is taken from Fig. 8.8.

10.4 Harmonic Pumping with Dependent Sideband Loading

A simple case of harmonic pumping occurs when ω_ℓ and ω_u are dependently

---

[1] See (4.38) and the footnote on page for further discussion of R_u.

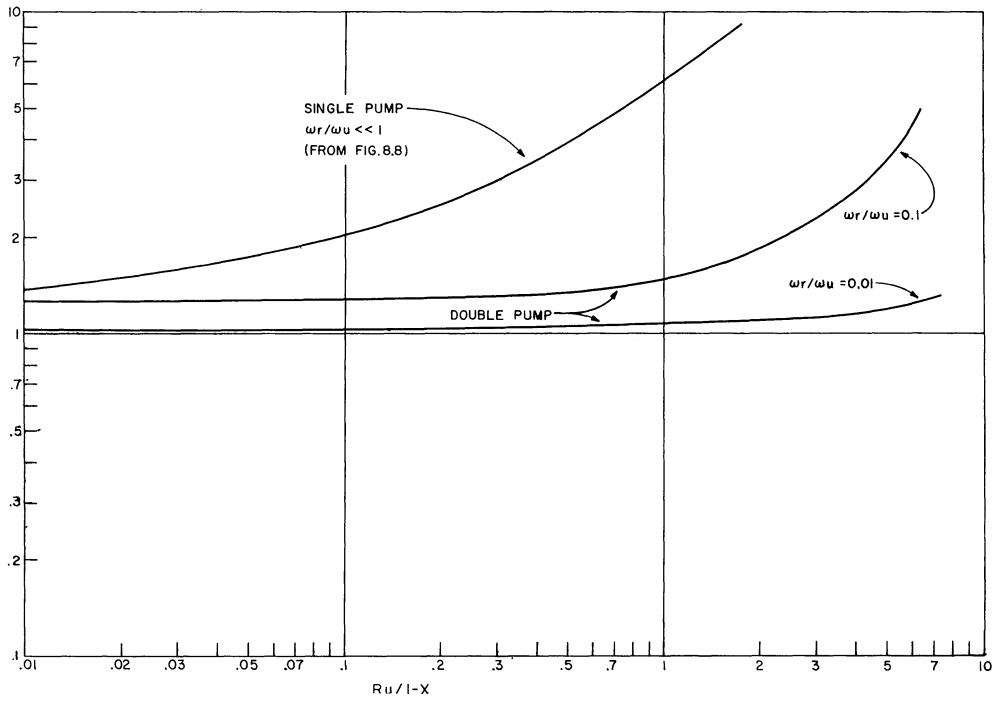

Fig. 10.6. A comparison of double- and single-pump, down-conversion, noise temperatures. In both cases the lower-sideband is present to yield high gains. Its load is assumed to be at diode temperature.

loaded; for example, by being closely spaced in the same resonance. This basic configuration was treated in Chapter IX for the case of a single pump, and was found to be a means of very wideband video amplification. The question that now arises is, "What further benefits could be obtained by adding the pump harmonic in this case?"

A simple qualitative viewpoint of this system is suggested in Fig. 10.7. All frequencies in the normal pump pass band are in a degenerate parametric amplifier configuration with respect to the pump harmonic. Therefore, when ω_ℓ and ω_u are created by the mixing of ω_r and ω_p, they will receive further amplification from ω_{2p}. However, ω_u and ω_ℓ are phase coherent with respect to both ω_p and ω_{2p}. Therefore, it may be anticipated that an optimum gain improvement will require a proper phase between ω_p and ω_{2p}.

There are two ways in which this problem can be treated analytically. The most convenient, at this point, would be to use the formulation in (10.3), which is based on a model that treats pumping signals as time-varying capacitors. But the equivalent model,

based on (2.33a), considers instead the pump harmonic and the modulating signal as time-varying capacitors. The latter is a more descriptive model, because it yields directly the output waveform consisting of ω_p, ω_u, and ω_ℓ. However, the further pursuit of this second method will be postponed for a later study. While not as elegant, the original formulation gives the desired answers, and hence the second model will be used only as a means of supplementary interpretation.

To proceed with the analysis of phase modulation gain with harmonic pumping, (10.3) will first be solved for the sideband voltages due to a modulating current $\mathbb{I}_r$. This step yields

$$\frac{V_u}{\mathbb{I}_r} = \frac{\tau_\ell + (je^{-j\xi})}{j\omega_r\gamma_p^*[\tau_r\tau_\ell\tau_u + \tau_\ell - \tau_u - (\tau_r - 2j\cos\xi)]} \tag{10.59a}$$

$$\frac{V_\ell}{\mathbb{I}_r} = \frac{\tau_u - (je^{j\xi})}{j\omega_r\gamma_p^*[\tau_r\tau_\ell\tau_u + \tau_\ell - \tau_u - (\tau_r - 2j\cos\xi)]} \tag{10.59b}$$

where the terms in parenthesis vanish as $|\gamma_{2p}| \to 0$. Therefore, when these terms are deleted, the resulting expressions in (10.59) must describe the phase modulation configuration of Chapter IX.

Referring to (9.17b), maximum phase modulation gain occurs when V_u and V_ℓ are in quadrature with γ_p, the pump fundamental. Maximum gain also occurs when ω_u and ω_ℓ are nearly centered in the pump tank, which means $\omega_r \approx 0$. Then, all the τ's are real, and the optimum value of ξ can be seen to be $\pi/2$. It is of interest that this value of ξ corresponds to (5.38), which places γ_p and γ_{2p} in the phase relationship for minimum gain by degenerate parametric amplification. Therefore, when the pump harmonic has maximum effectiveness with respect to ω_r, ω_ℓ, and ω_u, it also has maximum stability with respect to the degenerate frequency ω_p. Now using $\xi = \pi/2$, the remaining quantities in (9.17b) can be calculated, which results in the following expression for phase modulation gain:

$$G_{PM} = \frac{8\omega_p^2 k_p^2}{\beta_r\beta_p} \frac{\left(1 + \dfrac{\omega_p k_{2p}/\beta_p}{1 + j\omega_r/\beta_p}\right)^2}{1 + (k_p^2 - 1)\dfrac{\omega_r^2}{\beta_r\beta_p} - \dfrac{\omega_p^2 k_{2p}^2 (1 + j\omega_r/\beta_r)}{\beta_p^2 (1 + j\omega_r/\beta_p)} + j\left(\dfrac{\omega_r}{\beta_r} + \dfrac{\omega_r}{\beta_p}\right)} \tag{10.60a}$$

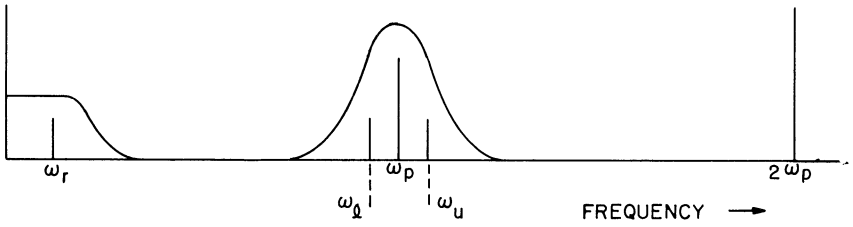

(a)

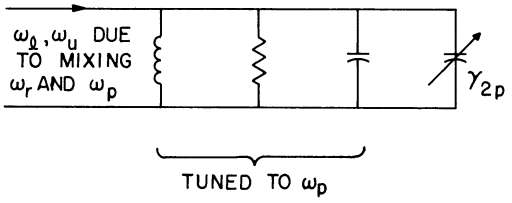

(b)

Fig. 10.7. Harmonic pumping in a phase modulation amplifier; (a) shows the spectral configuration, and (b) pictures the normal pump pass band as a degenerate parametric amplifier.

where

$$Y_u = Y_\ell^* = g_p(1 + j\omega_r/\beta_p) \tag{10.60b}$$

$$Y_r = g_r(1 + j\omega_r/\beta_r) \tag{10.60c}$$

$$k_p^2 = \frac{|\gamma_p|^2}{C_r C_p}\,; \quad k_{2p}^2 = \frac{|\gamma_{2p}|^2}{C_p^2}\,. \tag{10.60d}$$

This expression differs from (9.22) only by the terms in k_{2p}. But, as the latter quantity increases, the gain increases and becomes essentially infinite as $\omega_p k_{2p} \to \beta_p$. To explore this case, let

$$\left(\frac{\omega_p k_{2p}}{\beta_p}\right)^2 = 1 - \delta \tag{10.61}$$

and then if δ is small, the midband gain becomes

$$\overline{G}_{PM} = \frac{16\,\omega_p^{\,2} k_p^{\,2}}{\beta_r \beta_p} \left(\frac{2}{\delta}\right)^2 . \tag{10.62}$$

Now, the bandwidth will be quite small (i.e., $\beta << \beta_p$ or β_r). Therefore, assuming $\beta_p = \beta_r$ for illustration, the bandwidth becomes

$$\frac{\beta}{\beta_r} = \frac{\delta}{2} \tag{10.63}$$

from which the gain-bandwidth product can be found to be

$$\sqrt{\overline{G}_{PM}}\,\beta = 2.82\,\omega_p k_p . \tag{10.64}$$

It is of interest that the latter is 60 percent larger than the corresponding result for the single-pump case [see (9.31)].

This improvement in gain-bandwidth product is due to the factor

$$1 + \frac{\omega_p k_{2p}}{\beta_p} \tag{10.65}$$

in the numerator of (10.60a), which doubles as k_{2p} increases from zero to the high gain value in (10.61). This factor of two is precisely the improvement that would result in the single-pump case if the pump fundamental were increased to $2\omega_p$. Therefore, the main advantage of harmonic pumping in this application is as a convenient way of trading gain for bandwidth. Harmonic pumping produces a narrowing down of the output pass band at ω_p, which increases the apparent varactor Q. This multiplies the gain, but it decreases the bandwidth proportionately.

It is interesting to also inquire about the effect of harmonic pumping on the input admittance. From (10.4a)

$$Y_{r_{in}} = Y_r \left\{ 1 + \frac{2\omega_r^{\,2} k_p^{\,2}}{g_r g_p (1+j\beta_r)(1+j\beta_p)} \left[\frac{1}{1 - \dfrac{\omega_p^{\,2} k_{2p}^{\,2}}{\beta_p^{\,2}\left(1 + j\dfrac{\omega_r}{\beta_p}\right)^2}} \right] \right\} . \tag{10.66}$$

But, in the high gain case ω_r will be much less than β_r or β_p in the overall pass band; so if

$\omega_p^2 k_{2p}^2/\beta_p^2 = 1 - \delta$, then

$$Y_{r_{in}} \longrightarrow Y_r \left[1 + \frac{2\omega_r^2 k_p^2}{\beta_r \beta_p} \left(\frac{1}{\delta}\right)\right] .$$

At the half power point, $\omega_r = \delta \beta_p/2$, so

$$Y_{r_{in}} \longrightarrow Y_r + \frac{\delta k_p^2}{2} \xrightarrow[\delta \to 0]{} Y_r$$

which shows that the reflected admittance is insignificant over the conversion pass band with double pumping, just as it is with single pumping.

Therefore the main advantage of double pumping in this case is greater circuit flexibility. While a single-pump converter can yield the same gain-bandwidth product, the circuit bandwidths, β_r and β_p, must then be controlled by passive design, or by varactor fabrication. Often, these designs will call for unsuitable impedance levels and hence will require transformers. With double pumping, one can use natural impedance levels and then rely on the pump harmonic to sharpen the bandwidth and yield the optimum gain-bandwidth product. This could be an important advantage in many cases.

10.5 Conclusion

The introduction of harmonic pumping has been shown to yield an interesting set of circuit properties. Due to the phase coherence of the pump and its harmonic, unilateral conversions are possible. Also, a pseudo-circulation effect arises that improves circuit stability with respect to external parameter variations.

One interesting configuration has shown arbitrarily large conversion gains between ω_r and ω_u, with matched input and output terminals. The gain depends on the load at ω_ℓ, but the match is essentially independent of this load. The noise figure of this converter is as good as a conventional lower-sideband converter with infinite gain; yet, it is more stable than the latter. Also, it offers larger gain-bandwidth products.

The application of harmonic pumping to down-conversion has also been successful, particularly from the point of view of noise figure. Noise figures that are significantly improved over those by other down-conversion methods have been calculated.

CHAPTER XI

EXPERIMENTAL WORK AND CONCLUSIONS

Throughout the course of this research considerable experimental work has been performed, but it has been exploratory in nature. While it is difficult to summarize this work precisely, two important experimental functions have been served, which are noted below:

(1) In the course of each experiment, a number of more or less unexpected effects were observed. Often these effects called for critical circuit adjustments, particularly those dealing with stability, so precise data were difficult to take. Nevertheless, these effects were clear enough so that appropriate problems for theoretical study could be defined. As such, they served to show the importance of certain parameters that may otherwise have been neglected in analysis.

(2) In one case, the preceding theory was used to design a working circuit. Using the principle discussed in Chapter IX, an ultra-wideband video amplifier was designed and constructed--with 20 db gain from dc to 100 Mc. A laboratory version of this amplifier is pictured in Fig. 11.1.

The results of these experimental programs will be the subject of the next two sections of this chapter.

11.1 An Ultra-Wideband Video Amplifier

The configuration of Fig. 11.1 is a realization of the schematic shown in Fig. 9.12. The circuit pictured is unnecessarily large, since it contains several nonessential

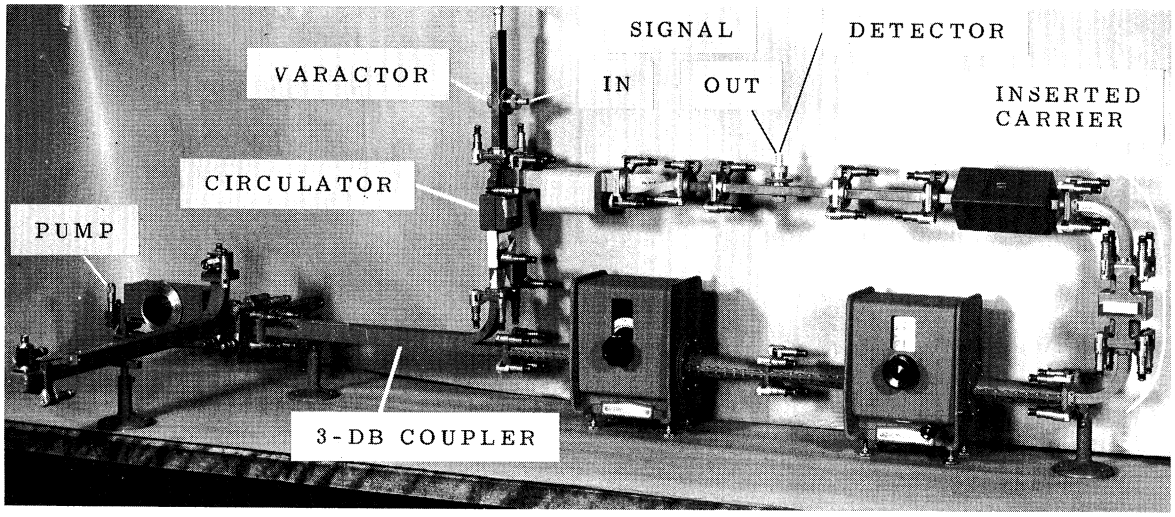

Fig. 11.1. A "breadboard" model of the phase modulation amplifier. Pump frequency 9.4 kMc. Signal bandwidth 100 Mc.

components that were added to simplify instrumentation, so a working amplifier could have been realized in a much smaller package. The essentials of this circuit are the varactor mount and the circulator, which are shown more clearly in Fig. 11.2. In the operation of Fig. 11.1, the applied pump signal is split in a 3 db coupler and one part applied to the varactor. This part should experience a matched resonant circuit at the varactor. The other part, which is available to the detector through a phase shifter and attenuator, is used for carrier insertion.

Regarding the varactor, it was found that a commercially available varactor in shunt across an X-band waveguide just happened to exhibit a matched resistance over approximately a 10 percent frequency range. The optimum frequency for this effect was about 9.4 kMc, but it varied somewhat with pump level. This matching effect can be attributed to parasidic lead inductance, which reduces the effective shunt resistance of the varactor. Therefore, by choosing a frequency where the shunt resistance equals the characteristic impedance of the waveguide, and by tuning the remaining varactor susceptance by means of a sliding short, the varactor will behave like a matched load at this frequency. Since pump power will be reflected

(a)

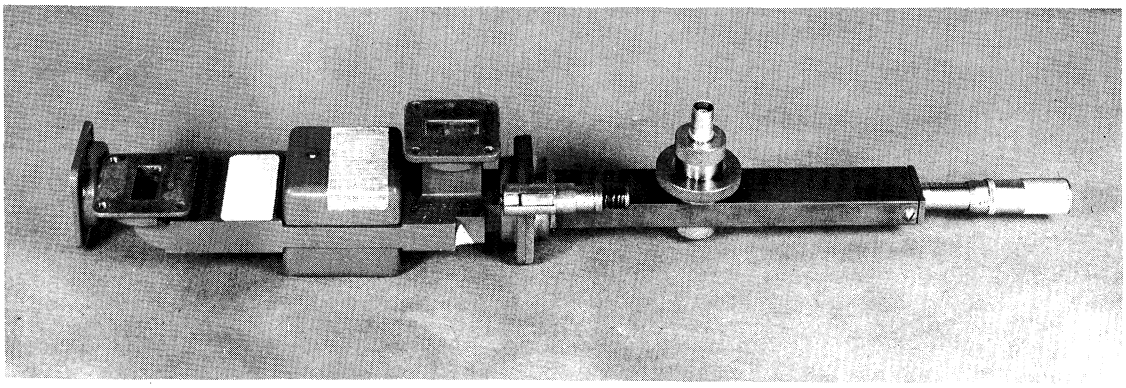

(b)

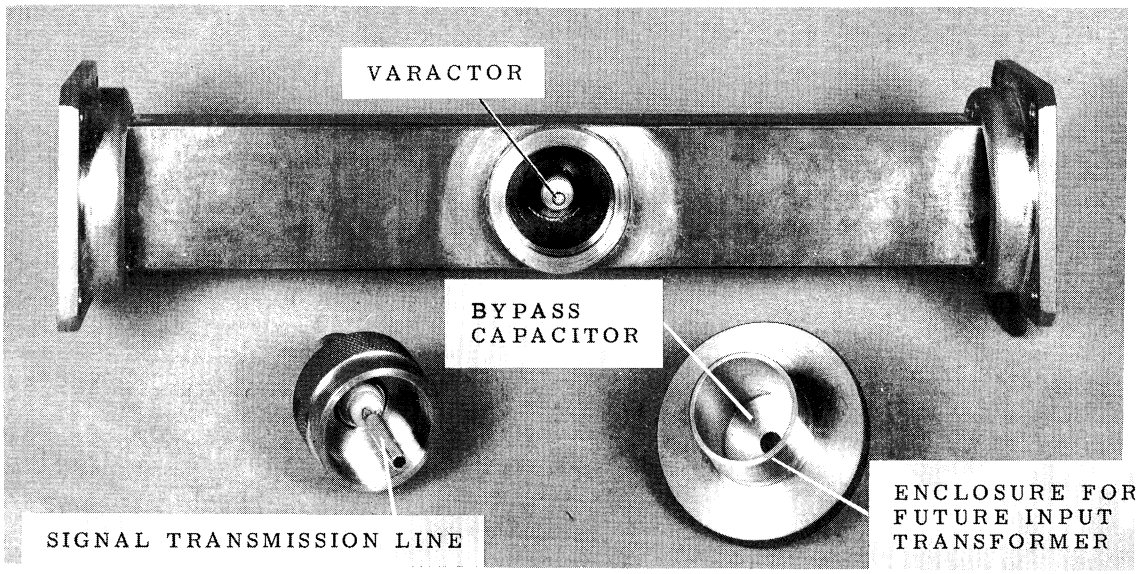

Fig. 11.2. A close up of the varactor mount in Fig. 11.1.
(a) shows the varactor mount and circulator.
(b) shows the varactor mount disassembled.

only when a modulating signal is applied, the circulator acts like a balanced modulator in this case. A similar form of balanced modulator, although not as a gain-producing device, has been described recently by Mackey (Ref. 43).

If the varactor in Fig. 11.1 is matched and tuned in the absence of modulation, the reflection coefficient due to a modulation of the varactor capacity (ΔC) will be

$$\rho = \frac{j\omega_p \Delta C}{\sqrt{(2Y_o)^2 + (\omega_p \Delta C)^2}} \approx \frac{j\omega_p \Delta C}{2Y_o} \qquad (11.1)$$

If this reflected voltage can be converted entirely into useful output, the voltage gain will be

$$\left|\frac{\rho V_p}{V_r}\right| = \frac{Q}{2}\left(\frac{\partial C}{\partial V}\frac{V_p}{C}\right) \tag{11.2}$$

where the quantity in parenthesis can be of the order of 1/2 for a typical varactor. Therefore, the voltage gain can be as large as 1/4 the varactor Q. Similarly, the voltage gain times bandwidth will be

$$\left|\frac{\rho V_p}{V_r}\right| \beta = \frac{\omega_p}{4}\left(\frac{\partial C}{\partial V}\frac{V_p}{C}\right) \tag{11.3}$$

which shows the value of a high pump frequency. By pumping at 10,000 Mc for example, one can obtain gain-bandwidth products in excess of 1000 Mc.

Returning now to Fig. 11.1, the reflected signal is passed through the circulator to the detector, where it adds to the second (inserted-carrier) component. The latter is adjusted in phase so the resultant signal across the detector is amplitude modulated. Detection then recovers the original modulating signal in an amplified form.

It is of interest that (11.2) is consistent with the sideband voltage expression in (9.3). However, one factor not accounted for in Chapter IX is the parasitic series inductance of the varactor, which produces a series resonance at about 3 kMc in the varactors that we tested. Above series resonance, the varactor Q will increase with frequency, as indicated in Fig. 11.3. Also, shown in Fig. 11.3 are gain and bandwidth [based on (11.2)] both above and below the frequency where the parasitic inductance is dominant. It can be seen, in spite of parasitic inductance, that the maximum gain-bandwidth product remains proportional to pump frequency even though the voltage gain itself falls off with pump frequency below self-resonance. The maximum bandwidth is limited by the R/L ratio of the varactor parasitics.

Some typical experimental results are shown in Figs. 11.4 through 11.6. The first of these shows the response to a low-frequency triangular input signal. The detector output in the absence of the inserted carrier is the typical folded response of a balanced modulator. However, when the second carrier is inserted, the ac envelope "blooms," giving the response shown in Fig. 11.4. Therefore, the inserted carrier performs two important roles. One is to restore fidelity to the detected output waveform and the other is to provide coherent

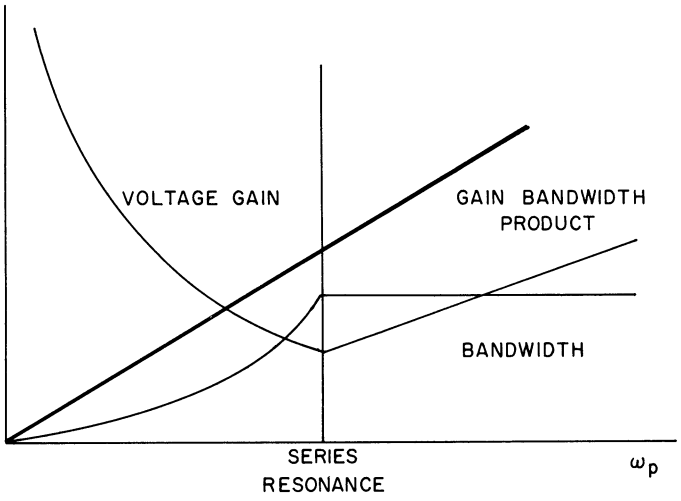

Fig. 11.3. Theoretical circuit properties of a phase shift amplifier vs. pump frequency. At each frequency the varactor is assumed to be matched to a circulator.

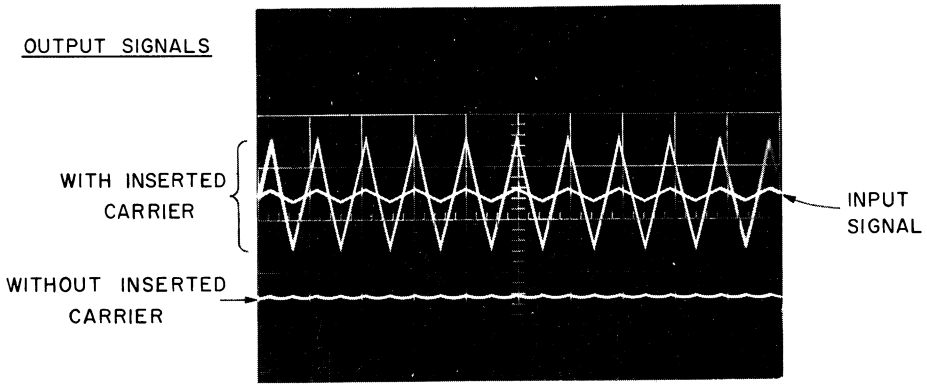

Fig. 11.4. Signal waveforms from phase modulation amplifier in Fig. 11.1.

RF bias for the detector. The latter greatly enhances the sensitivity of the detector.

Figure 11.5 shows the voltage gain vs. pump power. For each change in pump power it is appropriate to readjust both the short behind the varactor and detector tuning. The gain shown in Fig. 11.5 is essentially G_{PM}, because the output detector was not loaded. Undoubtedly, the greatest weakness in this amplifier system is the output detector. To date, a 1N23B has been the most successful diode used, but it has a rather high output impedance. Also, its output impedance depends rather strongly on the RF matching used in the waveguide.

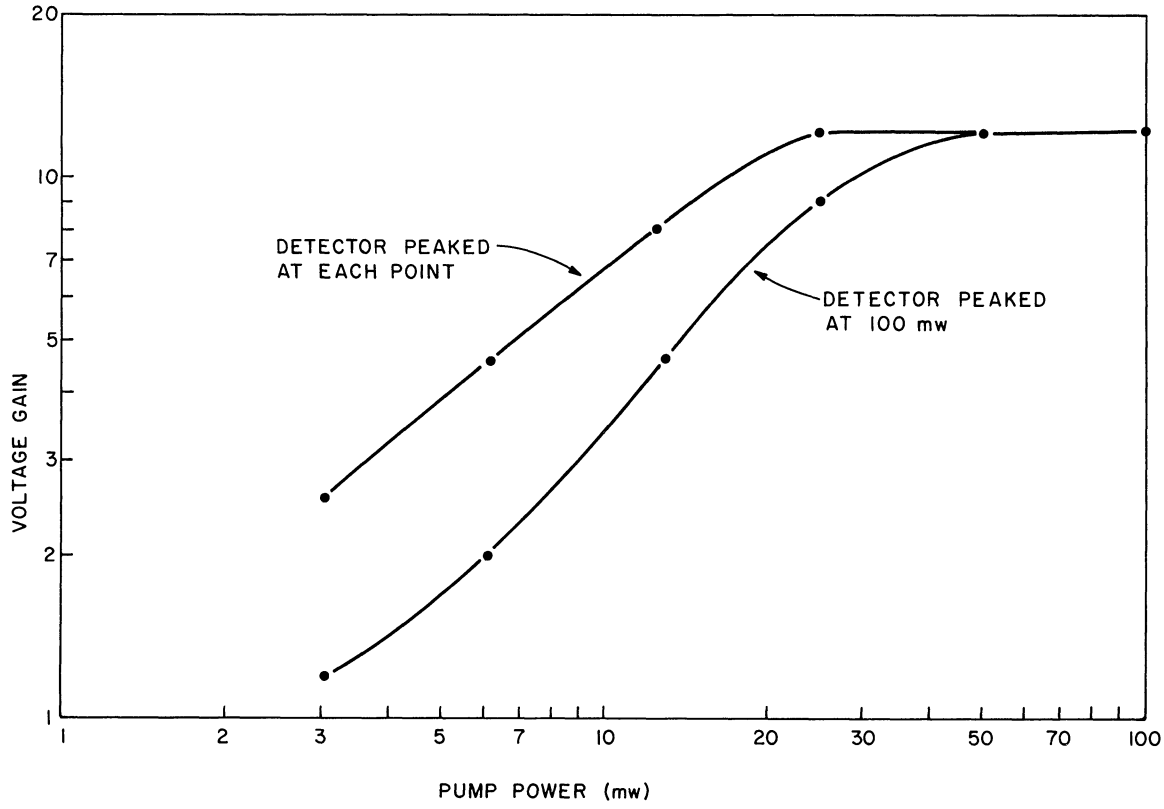

Fig. 11. 5. Voltage gain vs. pump power for 9. 5 kMc pump.

It has been found that the voltage gain can be enhanced by matching the detector diode, but it also raises the impedance. Because the detector output impedance is high, it is hard to couple this output efficiently into a receiver or other measuring device. For example, a typical output impedance is 1000 ohms. In this case the output capacity should not exceed 1 $\mu\mu$f if 100 Mc bandwidth is required. It is anticipated that future work will concentrate on improving the characteristics of the output detector. One possible approach is to pump at S-band, so a 1N21B diode could be used for detection. Experiments show a much lower output impedance for this diode.

The data in Fig. 11. 5 was taken with a 10 kc signal. The X-band bandwidth of the varactor and detector mounts are shown in Fig. 11. 6 which shows that a video bandwidth of 300 Mc is possible if appropriate video input and output networks can be constructed. One possible solution to this problem is to use a high gain traveling wave tube for further X-band amplification prior to detection. The detector could be heavily loaded to yield the desired

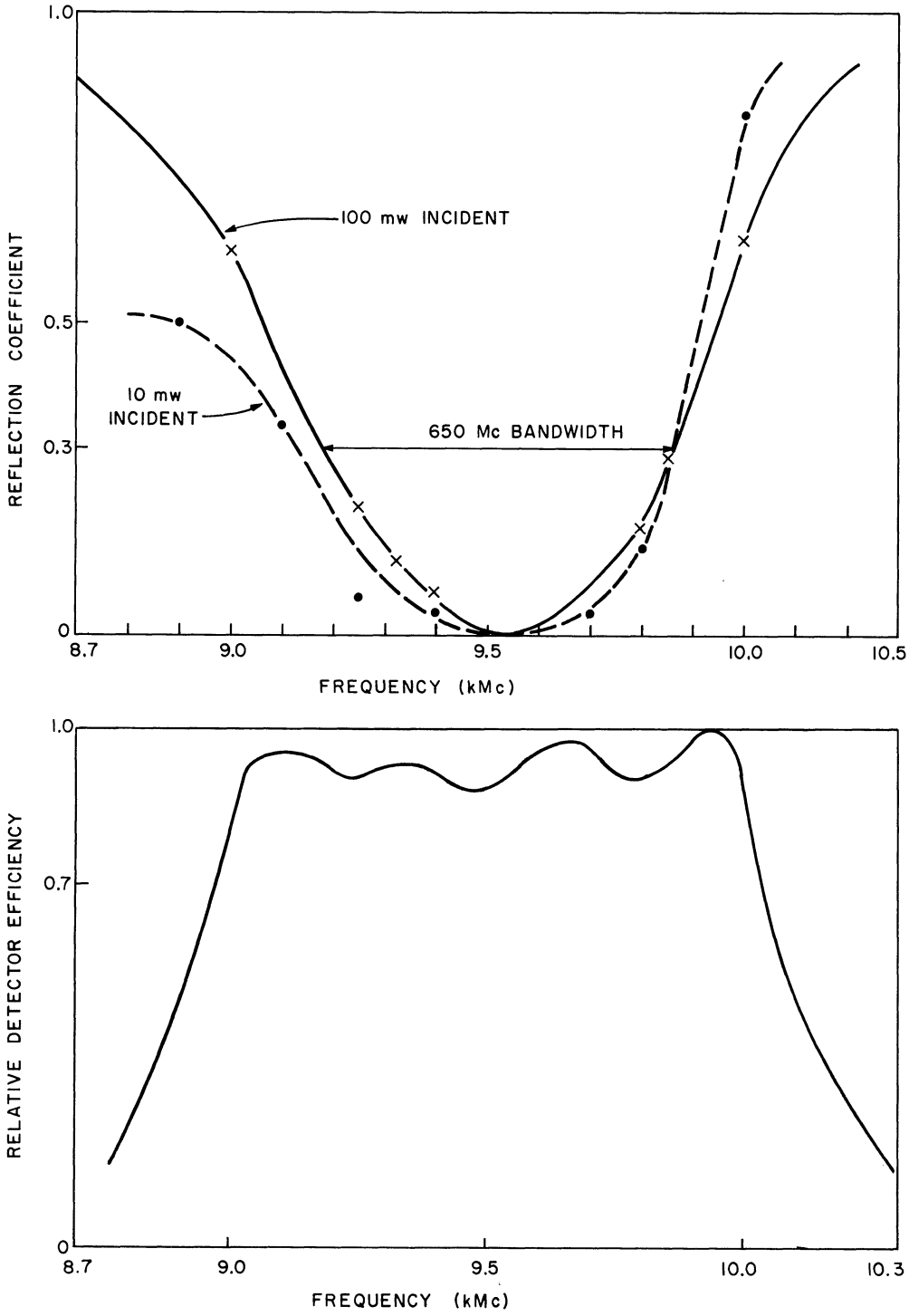

Fig. 11.6. Measured pass bands of the varactor mount and the detector. The latter curve is taken from an oscilloscope trace and is for a 1N23B diode in a triple-tuned mount.

video bandwidth, even though its efficiency is low. The net result would be a wideband video amplifier system, with noise figure determined by the varactor stage, and a net gain that is essentially that of the traveling wave tube.

These observations illustrate that much work remains to be done on this principle of amplification. Therefore, plans have been made to extend this study in the following directions:

1. To further evaluate the practical limitations on the basic version of this amplifier, by trying to improve detection efficiency and by comparing the performance obtained with different varactor types.
2. To consider multiple varactor structures for the purpose of greatly extending bandwidth.
3. To consider the use of predetection amplifiers, of a more conventional type, to obtain very wideband amplifier systems with low over-all noise figures.

11.2 Experiments with Double-Pump Circuits

The earliest experimental efforts were with the double-pump circuit described in Section 10.3. A low frequency version of this circuit was built, which is shown in Fig. 11.7. It has the schematic shown in Fig. 11.8, which is basically a three-pole network containing two time-varying capacitors; one pumped at ω_p and one at $2\omega_p$. Each pump circuit is balanced so pump tuning can be done independently of signal tuning. The signal circuit was then designed to be simultaneously resonant at 2.4 Mc ($= \omega_r/2\pi$), 5.4 Mc ($= \omega_\ell/2\pi$), and 10.2 Mc ($= \omega_u/2\pi$). Appropriately tuned networks were then coupled to the signal network to allow for independent sideband loading.

This circuit did show the predicted gain improvement due to harmonic pumping. It also showed the predicted phase criticality between ω_p and $2\omega_p$. However, it was hard to keep the three signal frequencies aligned well enough to obtain useful data. The alignment difficulty was further enhanced by the generation of negative resistance, which greatly narrows the conversion bandwidth. Therefore, it became apparent that a low-frequency version of this circuit was probably not a simplification. In fact, Y. Kaito of the Nippon Electric Company in

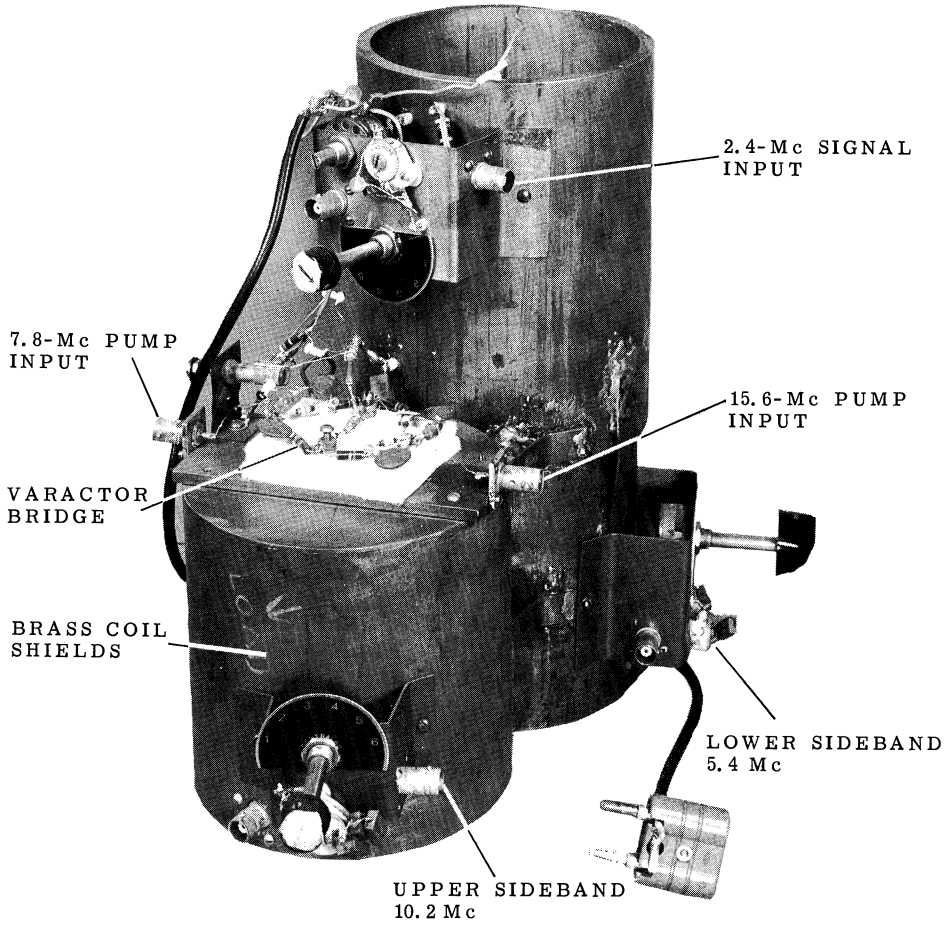

Fig. 11.7. A low frequency version of the double-pump reactive mixer.

Japan has recently employed this double-pumping technique at microwave frequencies (Ref. 39). He converted from 190 Mc to 1220 Mc with 13 db gain and 500 kc bandwidth. His pumping signals were 0.5 Mw at 1030 Mc and 4 Mw at 2060 Mc, and to further support the theory in Section 10.3, Kaito measured an input VSWR of two and an output VSWR of three, which shows a fair condition of match.

The circuit in Fig. 11.7 has had its greatest success in studying stability. In the initial experiments, only the pump fundamental was applied and then the loading at ω_ℓ and ω_u was varied independently. In following this procedure, the regenerative and degenerative effects of the lower and upper sideband respectively were clearly seen. A typical result is

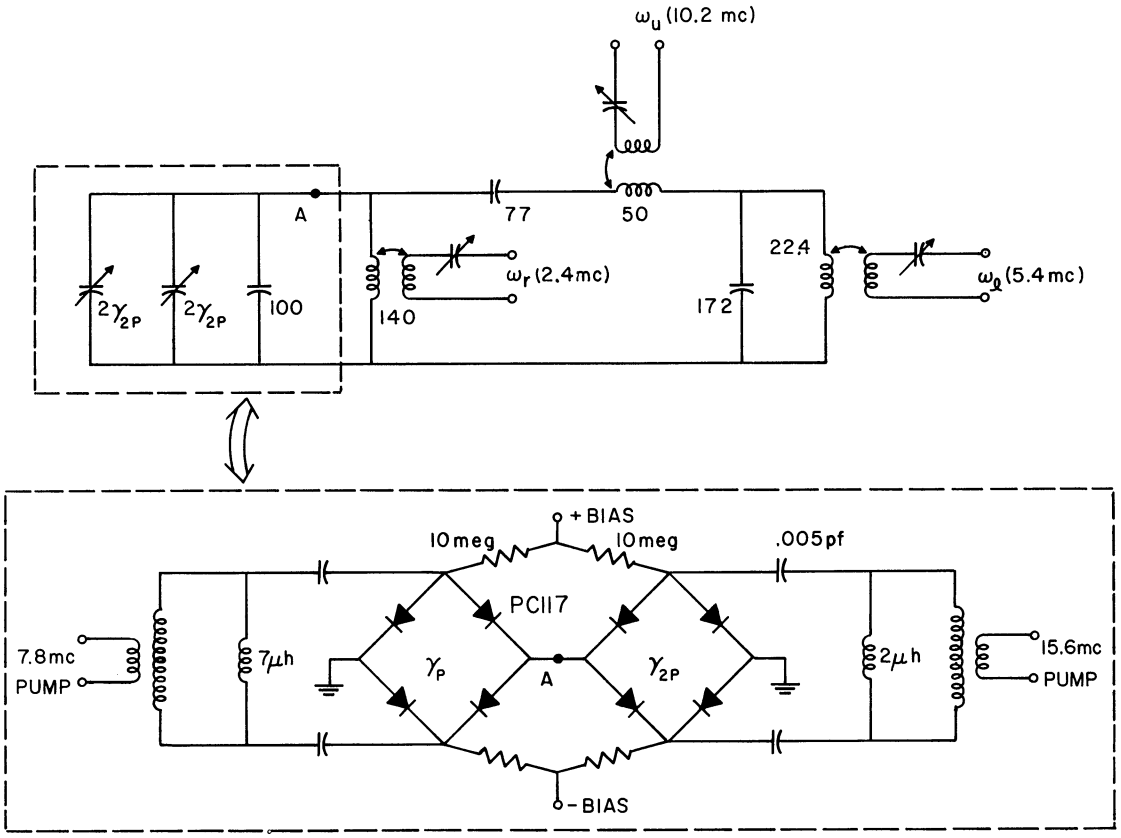

Fig. 11.8. Schematic for Fig. 11.7.

shown in Fig. 11.9, which shows the effect of a swept signal applied to the ω_r coupling network. In the absence of pumping, the latter experiences a suck-out (curve A) due to the resonance of the secondary three-pole network. When the pump was applied, the suck-out was modified according to the relative loading at ω_u and ω_ℓ, as shown in curves B and C. The influence of ω_ℓ was to reflect negative resistance that greatly sharpened the effect of the secondary. In fact, the primary current could be reduced to zero by loading the lower sideband lightly with respect to the upper sideband. This case corresponds to a net resistance of zero in the secondary. Further, pumping was found to reflect large negative resistances into the primary, but these were expected to cause instability according to the criterion adopted in the early investigations of this problem (Ref. 19).

But this experiment made it apparent that some distinction had to be made between short and open circuit stability, which lead to the analysis in Chapter VI. From the

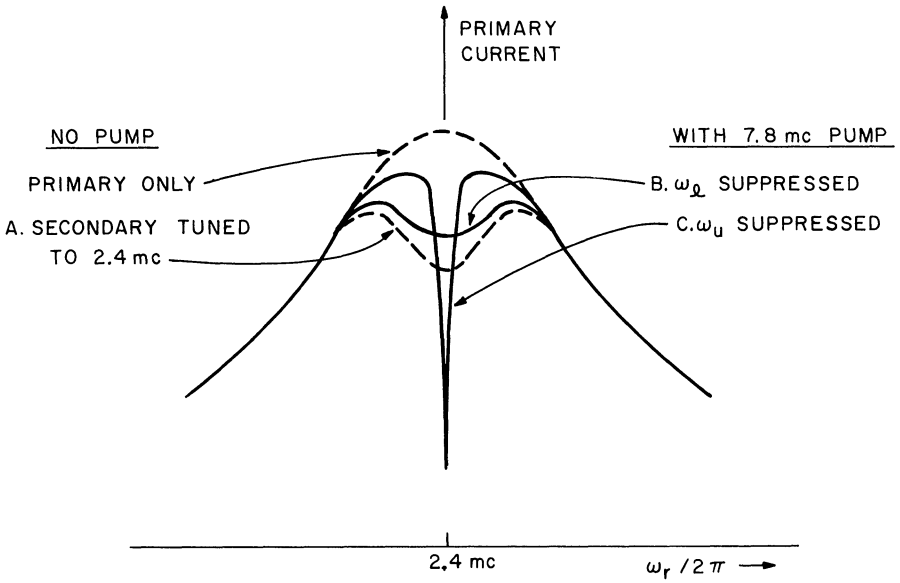

Fig. 11.9. The response to a swept signal at ω_r terminals in Fig. 11.8. The regenerative effects of the lower sideband are clearly distinguishable from the regenerative effects of the upper sideband.

latter, it could be concluded that the net series resistance in the primary of Fig. 11.9 must go through zero, rather than infinity, to produce instability. This criterion is supported by the stable response curves shown in Fig. 11.10, which show the net primary resistance going negative, first through infinity, and then through zero. Only the latter was found to be unstable.

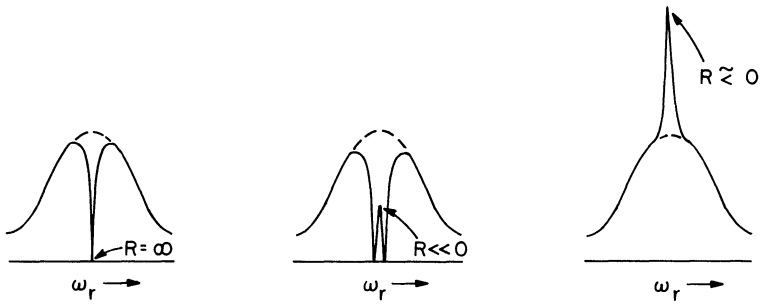

Fig. 11.10. Stable response curves for Fig. 11.8, similar to those in Fig. 11.9. Instability occurs when R = 0, where R is the net primary resistance (initial plus reflected).

Although the added complexity of double-pump circuits with independent sideband loading make their application more tedious, they do offer greater flexibility. Still their use may have to wait for more demanding applications that will undoubtedly accompany future advances in the state-of-the-art. However, the relative simplicity of double pumping with dependent sideband loading, as depicted in Fig. 10.7, may lead to an immediate application of double pumping. To date, no experiments have been conducted on this effect, but the theory offered in Section 10.4 motivates such an effort.

11.3 Conclusions

The advent of time-varying circuit elements at microwave frequencies has added exciting new degrees of freedom to circuit theory. In this study, a thorough examination has been made of a representative system of this new work area. In particular, the circuit properties of a nonreciprocal three-port network have been analyzed. It is defined by the admittance matrix in (2.27). The active elements in this network are two time-varying capacitors (i.e., pumps) at harmonically-related frequencies.

In addition to the general case, several special cases have been treated. They have been obtained by restricting the original network to: one pump frequency, and two or three signal frequencies. The simplest case of reactive mixing occurs with one pump and two signal frequencies. Since the properties of the latter were well known prior to this study, they have been used as a basis of comparison for the more complex cases that are introduced in this study. The latter have shown advantages in the form of higher gain-bandwidth products, lower noise figures, and greater stability, but by incurring greater system complexity. While the above advantages do not occur simultaneously, it is encouraging that some configurations have shown improvements in one property, without being seriously degraded in others.

A number of original contributions have been made in this study, which include the following:

1. Improvements have been made in the conversion between ω_r and ω_u, by introducing ω_ℓ, but by retaining a single pump frequency. These include:
   (a) A 6 db improvement in up-conversion gain, while retaining an optimum gain-bandwidth product.

(b) Infinite gain improvement, with a 30 percent reduction in gain-bandwidth product.

(c) A small reduction in up-conversion noise figure that is further enhanced by cooling the lower sideband load.

(d) A significant reduction in down-conversion noise figures.

2. When the pump harmonic is added, further improvements in conversion between ω_r and ω_u have been noted. These include:

(a) Infinite nonreciprocal gains, with matched inputs and outputs.

(b) Less sensitivity to external parameter variations.

(c) Increased gain-bandwidth products.

(d) Optimum noise figures, which are the same as those for conventional infinite gain converters, but that can be improved by cooling the lower sideband load.

(e) Greatly improved down-conversion noise figures with an asymptotic limit of 3 db. The latter is nearly realizable over a wide parameter range.

3. A new method of parametric video amplification has been treated that offers very wide bandwidths (dc to 100 Mc) and low noise figures. When realized with modern reactive mixer components (i. e., varactors), it yields an extremely useful amplifier that can operate in several ways. The method corresponding to phase modulation has been shown to be the most successful.

4. A simple method of estimating the stability of a periodically varying network has been derived. It depends only on a

knowledge of the steady-state response, and it is considerably easier than the conventional method of calculating characteristic roots.

5. Experimental observations have been made on all of the effects cited above, and each has been confirmed at least qualitatively.

Regarding areas for further study, it should be noted that much work remains to be done in the analysis of time-varying systems. Even in relatively simple systems the number of sensitive parameters tends to be large, so many useful effects remain undiscovered. Hopefully, by building system complexity one layer at a time, the basic properties of time-varying networks will become more evident. Perhaps this will aid the development of a more complete theory.

Also, much work remains in practical applications. It takes considerable time to learn techniques for working with nonlinear reactance elements, but once mastered these elements can often be used in relatively simple circuit configurations. Then, as each circuit is reduced to its simplest form, it becomes ready for the next level of sophistication.

APPENDIX A

THE DERIVATION OF OPTIMUM NOISE FIGURE FORMULAS

The basic noise figure formula for lower-sideband reactive mixers has been given in (5.27). This formula can be written more simply as

$$F = 1 + \frac{g_{dr} T_d}{g_S T_o} + \frac{1}{\rho_\ell}\left(\frac{\bar{\omega}_r}{\bar{\omega}_\ell}\right)\left(\frac{g_r T_\ell}{g_S T_o}\right) \qquad \text{(A-1)}$$

where T_ℓ is the effective noise temperature of the total conductance at ω_ℓ [see (5.27c)]. Considerably study has been given to this relation, which applies both to conversion gain and to parametric amplification. Perhaps the earliest of these studies was by Knechtli and Weglein (Ref. 40), although it was followed closely by Kotzebue (Ref. 41). A more elegant, but somewhat later treatment, was by Greene and Sard (Ref. 42) who studied (A-1) as it applies to a one-port parametric amplifier with circulator (see Section 5.3). Their approach is followed here.

Using the notation

$$R_r = \left(\frac{\bar{\omega}_r}{\omega_d}\right)^2 \left(\frac{C}{\gamma_p}\right)^2 ; \qquad t = \frac{T_L}{T_d}$$

$$x = \frac{g_S}{g_r} ; \qquad z = \frac{g_L}{g_\ell}$$

then

$$\frac{T_\ell}{T_d} = 1 + z(t-1)$$

and (A-1) becomes

$$F = 1 + \frac{T_d}{T_o}\left[\frac{1}{x}\left\{1 + \frac{1}{\rho_\ell}\frac{\overline{\omega}_r}{\omega_\ell}[1 + z(t-1)]\right\} - 1\right] \tag{A-2}$$

An added constraint on (A-2) is that for large gains

$$\rho_\ell = \left(\frac{\overline{\omega}_r}{\overline{\omega}_\ell}\right)\left[\frac{(1-x)(1-z)}{R_r}\right] \approx 1 \tag{A-3}$$

Eliminating $\overline{\omega}_r/\overline{\omega}_\ell$ from the last two relations yields

$$F = 1 + \frac{T_d}{T_o}\left[\frac{1}{x}\left\{1 + \frac{R_r[1+z(t-1)]}{(1-z)(1-x)}\right\} - 1\right] \tag{A-4}$$

Two basic observations can now be made regarding (A-4):

(1) Because this relation increases monotonically with z, any external loading at ω_ℓ (i.e., $z \neq 0$) will raise the noise figure, unless this extra loading has a zero degree noise temperature ($t = 0$).

(2) There is an optimum input efficiency x for any R, t, and output efficiency z. Each optimum x corresponds to a unique $\overline{\omega}_\ell/\overline{\omega}_r$ ratio, so F will improve with increasing ω_p only up to a point. This point depends basically on varactor quality.

The noise figure relation in (A-4) has a general form that appears frequently in reactive mixer analysis, which is

$$F = 1 + \frac{T_d}{T_o}\left[\frac{1}{x}\left(1 + \frac{\alpha}{1-x}\right) - 1\right] \tag{A-5}$$

The parameter α depends basically upon properties of the varactor, but other effects may be included. When (A-5) is minimized with respect to x, the optimum input efficient is found to be

$$x_{opt} = 1 + \alpha - \sqrt{\alpha + \alpha^2} = 1 - \frac{1}{1 + \sqrt{1 + \frac{1}{\alpha}}} \qquad \text{(A-6)}$$

which is plotted in Fig. A. 1. The corresponding optimum noise figure is

$$(F)_{opt} = 1 + 2\alpha \frac{T_d}{T_o} \left[1 + \sqrt{1 + \frac{1}{\alpha}}\right] \qquad \text{(A-7a)}$$

so the optimum noise temperature is

$$(T)_{opt} = 2\alpha \, T_d \left[1 + \sqrt{1 + \frac{1}{\alpha}}\right] \qquad \text{(A-7b)}$$

which is also plotted in Fig. A. 1. From this figure it is evident that small α's are desirable. For example, T is less than T_d if α is less than 0. 1.

For lower-sideband mixers, whose noise figures are given by (A-4), the parameter α has the value

$$\alpha = \frac{R_r[1+z(t-1)]}{1-z} \qquad \text{(A-8)}$$

Therefore, by (A-3), the optimum choice of frequencies is

$$\left(\frac{\omega_r}{\omega_\ell}\right)_{opt} = \frac{R_r}{(1-x_{opt})(1-z)} \qquad \text{(A-9a)}$$

$$= \left(\frac{R_r}{1-z}\right)\left[1 + \sqrt{1 + \frac{1-z}{R_r[1+z(t-1)]}}\right] \qquad \text{(A-9b)}$$

and by (A-7a)

$$(F)_{\text{lower sideband}} = 1 + \frac{2R_r[1+z(t-1)]}{1-z} \left[1 + \sqrt{1 + \frac{1-z}{R_r[1+z(t-1)]}}\right] \qquad \text{(A-10)}$$

The previous studies cited (Refs. 40, 41, and 42) have considered (A-10) as it applies to the one-part parametric amplifier. A later study, by Karokawa and Uenohara (Ref. 30), has shown that (A-1) through (A-4) also apply to conversion from ω_r to ω_ℓ, so (A-10) is the optimized value of (A-4) in this case too. The latter optimization is further discussed in Section 5. 2. 2.

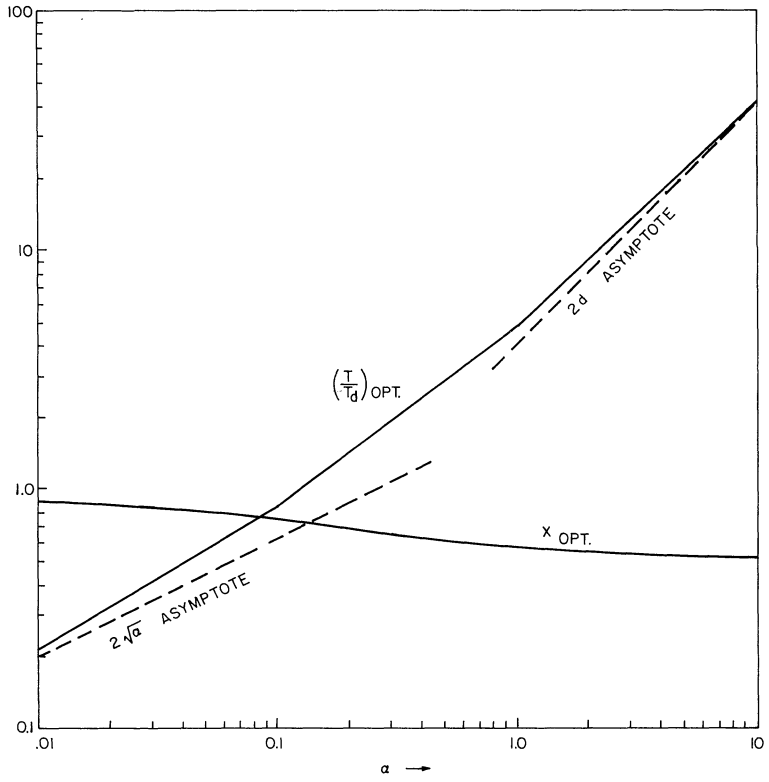

Fig. A. 1. Optimum noise temperatures for (A-5) vs. the general parameter α .

The main difference that arises between the amplifier and the converter is that z is proportional to the output load in the converter and hence cannot be zero. However, for a given z, the optimum noise figure of the converter can be found as above, which yields the result in (5. 32). Therefore, the optimum converter noise figure exceeds that of an amplifier with the same input frequency $\overline{\omega}_r$. This fact should serve to correct some misleading statements in the literature. For example, on p. 721, Ref. 30 says that "... the amplifier and converter give the same noise figure ..." A more accurate statement would be that they give the same noise figure formula (for high gains) but not with the same minimum obtainable value.

The more general optimum noise figure relations in (A-7) will be shown to apply to many reactive mixer configurations. Therefore, they provide a convenient basis for comparing various reactive mixers, which is the purpose of this study.

APPENDIX B

THE DERIVATION OF PHASE MODULATION NOISE FIGURE

The derivation of (9.63) and (9.64) proceeds as follows. Letting

$$p = \frac{\omega_r}{\sqrt{\beta_r \beta_p}} ; \quad q = \frac{\omega_p}{\sqrt{\beta_r \beta_p}} ; \quad \mu = \sqrt{\frac{\beta_r}{\beta_p}} + \sqrt{\frac{\beta_p}{\beta_r}} \tag{B-1}$$

then (9.61) and (9.62) become

$$\left| Y_{u_{in}} \right|^2 = g_p{}^2 \left(1 + \frac{\beta_r}{\beta_p} p^2 \right) \left| \frac{1 - p^2 + k_p{}^2 p^2 + jpu}{1 - p^2 - 1/2\, p(q - p)k_p{}^2 + jpu} \right|^2 \tag{B-2}$$

$$\left| Y_{u\ell} \right|^2 = g_p{}^2 \left(1 + \frac{\beta_s}{\beta_o} p^2 \right) \left| \frac{1 - p^2 + k_p{}^2 p^2 + jpu}{1/2\, p(q + p)k_p{}^2} \right|^2 \tag{B-3}$$

When these equations are combined to form (9.60), terms of odd symmetry in ω_r can be dropped, since the integral of (9.60) is desired. The noise power delivered to $\tilde{g}_p$ now becomes

$$\tilde{P}_p = \int_{-\infty}^{\infty} P(\omega_r) d\omega_r = \frac{4kT_p}{2\pi} \int_{-\infty}^{\infty} \frac{\beta_r \beta_p \, dp}{\left(1 + \frac{\beta_r}{\beta_p} p^2 \right)} \times \left\{ \frac{\left[1 - p^2 \left(1 - \frac{k_p{}^2}{2} \right) \right]^2 + (pu)^2 + \left(\frac{k_p{}^2}{2} \right) p^2 (p^2 + 2q^2)}{\left[1 - p^2 (1 - k_p{}^2) \right]^2 + (pu)^2} \right\} \tag{B-4}$$

and if $k_p{}^2 << 1$ and $p^2 << q^2$, this relation can be reduced to

$$P_p = \frac{4kT_p}{2\pi} \int_{-\infty}^{\infty} \frac{\sqrt{\beta_r \beta_p} \, dp}{\left(1 + \frac{\beta_r}{\beta_p} p^2 \right)} \left[1 + \frac{1/2 \, (k_p{}^2 pq)^2}{(1 - p^2)^2 + (pu)^2} \right] \tag{B-5}$$

which is equivalent to (9.63).

When (B-5) is integrated term by term, the first term yields (Dwight 120.01)

$$\frac{4kT_p}{2\pi} \int_{-\infty}^{\infty} \frac{\sqrt{\beta_r \beta_p}\, dp}{\left(1 + \frac{\beta_r}{\beta_p} p^2\right)} = \left(\frac{4kT_p}{2\pi}\right)\left(\pi \beta_p\right) \qquad \text{(B-6)}$$

In the second term,

$$(1 - p^2)^2 + (pu)^2 \approx (p^2 + \frac{1}{u^2})(p^2 + u^2 - 2)$$

if $u^2 > 4$. Therefore, for the case where $\beta_p >> \beta_p$, so that $u^2 \approx \frac{\beta_p}{\beta_r} >> 1$, the second term in (B-6) becomes approximately (Dwight 120.2).

$$\left(\frac{4kT_p}{2\pi}\right)\sqrt{\beta_r \beta_p} \int_{-\infty}^{\infty} \frac{1/2\left(\frac{k_p{}^2 q}{u}\right)^2 dp}{[1 + (\frac{p}{u})^2]^2} = \left(\frac{4kT_p}{2\pi}\right) k_p{}^4 q^2 (\frac{\pi}{4u}) \sqrt{\beta_r \beta_p} \qquad \text{(B-7)}$$

However, at the other extreme, if $\beta_p = \beta_r$ so $u = 2$

$$\left(\frac{4kT_p}{2\pi}\right) \beta_p \int \frac{1/2\,(k_p{}^2 q)^2 p^2\, dp}{(1 + p^2)^3} = \left(\frac{4kT_p}{2\pi}\right) k_p{}^4\, q^2\, (\frac{\pi}{8})\, \beta_o \qquad \text{(B-8)}$$

which is the same as (B-7) with $u = 2$. Therefore (B-7) is valid for $u \geq 2$.

Equation (9.64) can now be obtained directly from (B-6) and (B-7). It should be noted that the approximations made in obtaining (B-7) introduce positive errors, so (9.64) is a slightly conservative estimate of output noise power.

REFERENCES

1. W. W. Mumford, "Some Notes of the History of Parametric Transducers," Proc. IRE, Vol. 48, May 1960, pp. 848-853.

2. E. F. W. Alexanderson, "A Magnetic Amplifier for Radio Telephony," Proc. IRE, Vol. 4, April 1916, pp. 101-149.

3. H. Torry and O. A. Whitmer, Crystal Rectifiers, MIT Radiation Laboratory Series, McGraw-Hill Book Co., Inc., New York, New York, Vol. 15, 1948.

4. J. M. Manley and E. Peterson, "Negative Resistance Effects in Saturable Reactor Circuits," Trans. AIEE, Vol. 65, December 1946, pp. 870-881.

5. L. C. Peterson and F. B. Llewellyn, "The Performance and Measurements of Mixers in Terms of Linear Network Theory," Proc. IRE, Vol. 33, July 1945, pp. 458-476.

6. A. Van der Zeil, "On the Mixing Properties of Nonlinear Condensers," Journal of Applied Physics, November 1948, pp. 999-1006.

7. R. V. Pound, Microwave Mixers, MIT Radiation Laboratory Series, McGraw-Hill Book Co., Inc., New York, New York, Vol. 16, 1948.

8. A Uhlir, Jr., Possible Uses of Nonlinear Capacitor Diodes, Bell Telephone Laboratories, Eighth Interim Report on Task 8, Signal Corps Contract No. DA-36-039-565589, July 1956.

9. A. E. Bakanowski, The Nonlinear Capacitor as a Mixer, Second Interim Report on Task 8, Crystal Rectifiers, Signal Corps Project 2-7-323A, December 1954.

10. A. C. Macpherson, "An Analysis of the Diode Mixer Consisting of Nonlinear Capacitance and Conductance and Ohmic Spreading Resistance," IRE Trans. on Microwave Theory and Techniques, Vol. MIT-5, January 1957, pp. 43-51.

11. J. M. Manley and H. E. Rowe, "Some General Properties of Nonlinear Elements, Part I. General Energy Relations," Proc. IRE, Vol. 44, July 1956, pp. 904-913.

12. C. F. Edwards, "Frequency Conversion by Means of a Nonlinear Admittance," Bell System Technical Journal, Vol. 35, November 1956, pp. 1403-1416.

13. S. Duinker, "General Properties of Frequency Converting Networks," Phillips Research Reports, Vol. 13, February 1958, pp. 37-78, April 1958, pp. 101-148.

14. H. Heffner and G. Wade, "Noise, Gain and Bandwidth Characteristics of the Variable Parameter Amplifiers," presented at IRE PGED meeting, Washington, D. C., October 31 to November 1, 1957. (Abstract, IRE Trans. on Electron Devices, Vol. ED-5, April 1958, p. 112.)

15. G. G. Herrmann, M. Uenohara, and A. Uhlir, Jr., "Noise Figure Measurements on Two Types of Variable Reactance Amplifiers Using Semiconductor Diodes," Proc. IRE, Vol. 46, June 1958, pp. 1301-1303.

REFERENCES (Cont.)

16. D. Leenov, "Gain and Noise Figure of a Variable Capacitance Up-Converter," Bell Systems Technical Journal, Vol. 37, July 1958, pp. 989-1008.

17. C. L. Hogan, R. L. Jepsen, and P. H. Vartanian, "New Type of Ferromagnetic Amplifier," Journal of Applied Physics, Vol. 29, March 1958, pp. 422-423.

18. Hsu Hsiung, "Multiple Frequency Parametric Devices," Digest of Technical Papers, 1959 Solid-State Circuits Conference, Philadelphia, Pennsylvania, February 1959.

19. D. K. Adams, "An Analysis of Four-Frequency Nonlinear Reactance Circuits," IRE Transactions on Microwave Theory and Techniques, Vol. MIT-8, No. 3, May 1960, pp. 274-283. (See also, D. K. Adams, Some Considerations of Four-Frequency Nonlinear Reactance Circuits, Cooley Electronics Laboratory Technical Report No. 96, The University of Michigan, Ann Arbor, Michigan, September 1959.)

20. D. K. Adams, "Circuit Properties of a Double-Sideband, Doubly-Pumped Nonlinear Reactance Modulator," Proc. of National Electronics Conference, Vol. XVI, October 1960, pp. 480-486.

21. H. Brett, F. A. Brand, and W. G. Matthei, "A Varactor Diode Parametric Standing-Wave Amplifier," Proc. IRE, Vol. 49, No. 2, February 1961, pp. 509-510.

22. D. K. Adams, An Analysis of the Brett Ultra-Wideband Video Amplifier, Cooley Electronics Laboratory Technical Report No. 122, The University of Michigan, Ann Arbor, Michigan, July 1961.

23. B. J. Leon, "A Frequency Domain Theory for Parametric Networks," IRE Trans. on Circuit Theory, Vol. CT-7, September 1960, pp. 321-329.

24. J. M. Manley and H. E. Rowe, "General Energy Relations in Nonlinear Reactances," Proc. IRE, Vol. 47, December 1959, pp. 2115-2116.

25. J. M. Manley and H. E. Rowe, "General Energy Relations in Nonlinear Reactances," Proc. IRE, Vol. 44, July 1956, pp. 904-913.

26. S. Sensiper and R. D. Weglein, "Capacitance and Charge Coefficients for Parametric Diode Devices," Proc. IRE, Vol. 48, August 1960, pp. 1482-1483.

27. M. T. Weiss, "Quantum Derivation of Energy Relations Analogous to Those for Non-Linear Reactances," Proc. IRE, Vol. 45, July 1957, pp. 1012-1013.

28. F. E. Terman, Electronic and Radio Engineering, McGraw-Hill Book Co., Inc., New York, New York, 1955.

29. E. M. T. Jones and J. S. Honda, "A Low-Noise Up-Converter Parametric Amplifier," IRE Wescon Convention Record, August 18-21, 1959, pp. 99-107.

30. K. Kurokawa and M. Uenohara, "Minimum Noise Figure of the Variable-Capacitance Amplifier," The Bell System Technical Journal, Vol. XL, No. 3, May 1961.

31. H. E. Rowe, "Some General Properties of Nonlinear Elements, II. Small Signal Theory," Proc. IRE, Vol. 46, May 1958, pp. 850-860.

32. P. P. Lombardo and E. W. Sard, "Low-Noise Microwave Reactance Amplifiers with Large Gain-Bandwidth Products," 1959 IRE Wescon Convention Record, August 18-21, 1959, pp. 83-98.

REFERENCES (Cont.)

33. F. R. Moulton, Differential Equations, Dover Publications, Inc., New York, New York, 1958.

34. S. Bloom and K. K. N. Chang, "Parametric Amplification Using Low Frequency Pumping," Journal of Applied Physics, Vol. 29, March 1958, p. 594.

35. K. K. N. Chang and S. Bloom, "Parametric Amplifier Using Lower Frequency Pumping," Proc. IRE, Vol. 46, July 1958, pp. 1383-1386.

36. K. K. N. Chang and S. Bloom, "A Parametric Amplifier Using Low Frequency Pumping," 1958 Wescon Convention Record, Pt. 3, pp. 23-27.

37. L. A. Blackwell and K. L. Kotzebue, Semiconductor-Diode Parametric Amplifiers, Prentice-Hall, Inc., Englewood Cliffs, New Jersey, 1961.

38. R. C. Mackey, "Some Characteristics of Microwave Balanced Modulators," IRE Trans. on Microwave Theory and Techniques, Vol. MTT-10, March 1962, pp. 114-117.

39. Y. Kaito, "Two-Frequency Pumping Parametric Amplifier," Convention Record of the Institute of Electrical Communication Engineers of Japan, May 1962.

40. R. C. Knechtli and R. D. Weglein, "Low-Noise Parametric Amplifiers," Proc. IRE, Vol. 47, April 1959, pp. 584-585.

41. K. L. Kotzebue, "Optimum Noise Performance of Parametric Amplifiers," Proc. IRE, Vol. 47, October 1959, pp. 1782-1783.

42. J. C. Greene and E. W. Sard, "Optimum Noise and Gain-Bandwidth Performance for a Practical One-Port Parametric Amplifier," Proc. IRE, Vol. 48, September 1960, pp. 1583-1590.

DISTRIBUTION LIST

Copy No.	
1-2	Commanding Officer, U. S. Army Electronics Research and Development Laboratory, Fort Monmouth, New Jersey, ATTN: Senior Scientist, Electronic Warfare Division
3	Commanding General, U. S. Army Electronic Proving Ground, Fort Huachuca, Arizona, ATTN: Director, Electronic Warfare Department
4	Chief, Research and Development Division, Office of the Chief Signal Officer, Department of the Army, Washington 25, D. C., ATTN: SIGEB
5	Commanding Officer, Signal Corps Electronic Research Unit, 9560th USASRU, P. O. Box 205, Mountain View, California
6	U. S. Atomic Energy Commission, 1901 Constitution Avenue, N. W., Washington 25, D. C., ATTN: Chief Librarian
7	Director, Central Intelligence Agency, 2430 E Street, N. W., Washington 25, D. C., ATTN: OCD
8	Signal Corps Liaison Officer, Lincoln Laboratory, Box 73, Lexington 73, Massachusetts, ATTN: Col. Clinton W. James
9-18	Commander, Armed Services Technical Information Agency, Arlington Hall Station, Arlington 12, Virginia
19	Commander, Air Research and Development Command, Andrews Air Force Base, Washington 25, D. C., ATTN: SCEC, Hq.
20	Directorate of Research and Development, USAF, Washington 25, D. C., ATTN: Electronic Division
21-22	Hqs., Aeronautical Systems Division, Air Force Command, Wright-Patterson Air Force Base, Ohio, ATTN: WWAD
23	Hqs., Aeronautical Systems Division, Air Force Command, Wright-Patterson Air Force Base, Ohio, ATTN: WCLGL-7
24	Hqs., Aeronautical Systems Division Air Force Command, Wright-Patterson Air Force Base, Ohio - For retransmittal to - Packard Bell Electronics, P. O. Box 337, Newbury Park, California
25	Commander, Air Force Cambridge Research Center, L. G. Hanscom Field, Bedford, Massachusetts, ATTN: CROTLR-2
26-27	Commander, Rome Air Development Center, Griffiss Air Force Base, New York, ATTN: RCSSLD - For retransmittal to - Ohio State University Research Foundation
28	Commander, Air Proving Ground Center, ATTN: Adj/Technical Report Branch, Eglin Air Force Base, Florida

DISTRIBUTION LIST (Cont.)

Copy No.

29 Chief, Bureau of Naval Weapons, Code RRR-E, Department of the Navy, Washington 25, D. C.

30 Chief of Naval Operations, EW Systems Branch, OP-35, Department of the Navy, Washington 25, D. C.

31 Chief, Bureau of Ships, Code 691C, Department of the Navy, Washington 25, D. C.

32 Chief, Bureau of Ships, Code 684, Department of the Navy, Washington 25, D. C.

33 Chief, Bureau of Naval Weapons, Code RAAV-33, Department of the Navy, Washington 25, D. C.

34 Commander, Naval Ordnance Test Station, Inyokern, China Lake, California ATTN: Test Director - Code 30

35 Director, Naval Research Laboratory, Countermeasures Branch, Code 5430, Washington 25, D. C.

36 Director, Naval Research Laboratory, Washington 25, D. C., ATTN: Code 2021

37 Director, Air University Library, Maxwell Air Force Base, Alabama, ATTN: CR-4987

38 Commanding Officer - Director, U. S. Naval Electronic Laboratory, San Diego 52, California

39 Office of the Chief of Ordnance, Department of the Army, Washington 25, D. C., ATTN: ORDTU

40 Chief, West Coast Office, U. S. Army Electronics Research and Development Laboratory, Bldg. 6, 75 S. Grand Avenue, Pasadena 2, California

41 Commanding Officer, U. S. Naval Ordnance Laboratory, Silver Spring 19, Maryland

42-43 Chief, U. S. Army Security Agency, Arlington Hall Station, Arlington 12, Virginia, ATTN: IADEV

44 President, U. S. Army Defense Board, Headquarters, Fort Bliss, Texas

45 President, U. S. Army Airborne and Electronics Board, Fort Bragg, North Carolina

46 U. S. Army Antiaircraft Artillery and Guided Missile School, Fort Bliss, Texas

47 Commander, USAF Security Service, San Antonio, Texas, ATTN: CLR

48 Chief, Naval Research, Department of the Navy, Washington 25, D. C., ATTN: Code 931

Copy No.

49 Commanding Officer, U. S. Army Security Agency, Operations Center, Fort Huachuca, Arizona

50 President, U. S. Army Security Agency Board, Arlington Hall Station, Arlington 12, Virginia

51 Operations Research Office, Johns Hopkins University, 6935 Arlington Road, Bethesda 14, Maryland, ATTN: U. S. Army Liaison Officer

52 The Johns Hopkins University, Radiation Laboratory, 1315 St. Paul Street, Baltimore 2, Maryland, ATTN: Librarian

53 Stanford Electronics Laboratories, Stanford University, Stanford, California, ATTN: Applied Electronics Laboratory Document Library

54 HRB - Singer, Inc., Science Park, State College, Pennsylvania, ATTN: R. A. Evans, Manager, Technical Information Center

55 ITT Laboratories, 500 Washington Avenue, Nutley 10, New Jersey, ATTN: Mr. L. A. DeRosa, Div. R-15 Lab.

56 Director, USAF Project Rand, via Air Force Liaison Office, The Rand Corporation, 1700 Main Street, Santa Monica, California

57 Stanford Electronics Laboratories, Stanford University, Stanford, California, ATTN: Dr. R. C. Cumming

58 Stanford Research Institute, Manlo Park, California, ATTN: Dr. Cohn

59-60 Commanding Officer, U. S. Army Signal Missile Support Agency, White Sands Missile Range, New Mexico, ATTN: SIGWS-EW and SIGWS-FC

61 Commanding Officer, U. S. Naval Air Development Center, Johnsville, Pennsylvania, ATTN: Naval Air Development Center Library

62 Commanding Officer, U. S. Army Electronics Research and Development Laboratory, Fort Monmouth, New Jersey, ATTN: U. S. Marine Corps Liaison Office, Code AO-C

63 President, U. S. Army Signal Board, Fort Monmouth, New Jersey

64-72 Commanding Officer, U. S. Army Electronics Research and Development Laboratory, Fort Monmouth, New Jersey

ATTN: 1 Copy — Director of Research
1 Copy — Technical Documents Center ADT/E
1 Copy — Chief, Special Devices Branch, Electronic Warfare Div.
1 Copy — Chief, Advanced Techniques Branch, Electronic Warfare Div.
1 Copy — Chief, Jamming and Deception Branch, Electronic Warfare Div.
1 Copy — File Unit No. 2, Mail and Records, Electronic Warfare Div.

Copy No.

3 Cpys — Chief, Security Division
(for retransmittal to - EJSM)

73 Director, National Security Agency, Fort George G. Meade, Maryland, ATTN: TEC

74 Dr. B. F. Barton, Director, Cooley Electronics Laboratory, The University of Michigan, Ann Arbor, Michigan

75-96 Cooley Electronics Laboratory Project File, The University of Michigan, Ann Arbor, Michigan

97 Project File, The University of Michigan Office of Research Administration, Ann Arbor, Michigan

98 Bureau of Naval Weapons Representative, Lockheed Missiles and Space Co., P. O. Box 504, Sunnyvale, California - For forwarding to - Lockheed Aircraft Corp.

99 U. S. Army Research Liaison Office, MIT, Lincoln Laboratory, Lexington 73, Massachusetts

100 Lockheed Aircraft Corp., Technical Information Center, 3251 Hanover Street, Palo Alto, California

Above distribution is effected by Electronic Warfare Division, Surveillance Department, USAELRDL, Evans Area, Belmar, New Jersey. For further information contact Mr. I. O. Myers, Sr. Scientist, Telephone 5961262